

μ SR MEASUREMENT OF THE MAGNETIC PENETRATION DEPTH AND
COHERENCE LENGTH IN THE HIGH- T_C SUPERCONDUCTOR $YBa_2Cu_3O_{6.95}$

By

Tanya Maria Riseman

B.S. Stanford University, 1986

M.Sc. University of British Columbia, 1989

A THESIS SUBMITTED IN PARTIAL FULFILLMENT OF
THE REQUIREMENTS FOR THE DEGREE OF
DOCTOR OF PHILOSOPHY

in

THE FACULTY OF GRADUATE STUDIES
DEPARTMENT OF PHYSICS

We accept this thesis as conforming
to the required standard

THE UNIVERSITY OF BRITISH COLUMBIA

1993

© Tanya Maria Riseman, May 1993

In presenting this thesis in partial fulfilment of the requirements for an advanced degree at the University of British Columbia, I agree that the Library shall make it freely available for reference and study. I further agree that permission for extensive copying of this thesis for scholarly purposes may be granted by the head of my department or by his or her representatives. It is understood that copying or publication of this thesis for financial gain shall not be allowed without my written permission.

Department of PHYSICS

The University of British Columbia
Vancouver, Canada

Date MAY 27, 1993

Abstract

This thesis is concerned with the temperature dependence and anisotropy of the magnetic penetration depth (λ) and the Ginzburg-Landau parameter $\kappa = \lambda/\xi$ in the high temperature superconductor $\text{YBa}_2\text{Cu}_3\text{O}_{6.95}$ as observed by μSR measurements of the local field inhomogeneity produced by the vortex state. Measurements were taken on a mosaic of single crystals in applied fields in three field regimes: low ($\lambda < L$), moderate ($\lambda > L$) and high ($\lambda \gg L > \xi$), where L is the intervortex spacing and ξ is the coherence length.

The anisotropy of λ leads to variation in the measured field inhomogeneity as a function of the angle between the applied field and \hat{c} axis of the crystal. Measurements in 100 G are consistent with an anisotropy of five.

If the applied field is not parallel to one of the superconductor's principal axes, an attractive force between vortices along one direction arises when the superconductor is cooled in a constant and low field. When the net intervortex repulsion exceeds the forces pinning the vortices in place, the aspect ratio of the isosceles triangle defining the vortex lattice will change. Unfortunately, the degree of disorder, where disorder is defined as the mean deviation of the vortices from their ideal positions in the lattice relative to the distance between vortices, makes it impossible to determine the low temperature aspect ratio in $\text{YBa}_2\text{Cu}_3\text{O}_{6.95}$ using μSR . In the high field data, the degree of disorder has an upper limit of $\approx 5.5\%$.

In the vortex lattice, the maximum field is reached at the vortex core, which has a radius of $\approx \xi$. In the low and moderate field regimes, the core occupies a very small percentage of the unit cell of the lattice, so the maximum field is not observable by μSR . In the high field regime, the core results in a high field cutoff in the distribution of local fields, which can be observed directly in the Fourier transform of μSR data. Fitting both λ_{ab} and ξ_{ab} simultaneously in fields of 1.9 T, 4.1 T, 4.7 T and 6.5 T applied parallel to the \hat{c} axis of $\text{YBa}_2\text{Cu}_3\text{O}_{6.95}$ yields $\kappa_{ab} = 70 \pm 6$ between 30 K and 75 K. At 10 K, λ_{ab} is measured to be $0.1490 \pm 0.0120 \mu\text{m}$.

Table of Contents

Abstract	ii
List of Tables	vii
List of Figures	viii
Acknowledgements	xi
1 Introduction	1
1.1 Superconductivity: A Brief Historical Perspective	1
1.2 The London Formalism	3
1.3 The Superconducting Gap and the Pairing State	7
1.4 High Temperature Superconductivity [HTSC]	8
1.4.1 Magnetic Properties and the Underlying Mechanism of HTSC	8
1.5 $\xi(T)$, $\lambda(T)$ and $\kappa(T)$ in $\text{YBa}_2\text{Cu}_3\text{O}_{6.95}$	10
1.5.1 Flux Pinning and the Irreversibility Temperature	11
1.6 μSR in High T_c Superconductors	12
1.7 Sample	13
1.8 A note about units, etc.	14
2 Basics of Muon Spin Rotation and Relaxation	15
2.1 Overview	15
2.2 Production of Low Momentum μ^+	16
2.3 Experimental Apparatus	18
2.4 μSR Data	23
2.5 Sources of Experimental Distortions	27
2.5.1 Corrected Asymmetry Plots	27

2.5.2	Random Background	31
2.5.3	Relative Phase of Counters	32
2.6	Full Vector Treatment of Polarization Evolution	36
2.6.1	Motivation	36
2.6.2	Positron Counter and Local Field Reference Frames	37
2.6.3	Vectorized Polarization Functions	40
2.6.4	Discussion of Different Categories of Field Distributions	45
2.6.5	Uniaxial Local Field Polarization Functions	47
2.6.6	Some Visual Examples	50
2.6.7	Compounding Polarization Functions	53
3	Manipulation of μSR data	55
3.1	Introduction	55
3.2	The Rotating Reference Frame and The Art of Packing Data	55
3.2.1	The RRF Transformation in μ SR	55
3.2.2	RRF in high Fields	61
3.3	The Art of Fourier Transforms	62
3.3.1	The Fourier Transform in μ SR: $B_X(\vec{r}) = B_Y(\vec{r}) = 0$	62
3.3.2	The Fourier Transform in μ SR: General Case	66
3.3.3	Basics of a μ SR FFT Program	73
3.3.4	Apodization in FFTs	74
3.4	Convolution Versus Compounding	83
3.4.1	Convolution Theorem	83
4	Anisotropic London Theory	88
4.1	Treatment of Anisotropy	88
4.2	Derivation of the Anisotropic London Model	89
4.3	Choice of Reciprocal Lattice	94
4.3.1	High Field Limit	96
4.3.2	Vortex Chains for Low Fields	97

4.4	Effect of Vortex Core	98
4.5	The Magnetic Field Distribution and the μ SR Lineshape	98
4.5.1	Isotropic Case	98
4.5.2	Anisotropic Case	100
4.6	The Effect of Non <i>s</i> -Wave Pairing on the Lineshape	103
4.7	Disorder in the Flux Line Lattice	104
4.8	Discussion of Non-oscillatory Amplitude	107
4.9	The Demagnetizing Factor	110
5	Anisotropy of $\lambda(\theta)$ as Measured in Low Fields	113
5.1	Introduction and Motivation	113
5.2	Apparatus	113
5.3	The Chains Model Versus the Frozen Model	115
5.3.1	A Pictorial Exposé of the Chains Model and the Frozen Model	116
5.4	Experimental Results	122
5.4.1	Fourier Transforms of RIGHT/LEFT Counters	122
5.4.2	Simple Gaussian fits	125
5.4.3	Fits to the Chains and Frozen Models	132
5.4.3.1	Data Analysis	132
5.4.3.2	Results of Fits to the Chains Model	134
5.4.3.3	Results of Fits to the Frozen Model	138
5.5	Discussion	140
6	Intermediate Fields	142
6.1	Introduction	142
6.2	Analysis and Results	143
6.2.1	Fits to Exponentials	144
6.2.2	Fits to Gaussians	150
6.3	Discussion and Conclusions	150

7	High Field Lineshapes; Determination of H_{c2} and κ	157
7.1	Introduction	157
7.2	Apparatus for High Timing Resolution in High Fields	159
7.2.1	Motive	159
7.2.2	Apparatus	160
7.2.3	Muon Beam Oscillations	166
7.3	Modified London Model	172
7.4	Ambiguity in the Determination of λ and ξ	173
7.5	Data Analysis	173
7.6	Results	179
7.6.1	Sample	179
7.6.2	Intermediate Results	179
7.6.3	$\lambda_{ab}^{-2}(T)$, $H_{c2,\parallel,\hat{c}}(T)$ and $\kappa_{ab}(T)$	181
7.6.4	The Local Fields Versus Temperature	183
7.6.5	Degree of Disorder in the FLL	188
7.7	Discussion and Conclusions	192
8	Conclusions	197
	Bibliography	201
A	Preferred Rotating Reference Frame Frequencies	210
B	High Field χ^2 Scans and Lineshapes	214

List of Tables

3.1	Constants for Special Apodization	78
7.1	Distance between Beam Oscillation Nodes	170
7.2	Estimated Optimal Focusing Fields	171
7.3	Fits to Minimum, Cusp and Maximum Fields	187
A.1	Preferred RRF Frequencies 16 MHz to 1000 MHz	210
B.1	Temperatures and Number of Events per Run	215

List of Figures

2.1	Radial Plot of Positron Emission Probability	18
2.2	Omni Prime Apparatus	20
2.3	High Transverse Field (TF) Geometry	21
2.4	μ SR Time Differential Electronics Schematic	22
2.5	Single Histogram Experimental Time Spectrum	24
2.6	Experimental Two-Spectrum Raw Asymmetry <i>vs.</i> Time	25
2.7	Effects of α and β on Asymmetry	30
2.8	Effects of Poor Background Subtraction on Asymmetry	33
2.9	Effect of Relative Phase Between Counters on Asymmetry	34
2.10	Cube of Positron Counters	38
2.11	Initial Polarization and Average Field Directions	39
2.12	Muon Polarization in Transverse Field Geometry with Disorder	51
2.13	Muon Polarization in Longitudinal Field Geometry with Disorder	52
3.1	Lab Frame <i>vs.</i> Rotating Reference Frame	56
3.2	Polarization Projections and Corresponding Fourier Transforms	72
3.3	Comparison of Apodization Functions	79
3.4	Time Spectrum with Various Degrees of Gaussian Apodization	80
3.5	Frequency Spectrum with Various Degrees of Gaussian Apodization	81
3.6	Convolution with Complete Signal <i>vs.</i> Oscillatory Portion Only	86
4.1	Coordinate and Crystal Axes	91
4.2	Magnetic Penetration Depths	95
4.3	Flux Line Lattice and Corresponding μ SR Lineshape	99
4.4	Field Distribution in an Anisotropic Superconductor, $\theta = 60^\circ$	101

5.1	Schematic of Spin Rotator and Experimental Magnets	114
5.2	Theoretical Lineshapes in Low Fields (Chains and Frozen Models)	118
5.3	Polarization Projections as a Function of $\bar{\lambda}^{-2}$ (Chains Model)	119
5.4	Polarization Projections as a Function of $\bar{\lambda}^{-2}$ (Frozen Model)	120
5.5	Polarization Projections as a Function of Angle (Chains Model)	121
5.6	Muon Polarization Projections Limits	123
5.7	Angular Dependence of Lineshape in 100 G	124
5.8	Angular Dependence of Asymmetry and Fields in 100 G	127
5.9	Expected Angular Dependence of Second Moment and Cusp (Chains Model) . . .	128
5.10	Angular Dependence of Field Inhomogeneity and Cusp in 100 G	130
5.11	Initial Phase in 100 G (Chains Model)	134
5.12	Angular Dependence of λ_{ab} in 100 G (Chains Model)	135
5.13	Angular Dependence of Gaussian Convolution in 100 G (Chains Model)	136
5.14	Angular Dependence of Vortex Disorder in 100 G (Chains Model)	137
5.15	Angular Dependence of λ_{ab} in 100 G (Frozen Model)	138
5.16	Angular Dependence of Gaussian Convolution in 100 G (Frozen Model)	139
6.1	Cusp Field <i>Vs.</i> <i>T</i> at 0.25 T with Flux Expulsion	146
6.2	Temperature Dependence of Cusp Field at 0.25 T with Fixed Flux Expulsion . . .	148
6.3	Temperature Dependence of Cusp Field at 0.25 T without Flux Expulsion	149
6.4	Temperature Dependence of Gaussian Field Inhomogeneity and Cusp Field at 0.25 T	154
6.5	Fit of BCS to a Power Law	155
6.6	Temperature Dependence of Linewidth in Unoriented Sintered Powders	156
7.1	Lineshape for the Modified London Model	158
7.2	High Timing Resolution Apparatus	161
7.3	High Timing Resolution Counters	162
7.4	Asymmetry Loss in High Fields	166
7.5	Calculated Beam Envelope Oscillations	168
7.6	Muon Beam Focusing In Helios	169

7.7	$B(\vec{r}) - B_o/B_o$ Versus λ_r and ξ_r	174
7.8	$B(\vec{r}) - B_o/B_o$ Versus λ_r^{-2} and H_{c2}/B_o	175
7.9	$\lambda_{ab}^{-2}(T)$ from Global Fits	181
7.10	$H_{c2}(T)$ from Global Fits	182
7.11	λ and ξ from Global Fits	184
7.12	κ from Global Fits	185
7.13	Maximum, Cusp and Minimum Fields	186
7.14	Local Field Inhomogeneity Above T_c	189
7.15	Corrected Convolution Width	190
7.16	Vortex Deviation Due to Random Compression and Shear	191
B.1	10 K: χ^2 and B_o for individual runs	216
B.2	20 K: χ^2 for individual runs	217
B.3	30 K: χ^2 and B_o for individual runs	218
B.4	40 K: χ^2 and B_o for individual runs	219
B.5	50 K: χ^2 and B_o for individual runs	220
B.6	60 K: χ^2 and B_o for individual runs	221
B.7	70 K: χ^2 and B_o for individual runs	222
B.8	75 K: χ^2 and B_o for individual runs	223
B.9	Overall χ^2 for 10 K, 20K, 30K, and 40K	224
B.10	Overall χ^2 for 50 K, 60K, 70K, and 75K	225
B.11	High Field μ SR lineshapes, $B = 1.9$ T	226
B.12	High Field μ SR lineshapes, $B = 4.1$ T	227
B.13	High Field μ SR lineshapes, $B = 4.7$ T	228
B.14	High Field μ SR lineshapes, $B = 6.5$ T	229
B.15	High Field μ SR lineshapes, $T = 10$ K	230
B.16	High Field μ SR lineshapes, $T = 30$ K	231
B.17	High Field μ SR lineshapes, $T = 50$ K	232
B.18	High Field μ SR lineshapes, $T = 70$ K	233

Acknowledgements

I'd like to thank my thesis advisor Jess H. Brewer, who has provided an open research environment, opportunities to work with people from other groups, and freedom coupled with support. The experiments reported in this thesis would not have been possible without the excellent $\text{YBa}_2\text{Cu}_3\text{O}_{6.95}$ crystals grown by Ruixing Liang, of U.B.C. I appreciate the effort Christof Niedermayer spent designing and overseeing the construction of the high timing resolution counters. I am extremely grateful to the following people who helped me set up my experiments and who helped take the data: James J. Boyle, Jess H. Brewer, Kim H. Chow, Tim L. Duty, Rob F. Kiefl, Syd Kreitzman, Steve L. Lee, Andrew MacFarlane, Philippe Mendels, Gerald D. Morris, Christof Niedermayer, Thomas Pfiz and Jürg W. Schneider. Keith Hoyle and Curtis Ballard provided valuable technical assistance.

Luke L. Daemen of Los Alamos National Laboratory provided the magnetic field distributions for low applied fields and I appreciate our many discussions. Josef Rammer of Siemens Electronics, formerly a postdoc at U.B.C., provided the impetus for taking the high field data with his theoretical calculations of the μSR lineshapes corresponding to $\text{YBa}_2\text{Cu}_3\text{O}_{6.95}$ using Gorkov's equations.

I appreciate many useful discussions in person and by electronic mail with E.H. Brandt, Larry J. Campbell, Elizabeth J. Nicol, Walter N. Hardy, Rob F. Kiefl, and Donald J. Arseneau. I gained valuable experience with high temperature superconductors in early collaborations with both Tomo Uemura and Dale Harshman. Paul Kienzle helped a great deal with editing.

The experiments reported in this thesis were conducted on the M15 and M20B beamlines at the TRIUMF cyclotron, with the financial support of the Natural Sciences and Engineering Council of Canada.

Chapter 1

Introduction

1.1 Superconductivity: A Brief Historical Perspective

Superconductivity in a given material is characterized by the complete disappearance of electrical resistance when the material is cooled below a certain finite critical temperature, T_c , which was first observed by Kamerlingh Onnes in 1911 in mercury. This alone is not enough to guarantee the formation of a true superconducting state, and the phenomenon of superconductivity should not be confused with that of perfect conductivity (a normal metal in the limit of zero resistance). Superconductivity in a material is confirmed by the presence of the Meissner effect, which manifests itself as complete magnetic flux expulsion when the material is cooled below the critical temperature in a constant applied magnetic field—*i.e.*, a superconductor below its critical temperature behaves as a perfect diamagnet. In contrast, a perfect conductor resists changes in the applied field (by producing eddy currents), but does not expel flux.

In 1935, shortly after the discovery of the Meissner effect,[1] F. London and H. London proposed a phenomenological description of the electrodynamics of the superconducting state.[2] With minor modifications, their ideas remain the basis of a very useful and successful description of the electrodynamics of superconductors and will be described in more detail in the next section. In 1950, rather than attacking the problem from the point of view of electrodynamics, Ginzburg and Landau[3] adopted a more general description of a superconductor based on thermodynamics. They described the superconducting state by a pseudo-wave function $\psi(\vec{r})$ such that the magnitude of $|\psi|^2$ would be equal to one half the density of electrons (or holes) in the superconducting state at a given location \vec{r} in the superconductor: $|\psi(\vec{r})|^2 = \frac{1}{2}n_s$. They assumed that the free energy, F , of the superconducting electron gas is a function of n_s and expanded F in powers of

$|\psi(\vec{r})|^2$ and $|\vec{\nabla}\psi(\vec{r})|^2$:

$$F - F_n = \int \left(\frac{\hbar^2}{4m} |\nabla\psi|^2 + a|\psi|^2 + \frac{1}{2}b|\psi|^4 \right) dV \quad (1.1)$$

A variational minimization of F lead to a Schrödinger-like equation for ψ , but with an additional nonlinear term,

$$\frac{1}{4m} \left(-i\hbar\nabla - \frac{2e}{c}\vec{A} \right)^2 \psi + a\psi + b|\psi|^2\psi = 0. \quad (1.2)$$

In zero applied field, $|\psi(\vec{r})|^2 = \frac{1}{2}n_s = -a/b$. Eq. 1.2 is the first Ginzburg-Landau equation. From a phenomenological point of view, $|\psi|^2$ appeared as a useful order parameter to describe the transition to the superconducting state, $|\psi|^2$ being zero above T_c and different from zero below T_c .

Even though successful phenomenological descriptions of superconductivity appeared early on, it was not until 1957 that Bardeen, Cooper, and Schrieffer (BCS) provided a useful microscopic description of the superconducting state. They showed that a weak attraction between electrons in a Fermi gas causes pairs of electrons with opposite momenta and spins to form so-called Cooper pairs. This in turn leads to an instability in the electron gas characterized by a “condensation” of the Cooper pairs into a coherent quantum mechanical state $\psi(\vec{r})$ and by the appearance of an energy gap $\Delta(T)$ at the Fermi surface. The fact that the Cooper pairs condense into a single quantum state accounts for their ability to carry electric current without dissipation. It is also possible to show that this leads to the Meissner effect, although this is less intuitively obvious. Analogies with a Bose-condensed state of Cooper pairs were suggested shortly after BCS, but it should be emphasized that it is not entirely correct: the Cooper pairs are not bosons and the quantum mechanical state into which they condense is not a Bose condensate. Nevertheless, this crude analogy is useful as a simple way to understand the phenomena of superconductivity. Finally, note that the BCS description does not specify what mechanism is responsible for the attraction of two electrons (or holes) to form a Cooper pair. In principle any attractive interaction could lead to the formation of Cooper pairs. BCS showed that the interaction between electrons and phonons in a metal is a *likely* pairing mechanism. This idea has been confirmed experimentally many times since then, in particular *via* measurements of the so-called isotope effect, which is the

variation of T_c with isotopic mass. A more specialized version of the BCS theory was subsequently derived by Eliashberg to incorporate a phonon pairing mechanism more accurately in the theory. Other pairing mechanisms have been proposed, but so far none has been established on firm grounds.

1.2 The London Formalism

In 1935, F. and H. London[2] showed that the phenomenon of perfect diamagnetism observed in 1933 by Meissner and Ochsenfeld[1] could be described easily if one assumed that the supercurrent density \vec{j}_s is proportional to the vector potential $\vec{A}(\vec{r})$ (in the appropriate gauge known today as the London gauge, $\vec{\nabla} \cdot \vec{A} = 0$, which leads to $\vec{\nabla} \cdot \vec{j} = 0$). More precisely, they suggested that in a superconductor

$$\vec{j}_s(\vec{r}) = -\frac{c}{4\pi\lambda^2}\vec{A}(\vec{r}), \quad (1.3)$$

where λ is a phenomenological parameter known as the London penetration depth. After substitution of Eq. 1.3 into Maxwell's equations, one can show by trivial algebraic manipulations that the magnetic field $\vec{B} = \vec{\nabla} \times \vec{A}$ in a London superconductor obeys London's equation:

$$\vec{\nabla}^2 \vec{B} - \frac{1}{\lambda^2} \vec{B} = 0. \quad (1.4)$$

So, λ appears as the length scale over which the magnetic field varies in a superconductor. With the appropriate boundary condition for the continuity of \vec{B} at the surface of the superconductor, it is easy to show that, typically, \vec{B} is screened out by the supercurrents \vec{j}_s over a characteristic distance, the "magnetic penetration depth" λ , and hence \vec{B} does not penetrate inside the superconductor. London and London showed that λ is related to the density of superconducting charge carriers (either electrons or holes):

$$\lambda = \sqrt{\frac{mc^2}{4\pi e^2 n_s}}, \quad (1.5)$$

where m is the effective mass of one charge carrier, $2e$ is the charge of the Cooper pair (because it is formed from two charge carriers), c is the speed of light and n_s is the number density of superconducting charge carriers (or $\frac{1}{2}n_s$ is the number density of Cooper pairs) in the absence

of applied magnetic or electric fields. Notice that n_s is assumed to be constant, *i.e.*, the London formalism is, strictly speaking, not valid if n_s varies spatially.

When in 1950 Ginzburg and Landau[3] proposed the phenomenological description of the superconducting state, they showed that they could recover the London electrodynamics from the Ginzburg-Landau (GL) equations. More precisely, if $\psi(\vec{r}) = |\psi(\vec{r})|e^{i\varphi(\vec{r})}$ is the complex GL pseudo-wave function (also referred to as the order parameter), Ginzburg and Landau showed that in the presence of a magnetic field the supercurrent density is related to the vector potential and the order parameter by the second GL equation:

$$\vec{j}_s = \frac{e\hbar}{m}|\psi(\vec{r})|^2\vec{\nabla}\varphi(\vec{r}) - \frac{2e^2}{mc}|\psi(\vec{r})|^2\vec{A}. \quad (1.6)$$

If we identify $|\psi(\vec{r})|^2$ with $\frac{1}{2}n_s$ and assume no spatial dependence of the magnitude or phase of ψ , we recover the London equation, (Eq. 1.3), and hence London electrodynamics. The GL theory goes one step further in that it can treat situations where the order parameter varies spatially. This was an important step forward as we shall see. It should be mentioned that allowing $|\psi(\vec{r})|$ to vary spatially introduces a second length scale, the coherence length ξ

$$\xi = \frac{\hbar}{2\sqrt{m|a|^2}} \quad (1.7)$$

which for a given material, depends only on temperature according to a from the first Ginzburg-Landau equation (Eq. 1.2). Likewise, the magnetic penetration depth depends only on temperature through the temperature dependence of $n_s = 2|a|/b$, which varies smoothly from zero at T_c to its maximum value at low temperature. The effective mass m is assumed to be constant.

For a given material, ξ can be larger or smaller than λ . The ratio

$$\kappa \equiv \lambda/\xi = \frac{mc}{\sqrt{2\pi}|e|\hbar}b^{1/2} \quad (1.8)$$

is a important quantity. In 1957, Abrikosov studied the problem of surface tension between superconducting and normal regions.[4, Sec 46] He showed that when the surface tension is positive, which occurs when $\kappa < 1/\sqrt{2}$, and when the applied field is less than a certain critical field $H_c(T)$, the superconductor will be in the superconducting state throughout, and hence will exhibit the Meissner effect. These superconductors are conventionally called type I superconductors. In type

II superconductors, where $\kappa > 1/\sqrt{2}$, the surface tension is negative, so under certain circumstances it will be energetically favorable to have co-existing superconducting and normal regions. The type II superconductor will be completely superconducting and will exhibit the Meissner effect (where the magnetic flux is completely expelled) when the applied field is below the lower critical field $H_{c1}(T)$, because the negative surface tension energy cannot compensate for the extra energy required to support normal regions within the superconductor. However, superconductivity does not disappear immediately as the magnetic field is increased above $H_{c1}(T)$. Instead, a phase transition occurs to a state where there are both normal and superconducting regions; this is known as the mixed state. When the applied field is greater than the upper critical field $H_{c2}(T)$, the superconductor is driven completely normal. (The high temperature superconductor $\text{YBa}_2\text{Cu}_3\text{O}_{7-\delta}$ has κ between 55[5] and 77,[6] which is well within the type II regime.)

The normal regions in a mixed state superconductor (known as ‘vortices’, ‘flux lines’ or ‘flux tubes’) are configured to maximize surface area and minimize volume while conserving magnetic flux. Abrikosov was also able to show that this occurs if they are cylindrical and parallel to the average field direction. At the center of each vortex, superconductivity is totally destroyed, *i.e.*, the density of superconducting carriers (and hence $|\psi|^2$) vanishes. As we move away from the center in the radial direction, the density increases gradually, reaching its bulk value within a distance of ξ . The cylindrical volume of radius $\simeq \xi$ inside of which the magnitude of the order parameter varies spatially is called the vortex core. Each vortex carries exactly one magnetic flux quantum $\phi_o = \frac{ch}{2e}$ and is surrounded by a ‘vortex’ of supercurrent. Flux quantization is required to ensure that the phase of the order parameter is a single-valued function in the vicinity of a vortex. More precisely, the phase φ of the order parameter must change by an integer multiple of 2π for all closed loops within the superconductor. If the loop surrounds a region which is entirely in the superconducting state, φ will not change. If the loop surrounds non-superconducting regions, either holes in the superconductor or regions in the normal state (*e.g.* vortex cores), the integer will be non-zero and the magnetic flux through the loop will be that integer times the magnetic flux quantum. The supercurrent flowing around the vortex produces a magnetic field which is maximum at the center of the vortex core and decays approximately exponentially (with a length scale of λ) in the radial direction. The vortices arrange themselves in a periodic lattice[7] known

as the Abrikosov lattice, the flux lattice or the flux line lattice. In an isotropic superconductor, under normal circumstances, the lattice is triangular—extensive flux decoration pictures of both triangular and square lattices are shown in Ref. [8].

Because the London formalism was not tailored to allow for spatial variations of the order parameter, one might think that it is not useful for describing the mixed state. This is not true, however, and in the limit of very large κ , the London formalism can be slightly modified to account for the presence of vortices. When κ is very large (*i.e.*, $\lambda \gg \xi$), the vortex core (the region where $|\psi|$ varies rapidly and which cannot be described by the London formalism), is very small compared to the length scale λ over which the magnetic field (the solution to London's equation, Eq. 1.4) varies. Therefore, it is not unreasonable to neglect the spatial variations of $|\psi|$ when determining the magnetic field distribution. Of course, by doing this we have given up the possibility of determining physical quantities on a scale comparable to ξ but for many purposes this is adequate. Let us now derive the London equation (Eq. 1.4), but this time starting from the second GL equation (Eq. 1.6), rather than Eq. 1.3. In other words, we keep the term containing the phase $\varphi(\vec{r})$ of the order parameter $\psi(\vec{r})$, which is still allowed to have a spatial dependence while the magnitude of the order parameter $|\psi|$ is now assumed to be constant. The derivation is the same as before, but we now have one additional term of the form $\vec{\nabla} \times \vec{\nabla} \varphi$. Below H_{c1} this term vanishes, but when $H_{c1} < H < H_{c2}$ and vortices are allowed, it does not vanish due to the fact that near a vortex the phase is a multi-valued function which changes by 2π when a closed loop around a vortex core is traversed. One can show that $\vec{\nabla} \times \vec{\nabla} \varphi$ is in fact proportional to a Dirac delta function, and the London equation is now identical to Eq. 1.4, but with an additional source term describing the presence of a singularity in the order parameter, *i.e.*, a vortex:

$$\vec{\nabla}^2 \vec{B} - \frac{1}{\lambda_L^2} \vec{B} = \phi_0 \delta(\vec{r}) \hat{z}. \quad (1.9)$$

where \hat{z} is the vortex direction. The core (with radius $\approx \xi$) is so small on the scale of λ that it is reasonable to approximate it by a point singularity; this is the physical origin of the delta function in Eq. 1.9. Thus we have allowed for the presence of vortices in the London formalism without violating the restriction of a constant superconducting electron density.

The above equation for the magnetic field in the presence of a single vortex allows us to

study the spatial variations of the magnetic field in a type II superconductors by solving a *linear* equation, as opposed to the much more complicated problem of having to solve the *nonlinear* GL equations for ψ and \vec{A} . We can now think in terms of interacting point particles (vortices) rather than in terms of two continuous fields ψ and \vec{A} . Therefore, Eq. 1.9 can be extended to the case of multiple vortices at locations \vec{r}_ν ,

$$\vec{\nabla}^2 \vec{B} - \frac{1}{\lambda_L^2} \vec{B} = \phi_0 \delta(\vec{r} - \vec{r}_\nu) \hat{z}. \quad (1.10)$$

Generally speaking, when the combination of field and temperature is such that the magnitude of the order parameter is constant but the phase depends on the position, the superconductor can be described by the above London equation. In the context of this thesis, this is the case when the coherence length is negligible compared to both the magnetic penetration depth ($\kappa \gg 1$) and the inter-vortex spacing.

The solution to Eq. 1.9 for the magnetic field set up by a vortex has a singularity at $\vec{r} = 0$. This is of course due to the fact that what happens close to the core cannot be described adequately by the London formalism. In order to properly evaluate the field in this region, it is necessary to take into account the spatial variation of the order parameter. However, introducing a suitable cutoff (on the order of ξ) when evaluating integrals and sums over space of functions containing \vec{B} as obtained from the London equations, while not completely rigorous, is adequate for most purposes.

1.3 The Superconducting Gap and the Pairing State

In an *s*-wave superconductor, Cooper pairs of carriers are in a spin singlet state with equal and opposite momenta (\vec{k} and $-\vec{k}$) with zero angular momentum and their spins are antiparallel and a total angular momentum of zero. The superconducting gap $\Delta(\vec{k}, T)$ is the minimum energy above the Fermi energy that quasi-particles excitations can have, which means that the energy needed to break up a Cooper pair is twice the energy gap. Using the Heisenburg uncertainty principle and the Fermi velocity, it is more precise to view the Cooper pairs as correlations between pairs of particles in momentum space over a length scale called the coherence length $\xi \approx \hbar v_F / \Delta$. [4, Sec

39] In the case of an s -wave singlet state, the gap is assumed to be independent of momentum. For more elaborate pairing states, it may depend on the direction of \vec{k} . Other possible pairing states may have higher angular momentum and/or a triplet spin state as long as the total wave function is antisymmetric with respect to the exchange of two of the fermion charge carriers (either electrons or holes). In the case of d -wave superconductivity, the carrier's spins are antisymmetric and the gap may be of the form

$$\Delta(\vec{k}_F) = \Delta_o (\hat{k}_x^2 - \hat{k}_y^2) \quad (1.11)$$

where \vec{k}_F is on the Fermi surface, although there are other allowed d -wave symmetries. Note that, in this case, along the diagonal directions ($|k_x| = |k_y|$), the gap is zero which means that it is very easy to reduce the number of carriers in the superconducting ground state by thermal excitations. Consequently, this will affect physically measurable quantities, such as the magnetic penetration depth, which depend on the density of superconducting carriers. The effect of different energy gap structures (isotropic or having nodes where the gap is zero) upon the temperature dependence of the magnetic penetration depth is discussed further in Sec. 6.3.

1.4 High Temperature Superconductivity [HTSC]

In 1986, Bednorz and Müller[9] discovered that the compound $\text{La}_{2-x}\text{Ba}_x\text{CuO}_{4+y}$ was superconducting, with a critical temperature greater than 30 K, which was unprecedentedly high. In 1987, $\text{YBa}_2\text{Cu}_3\text{O}_{7-y}$ [10] was discovered, which, with optimization of its oxygen concentration, has T_c as high as 93.5 K. Many other related compounds, all with two dimensional layers of coppers and oxygens separated by rare earth, alkaline earth, Tl, Bi, Pb and other elements, have critical temperatures ranging from a few degrees Kelvin to 130 K.

1.4.1 Magnetic Properties and the Underlying Mechanism of HTSC

In its simplest form, BCS theory describes an s -wave pairing state, where the spins of Cooper pairs are anti-symmetric and the gap function $\Delta(T_c)$ is isotropic. Other pairing states, such as d -wave and p -wave, are also possible. As explained above, the pairing state[11] will affect the temperature

dependence of quantities such as the magnetic penetration depth (which can be measured by μ SR or microwave radiation), the nuclear spin-lattice relaxation rates ($1/T_1$) and Knight shifts (both of which can be measured by NMR). Precise measurements of such quantities are essential if we are to determine the pairing state of high temperature superconductors.

Moreover, most of the high temperature superconductors are magnetic insulators when the carrier concentration is reduced enough to destroy superconductivity. Is this a coincidence or is it related to the mechanism producing the superconductivity? Would the symmetry of the magnetism influence the symmetry of the pairing state?

The critical temperature T_c is quite sensitive to the number of superconducting carriers present, which can be adjusted through doping (x or y in $\text{La}_{2-x}\text{Ba}_x\text{CuO}_{4+y}$ and $\text{YBa}_2\text{Cu}_3\text{O}_{7-y}$). [12,13,14] When doping is reduced enough that superconductivity is lost, most copper-oxide based high temperature superconductors become antiferromagnetic insulators with the magnetic moments on copper atoms in at least one copper-oxide plane per unit cell. [15] (Refs. [16], [17] and [18] report μ SR measurements of the magnetic phase diagram for $\text{YBa}_2\text{Cu}_3\text{O}_{7-y}$.) Even in superconducting samples, dynamic antiferromagnetic spin fluctuations have been observed by neutron scattering. [19,20] These result from electronic magnetic moments on those copper atoms which lie in the same copper-oxygen planes as the superconducting carriers. The normal state ($T > T_c$) nuclear spin-lattice relaxation rates $1/T_1$ for oxygen nuclei which lie in the planes [21] and for the yttrium nuclei [22] in superconducting $\text{YBa}_2\text{Cu}_3\text{O}_{7-y}$ show the Korringa behavior ($1/T_1 \propto T$) expected for metals. Strong deviations from Korringa behavior are observed for the copper atoms in the planes [21] due to antiferromagnetic fluctuations at these copper sites. The effects of antiferromagnetic fluctuations are cancelled for both oxygen and yttrium because they are positioned symmetrically with respect to the planar copper. The fundamental question is whether high temperature superconductivity is phonon mediated as in conventional superconductors (in which case any accompanying magnetism and magnetic fluctuations are incidental and unrelated to the superconductivity mechanism), or if it is mediated by antiferromagnetic spin fluctuations.

Bulut and Scalapino [23] modeled superconductivity mediated by spin fluctuations rather than

phonons and compared their predictions for s -wave and d -wave pairing states with observed nuclear spin-lattice relaxation rates $1/T_1$ below T_c and Knight shifts for both the oxygen and copper nuclei in copper-oxygen layers of $\text{YBa}_2\text{Cu}_3\text{O}_7$ (where both the moments and the superconducting carriers reside). They found that the measured Knight shifts are consistent with s -wave pairing while the nuclear spin-lattice relaxation rates are consistent with d -wave pairing. Other experiments were no more definitive; there is (at this writing) no strong evidence in favor of any particular pairing state.[11] If the accuracy of the magnetic penetration depth measurements is improved, it may help to determine the pairing state in $\text{YBa}_2\text{Cu}_3\text{O}_{7-y}$. In this work I have sought to accomplish this by detailed fitting of μSR data taken in a mosaic of oriented $\text{YBa}_2\text{Cu}_3\text{O}_{6.95}$ crystals, which removes many of the uncertainties inherent in magnetic penetration depth measurements taken on unoriented sintered powders[24,25,26] and is an improvement over earlier μSR studies of oriented $\text{YBa}_2\text{Cu}_3\text{O}_{6.95}$ crystals[27,28,29] which used only *Ansatz* fitting functions.

1.5 $\xi(T)$, $\lambda(T)$ and $\kappa(T)$ in $\text{YBa}_2\text{Cu}_3\text{O}_{6.95}$

The coherence length ξ is not only the size of the vortex core, but it is of fundamental interest as the length scale over which the superconducting carriers interact to form Cooper pairs. Measurements of $H_{c2}(T)$ can be used to determine the temperature dependence of the coherence length $\xi(T)$, but due to the extremely high value of $H_{c2}(0)$ in $\text{YBa}_2\text{Cu}_3\text{O}_{6.95}$, $H_{c2}(T)$ has only been reliably measured within a few degrees of T_c . Assuming s -wave BCS temperature dependence, Lee *et al.*[30] deduced that $\xi_{ab}(0) = 13.6 \pm 0.8 \text{ \AA}$ and $\xi_c(0) = 1.2 \pm 0.2 \text{ \AA}$, from measurements of the superconducting fluctuations between T_c and $0.65 T_c$ in $\text{YBa}_2\text{Cu}_3\text{O}_7$. One of the problems in the measurements of H_{c2} and ξ is that the number of superconducting carriers n_s continues to increase with increasing doping y in $\text{YBa}_2\text{Cu}_3\text{O}_{7-y}$, while the critical temperature has plateaued.[13,14] This means that samples with similar critical temperatures may have significantly different values for fundamental parameters, such as the magnetic penetration depth[13,14] and the coherence length, which depend on the number of superconducting carriers. This may be the source of the range of values reported for the slope of H_{c2} near T_c (for $H_{c2} \parallel \hat{c}$), varying from -1.65 T/K [5] to -1.90 T/K [6] and higher.

As seen in the measurement of the penetration length, $\text{YBa}_2\text{Cu}_3\text{O}_{7-y}$ is anisotropic, with a magnetic penetration depth for fields in the copper-oxide planes (λ_c) about five times larger than that for fields perpendicular to the planes (λ_{ab}).[28] The λ_c/λ_{ab} ratio can be much larger in other high T_c superconductors. This anisotropy arises from the layered chemical structure of the superconductor, and suggests that the Fermi surface may be closer to cylindrical than to the roughly spherical surface expected in isotropic superconductors. This will also affect the temperature dependences of characteristic parameters such as H_{c2} . [31]

The temperature dependence of the Ginzburg-Landau parameter κ is of particular importance, as it reflects the strength of the charge carrier coupling which produces the superconductivity: in BCS theory it is constant with weak coupling but with strong coupling increases as temperature decreases. Different theories (such as phonons *vs.* magnons) require different coupling strengths in order to describe the observed behavior; if the coupling strength were measured independently, it could eliminate a number of possible theories. Moreover, since both the coupling strength and the pairing state affect the temperature dependence of $\lambda(T)$, knowing the coupling strength would narrow down the possible pairing states. Reversible magnetization measurements of κ can only measure a small region between T_c and the irreversibility temperature T_{ir} at which vortex pinning sets in.[5,6] This thesis reports the first measurement to date of $\kappa(T)$ in $\text{YBa}_2\text{Cu}_3\text{O}_{6.95}$ below the irreversibility temperature.

1.5.1 Flux Pinning and the Irreversibility Temperature

While the irreversibility temperature and the strength of the pinning are not related to the mechanism of superconductivity, they are also important. When a current is applied to a superconductor without pinning in an applied field, the vortices move perpendicular to the current *via* a Lorentz force. This is observed as resistance since, unlike that of the superconducting region, the motion of the normal vortex cores produces dissipation. Practical applications for superconductors (*e.g.* use in high field magnets) require that the vortices be well pinned in place. While the effects of pinning are usually investigated under dynamic situations (AC applied fields, applied currents, *etc.*), in this thesis the effect of disorder in the vortex lattice due to pinning is investigated in static

low, intermediate and high fields, *via* the “smearing” effect on the μ SR lineshape. In contrast, flux decoration experiments, which directly image the individual vortices within the vortex lattice (and, hence, any disorder in it), are limited to applied fields of about 120 G.[32] In principle, the degree of disorder can be correlated with the strength of the pinning centers.[33]

1.6 μ SR in High T_c Superconductors

Positive and negative muons are spin 1/2 leptons, which are heavy “cousins” to positrons and electrons; μ^+ SR is a technique in which polarized positive muons are implanted in samples and the time dependence of the depolarization of the muons’ spin polarization (due to an inhomogeneous field distribution) or the relaxation of the muons’ spin polarization (due to spin-lattice interactions) are observed *via* the decay of the muons into positrons. The decay positron is emitted in a direction which is correlated with the muon spin direction at the time of decay.

The positive muon forms a hydrogen-like bond with oxygen in the copper-oxide based high temperature superconductors[34,35,36,37,38] within picoseconds of entering the sample. Because the superconductors are metals, the bonding electrons are delocalized, and the muons are observed to be diamagnetic with a gyromagnetic ratio essentially identical to that for bare muons in vacuum, $\gamma_\mu/2\pi = 0.01355342$ MHz/G. They show no evidence of diffusing in $\text{YBa}_2\text{Cu}_3\text{O}_{7-\delta}$ below 150 K.[39] Therefore, motional narrowing effects on the μ SR signal are of no concern unless the magnetic structure in the sample is changing on a time scale comparable to the muon lifetime. For static applied fields and no applied current, the vortices in $\text{YBa}_2\text{Cu}_3\text{O}_{7-\delta}$ are static in the time frame of the muon, except perhaps very close to T_c .

This thesis is concerned with the muon depolarization produced by the particular inhomogeneous magnetic field distribution arising from a vortex lattice in a type II superconductor. “True” relaxation (in the sense of loss of muon polarization due to actual energy transfer between the muon spins and the lattice) is not important in the copper oxide based perovskite superconductors because the time scale is too long to be observable by time differential μ SR (on the order of milliseconds in NMR measurements), and therefore is ignored in this thesis.

It is not uncommon to fit high transverse field μ SR data taken in solid state systems with a Gaussian function for the depolarization [$e^{-\frac{1}{2}(\sigma t)^2} \cos(\gamma_\mu B t)$] when the local fields are static and the muons are not diffusing. While Gaussian fits give the average field and the second moment of the local field distribution, they are not always appropriate. The field distribution due to the vortex lattice in a type II superconductor is particularly asymmetric and the Gaussian is not a good *Ansatz* fitting function. This thesis discusses the μ SR lineshape (which is the Fourier transform of the time dependence of the muon polarization) and the results of fitting to the theoretical lineshape when statistics allow, and to a Gaussian or a Lorentzian when they don't. The goal is to accurately determine the magnetic penetration depth, the coherence length and the degree of disorder in the vortex lattice (and their respective temperature dependences) from the experimental lineshape.

1.7 Sample

The high quality $\text{YBa}_2\text{Cu}_3\text{O}_{6.95}$ crystals used in the experiments reported on in this thesis were made by Ruixiang Liang of the University of British Columbia. A flux method was used to make the crystals, which were grown in yttria-stabilized zirconia crucibles. They were carefully oxygen annealed. Details of the method are described in Ref. [40], which also reports on low field magnetization, *a-b* resistivity, microwave resistance and heat capacity measurements. The critical temperature transition width is less than 0.25K and the onset T_c is 93.5 K.

The crystals were originally mounted as a mosaic on a 25.4 mm diameter 99.999% pure silver disk using Apiezon N grease, with the *c* axis normal to the plane of the disk. The center 1 cm diameter region was composed of the six largest crystals, with areas of $3.0 \times 3.0 \text{ mm}^2$, $3.3 \times 2.4 \text{ mm}^2$, $3.0 \times 2.4 \text{ mm}^2$, $3.0 \times 2.5 \text{ mm}^2$, $2.4 \times 2.4 \text{ mm}^2$, and $3.0 \times 1.5 \text{ mm}^2$. The mosaic was filled out to a 1.5 cm diameter with smaller crystals, as small as $0.5 \times 0.5 \text{ mm}^2$. The large crystals were 200–300 μm thick but the smaller crystal near the edges of the mosaic were as thin as 100 μm . This mosaic was used in the low and moderate field experiments described in Chapters 5 and 6. The mosaic was fitted together tightly, so that as little as possible of the silver backing showed through.

For the high field experiment, a portion of these crystals were mounted as a mosaic on a 8 mm diameter 99.999% pure silver disk. The mosaic was comprised of 19 flat crystals, ranging in area from 7.4 mm² to 0.26 mm². The typical thickness was 0.2 mm. This mosaic was also closely fitted.

1.8 A note about units, etc.

In this thesis, I strive to report results in terms of magnetic fields in units of gauss or tesla (1 T = 10⁴ G) rather than in muon precession frequencies, which are proportional to the magnetic fields. I feel that the general reader is more interested in the behavior of the local field in the superconductor YBa₂Cu₃O_{6.95} than in the muon gyromagnetic ratio.

I have chosen to report the magnetic penetration depth in units of μm rather than nm or \AA , which allows the scaling factor λ^{-2} to have convenient values between 10 and 50 for YBa₂Cu₃O_{6.95}. The constant for magnetic flux quantum is used with units of G μm^2 , which allows calculation of the distance between vortices without having to keep track of several powers of ten.

Chapter 2

Basics of Muon Spin Rotation and Relaxation

2.1 Overview

The use of muons to probe solids, liquids and gases is collectively referred to as μ SR: Muon Spin Rotation/Relaxation/Resonance, where the choice of word beginning with the letter “R” depends on the specifics of the application. (For additional general information on μ SR, refer to the review article by S.F.J. Cox[41] and the books by A. Schenck[42] and J. Chappert and R.I. Grynszpan.[43])

Muons are spin 1/2 leptons with a mean life $\tau_\mu = 2.19709(5) \mu\text{s}$ and a mass

$$105.65839(29) \text{ MeV } c^{-2} = 206.7291(11) m_e = 0.11261(28) m_p, \quad (2.1)$$

where m_e is the mass of an electron and m_p is the mass of a proton (values from Ref. [44]). From a chemical standpoint the positively charged muon can be treated as a light proton, while the negative muon can be thought of as a *very* heavy electron. When a negative muon is implanted in a solid, it is captured by one of the atoms and cascades down into the lowest muonic orbital. Since that orbital is comparable in extent with the radii of heavy nuclei, the muon usually undergoes nuclear capture, converting a proton into a neutron ($\mu^- p \rightarrow n\nu_\mu$). This results in complicated behavior such as a shortened lifetime and rapid muon spin depolarization. This thesis is concerned only with the use of positive muons.

Positive muons implanted in a sample will precess at an angular frequency $\omega_\mu = \gamma_\mu B$ in the presence of a local magnetic field B , which is the sum of the applied field and the local internal fields due to local magnetic moments and screening currents. The muon gyromagnetic ratio[42]

is

$$\frac{\gamma_\mu}{2\pi} = 0.01355342(\pm 0.51 \text{ ppm}) \text{ MHz G}^{-1}. \quad (2.2)$$

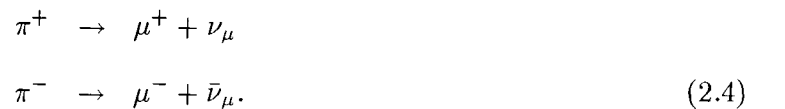
The ensemble spin polarization will experience dephasing because muons which stop in different local fields will precess at different rates. Dephasing due to inhomogeneities in the field distribution throughout the sample (which can be reversed using the spin echo technique) is sometimes mistakenly referred to as muon spin relaxation. These inhomogeneities can be caused by such things as imperfections in the experimental magnet, spin disorder in a ferromagnetic or antiferromagnetic sample, spin glass magnetism, random nuclear dipolar fields or the mixed state of a type II superconductor. Depolarization due to irreversible processes, such as muon diffusion and muon spin flipping due to hyperfine interactions with electrons and nuclei in the sample, is more correctly referred to as muon spin relaxation.

2.2 Production of Low Momentum μ^+

When protons accelerated to an energy of $\gtrsim 500$ MeV by an accelerator such as the TRIUMF cyclotron hit a “production target,” pions (π) are produced via the reactions of the projectile proton (p) with the protons and neutrons (n) of the target’s nuclei:



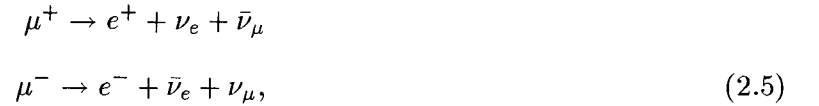
The resulting pions decay via the weak interaction into muons (μ) and muon neutrinos (ν_μ) with a lifetime of 26.030(23) ns[44]



As this is a two body decay, the muon and the neutrino are emitted in opposite directions in the rest frame of the pion in order to conserve momentum. The muon carries a kinetic energy of 4.12 MeV in the rest frame of the pion which implies a momentum of 29.79 MeV/c. Because

the pion has spin zero, the combined spin of the muon and the neutrino must also be zero. Since neutrinos are exclusively left handed—that is, their spins are antiparallel to their momentum—the muon from the pion decay must also be left handed. Therefore, the decay of positive pions produces 100% longitudinally polarized positive muons with total relativistic energy of 109.8 MeV. The decay muons are emitted isotropically in the pion rest frame.

The muon itself decays in vacuum with a mean lifetime (τ_μ) of 2.19709(5) μs [44] into an electron or positron and a neutrino-antineutrino pair:



where the combination of muon and electron neutrinos and antineutrinos is such that both lepton numbers are conserved. Due to the facts that:

1. this is a three body decay of a particle with spin 1/2,
2. only left-handed neutrinos exist, and
3. a highly relativistic e^+/e^- behaves like a $\bar{\nu}/\nu$ in a weak interaction,

the positron/electron will be emitted in a direction which is correlated with the muon spin. After integrating over all possible neutrino momenta, the probability W per unit time that a positron will be emitted at angle θ with respect to the μ^+ spin polarization direction is given by

$$dW(\epsilon, \theta) = \frac{e^{-t/\tau_\mu}}{\tau_\mu} [1 + a(\epsilon) \cos \theta] n(\epsilon) d\epsilon d \cos \theta dt\tag{2.6}$$

where $a(\epsilon) = (2\epsilon - 1)/(3 - 2\epsilon)$ and $n(\epsilon) = 2\epsilon^2(3 - 2\epsilon)$. The reduced positron energy is defined by $\epsilon = E/E_{\text{max}}$ where the maximum positron energy $E_{\text{max}} = 52.83$ MeV is approximately equal to half the muon rest energy. The probability as a function of polar angle θ is shown in Fig. 2.1 for the values of $\epsilon = 1.0$ and $\epsilon = \bar{\epsilon} = 0.682$, of which the latter corresponds to the average positron energy. The energy average of the asymmetry function $a(\epsilon)$ is $\bar{a} = 1/3$, while the low energy limit is $a(\epsilon \rightarrow 0) = -1/3$ and the high energy limit is $a(\epsilon \rightarrow 1) = 1$.

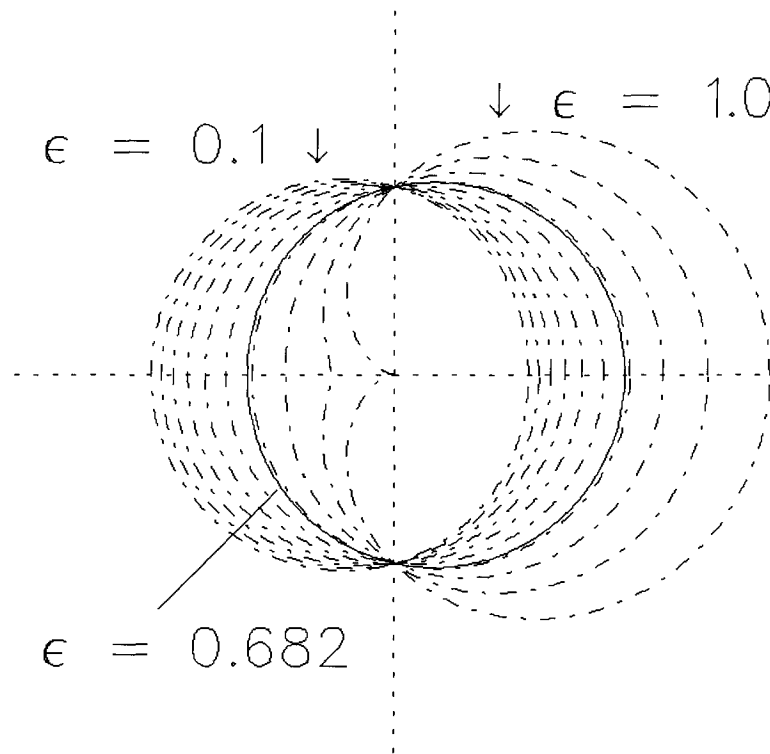


Figure 2.1: Radial plot with respect to μ^+ spin of positron emission probability for $\epsilon = \bar{\epsilon}$ (solid line) and ϵ between 0.1 and 1.0 (dot-dashed lines).

The muon spin polarization will be very nearly 100% for muons produced by those pions which decay near the surface of the production target.[45,46,47] These muons are commonly referred to as “surface” muons and have a typical momentum of 28 MeV/c—much lower than those usually obtained from pions which decay in flight. The surface muons have a total range of about 140 mg/cm² in water and a straggling range about 20 mg/cm² in water so denser samples as thin as 100 μm can be studied. In YBa₂Cu₃O_{6.95} crystals, the average range is about 140 mg/cm², which corresponds to a thickness of approximately 200 μm .

2.3 Experimental Apparatus

Along the beam line there are bending magnets and momentum slits which select particle momenta corresponding to surface muons. Just before the experimental area, there is a Wien filter which has mutually perpendicular electric and magnetic fields that are both perpendicular to the

beam. The relative strength of the fields can be adjusted to pass a specific velocity of particle without deflection, so the positron contamination can be virtually eliminated from the beam while transmitting the muons undeflected. Because the muon spin will precess during the time of flight through a magnetic field, careful choice of fields in the Wien filter can rotate the muon spin as much as 90° from the beam momentum axis.[47] Since the beam is polarized, rotating the spin until it is perpendicular to the momentum moves the anisotropic distributions of decay positrons that we wish to detect into the plane perpendicular to the background produced by the final collimator, thus lowering the detected background. Because of its dual purpose, a Wien filter is also referred to as a muon-positron separator and a spin rotator.

Spin rotation is absolutely essential for high transverse field (TF) μ SR experiments in which the muon spin must be perpendicular to the experimental magnetic field and the muon momentum must be parallel to the field to avoid beam deflection *via* the Lorentz force

$$F = q|(\vec{v} \times \vec{B})| = mv^2/R. \quad (2.7)$$

A particle with charge q and momentum $p = mv$ perpendicular to an applied field B will have a radius of curvature R where

$$R = \frac{mv^2}{qvB} = \frac{p}{qB}, \quad (2.8)$$

which gives a radius of 9.22 cm at a field of 1 T for surface muons with momentum of 28.0 MeV/c. In 100 G, the radius of curvature is 9.22 m. The Omni Prime μ SR spectrometer (Fig. 2.2) consists of two sets of Helmholtz coils which produce magnetic fields up to 0.35 T longitudinally and 120 G vertically. Using its vertical coils (each with radius 0.4445 m, spaced 0.4445 m apart), there is a horizontal displacement of the beam spot of approximately 0.08 cm at 100 G due to the muon's passage through the fringe field ($\approx 0.183B$ from 2 m upstream to the center of the coils). Omni Prime's longitudinal coils apply a field parallel to the muon momentum direction. Its fringe field ($\approx 0.160B$ from 2 m upstream to the center of the coils) is also parallel to the muon momentum and therefore causes no displacement.

The muon beam leaves the beam pipe through a thin vacuum window, passes through a thin (127 μ m to 381 μ m) scintillator and enters the μ SR apparatus containing the sample (see Fig. 2.2).

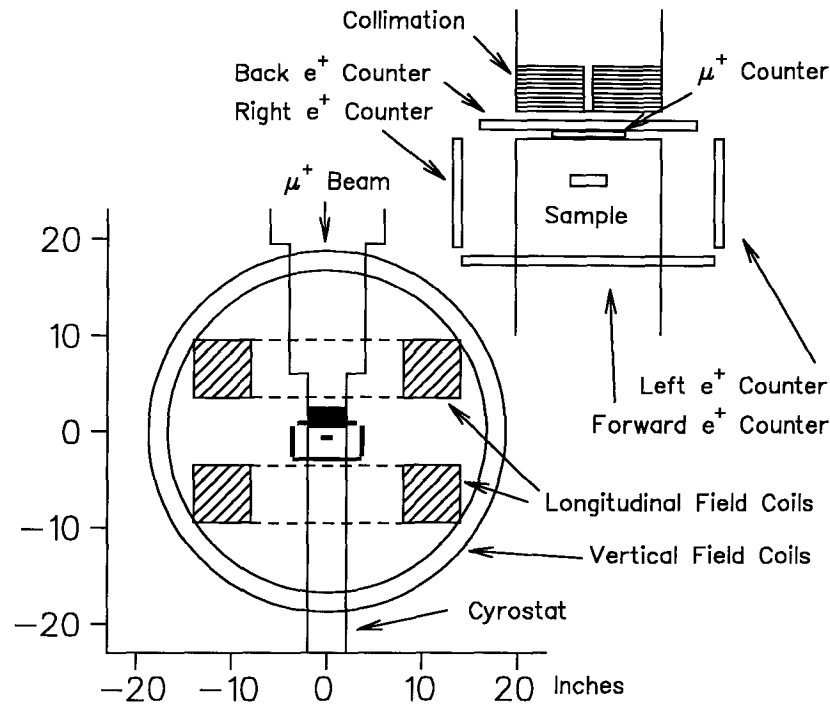


Figure 2.2: “Omni Prime” μ SR spectrometer, shown with a three inch diameter axial gas flow cryostat. A blow up of area with the counters (represented by only the scintillating portion) is shown in the upper right hand corner. The forward counter is split, with each half counter having a three inch diameter semi circle cut out. The back counter has a one inch hole cut out for the muon beam. Up and down counters have been left out for clarity.

The apparatus is inside one or more magnets, which are usually placed with the largest applied field parallel to the muon momentum to avoid beam deflection. If the magnetic field is applied parallel to the muon spin, the configuration is referred to as a longitudinal field (LF) geometry and the technique is Longitudinal Field Muon Spin Relaxation (LF- μ SR). If the magnetic field is applied perpendicular to the muon spin, the configuration is referred to as a transverse field (TF) geometry (Fig. 2.3) and the technique is Transverse Field Muon Spin Rotation (TF- μ SR). If no external magnetic field is applied, the technique is Zero Field Muon Spin Relaxation (ZF- μ SR).

The incoming muons and the decay positrons are detected with counters made of scintillating plastic connected by ultraviolet-transmitting (UVT) plastic light guides to photomultipliers. A scintillator emits light when charged particles (such as positrons and muons) pass through it; the

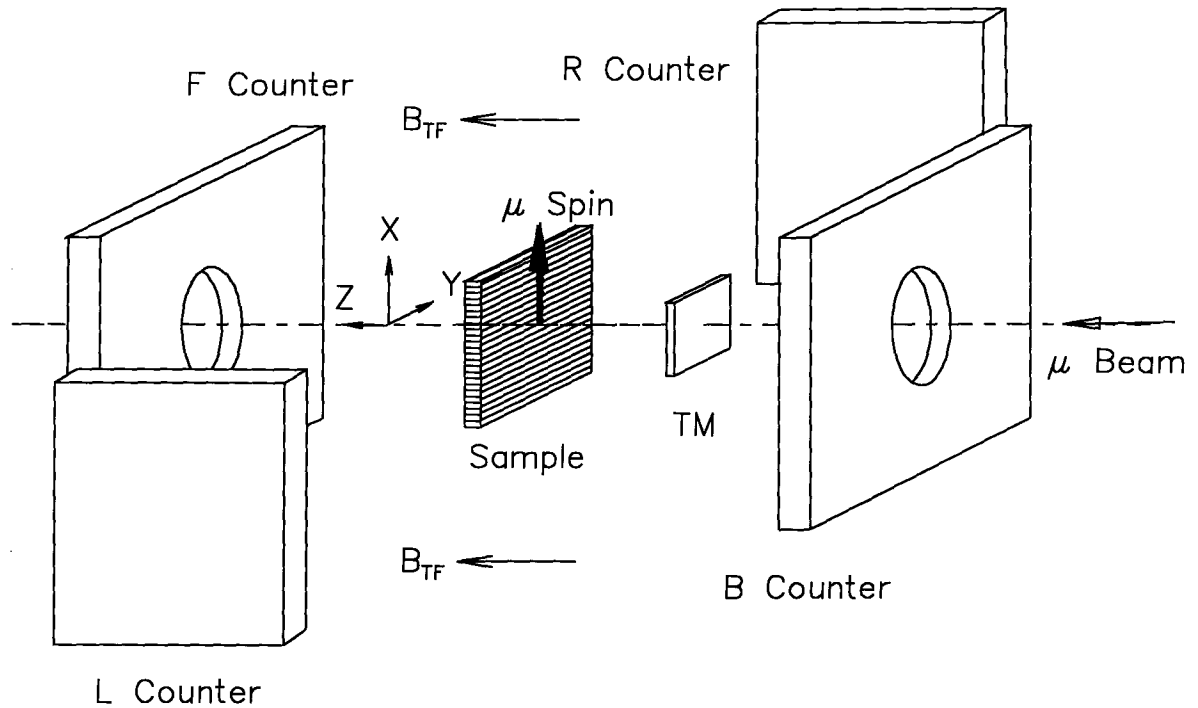


Figure 2.3: High transverse field (TF) geometry with full spin rotation (90°). The UP and DOWN counters are not shown for the sake of clarity. The BACKWARD and FORWARD counters are usually used for ZF and LF experiments with non spin-rotated muons. The coordinate origin has been displaced from the center of the sample for clarity. TM labels the muon counter.

light is collected and guided to the photomultipliers by total internal reflection in the light guide. The photomultipliers convert the light into an electrical signal, which is transmitted via coaxial cable to a counting room where fast electronics (see Fig. 2.4) are used to interpret and store the information.

Between the end of the beam pipe and the sample is a thin scintillator used to detect incoming muons. This muon counter must be thin, on the order of $250 \mu\text{m}$, and positioned as close as possible to the sample to minimize the effects of multiple scattering in the scintillator which causes the beam to spread. A large beam spot is especially undesirable with small samples since some of the muons will miss the sample and produce a background signal. The muon counter will also detect beam contamination positrons and decay positrons from stopped muons, but with a far lower efficiency than it has for muons. False events due to positrons can usually be rejected by threshold set points in the constant fraction discriminators in the electronics (labeled CFD in

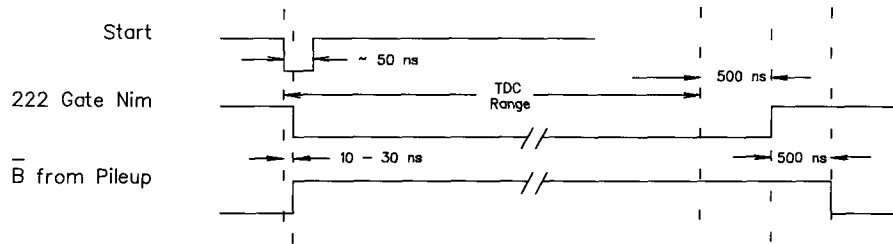
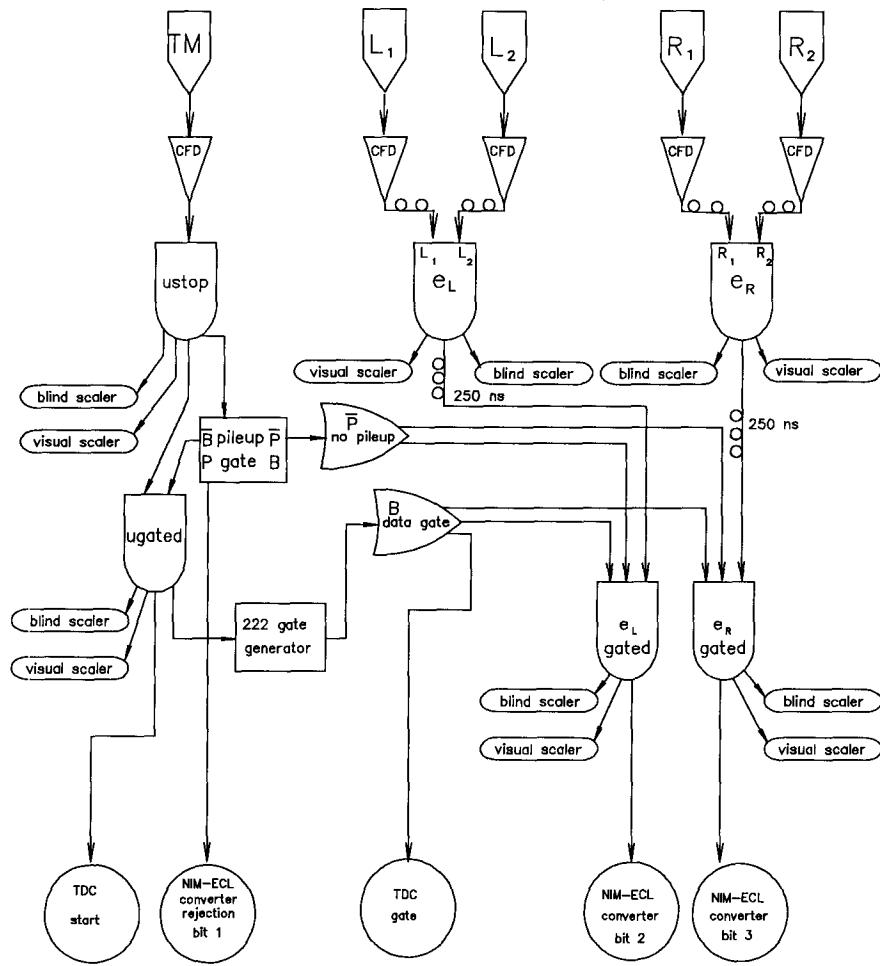


Figure 2.4: μ SR Time Differential Electronics Schematic. The 250 ns delay line from the positron counters allows a histogram to accumulate the positron events which occur *before* a muon enters the sample. If these events are not correlated with the muon entering the sample, this provides a good estimate of the random background. Note that only two of the counters are shown (L and R).

Fig. 2.4).

Between the magnet and the sample are the decay positron counters (Fig. 2.2). For an LF geometry, one (BACKWARD) will be between the beam pipe and the sample (with a hole cut out for the beam to pass through) and another (FORWARD) on the opposite side of the sample. For a spin-rotated TF geometry, the counters are placed surrounding the beam rather than intersecting it. One (UP) will be in the direction of the pre-rotated muon spin and another (DOWN) 180° opposite. Whenever possible, two more are used, LEFT and RIGHT (Fig. 2.3). If all six counters are used, it is in principle possible to subtend all angles (save the two holes for the beam entrance and the cryostat) and not waste any of the decay positrons. Overlap of detector solid angles must be carefully avoided since “multiple hits” render the trigger ambiguous.

Time differential μ SR maps the time evolution of the muon spin polarization. First, the beam rate is reduced until less than one muon on average enters the sample during the time window Δt over which one wishes to examine the muon behavior (typically $\Delta t \approx 10 \mu s$). The time window (“gate”) is generally chosen to be between two and five muon lifetimes; since the number of events falls off exponentially with time, longer gates are impractical. The signal from the muon counter (indicating an incoming muon) starts a clock, subject to a pile-up gate. The muon thermalizes and stops in the sample, where it precesses in the local field until it decays. When the decay positron is detected in one of the positron counters (BACKWARD, FORWARD, UP, DOWN, LEFT or RIGHT) the clock is stopped and the event is added to the appropriate time bin in the histogram corresponding to that positron counter. If more than one event occurs within a data gate, then they are all rejected. The accumulation of many single events provides an ensemble average of the behavior of a single muon.

2.4 μ SR Data

The most obvious feature of a positron counter histogram is the exponential decay of the number of histogrammed events reflecting to the muon lifetime of $\tau_\mu = 2.19709(5) \mu s$ (Fig. 2.5). For the

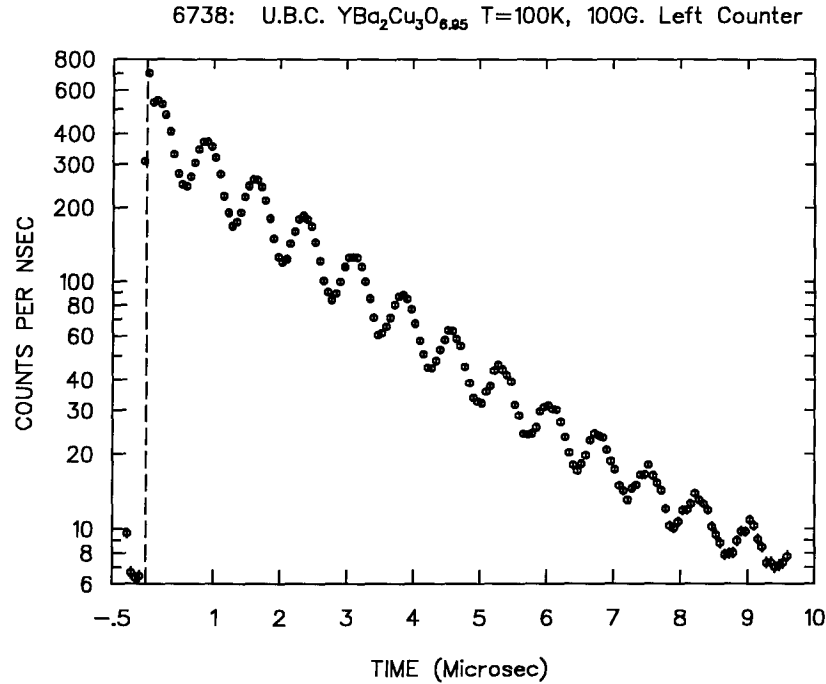


Figure 2.5: Single histogram experimental time spectrum showing the exponential decay of the muons and muon precession. The events recorded at negative times (about 6.5 counts per ns) reflect the size of the random background (see Sec. 2.5.2).

i^{th} counter, the number of events in the histogram has the form

$$N_i(t) = N_o^i [1 + A_i(t)] e^{-t/\tau_\mu} + B_i, \quad (2.9)$$

where B_i is the random background and $A_i(0)$ is the positron asymmetry. Since Poisson statistics apply to any “rare” event (such as obtaining a particular time interval for muon decay), N events between times $t - \delta t/2$ and $t + \delta t/2$ implies a statistical uncertainty of $\sqrt{N + 1}$. For large numbers of events, this reduces to \sqrt{N} . The histograms for two matched counters, *e.g.*, LEFT and RIGHT, would contain the same number of events if there were no net spin polarization (assuming that the counter geometries and photomultiplier efficiencies are exactly the same—Sec. 2.5 shows how to account for the differences). However, if the polarization were predominantly in the direction of one of the counters, a higher percentage of the decay positrons would be detected in that counter compared to the others. The precession of the ensemble muon polarization will be detected as a periodic oscillation in the number of positron events recorded for a particular counter.

Since the overall decay in the histogram due to the lifetime of the muon is unrelated to the

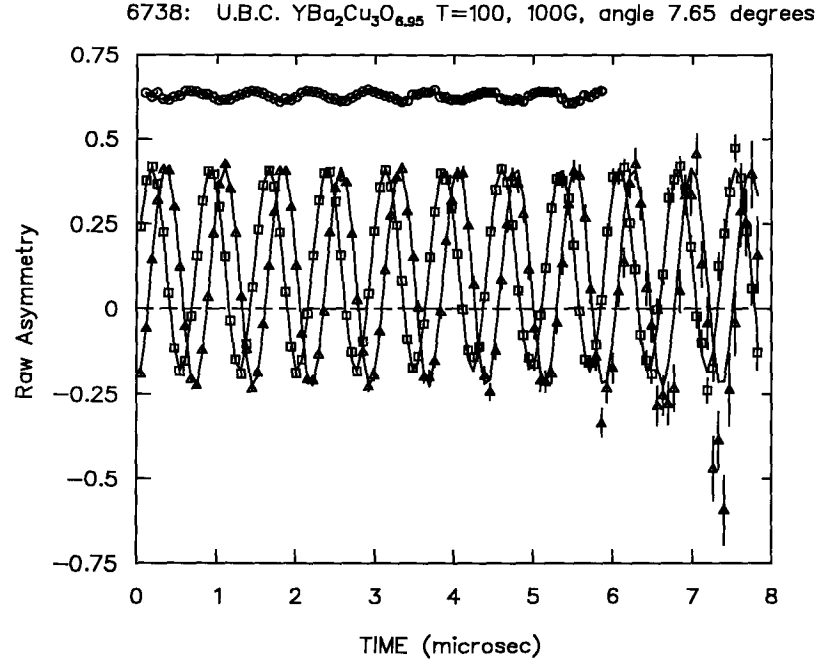


Figure 2.6: Experimental two-spectrum histogram of raw asymmetry *vs.* time showing muon precession. Both the applied field and the muon spin are in the \hat{X} - \hat{Z} plane (see Fig. 2.10), with the muon spin at an angle of 97.85° from the \hat{Z} axis and the applied field of 100 G at an angle of 7.85° from the \hat{Z} axis. The UP-DOWN (\hat{X}) raw asymmetry is shown by the squares, the RIGHT-LEFT (\hat{Y}) by triangles and FORWARD-BACKWARD (\hat{Z}) by circles. If the applied field were exactly along the \hat{Z} axis, the FORWARD-BACKWARD asymmetry would show *no* oscillations. (The laboratory coordinate system \hat{X} - \hat{Y} - \hat{Z} is defined in Fig. 2.3. The coordinate system \hat{x} - \hat{y} - \hat{z} is reserved for the sample.)

information we want to extract, it is useful to combine pairs of histograms in such a way that the muon lifetime is removed. The relative asymmetry $A_{LR}(t)$ of two paired histograms $N_L(t)$ and $N_R(t)$ is defined by

$$A_{LR}(t) = \frac{[N_L(t) - B_L] - [N_R(t) - B_R]}{[N_L(t) - B_L] + [N_R(t) - B_R]}, \quad (2.10)$$

where B_L and B_R are the random backgrounds (see Secs. 2.5.2 and 2.5.1) for the respective histograms (Fig. 2.6). The only reminder of the muon's exponential decay (e^{-t/τ_μ}) will be that, neglecting the random background, the error bars increase approximately exponentially ($\propto e^{+\frac{1}{2}t/\tau_\mu}$) for the bins corresponding to longer times. Except for the exponential growth of the error bars, the asymmetry $A_{LR}(t)$ is analogous to an NMR free induction decay (FID).

The experimental asymmetry A in the positron distribution registered by scintillation counters

is approximately, but *not* exactly, equal to \bar{a} (see Eq. 2.6). It is reduced because the muon beam is not always 100% polarized and because the positron polarization is averaged over the solid angle which a counter subtends, but at the same time it is increased because there is positron degrader between the decaying muon and the positron counters. Any material which positrons pass through acts as positron degrader by absorbing the lower energy positrons with their lower asymmetry but transmitting higher energy positrons with their higher asymmetry. In our apparatus, the sample itself, the cryostat walls and optional carbon degraders* all act as positron degrader.

For a TF geometry with the applied field \vec{H} (giving rise to an internal field $\vec{B} = B\hat{Z}$) perpendicular to \hat{Y} (LEFT and RIGHT counters), the signal observed in the absence of depolarization is

$$A_{LR}(t) = A_o^{LR} P_Y(t) = A_o^{LR} \cos(\gamma_\mu B t + \phi) = A_o^{LR} \cos(2\pi\nu t + \phi), \quad (2.11)$$

where A_o^{LR} is the empirical asymmetry maximum (obtained when $P_Y = 1$), $\nu = \frac{\gamma_\mu}{2\pi} B$ is the muon precession frequency, $\frac{\gamma_\mu}{2\pi} = 0.01355342(\pm 0.51 \text{ ppm}) \text{ MHzG}^{-1}$ [42] is the gyromagnetic ratio and ϕ is the initial phase. The maximum measurable asymmetry A_o^{LR} will be $\sim 33\%$ (see Sec. 2.2) due to the kinematics of muon decay; this may be reduced by counter geometry or increased by addition of degraders.

If the local field $[\vec{B}(\vec{r}) = B_X(\vec{r})\hat{X} + B_Y(\vec{r})\hat{Y} + B_Z(\vec{r})\hat{Z}]$ is not exactly equal to the average total internal field $\vec{B}_o = B_o\hat{Z}$, the polarization $P_Y(t)$ in the \hat{Y} direction (LEFT and RIGHT counters) for a muon stopping at position \vec{r} can be expressed as[48]

$$P_Y(t, \vec{r}) = \frac{B_Y^2(\vec{r})}{B^2(\vec{r})} + \frac{B_X^2(\vec{r}) + B_Z^2(\vec{r})}{B^2(\vec{r})} \cos(\gamma_\mu B t + \phi). \quad (2.12)$$

with $\phi = \pi/2$ when the initial polarization $\vec{P}(0)$ is along the \hat{X} direction. If the local field is not constant over the sample, there will be a range of muon precession frequencies. Averaging over the sample volume gives the time dependence of the ensemble polarization as

$$P_Y(T) = \int_V P_Y(T, \vec{r}) d\vec{r} \rightarrow G_o + G_{YY}(t) \cos(\gamma_\mu B_o t + \phi), \quad (2.13)$$

*In the past, blocks of carbon have been placed between the sample and the positron counters. Because this lowers the measured positron event rate and because detector geometries are rather tight, it is now common practice at TRIUMF to leave out additional positron degrading material.

where

$$G_o = \int_V \frac{B_Y^2(\vec{r})}{B^2(\vec{r})} d\vec{r} \quad (2.14)$$

is a constant corresponding to portion of the average field which is parallel to the initial muon spin and $G_{YY}(t)$ is a “dephasing” function representing a decrease in the magnitude of the average polarization. (This simple treatment is only valid for symmetric local field distributions as discussed in Sec. 2.6.3.) Exponential relaxation $[G_{YY}(t) = e^{-\Gamma t}]$ is usually assumed when the local fields are fluctuating fast enough that the “motional narrowing” limit is in effect.[49, Sec. X.I] When the muons are static and any magnetic structure in the solid is static, Gaussian dephasing $G_{YY}(t) = e^{-\frac{1}{2}\sigma^2 t^2}$ is often used as an *Ansatz* until an appropriate theoretical description of the muon depolarization is formulated. In a high precision experiment, this *Ansatz* can lead to qualitative and quantitative misinterpretation.

2.5 Sources of Experimental Distortions

The previous section briefly described how the asymmetry $A(t)$ is extracted from the data. However, experimental realities such as differences in efficiency within a pair of counters (which includes the response of the PMTs, the discrimination threshold in the electronics and the physical characteristics of the scintillators and light guides), differences in solid angle subtended by a pair of counters and errors in the random background estimate can distort the calculations. This section describes the expected distortions and explains how to correct for them. Parts of this discussion also appear in Ref. [50].

2.5.1 Corrected Asymmetry Plots

The events recorded in a single histogram (labelled i) can be described by

$$N_i(t) = N_o^i e^{-t/\tau_\mu} [1 + A_i(t)] + B_i, \quad (2.15)$$

where $\tau_\mu = 2.19709(5) \mu\text{s}$ is the muon lifetime. The index i is one of $\pm X$, $\pm Y$ or $\pm Z$ (see Fig. 2.10). The asymmetry function $A_i(t)$ is equal to a constant A_o^i times $P_i(t)$, the projection

of the muon polarization function $\vec{P}(t)$ onto the i^{th} detector symmetry axis. The initial asymmetry A_o^i , which is usually between 0.2 and 0.4, contains factors related to the positron emission probability distribution (Sec. 2.2), positron absorption in the apparatus and the solid angle of the counter. With larger counter solid angles, the asymmetry is reduced due to a spatial averaging of $\cos \theta$ in Eq. 2.6. (On the other hand, a larger counter has a higher detection efficiency.) The constant term B_i is the random background signal due to false events caused by, for instance, the portion of the dark current noise in the photomultiplier tubes (PMTs) which has a larger voltage than the discrimination level set in the electronics. Cosmic rays and positron contamination in the muon beam can also contribute to the random background. The random background is assumed to be independent of the muon arrival time which starts the clock for the histogram. This contrasts with the exponential decay (due to the muon lifetime) in the number of “good” events.

In the ideal case, opposing counters (i and $-i$) should see the same signal 180° out of phase. However, differences in positron absorption, PMT efficiency, discrimination level and counter position relative to the beam axis (since the beam has positron contamination) will affect both the random background levels (B_i and B_{-i}) and the normalization of the number of events (N_o^i and N_o^{-i}). Differences in counter solid angle, counter efficiency and positron absorption will affect the normalization and the average decay asymmetry (A_o^i and A_o^{-i}). For a pair of counters (i and $-i$), these effects can be summarized as

$$\begin{aligned} N_i(t) &= N_o^i e^{-t/\tau_\mu} [1 + A_i P(t)] + B_i, \\ N_{-i}(t) &= \alpha N_o^i e^{-t/\tau_\mu} [1 - \beta A_i P(t)] + B_{-i}, \end{aligned} \quad (2.16)$$

where $\alpha = N_o^{-i}/N_o^i$ and $\beta = |A_{-i}|/|A_i|$. Note that the second equation assumes that the counters are *exactly* opposite each other so that

$$P_{-i}(t, \phi) = P_i(t, \phi + \pi) = -P_i(t, \phi) \quad (2.17)$$

where ϕ is the initial phase of the muon polarization.

The experimental “raw asymmetry” is defined by

$$A_{\text{raw}}(t) = \frac{[N_i(t) - B_i] - [N_{-i}(t) - B_{-i}]}{[N_i(t) - B_i] + [N_{-i}(t) - B_{-i}]}, \quad (2.18)$$

where the random background has been explicitly subtracted from each histogram. The exponential decay is automatically removed by cancellation in the numerator and the denominator. This means that the raw asymmetry can be used to present experimental data quickly in such a way that the muon lifetime is removed without fitting beforehand. It is particularly useful for viewing zero- and longitudinal-field data. However, the raw asymmetry depends on α and β , which can only be accurately determined by fitting. In its favor, the statistical error associated with the raw asymmetry is approximately a factor of $1/\sqrt{2}$ smaller than that for a single histogram; this improves the results of fits to the asymmetry and reduces noise in the Fourier transform of the asymmetry (see Secs. 3.3.1 and 3.3.2.)

The raw asymmetry can be related to the “corrected” asymmetry $A(t) = A_o^i P_i(t)$ by

$$A_{\text{raw}}(t) = \frac{A(t)(\alpha\beta + 1) - (\alpha - 1)}{(\alpha + 1) - A(t)(\alpha\beta - 1)}. \quad (2.19)$$

Conversely, the corrected asymmetry can be extracted from the raw asymmetry by

$$A(t) = A_o^i P(t) = \frac{A_{\text{raw}}(t)(\alpha + 1) - (\alpha - 1)}{(\alpha\beta + 1) + A_{\text{raw}}(t)(\alpha\beta - 1)}. \quad (2.20)$$

In the case of $\beta = 1$, the corrected asymmetry is given expressly in terms of “primitive” quantities by

$$A(t) = \frac{[N_i(t) - B_i] - [N_{-i}(t) - B_{-i}]/\alpha}{[N_i(t) - B_i] + [N_{-i}(t) - B_{-i}]/\alpha}. \quad (2.21)$$

Interesting distortions arise in the raw asymmetry due to the effects of α , β and poor background subtraction. Figs. 2.7.a and 2.7.b show the effect of $\alpha \ll 1$ on the raw histogram (normalized by N_o^i) and the asymmetry $A(t)$, with $A_o^i = 0.3$. The corrected asymmetry is centered about zero whereas the raw asymmetry has an asymptotic value of 0.6, which produces a large zero frequency peak in the real Fourier transform (Fig. 2.7.c). At early times, the raw asymmetry is not symmetric about the asymptotic value of 0.6, but appears slightly elongated below and compressed above. This produces spurious peaks in the Fourier transform at integer multiples of the signal’s true frequency alternatively in phase and 180° out of phase with the signal. The FORWARD/BACKWARD raw asymmetry in Fig. 2.6 is an example of experimental data which has a value of α far from unity. Figs. 2.7.d, 2.7.e, and 2.7.f show the effect of $\beta \ll 1$, which is

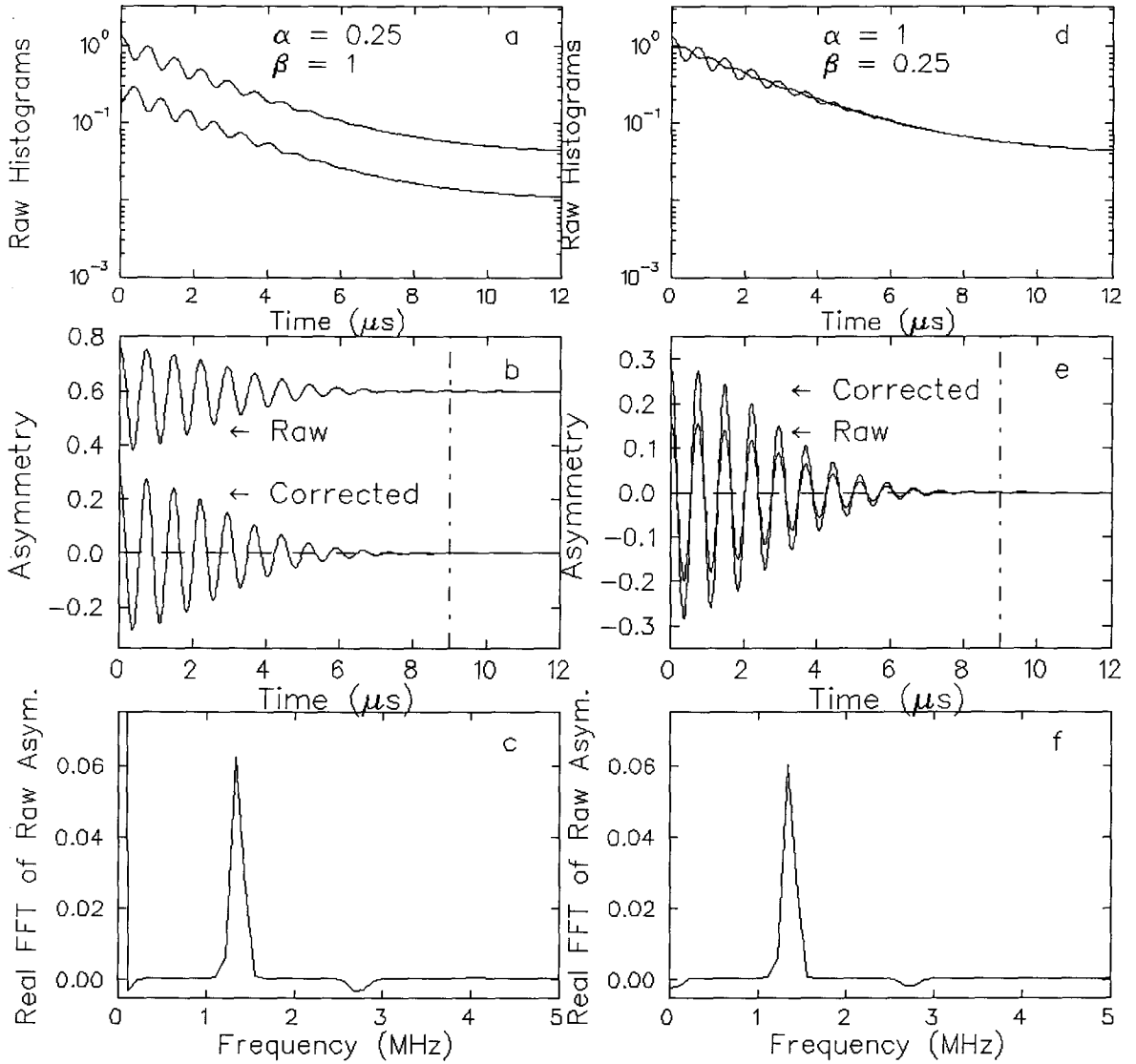


Figure 2.7:

- Raw histograms for two counters, with $\alpha = 0.25$ and $\beta = 1.0$. Backgrounds set to $B_i = 0.04$ and $B_{-i} = 0.01$. (N_o^i has been divided out of both spectra.)
- Raw asymmetry (centered about 0.6) and corrected asymmetry (centered about 0.0) for $\alpha = 0.25$ and $\beta = 1.0$.
- Real fast Fourier transform of the raw asymmetry for $\alpha = 0.25$ and $\beta = 1.0$ over only first 9 μs . The main peak at 1.355 Mhz corresponds to an average field of 100 G.
- Raw histograms for two counters, with $\alpha = 1.0$ and $\beta = 0.25$. Backgrounds set to $B_i = 0.04$ and $B_{-i} = 0.04$.
- Raw asymmetry [$A_{\text{raw}}(0) \approx 0.175$] and corrected asymmetry [$A(0) = 0.3$] for $\alpha = 0.25$ and $\beta = 1.0$.
- Real fast Fourier transform of the raw asymmetry for $\alpha = 1.0$ and $\beta = 0.25$ over only first 9 μs . The main peak at 1.355 Mhz corresponds to an average field of 100 G.

surprisingly similar to the effect of α . The major difference is that there is no offset in the asymmetry (hence nearly no zero frequency peak in the Fourier transform) and the second harmonic is smaller in the Fourier transform. Since these “distortions” in the raw asymmetry arise from mismatched counters, Fourier transforms of *single* histograms will *not* show them.

2.5.2 Random Background

The random background rate is estimated either by fitting or by accumulating the positron events which occur just before every muon enters the sample (see Fig. 2.4). Since the passage of the muon through the muon counter defines time zero, positron events occurring before that are said to be events at negative times. The background rate may be due to the following sources:

1. Dark current noise in the PMTs which has a larger voltage than the discrimination level set in the electronics.
2. Cosmic ray muons hitting the counters.
3. Positrons from the production target not filtered out of the beam.
4. γ -ray showers produced by positrons passing through the lead shielding around the final collimator. The positrons are predominantly those produced by the decay of muons stopped by the collimator.

Note that a γ -ray shower may trigger the muon counter and then a positron counter (or in the other order), so a lot of false events will be recorded close to zero time and a few false events will be recorded at long times. This is not a source of truly *random* background, nor does it have a time dependence exhibiting the muon lifetime. Assuming that γ -ray shower events are truly random will produce terrible distortions in the asymmetry spectra.

In TF experiments, one may easily determine the random background with complete fits over positive times. In zero field and longitudinal field experiments, it is often difficult to distinguish between the relative contributions of the asymmetry, the exponential muon decay, the mismatch in

counters and the background. In these cases, it is much better to *measure* the random background using negative times.

Problems in background subtraction are insidious. One can demonstrate the effect of an unexpected time dependent background in which the number of background events decreases linearly with time. Though collimator shielding problems probably produce a more rapidly decreasing behaviour, even a linearly decreasing background qualitatively shows the distortions observed experimentally. Overestimating a background signal which is truly random shows the same effect.

After subtracting an overestimated but random background from the single counter histogram, the background “corrected” data will be distorted, with the number of events actually going *negative* at long times! An asymmetry plot which combines two such histograms has a resonance-like distortion where the asymmetry goes to $\pm\infty$ at the time where the sum of the two spectra equals zero (see the denominator in Eq. 2.18) since the corrected number of counts have opposite signs. For an overestimated but random background, Fig. 2.8.a shows the absolute value of the raw histograms, after background subtraction, Fig. 2.8.b shows the asymmetry plot and Fig. 2.8.c shows the resulting real Fourier transform. If the Fourier transform is done over a time range which includes the distortion, it will be completely spoiled by an oscillatory signal with a period equal to the time at which the asymmetry crosses zero. Over a shorter time range, the downturn in the asymmetry produces a broad negative peak near zero frequency.

Figs. 2.8.d, 2.8.e and 2.8.f show what happens when a portion of the background is linearly decreasing. This is very similar to an incorrectly determined flat background, since making an asymmetry plot by combining two such histograms with slightly different slopes in the random background also results in a resonance-like distortion where the asymmetry goes to $\pm\infty$. This is a very serious problem since no existing μ SR data analysis software is equipped to handle time dependent background signals for single-histograms or for asymmetry plots. (Nor could it be—what time dependence would one assume?)

2.5.3 Relative Phase of Counters

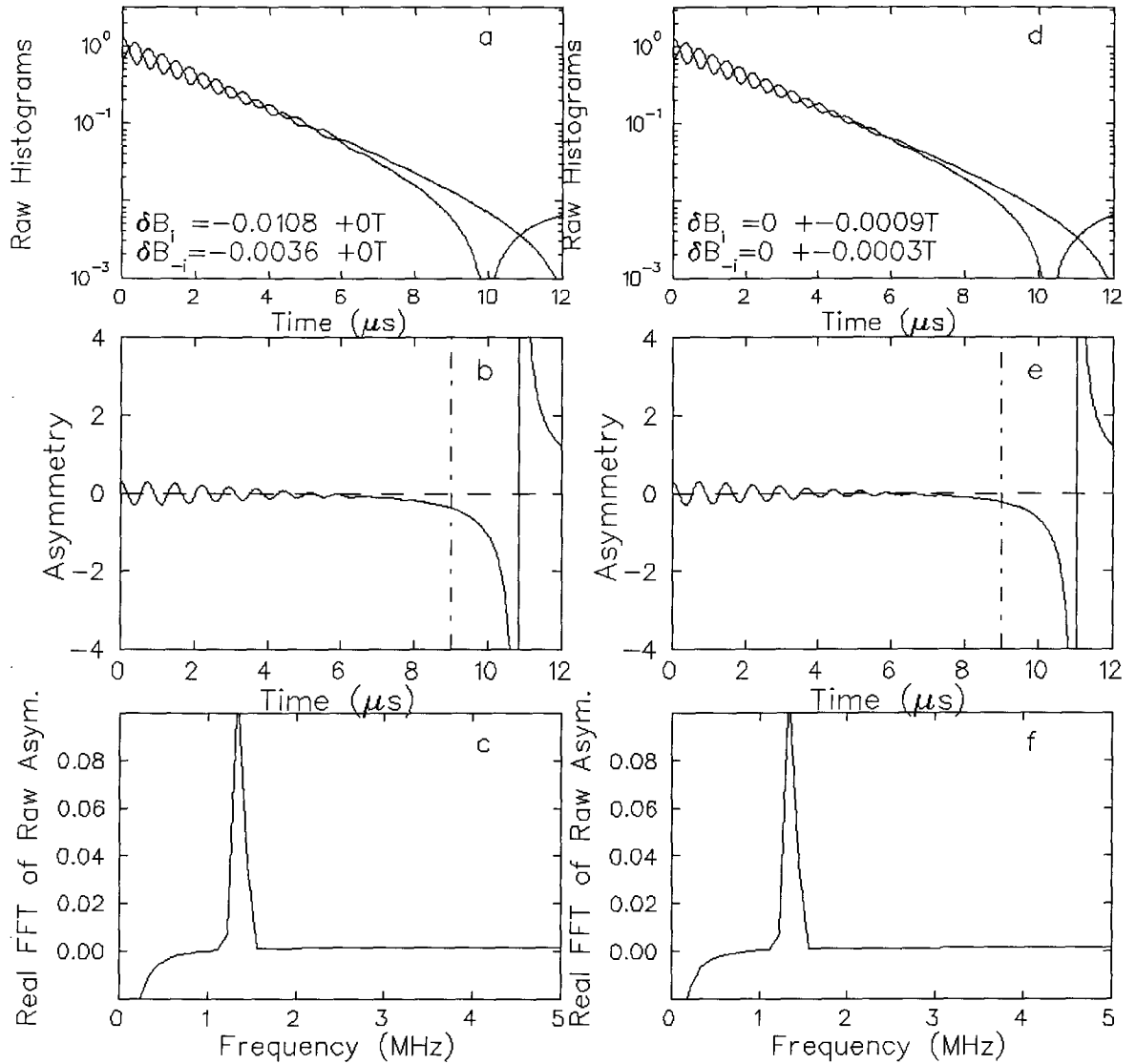


Figure 2.8:

- Absolute value of the raw histograms for two counters after incorrect background subtraction resulting in a residual constant background $\delta B_i = -0.0108$ and $\delta B_{-i} = -0.0036$.
- Raw asymmetry for $\delta B_i = -0.0108$ and $\delta B_{-i} = -0.0036$.
- Real fast Fourier transform of the raw asymmetry for $\delta B_i = -0.0108$ and $\delta B_{-i} = -0.0036$, over only first $9 \mu\text{s}$.
- Absolute value of the raw histograms for two counters, after incorrect background subtraction resulting in a residual time-dependent background $\delta B_i = -0.0009t$ and $\delta B_{-i} = -0.0003t$.
- Raw asymmetry for $\delta B_i = -0.0009t$ and $\delta B_{-i} = -0.0003t$.
- Real fast Fourier transform of the raw asymmetry for $\delta B_i = -0.0009t$ and $\delta B_{-i} = -0.0003t$, over only first $9 \mu\text{s}$.

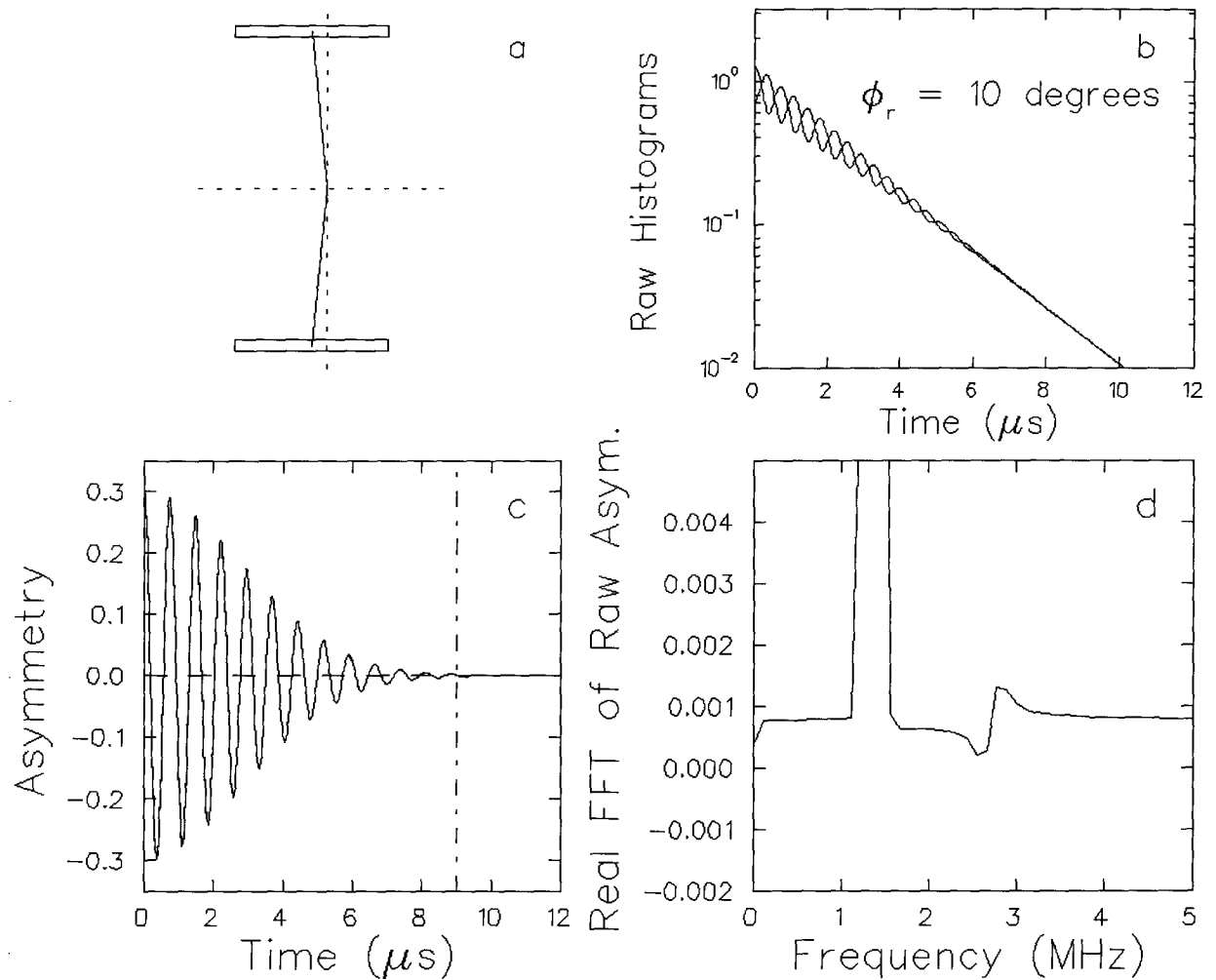


Figure 2.9: Effect of Relative Phase Between Counters

- a. Sketch of a pair of counters having a relative phase $\phi_r = 10^\circ$. (The sample is at the origin.)
- b. Raw histograms for two counters with relative phase of 10° (without random background).
- c. Raw asymmetry for relative phase of 10° . (Nothing looks unusual “by eye.”)
- d. Real fast Fourier transform of the raw asymmetry for relative phase of 10° , over the first $9 \mu\text{s}$. The amplitude has been restricted to emphasize the distortion at the second harmonic.

The distortions described in the above two sections show up in the Fourier transform as artificial enhancements of the zero frequency peak or as harmonics which are 0° or 180° out of phase from the true signal. The harmonics with phase 0° and 180° occur when the asymmetry plot is distorted vertically by α and β . In this section I describe distortions that show up as harmonics with phase 90° and 270° which occur when there are phase mismatches between opposite counters.

Fig. 2.9.a shows a pair of counters having a relative phase ϕ_r (over and above the assumed 180° taken into account by the opposite signs of the asymmetry in Eq. 2.16) because they are not centered about the sample. The effect of the relative phase on the raw histograms (Fig. 2.9.b) can be expressed as follows:

$$\begin{aligned} N_i(t) &= \exp(-1/\tau_\mu) \left[1 + A_o^i G(t) \cos\left(2\pi\nu t - \frac{\phi_r}{2}\right) \right] + B_i \\ N_{-i}(t) &= \exp(-1/\tau_\mu) \left[1 - A_o^i G(t) \cos\left(2\pi\nu t + \frac{\phi_r}{2}\right) \right] + B_i, \end{aligned} \quad (2.22)$$

where I have used

$$A_o^i P_i(t) = A_o^i G(t) \cos\left(2\pi\nu t - \frac{\phi_r}{2}\right) \quad (2.23)$$

to explicitly show the asymmetry's dependence on the relative phase ϕ_r .

The raw asymmetry (Fig. 2.9.c) is given by

$$A_{\text{raw}}^i(t) = \frac{A_o^i G(t) \cos(2\pi\nu t) \cos(\phi_r/2)}{1 + A_o^i G(t) \sin(2\pi\nu t) \sin(\phi_r/2)}, \quad (2.24)$$

which is just the true asymmetry [$A(t) = A_o^i P(t) = A_o^i G(t) \cos(2\pi\nu t)$] modified by a term with period $1/\nu$. For small angles ϕ_r , the raw asymmetry can be written in the form

$$A_{\text{raw}}^i(t) \approx a(t) \cos(2\pi\nu t) \cos(\phi_r/2) + b(t) \sin(4\pi\nu t) \sin(\phi_r). \quad (2.25)$$

As seen in Fig. 2.9.d, this produces a second harmonic in the FFT which is 90° out of phase relative to the real signal.

Relative phase distortions are often present due to geometrical misalignment of counters, inhomogeneous efficiencies of the detectors and timing misalignments, but it is not clear how to

correct for them.[†] In high magnetic fields (where the linewidth of the experimental data is much smaller than the applied field) relative phase is not a problem in the Fourier transforms because the harmonics are very far from the true signal. Distortions appeared for the data taken at fields of 100 G (see Fig. 5.7). Fortunately, the FFT for a *single* counter histogram is not affected. To my knowledge, no one has ever drawn attention to this problem before.

2.6 Full Vector Treatment of Polarization Evolution

2.6.1 Motivation

It is easy to visualize a single muon precessing in a magnetic field \vec{B} , even if the field and initial spin directions are not aligned with respect to the laboratory reference frame $\hat{X}\text{-}\hat{Y}\text{-}\hat{Z}$. The muon spin precesses as a function of time in a cone about the field. This action can be projected onto the plane perpendicular to the i^{th} coordinate axis using $s_i + a_i \cos(\gamma_\mu B t + \phi_i)$ for $i = X, Y$ and Z where the oscillatory amplitude a_i and the non-oscillatory amplitude s_i are ≤ 1 . These projections are simply the components of the muon spin in the laboratory reference frame. If the field and spin are mutually orthogonal then the cone is actually a plane and there are no non-oscillatory components (*i.e.*, $s_i \equiv 0$).

One can construct and combine the projections for an ensemble of muons stopping throughout the local field distribution of interest, creating a net polarization. Due to dephasing, the magnitude of the polarization vector will *decrease* in time. Generally, the ensemble polarization cannot conveniently be expressed analytically for arbitrary field distributions. An exception is the polarization produced by a Gaussian distribution of dipolar fields, which in zero applied field yields a static Gaussian Kubo-Toyabe function[51]

$$P_z(t) = \frac{1}{3} + \frac{2}{3}(1 - \Delta^2 t^2) e^{-\frac{1}{2}\Delta^2 t^2} \quad (2.26)$$

[†]Adjusting t_o (the place in the histogram defined as the time $t = 0$) such that $\phi_r = 0$ is tempting, but then the dephasing function $G(t)$ will not match at time t for the pair of counter histograms used to produce the asymmetry plot. This will of course introduce new distortions.

with the dephasing rate Δ determined by the mean square of the local field components

$$\frac{\Delta^2}{\gamma_\mu^2} = \langle B_x^2 \rangle = \langle B_y^2 \rangle = \langle B_z^2 \rangle. \quad (2.27)$$

For a field B_o which is much larger than the mean local field variation and is applied perpendicularly to the muon spin, the polarization is given by

$$P_x(t) = e^{-\frac{1}{2}\sigma^2 t^2} \cos(\gamma_\mu B_o t) \quad (2.28)$$

with the dephasing rate σ determined by

$$\frac{\sigma^2}{\gamma_\mu^2} = \langle (B_z - B_o)^2 \rangle. \quad (2.29)$$

This section describes the muon polarization function for an arbitrary distribution of local fields and an arbitrary initial muon spin direction. It expresses polarization (which can be difficult to visualize) using vector notation, with particular emphasis on the time-dependent oscillatory and non-oscillatory amplitudes. It describes how the theoretical net polarization can be cast in a form which is convenient for “table” fits. Secs. 3.3.2 and 4.8 discuss how this affects the results of Fourier transforms and how to fit data with more than one source of local field inhomogeneity. These skills are needed to rigorously fit μ SR data taken in the anisotropic superconductor $\text{YBa}_2\text{Cu}_3\text{O}_{6.95}$ in low fields applied at all angles relative to the \hat{c} axis (see Ch. 5).

Note that arbitrary vectors are indicated by “arrows” (*e.g.*, \vec{B}) while unit vector are indicated by “hats” (*e.g.*, \hat{x}). (In this thesis, “hats” never indicate quantum mechanical operators.)

2.6.2 Positron Counter and Local Field Reference Frames

Muon polarization can be examined from different reference frames. The positron counters form a reference frame $[\hat{X}\text{-}\hat{Y}\text{-}\hat{Z}]$, with the TOP-BOTTOM counters defining \hat{X} , the RIGHT-LEFT counters defining \hat{Y} and the FORWARD-BACKWARD counters defining \hat{Z} (see Fig. 2.10). The components in the counter frame are specified by subscripts of upper case X , Y and Z . The signal observed in a positron counter is simply a projection of the muon polarization on the plane perpendicular to one of the counter reference frame’s axes; this makes the counter reference frame convenient for data analysis.

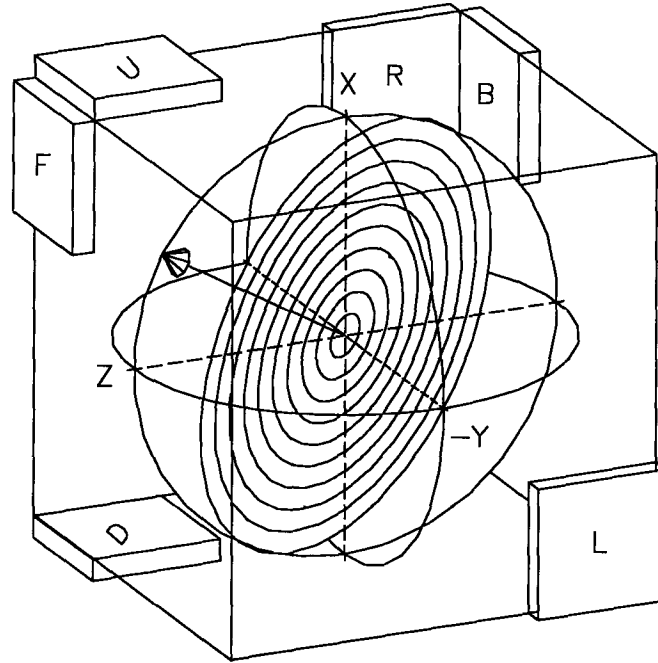


Figure 2.10: Cube of positron counters, with only a portion of each counter shown. The labels correspond as following: U = UP, D = DOWN, L = LEFT, R = RIGHT, B = BACK and F = FORWARD. The muon momentum is along the \hat{Z} direction, the initial muon spin is at an angle of 120° from \hat{Z} and the applied field (the arrow) is at an angle of 30° from \hat{Z} . The bull's eye shows the muon precession cone.

Another reference frame $[\hat{x}-\hat{y}-\hat{z}]$ is formed by setting \hat{z} parallel to the average internal field \vec{B}_o . The applied field \vec{H}_o is assumed to be parallel to \vec{B}_o but perpendicular to \hat{Y} , which places \hat{z} in the $\hat{X}-\hat{Z}$ plane. This is equivalent fixing $\hat{y} = \hat{Y}$, which in turn forces $\hat{X}-\hat{Z}$ and $\hat{x}-\hat{z}$ to be the same plane (though rotated by an angle θ ; see Fig. 2.11). The components of the average internal field frame are specified by subscripts of lower case x , y and z . This frame is better than the counter frame for some calculations, especially when the applied field is not along one of the counter frame axes. It corresponds to the coordinate system used in Ch. 4 for the field distribution in an anisotropic superconductor.

In the average internal field reference frame, the initial ensemble muon polarization $\vec{P}(0)$ is at an angle ϕ to the \hat{z} axis and is rotated by an angle of ψ in the $\hat{x}-\hat{y}$ plane. Assuming the muons

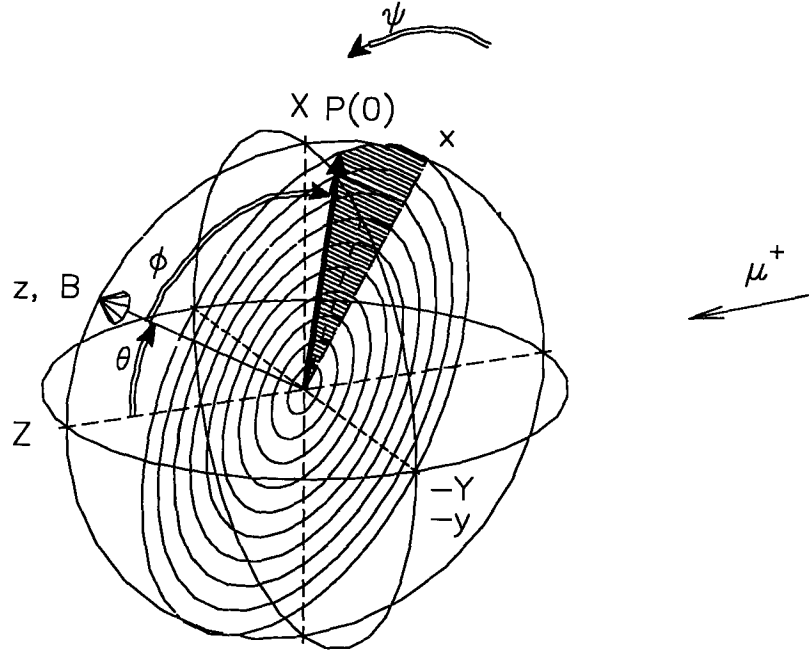


Figure 2.11: The muon momentum is along the \hat{Z} direction. The average internal field B_0 (the cone-headed arrow) is along the \hat{z} axis at an angle θ to \hat{Z} , and is constrained to lie in the \hat{X} - \hat{Z} plane. The initial muon polarization (solid arrow) is at an angle $\phi = 90^\circ$ from the \hat{z} axis and the shaded area shows the initial phase of ψ from the \hat{x} axis in the \hat{x} - \hat{y} plane. (If $\psi = 0$, then the initial muon polarization is also in the \hat{X} - \hat{Z} plane.) The bull's eye shows the muon precession cone, which is a flat plate in the \hat{x} - \hat{y} plane when $\phi = 90^\circ$. (For the low field experiment described in Chs. 4 and 5, ϕ was set to 90° when experimental constraints allowed.)

are initially fully polarized, $\vec{P}(0) = \hat{P}(0)$ is given by

$$\begin{pmatrix} P_x(0) \\ P_y(0) \\ P_z(0) \end{pmatrix} = \begin{pmatrix} \sin \phi \cos \psi \\ \sin \phi \sin \psi \\ \cos \phi \end{pmatrix} \quad (2.30)$$

where the angle ϕ is chosen by use of a muon spin rotator which operates in the \hat{x} - \hat{z} plane and the angle ψ is the “initial phase” of the muon polarization (which should not be confused with counter’s residual phase ϕ_r in Eq. 2.24). When the angle ϕ is 90° the applied field and muon polarization are perpendicular, so it is called a “transverse field” (TF) experiment. When the angle ϕ is 0° or 180° , the applied field and muon polarization are parallel so it is called a “longitudinal field” (LF) experiment. In between it is called a “skewed field” (SF) experiment.[52] For this thesis, I performed mostly TF experiments; when the spin-rotator did not allow for TF,

I performed SF experiments ($\phi < 90^\circ$) as close as possible to TF.

During the time of flight from the spin rotator to the sample, the net muon polarization may experience rotation because of the fringe fields from experimental magnets and any ambient magnetic field; this may contribute to either ϕ or ψ or both. Contributions to ϕ are ignored, though they could be approximately treated as a reduction in the transverse component of the polarization. Contributions to ψ , typically varying from a few degrees for ambient and fringe fields on the order of several gauss to one or more complete precessions for applied fields of several tesla, are accommodated using Eq. 2.30.

The counter frame is related to the internal field frame by rotation about the $\hat{y} = \hat{Y}$ axis using the rotation matrix

$$\mathbf{R}(\theta) = \begin{pmatrix} \cos \theta & 0 & \sin \theta \\ 0 & 1 & 0 \\ -\sin \theta & 0 & \cos \theta \end{pmatrix}. \quad (2.31)$$

This transformation gives the average field \vec{B}_o in the counter frame $[\hat{X}\hat{Y}\hat{Z}]$ as

$$\begin{pmatrix} B_X \\ B_Y \\ B_Z \end{pmatrix} = \mathbf{R}(\theta) \begin{pmatrix} B_x \\ B_y \\ B_z \end{pmatrix} = \begin{pmatrix} \sin \theta \\ 0 \\ \cos \theta \end{pmatrix} B_o \quad (2.32)$$

and the initial muon spin polarization $\vec{P}(0)$ as

$$\begin{pmatrix} P_X(0) \\ P_Y(0) \\ P_Z(0) \end{pmatrix} = \begin{pmatrix} \cos \theta \sin \phi \cos \psi + \sin \theta \cos \phi \\ \sin \phi \sin \psi \\ -\sin \theta \sin \phi \cos \psi + \cos \theta \cos \phi \end{pmatrix} = \mathbf{R}(\theta) \begin{pmatrix} P_x(0) \\ P_y(0) \\ P_z(0) \end{pmatrix}. \quad (2.33)$$

2.6.3 Vectorized Polarization Functions

Consider a sub-ensemble of muons stopped at positions \vec{r} in the sample which all have the same local field $\vec{B}(\vec{r})$ not necessarily equal to the average field $\vec{B}_o = B_o \hat{z}$ in either direction or magnitude. The unit vector in the direction of the local magnetic field is given by

$$\hat{B}(\vec{r}) = \frac{\vec{B}(\vec{r})}{|\vec{B}(\vec{r})|}. \quad (2.34)$$

The net polarization for the sub-ensemble is a vector precessing in space, forming a cone centered about the local magnetic field. The height of the cone is given by the amplitude of the non-oscillatory component of the polarization,

$$P_{\parallel}(0, \vec{r}) = \hat{P}(0) \cdot \hat{B}(\vec{r}) \quad (2.35)$$

and the radius of its base is given by the amplitude of the oscillatory component,

$$\begin{aligned} P_{\perp}(0, \vec{r}) &= \left| \hat{B}(\vec{r}) \times \hat{P}(0) \right| \\ &= \left| \hat{P}(0) - P_{\parallel}(0, \vec{r}) \hat{B}(\vec{r}) \right|. \end{aligned} \quad (2.36)$$

In Turner's nomenclature,[52] "coplanar transverse" polarization refers to the polarization projection along an axis lying in the plane defined by the average field direction \hat{z} and the initial muon spin direction and "perpendicular transverse" polarization refers to the projection along the axis perpendicular to that plane. For the sub-ensemble at \vec{r} , I will restrict the definition of coplanar transverse polarization to the projection along a coplanar axis which is perpendicular to the *local* field direction $\hat{B}(\vec{r})$. This gives the sub-ensemble coplanar transverse polarization direction as

$$\hat{u}_C(\vec{r}) = \hat{u}_P(\vec{r}) \times \hat{B}(\vec{r}) = \frac{\hat{P}(0) - P_{\parallel}(0, \vec{r}) \hat{B}(\vec{r})}{P_{\perp}(0, \vec{r})}, \quad (2.37)$$

and the sub-ensemble perpendicular transverse polarization direction as

$$\hat{u}_P(\vec{r}) = \hat{B}(\vec{r}) \times \hat{u}_C(\vec{r}) = \frac{\hat{B}(\vec{r}) \times \hat{P}(0)}{P_{\perp}(0, \vec{r})}. \quad (2.38)$$

Together, $\hat{B}(\vec{r})$, $\hat{u}_C(\vec{r})$ and $\hat{u}_P(\vec{r})$ form an orthogonal basis for a reference frame appropriate for the sub-ensemble of muons at position \vec{r} .

For example, if the initial phase ψ of the polarization is zero (see Fig. 2.11) and $\vec{B}(\vec{r}) \parallel \hat{z}$ (which is not always the case even though the average field direction \vec{B}_o defines \hat{z}), the unit vector for the non-oscillatory component of the polarization is $\hat{B}(\vec{r}) = \hat{z}$, the coplanar transverse direction is $\hat{u}_C(\vec{r}) = \hat{x}$ and the perpendicular transverse direction is $\hat{u}_P(\vec{r}) = \hat{y}$. Non-zero values for ψ will simply rotate $\hat{u}_C(\vec{r})$ and $\hat{u}_P(\vec{r})$ in the \hat{x} - \hat{y} plane. If, in addition, it is a TF experiment ($\phi = \pi/2$) then $P_{\parallel}(\vec{r}) = 0$ and $P_{\perp}(0, \vec{r}) = P(0)$.

Using the aforementioned muon sub-ensemble reference frame, we can look at the time evolution of the total muon polarization. At time zero, the polarization at point \vec{r} in the sample is given by

$$\hat{P}(0) \equiv P_{\parallel}(0, \vec{r})\hat{B}(\vec{r}) + P_{\perp}(0, \vec{r})\hat{u}_C(\vec{r}). \quad (2.39)$$

Usually we assume that the muons are initially fully polarized, hence $\vec{P}(0) = \hat{P}(0)$. If we assuming that $\vec{B}(\vec{r})$ is time independent and that there are no irreversible relaxation processes (*e.g.*, spin-spin interactions between the muon, electrons and/or nuclei or muon diffusion), then the magnitude of the sub-ensemble polarization is constant $\left[|\vec{P}(t, \vec{r})| \equiv 1\right]$ and its vector value is at time t is given by

$$\begin{aligned} \vec{P}(t, \vec{r}) = & P_{\parallel}(0, \vec{r})\hat{B}(\vec{r}) \\ & + P_{\perp}(0, \vec{r})\left\{\cos[\gamma_{\mu}B(\vec{r})t]\hat{u}_C(\vec{r}) + \sin[\gamma_{\mu}B(\vec{r})t]\hat{u}_P(\vec{r})\right\}. \end{aligned} \quad (2.40)$$

Averaging over the spatial distribution of local fields $\vec{B}(\vec{r})$, the muon polarization for the entire sample is given by

$$\begin{aligned} \vec{P}(t) = & \frac{1}{V} \int_V \left[P_{\parallel}(0, \vec{r})\hat{B}(\vec{r}) \right. \\ & \left. + P_{\perp}(0, \vec{r})\left\{\cos[\gamma_{\mu}B(\vec{r})t]\hat{u}_C(\vec{r}) + \sin[\gamma_{\mu}B(\vec{r})t]\hat{u}_P(\vec{r})\right\} \right] d\vec{r}. \end{aligned} \quad (2.41)$$

where V is the volume of the sample. The magnitude of $P(t)$ decreases with time because there is a range of local field magnitudes (the different sub-ensembles precess at different rates so the polarization amplitude decreases over time) and because there is a range of local field directions (the precession cones for different sub-ensembles point in different directions so the polarization amplitude decreases when they are averaged).

At long times, the oscillatory portion dies out and the polarization approaches a constant asymptote:

$$\begin{aligned} \vec{P}(t \rightarrow \infty) = \vec{P}_{\parallel}(t) &= \frac{1}{V} \int_V P_{\parallel}(0, \vec{r})\hat{B}(\vec{r}) d\vec{r} \\ &= \frac{1}{V} \int_V [\hat{P}(0) \cdot \hat{B}(\vec{r})] \hat{B}(\vec{r}) d\vec{r}, \end{aligned} \quad (2.42)$$

which is the average non-oscillatory polarization. It is the vector average of the axes of the precession cones for all sub-ensembles of muons at positions with different local field magnitudes

and directions. Due to the unit vector $\hat{B}(\vec{r})$, one might expect $\vec{P}_{\parallel}(t)$ to be in the direction in the direction of the average field, \hat{z} . However, when the initial muon polarization $\hat{P}(0)$ is perpendicular to the average field direction ($\phi = \pi/2$), positive and negative contributions from the inner product $\hat{P}(0) \cdot \hat{B}(\vec{r})$ will tend to cancel out the \hat{z} component in $\vec{P}_{\parallel}(t)$, leaving $\vec{P}_{\parallel}(t)$ approximately in the direction of the original polarization direction $\hat{P}(0)$. In the case of certain field distributions (see Secs. 2.6.4 and 2.6.5), $\vec{P}_{\parallel}(t)$ will be exactly parallel to $\hat{P}(0)$. If we define the precessing portion of the average polarization as

$$\vec{P}_{\perp}(t) = \frac{1}{V} \int_V P_{\perp}(0, \vec{r}) \left\{ \cos[\gamma_{\mu} B(\vec{r})t] \hat{u}_C(\vec{r}) + \sin[\gamma_{\mu} B(\vec{r})t] \hat{u}_P(\vec{r}) \right\} d\vec{r}, \quad (2.43)$$

the total time-dependent polarization vector can be expressed as

$$\vec{P}(t) = \vec{P}(t \rightarrow \infty) + \vec{P}_{\perp}(t). \quad (2.44)$$

While Eq. 2.41 clearly demonstrates the average over all sub-ensemble muon precession cones, some additional insights can be facilitated if, instead, it is expressed explicitly in terms of the initial muon polarization:

$$\begin{aligned} \vec{P}(t) = \frac{1}{V} \int_V \left\{ \hat{P}(0) \cdot \hat{B}(\vec{r}) \right\} & \hat{B}(\vec{r}) \\ & + \cos[\gamma_{\mu} B(\vec{r})t] \left\{ \hat{P}(0) - [\hat{P}(0) \cdot \hat{B}(\vec{r})] \hat{B}(\vec{r}) \right\} \\ & + \sin[\gamma_{\mu} B(\vec{r})t] \left\{ \hat{B}(\vec{r}) \times \hat{P}(0) \right\} d\vec{r}. \end{aligned} \quad (2.45)$$

where V is the volume of the sample. If there are positron counters along the $\pm \hat{C}$ directions, the measured time-dependent asymmetry signal $A_C(T) = A_C^C P_C(t)$ will be proportional to the projection of the polarization along the \hat{C} direction $P_C(t) = \vec{P}(t) \cdot \hat{C}$:

$$\begin{aligned} P_C(t) = \vec{P}(t) \cdot \hat{C} &= \frac{1}{V} \int_V [\hat{P}(0) \cdot \hat{B}(\vec{r})] [\hat{B}(\vec{r}) \cdot \hat{C}] d\vec{r} \\ &+ \hat{P}(0) \cdot \hat{C} \frac{1}{V} \int_V \cos[\gamma_{\mu} B(\vec{r})t] d\vec{r} \\ &- \frac{1}{V} \int_V [\hat{P}(0) \cdot \hat{B}(\vec{r})] [\hat{B}(\vec{r}) \cdot \hat{C}] \cos[\gamma_{\mu} B(\vec{r})t] d\vec{r} \\ &+ \frac{1}{V} \int_V [\hat{P}(0) \times \hat{C}] \cdot \hat{B}(\vec{r}) \sin[\gamma_{\mu} B(\vec{r})t] d\vec{r}, \end{aligned} \quad (2.46)$$

using the vector identity

$$[\hat{B}(\vec{r}) \times \hat{P}(0)] \cdot \hat{C} \equiv [\hat{P}(0) \times \hat{C}] \cdot \hat{B}(\vec{r}). \quad (2.47)$$

The initial muon polarization direction $\hat{P}(0)$ and the counter direction \hat{C} are obviously independent of the position \vec{r} of the sub-ensemble muons, so they can be moved outside the integral in Eq. 2.46. To achieve this result we define several quantities in terms of their average values over regions of space where the *magnitude* of the local field has approximately the same value. The first quantity is the “correlation density” matrix:

$$\tilde{U}_{jl}(B') dB' = \frac{1}{V} \int_{\left| |\vec{B}(\vec{r})| - B' \right| < \frac{dB'}{2}} [\hat{j} \cdot \hat{B}(\vec{r})] [\hat{B}(\vec{r}) \cdot \hat{l}] d\vec{r} \quad (2.48)$$

where $j, l \in \{x, y, z\}$ and the integral is restricted to those positions \vec{r} for which magnitude of the local field is within dB' of the value B' . The second quantity is the vector \vec{V} representing the partial average of the local field unit vector directions,

$$\vec{V}(B') dB' = \frac{1}{V} \int_{\left| |\vec{B}(\vec{r})| - B' \right| < \frac{dB'}{2}} \hat{B}(\vec{r}) d\vec{r}. \quad (2.49)$$

Finally, the scalar probability distribution of the magnetic field's magnitude is defined as:

$$\begin{aligned} n(B') dB' &= \frac{\text{volume with } \left| |\vec{B}(\vec{r})| - B' \right| < \frac{dB'}{2}}{\text{total volume}} \\ &= \frac{1}{V} \int_{\left| |\vec{B}(\vec{r})| - B' \right| < \frac{dB'}{2}} 1 d\vec{r}. \end{aligned} \quad (2.50)$$

These quantities allow the projection of the polarization in the \hat{C} direction to be expressed as

$$\begin{aligned} \vec{P}(t) \cdot \hat{C} &= \hat{P}(0) \cdot \left\{ \int \tilde{U}(B') dB' \right\} \cdot \hat{C} \\ &\quad + \hat{P}(0) \cdot \hat{C} \left\{ \int n(B') \cos[\gamma_\mu B' t] dB' \right\} \\ &\quad - \hat{P}(0) \cdot \left\{ \int \tilde{U}(B') \cos[\gamma_\mu B' t] dB' \right\} \cdot \hat{C} \\ &\quad + \left(\hat{P}(0) \times \hat{C} \right) \cdot \left\{ \int \vec{V}(B') \sin[\gamma_\mu B' t] dB' \right\}, \end{aligned} \quad (2.51)$$

where the integrals are only over the *magnitude* of the local field.

Note that in the \hat{x} - \hat{y} - \hat{z} reference frame, the initial polarization (Eq. 2.30) can be expressed as

$$\hat{P}(0) = \hat{P}_o = \sin \phi \cos \psi \hat{x} + \sin \phi \sin \psi \hat{y} + \cos \phi \hat{z}, \quad (2.52)$$

where \hat{P}_o is introduced as an abbreviation for $\hat{P}(0)$. Since Eq. 2.51 is linear in $\vec{P}(0)$, the time evolution of the polarization is expressed as

$$\vec{P}(t) = \sin \phi \cos \psi \vec{P}(t; \hat{P}_o = \hat{x}) + \sin \phi \sin \psi \vec{P}(t; \hat{P}_o = \hat{y}) + \cos \phi \vec{P}(t; \hat{P}_o = \hat{z}) \quad (2.53)$$

where $\vec{P}(t; \hat{P}_o = \hat{j})$ is the time-dependent polarization vector that would be observed *if the initial polarization were exactly along the direction \hat{j}* . If one wishes to fit many different data sets which have different values of the angles ϕ and ψ , it is usually more convenient to calculate $\vec{P}(t; \hat{P}_o = \hat{x})$, $\vec{P}(t; \hat{P}_o = \hat{y})$ and $\vec{P}(t; \hat{P}_o = \hat{z})$ once and use Eq. 2.53 than to calculate $\vec{P}(t)$ using Eq. 2.41 for each data set.

2.6.4 Discussion of Different Categories of Field Distributions

Note that the average field \vec{B}_o is *not* necessarily equal to its magnitude B_o times the volume average of its direction:

$$\begin{aligned} \vec{B}_o &= \frac{1}{V} \int_V \vec{B}(\vec{r}) d\vec{r} = \int B \vec{V}(B) dB \\ &\neq B_o \int \vec{V}(B) dB = B_o \frac{1}{V} \int_V \hat{B}(\vec{r}) d\vec{r}. \end{aligned} \quad (2.54)$$

The \hat{x} - \hat{y} - \hat{z} reference frame is partly defined by the average field being along the \hat{z} direction, $\vec{B}_o = B_o \hat{z}$. Therefore, while the transverse components of \vec{B}_o are zero

$$\begin{aligned} \langle B_x(\vec{r}) \rangle_V &= \frac{1}{V} \int_V \hat{x} \cdot \vec{B}(\vec{r}) d\vec{r} \equiv 0 \\ \langle B_y(\vec{r}) \rangle_V &= \frac{1}{V} \int_V \hat{y} \cdot \vec{B}(\vec{r}) d\vec{r} \equiv 0, \end{aligned} \quad (2.55)$$

the average of the transverse components of the local field unit vector direction are possibly non-zero:

$$\begin{aligned} \langle \hat{x} \cdot \hat{B}(\vec{r}) \rangle_V &= \frac{1}{V} \int_V \hat{x} \cdot \hat{B}(\vec{r}) d\vec{r} = \int \hat{x} \cdot \vec{V}(B') dB' \neq 0 \\ \langle \hat{y} \cdot \hat{B}(\vec{r}) \rangle_V &= \frac{1}{V} \int_V \hat{y} \cdot \hat{B}(\vec{r}) d\vec{r} = \int \hat{y} \cdot \vec{V}(B') dB' \neq 0. \end{aligned} \quad (2.56)$$

We will now define what is a “non-correlated” field distribution. The first condition is that *if* the average of the component of the local field along a certain direction is zero, *then* the average

of that component of the local field's *unit vector* along the same direction is also zero:

$$\langle \hat{j} \cdot \vec{B}(\vec{r}) \rangle_V = 0 \implies \langle \hat{j} \cdot \hat{B}(\vec{r}) \rangle_V = 0. \quad (2.57)$$

If we subtract the average field \vec{B}_o to form the mean deviation from the average, by definition

$$\langle \hat{j} \cdot [\vec{B}(\vec{r}) - \vec{B}_o] \rangle_V = 0, \quad (2.58)$$

then the first criterion for a non-correlated field distribution becomes simply

$$\langle \hat{j} \cdot [\hat{B}(\vec{r}) - \hat{B}_o] \rangle_V = 0 \quad (2.59)$$

which holds for all \hat{j} including $\hat{B}_o = \hat{z}$. The second condition is that the different components of the local field's unit vector are uncorrelated

$$\tilde{U}_{jl}(B') = \delta_{jl} \tilde{U}_{jj}(B'), \quad (2.60)$$

that is, the off-diagonal elements of $\tilde{U}(B')$ are zero. [The diagonal elements $\tilde{U}_{jj}(B')$ are always non-negative.] A field distribution which does not meet both of these restrictions is called “correlated.”

A *symmetric* field distribution is defined to be a non-correlated distribution with the additional restriction that the probability distribution of the magnetic field's magnitude is symmetric about the average field's magnitude:

$$n^{\text{sym}}(B_o - \Delta B) = n^{\text{sym}}(B_o + \Delta B). \quad (2.61)$$

In the case of a non-correlated field distribution, Eq. 2.51 reduces to

$$\begin{aligned} \vec{P}^{\text{nc}}(t) \cdot \hat{C} &= \hat{P}(0) \cdot \hat{C} \int \hat{C} \cdot \tilde{U}(B') \cdot \hat{C} dB' \\ &+ \hat{P}(0) \cdot \hat{C} \int \left[n(B') - \hat{C} \cdot \tilde{U}(B') \cdot \hat{C} \right] \cos[\gamma_\mu B' t] dB' \\ &+ \left(\hat{P}(0) \times \hat{C} \right) \cdot \hat{z} \int \hat{z} \cdot \vec{V}(B') \sin[\gamma_\mu B' t] dB', \end{aligned} \quad (2.62)$$

Note that if $\vec{B}(\vec{r}) = B(\vec{r})\hat{z}$, then $\vec{V}(B) = n(B)\hat{z}$. A non-correlated distribution with $\phi = \pi/2$ (*i.e.*, initial polarization perpendicular to \hat{z}) produces a non-oscillatory signal in the direction of the original polarization $\hat{P}(0)$, while the non-oscillatory polarization in correlated distributions

may or may not be parallel to $\hat{P}(0)$. Moreover, for non-correlated distributions with the initial polarization at an angle ϕ from the \hat{z} axis and ψ from the \hat{x} axis (see Eq. 2.53), the in-phase oscillatory signal for $\vec{P}^{\text{nc}}(t)$ [involving the integral over $\cos(\gamma_\mu Bt)$] will be in the $\hat{P}(0) - [\hat{P}(0) \cdot \hat{z}] \hat{z}$ direction and the out-of-phase oscillatory signal [involving the integral over $\sin(\gamma_\mu Bt)$] will be in the $\hat{z} \times \hat{P}(0)$ direction.

In the non-correlated case, if $\hat{P}_o = \hat{z}$, $\vec{P}^{\text{nc}}(t)$ will never develop any x or y components and if \hat{P}_o is along \hat{x} or \hat{y} then $\hat{z} \cdot \vec{P}^{\text{nc}}(t)$ will remain zero forever. For correlated field distributions, the terms which would be zero for the non-correlated case may produce some admixing of the in-phase and out-of-phase terms for the projections (Eq. 2.51) along the $\hat{P}(0) - [\hat{P}(0) \cdot \hat{z}] \hat{z}$, $\hat{z} \times \hat{P}(0)$ and \hat{z} directions.

2.6.5 Uniaxial Local Field Polarization Functions

In this section, we consider “uniaxial local field” (ULF) distributions where the local field is *always parallel* to the average field

$$\begin{aligned}\vec{B}(\vec{r}) \cdot \hat{x} &\equiv 0 \\ \vec{B}(\vec{r}) \cdot \hat{y} &\equiv 0 \\ \vec{B}(\vec{r}) &= B(\vec{r}) \hat{z} \quad \text{or} \quad \hat{B}(\vec{r}) = \hat{z}\end{aligned}\tag{2.63}$$

and the local field magnitudes have a distribution about B_o whose characteristic width

$$\begin{aligned}\Delta &= \left\langle \left| \vec{B}(\vec{r}) - B_o \hat{z} \right|^2 \right\rangle^{1/2} \\ &= \left\langle [B(\vec{r}) - B_o]^2 \right\rangle^{1/2}\end{aligned}\tag{2.64}$$

is independent (or nearly so) of the average field B_o . This is appropriate for isotropic superconductors and anisotropic superconductors with an applied field parallel to one of the principal axes (see Ch. 4).

When the local fields are parallel to the average field [$\vec{B}(\vec{r}) = B(\vec{r}) \hat{z}$] and the initial polarization is along \hat{z} , the time-dependent polarization vector is constant

$$\vec{P}^{\text{ULF}}(t; \hat{P}_o = \hat{z}) = \hat{z}.\tag{2.65}$$

When the initial polarization is along \hat{x} (corresponding to $\psi_t = 0$), the polarization function is given by

$$\begin{aligned}\vec{P}^{\text{ULF}}(t; \hat{P}_o = \hat{x}) &= \frac{1}{V} \int_V \left\{ \cos[\gamma_\mu B(\vec{r})t] \hat{x} + \sin[\gamma_\mu B(\vec{r})t] \hat{y} \right\} d\vec{r} \\ &= \int n(B) \left\{ \cos[\gamma_\mu Bt] \hat{x} + \sin[\gamma_\mu Bt] \hat{y} \right\} dB\end{aligned}\quad (2.66)$$

and when it is along \hat{y} (corresponding to $\psi_t = \pi/2$)

$$\begin{aligned}\vec{P}^{\text{ULF}}(t; \hat{P}_o = \hat{y}) &= \frac{1}{V} \int_V \left\{ -\sin[\gamma_\mu B(\vec{r})t] \hat{x} + \cos[\gamma_\mu B(\vec{r})t] \hat{y} \right\} d\vec{r} \\ &= \int n(B) \left\{ -\sin[\gamma_\mu Bt] \hat{x} + \cos[\gamma_\mu Bt] \hat{y} \right\} dB.\end{aligned}\quad (2.67)$$

From Eq. 2.53, the total polarization function in the special case of uniaxial local fields is

$$\vec{P}^{\text{ULF}}(t) = \hat{x} \sin \phi \int n(B) \cos[\gamma_\mu Bt + \psi] dB + \hat{y} \sin \phi \int n(B) \sin[\gamma_\mu Bt + \psi] dB + \hat{z} \cos \phi. \quad (2.68)$$

One would like to fit experimental data directly to the theoretical polarization function. If the average period $\frac{1}{\gamma_\mu B_o}$ of the precession is much shorter than the time scale over which the polarization envelope changes, then it may be convenient to store the data in a rotating reference frame with a frequency of ν_{TBL} which is relatively close to the polarization function's average frequency ν_o . [The rotating reference frame (RRF) is discussed in more detail in Sec. 3.2.1.] Consider the “real” and “imaginary” RRF polarization projections $G_{\text{R}}^{\text{TBL}}$ and $G_{\text{I}}^{\text{TBL}}$, which are defined as

$$\begin{aligned}G_{\text{R}}^{\text{TBL}}(t) &= \frac{1}{V} \int_V \cos\{\gamma_\mu [B(\vec{r}) - B_{\text{TBL}}] t\} d\vec{r} \\ &= \int_0^\infty n(B) \cos\{\gamma_\mu [B - B_{\text{TBL}}] t\} dB \\ &= \int_0^\infty n_\nu(\nu) \cos\{2\pi[\nu - \nu_{\text{TBL}}] t\} d\nu \\ G_{\text{I}}^{\text{TBL}}(t) &= \frac{1}{V} \int_V \sin\{\gamma_\mu [B(\vec{r}) - B_{\text{TBL}}] t\} d\vec{r} \\ &= \int_0^\infty n(B) \sin\{\gamma_\mu [B - B_{\text{TBL}}] t\} dB \\ &= \int_0^\infty n_\nu(\nu) \sin\{2\pi[\nu - \nu_{\text{TBL}}] t\} dB,\end{aligned}\quad (2.69)$$

where B_{TBL} is the magnetic field in the “rotating reference frame” (see Sec. 3.2.1) for the stored

tables $G_{\text{R}}^{\text{TBL}}(t)$ and $G_{\text{I}}^{\text{TBL}}(t)$ [†] and

$$n_{\nu}(\nu) d\nu = n_{\nu} \left(\frac{\gamma_{\mu}}{2\pi} B \right) \frac{\gamma_{\mu}}{2\pi} dB = n(B) dB \quad (2.70)$$

describes the probability distribution of local field strengths and/or muon precession frequencies (defined in Eq. 2.50.) The polarization functions can be expressed as

$$\begin{aligned} \vec{P}^{\text{TBL}}(t) = & \hat{z} \cos \phi + \hat{x} \sin \phi [G_{\text{R}}^{\text{TBL}}(t) \cos(\gamma_{\mu} t B_{\text{TBL}} + \psi) - G_{\text{I}}^{\text{TBL}}(t) \sin(\gamma_{\mu} t B_{\text{TBL}} + \psi)] \\ & + \hat{y} \sin \phi [G_{\text{R}}^{\text{TBL}}(t) \sin(\gamma_{\mu} t B_{\text{TBL}} + \psi) + G_{\text{I}}^{\text{TBL}}(t) \cos(\gamma_{\mu} t B_{\text{TBL}} + \psi)]. \end{aligned} \quad (2.71)$$

It is impractical to construct new functions $G_{\text{R}}^{\text{TBL}}(t)$ and $G_{\text{I}}^{\text{TBL}}(t)$ for every possible field distribution; however, in many cases, the *shape* of $n(B)$ stays the same and only the average field B_o changes in some family of field distributions. In these cases one may introduce an equivalent scaling of $G_{\text{R}}^{\text{TBL}}(t)$ and $G_{\text{I}}^{\text{TBL}}(t)$. When fitting, one retrieves $G_{\text{R}}^{\text{TBL}}(t)$ and $G_{\text{I}}^{\text{TBL}}(t)$ from the table using a scaling rule such as: *Experimental time t_{exp} corresponds to table time t_{th} by*

$$t_{\text{exp}} \Delta_{\text{exp}} = t_{\text{th}} \Delta_{\text{th}}, \quad (2.72)$$

where Δ_{th} is the characteristic width of the field distribution from which $G_{\text{R}}^{\text{TBL}}(t)$ and $G_{\text{I}}^{\text{TBL}}(t)$ were calculated and Δ_{exp} is the actual width in the sample. If we assume that B_{TBL} is chosen to be the theoretical polarization function's average field, $B_{\text{TBL}} = B_o^{\text{th}}$, and if the shape of $n(B)$ is also independent of the average field, then it is permissible to express the experimental vector polarization as

$$\begin{aligned} \vec{P}^{\text{exp}}(t) = & \hat{z} \cos \phi + \hat{x} \sin \phi \left[G_{\text{R}}^{\text{TBL}} \left(\frac{\Delta_{\text{exp}}}{\Delta_{\text{th}}} t \right) \cos(\gamma_{\mu} t B_o + \psi) \right. \\ & \left. - G_{\text{I}}^{\text{TBL}} \left(\frac{\Delta_{\text{exp}}}{\Delta_{\text{th}}} t \right) \sin(\gamma_{\mu} t B_o + \psi) \right] \\ & + \hat{y} \sin \phi \left[G_{\text{R}}^{\text{TBL}} \left(\frac{\Delta_{\text{exp}}}{\Delta_{\text{th}}} t \right) \sin(\gamma_{\mu} t B_o + \psi) \right. \\ & \left. + G_{\text{I}}^{\text{TBL}} \left(\frac{\Delta_{\text{exp}}}{\Delta_{\text{th}}} t \right) \cos(\gamma_{\mu} t B_o + \psi) \right]. \end{aligned} \quad (2.73)$$

Note that, in general, these equations cannot be further simplified unless the field distribution is symmetric (in both magnitude and direction) about \vec{B}_o and $B_{\text{TBL}} \equiv B_o$, in which case $G_{\text{I}}^{\text{TBL}}(t) \equiv 0$.

[†]For instance, one might chose B_{TBL} to be the average field in a type II superconductor's vortex lattice for some typical experimental field, or one might use the minimum field as B_{TBL} , or even $B_{\text{TBL}} \equiv 0$. The validity of this approach clearly depends on the B_{TBL} -independence of $n(\nu)$ over the desired range of B_{TBL} .

This method of fitting the data was used in Ref. [53], but is not used in this thesis.

In those μ SR experiments where the average field B_o is much larger than the rms variation in local fields $\left\langle \left| \vec{B}_o - \vec{B}(\vec{r}) \right|^2 \right\rangle_V^{1/2}$, the non-oscillatory portion is negligible in the transverse directions [$P_x(t \rightarrow \infty) \approx 0$, $P_y(t \rightarrow \infty) \approx 0$] even when the local fields are not strictly parallel to the \hat{z} axis. If the local field distribution is symmetric about the average field (see Eq. 2.61), the oscillatory signal may be fit with an *Ansatz* symmetric relaxation function in the time domain, such as a Gaussian or an exponential. When $B_{\text{TBL}} = B_o$ and $n(\nu)$ is exactly symmetric about $\nu_o \equiv \frac{\gamma_\mu}{2\pi} B_o$, then $G_I^{\text{TBL}}(t) \equiv 0$, $G_R^{\text{TBL}}(t) = G_{\text{sym}}(t)$ and Eq. 2.71 simplifies to

$$P_{\psi,i}^{\text{sym}}(t) = G_{\text{sym}}(t) \cos(\gamma_\mu B t + \psi + \psi_C) \quad (2.74)$$

for the projection along the C^{th} counter axis ($C = X, Y$), where ψ_C is an extra phase corresponding to the angle of the C^{th} counter axis relative to the initial muon polarization direction when $\psi = 0$.

2.6.6 Some Visual Examples

It can be difficult to have a physical sense of how different kinds of local field inhomogeneities affect the relative sizes of the oscillatory and non-oscillatory signals observed in the positron counters. This section presents some visual examples.

Fig. 2.12 illustrates the effect of a local field which varies in direction but not in magnitude in a TF experiment. The initial muon polarization is in the \hat{X} direction ($\psi = 0$) and the average applied field is in the $-\hat{Z}$ direction ($\theta = \pi$ and $\phi = -\pi/2$). Consider local field directions which vary in the $\hat{X}-\hat{Z}$ plane (Fig. 2.12.a). At time $t = 0$, the net polarization will be in the \hat{X} direction with its maximum magnitude [$\vec{P}(0) = \hat{P}_o = \hat{X}$]. At times $t = \frac{\pi}{2} \frac{1}{\gamma_\mu B_o}$ and $t = \frac{3\pi}{2} \frac{1}{\gamma_\mu B_o}$, the net polarization will be in the \hat{Y} and $-\hat{Y}$ directions respectively with decreased magnitude. At time $t = \pi \frac{1}{\gamma_\mu B_o}$, the net polarization will be in the $-\hat{X}$ direction with its minimum magnitude and at time $t = 2\pi \frac{1}{\gamma_\mu B_o}$ the full polarization will return to the \hat{X} direction. If the average field direction is $-\hat{Z}$, there will be a small constant polarization $\vec{P}(t \rightarrow \infty)$ in the $+\hat{X}$ direction. Now consider local field directions which vary in the $\hat{Y}-\hat{Z}$ plane (Fig. 2.12.b). At time $t = 0$, the net

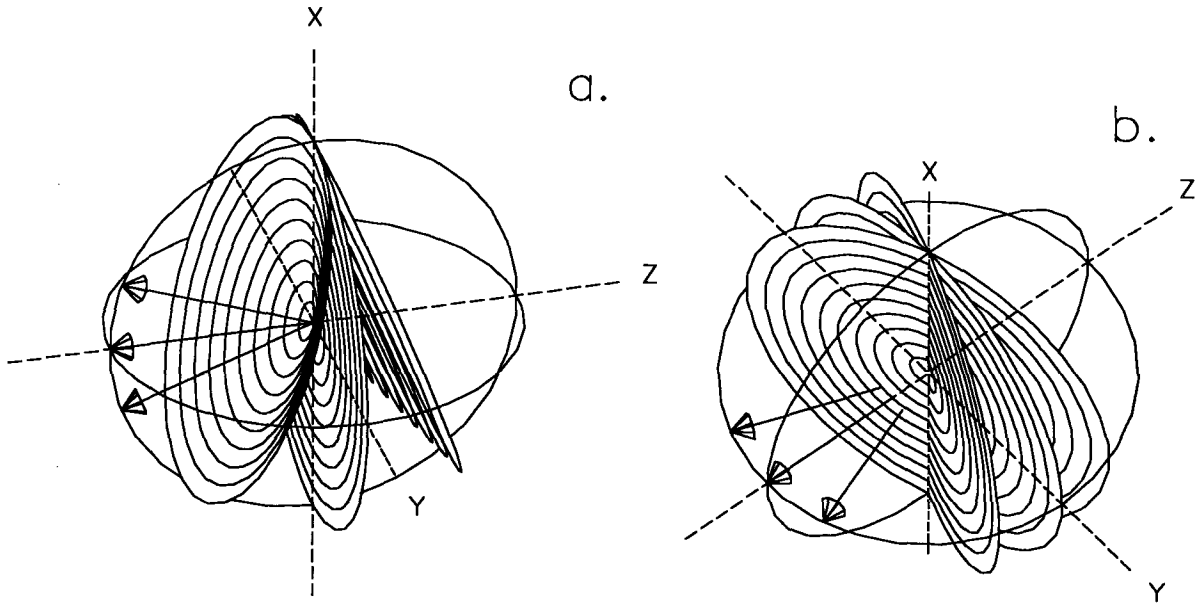


Figure 2.12: The initial muon spin is along \hat{X} and the local fields are indicated by the arrows. The bull's eye represents the muon precession cone.

- a. TF with field disorder in the \hat{X} - \hat{Z} plane.
 b. TF with field disorder in the \hat{Y} - \hat{Z} plane.

polarization will be in the \hat{X} direction with its maximum magnitude. At times $t = \frac{\pi}{2} \frac{1}{\gamma_{\mu} B_o}$, and $t = \frac{3\pi}{2} \frac{1}{\gamma_{\mu} B_o}$, the net polarization will be in the \hat{Y} and $-\hat{Y}$ directions respectively with decreased magnitude. At time $t = \pi \frac{1}{\gamma_{\mu} B_o}$, the net polarization will be in the $-\hat{X}$ direction with its original magnitude. It follows that the magnitude of $\vec{P}(t \rightarrow \infty)$ is zero because, in this case, the local field is always perpendicular to the initial muon polarization direction. Therefore, the time-dependent polarization along \hat{X} (recorded in the UP and DOWN counters) shows a non-oscillatory component in Fig. 2.12.a but not in Fig. 2.12.b. Also, in the second case (Fig. 2.12.b) the $\pm Y$ counters will record a smaller amplitude precessing signal than the $\pm X$ counters, which should *not* be misinterpreted as a difference between A_o^X and A_o^Y . Note that if the magnitudes of the local fields are all the same, as drawn here, then the magnitude of the polarization will be identical at times t , $t + \frac{2\pi}{\gamma_{\mu} B_o}$, $t + \frac{4\pi}{\gamma_{\mu} B_o}$, etc. If a distribution of local field magnitudes were added, the net polarization would “dephase” with increasing time (because muons experiencing

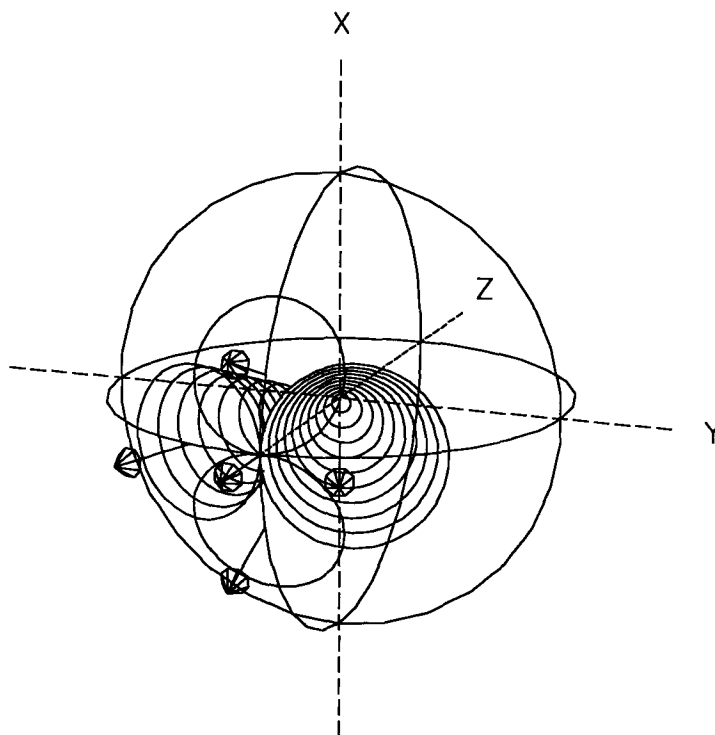


Figure 2.13: LF with directional disorder in the local fields. The initial muon spin is along $-\hat{Z}$ and the local fields are indicated by the arrows, which are the central axes of the muon precession cones.

different strength fields will precess at different rates), which would be observed as a reduction of the polarization over time.

Fig. 2.13 shows a local field with constant magnitude but varying directions for a LF experiment. Precession cones have only been drawn for some local fields in the $\hat{Y}\hat{Z}$ plane. If we assume a distribution symmetric about the $-\hat{Z}$ axis, the polarization in the $\hat{X}\hat{Y}$ plane cancels out by symmetry but along \hat{Z} there is a time dependence: at time $t = 0$ the net polarization is in the $-\hat{Z}$ direction with maximum magnitude whereas at time $t_{\min} = \pi \frac{1}{B_o \gamma_\mu}$ the magnitude has its minimum value. The relative proportion of the polarization along \hat{Z} which is oscillatory is determined by the characteristic size

$$\Delta/B_o \approx \langle 1 - \hat{Z} \cdot \hat{B} \rangle_V \quad (2.75)$$

of the directional disorder of the local field.

2.6.7 Compounding Polarization Functions

Eqs. 2.41, 2.42, 2.45 and 2.53 are quite general for static magnetic field distributions arising from such things as classical nuclear dipolar fields, vortex lattices in type II superconductors and ferromagnetic, antiferromagnetic or spin glass systems. They can be used to generate polarization functions either by spatially averaging over a simulation on a grid (as done in Ch. 4 for an anisotropic superconductor in low fields) or by deriving analytic expressions in simple cases. They are limited only by their classical approximation for the local fields as fixed constants in the problem: for example, if the magnetic field at the muon is due to a single spin- $\frac{1}{2}$ magnetic moment, that moment also experiences a field due to the muon and a proper description requires a full quantum mechanical treatment of the coupled spin system. In the case of vortex lattices in superconductors, the formulation used here should be rigorous.

Sometimes there may be more than one cause of variations in the local field. Two sources of field inhomogeneity which are *statistically independent* can be combined *ex post facto* into a single polarization function *only* if one of them acting alone produces an approximately *symmetrical field distribution*. For instance, a superconductor with a vortex lattice will not have a high enough critical current to screen out the effects of nuclear dipolar moments over very short distances. In high applied fields, nuclear dipolar fields can be approximately described by a Gaussian relaxation function $G_{\text{sym}}(t) = e^{-\frac{1}{2}\sigma_D^2 t^2}$, while the vortex lattice always produces an asymmetric function, described by the general theoretical polarization function (Eq. 2.53). Using Eqs. 2.42 and 2.43, the time dependent polarization (in the case of a vortex lattice, for example) can be expressed by

$$\begin{aligned} \vec{P}_{\phi=\pi/2}(t) &= \cos \psi \vec{P}(t; \hat{P}_o = \hat{x}) + \sin \psi \vec{P}(t; \hat{P}_o = \hat{y}) \\ &= \cos \psi \left\{ \vec{P}_{\parallel}(t; \hat{P}_o = \hat{x}) + \vec{P}_{\perp}(t; \hat{P}_o = \hat{x}) \right\} \\ &\quad + \sin \psi \left\{ \vec{P}_{\parallel}(t; \hat{P}_o = \hat{y}) + \vec{P}_{\perp}(t; \hat{P}_o = \hat{y}) \right\}, \end{aligned} \quad (2.76)$$

assuming that the initial muon polarization is perpendicular to the average field direction ($\phi = \pi/2$) and that there is an initial phase of ψ . In this case, the compounded polarization function including the effects of dipolar moments is given by

$$\begin{aligned} \vec{P}_{\phi=\pi/2}^{\text{comp}}(t) &= \cos \psi \vec{P}_{\parallel}(t; \hat{P}_o = \hat{x}) + \sin \psi \vec{P}_{\parallel}(t; \hat{P}_o = \hat{y}) \\ &\quad + G_{\text{sym}}(t) \left\{ \cos \psi \vec{P}_{\perp}(t; \hat{P}_o = \hat{x}) + \sin \psi \vec{P}_{\perp}(t; \hat{P}_o = \hat{y}) \right\}. \end{aligned} \quad (2.77)$$

The reason for compounding relative to the oscillatory portion of the polarization rather than to the total polarization will be discussed further in Sec. 3.4.

Chapter 3

Manipulation of μ SR data

3.1 Introduction

When analysing experimental data, a “bandwidth” of muon precession frequencies is selected by the choice of time range, initial time binning, subsequent bin packing, and compression through the use of a rotating reference frame (RRF) transformation. In effect, one is ultimately sensitive to a small range of frequencies centered about the experimental average frequency. If one does not choose wisely, statistical noise may overwhelm the details of interest or higher frequencies that are present may be inadvertently “binned over” in both the asymmetry signal and in the Fourier transform. Many μ SR researchers understand these concepts when fitting time-series asymmetry signals, but are less confident when performing Fourier transforms, because the mechanics are somewhat more complicated. I hope that this chapter will help other μ SR researchers to analyse μ SR data. I found Ch. 12 in Numerical Recipes[54] very helpful in understanding the relationship between ringing and apodization by various functions and for understanding the behavior of Fourier transforms.

3.2 The Rotating Reference Frame and The Art of Packing Data

3.2.1 The RRF Transformation in μ SR*

In many NMR and time differential (TD) high transverse field (HTF) μ^+ SR experiments, the essential information is contained in the precession frequencies of the probe spin and in the shape

*The contents of this section have been adapted from the paper entitled “The Rotating Reference Frame Transformation in μ SR”, by T.M. Riseman and J.H. Brewer, which originally appeared in the Proceedings of the 5th International Conference on Muon Spin Rotation, Relaxation and Resonance. See Ref. [55].

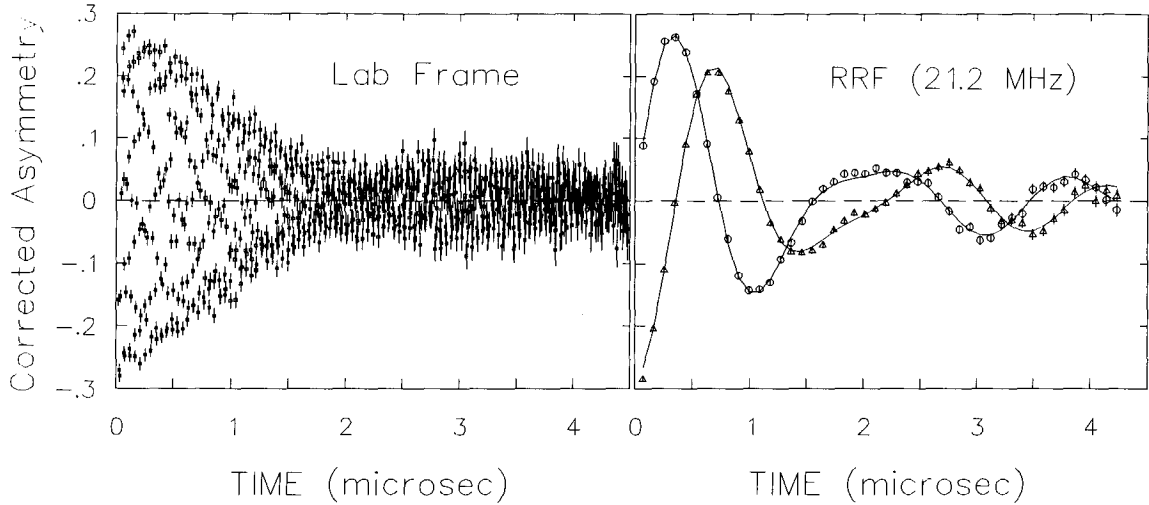


Figure 3.1: The first $4.5 \mu\text{s}$ of a μ^+ SR time spectrum taken at roughly 0.2 T in the “lab frame” where the data are recorded and in the rotating reference frame (RRF) to which it has been transformed numerically for display and fitting. The RRF frequency of 21.2 MHz is chosen to produce a slow precession signal for visual clarity. Because the original spectrum is real (no orthogonal detector arrays) the maximum amplitude in each of the complex RRF spectra (real part: circles; imaginary part: triangles) is actually a factor of two smaller than in the “lab frame”. The solid line in the RRF spectra is a fit to three frequencies; a single frequency (or even two) would result in a much poorer fit to the data.

of the depolarization envelope. Typically, the recorded NMR frequency is much lower than the actual precession frequency due to an analog rotating reference frame (RRF) transformation done in hardware. This allows economical digital storage of the data using a time bin size larger than the period of the precession. Since TD- μ^+ SR consists of recording for many discrete events the distribution of time intervals from when the μ^+ entered the sample to its decay ($\mu^+ \rightarrow e^+ + \nu_e \bar{\nu}_\mu$) rather than recording continuous changes in magnetization as in NMR, any sort of RRF transformation before data storage is very difficult and unforgiving. Therefore, the raw data from TD HTF- μ^+ SR [$N(t_n)$, where $t_n = n \delta t$ and δt is the raw bin size] must be stored in a relatively uneconomical way, with at least four data points (and more than ten if distortions are to be minimized) per μ^+ precession period T_μ which is given in microseconds by

$$T_\mu \equiv 1/\nu = \frac{2\pi}{\gamma_\mu B} = \frac{1}{0.0135534B} \quad (3.1)$$

where B is the average field in Gauss. The maximum field measurable with transverse field μ^+ SR is limited by the timing resolution of the electronics and the apparatus; it is typically $\gtrsim 0.5$ ns.

The analysis of TD HTF- μ^+ SR data can benefit greatly from a discrete RRF transformation of the stored data followed by coarser time binning (Fig. 3.1). Choosing a RRF near but not equal to the experimental frequency and rebinning by $\Delta t = n_p \delta t \gg T_\mu$ (where n_p is the packing factor) enables easy visual verification that the chosen theoretical form is qualitatively appropriate for the data. For example, from the rotating reference frame shown in Fig. 3.1 it is evident that three frequencies with slow exponential relaxation (as shown by the solid line) will fit the data better than a single frequency with Gaussian relaxation plus a non-relaxing background; the same is not evident from the lab frame. Such discrimination can often be achieved by inspecting a fast Fourier transform (FFT) of the data, but *fitting* with well-defined χ^2 and undistorted weighting of different time regions is best done in the time domain. Furthermore, the RRF transformation allows TD HTF data to be *displayed* in the same convenient manner as weak TF or ZF data. Coarser binning means that the corresponding error bars on each data point will be smaller by a factor $\sqrt{n_p}$ and that fitting efficiency will improve by a factor of n_p .

In the laboratory reference frame, as the muon spins precess in the sample's local fields, the distribution of decay positrons rotates from the direction of the initial muon polarization through the counters which form a box around the sample (*e.g.*, $+X$ to $+Y$ to $-X$ to $-Y$ back to $+X$ when a field is applied parallel to \hat{Z}). This could be generalized to an arbitrary number n of counters forming a polygon about the sample by substituting $e^{in/(2\pi)}$ for sines and cosines in the following derivation.

For HTF, it is a simple matter to numerically extract the asymmetry factor for each raw histogram (Eq. 2.16):

$$A_C(t) = \left[\frac{N_C(t) - B_C}{N_C^0} \right] e^{+t/\tau_\mu}, \quad (3.2)$$

where C indicates which histogram ($C = +X, -X, +Y$ or $-Y$ for fields $\vec{B} \parallel \hat{Z}$), N_C^0 is the normalization factor, B_C is the background and $\tau_\mu = 2.197 \mu\text{s}$ is the mean muon lifetime. These are then combined to form the lab-frame asymmetry,

$$\begin{aligned} \vec{A}_{\text{lab}}(t) &= \frac{1}{2}[A_{+X}(t) - A_{-X}(t)]\hat{X} + \frac{1}{2}[A_{+Y}(t) - A_{-Y}(t)]\hat{Y} \\ &\approx A_X(t)\hat{X} + A_Y(t)\hat{Y} \end{aligned} \quad (3.3)$$

$$\approx A_o[P_X(t)\hat{X} + P_Y(t)\hat{Y}].$$

[We assume $A_{+X} \approx A_{-X} \approx A_X$ and $A_{+Y} \approx A_{-Y} \approx A_Y$ and further that $A_X \approx A_Y \approx A_o$, which may introduce distortions—though not as severe as in Sec. 2.5.1—because the calculation of $A_C(t)$ by Eq. 3.2 removes the α term but not the β term in Eq. 2.16.] If counters $+Y$ and $-Y$ are unavailable, the projection $A_Y(t)$ along \hat{Y} is zero; if only counter $+X$ is present the factor of $\frac{1}{2}$ is dropped; *etc.* Note that this method of calculating a raw asymmetry differs from that in Eq. 2.18 in that the α parameter is automatically removed. Therefore $\vec{A}_{\text{lab}}(t)$ would be exactly equal to the expected asymmetry $A_o[P_X(t)\hat{X} + P_Y(t)\hat{Y}]$ if the counters were the same size and shape (so that β is identical to one—see Sec. 2.5.1) and perfectly aligned (so that ϕ_r is identical to zero—see Sec. 2.5.3). For the sake of clarity, we will carry these assumptions through the remainder of the discussion. This makes the treatment for the experimental data identical with that for the theory we wish to fit.

Consider a “theoretical” probability distribution of muon frequencies (also known as a frequency lineshape) $n_\nu(\nu)$ centered about a mean frequency $\nu_o = \frac{\gamma\mu}{2\pi}B_o$. In a reference frame rotating at a frequency ν_r (the rotating reference frame, RRF) near ν_o , the Fourier transform of $n_\nu(\nu)$ is the theoretical complex muon polarization function

$$\vec{P}^{\text{RRF}}(\psi, t) = P_X^{\text{RRF}}(\psi, t)\hat{X} + P_Y^{\text{RRF}}(\psi, t)\hat{Y} \quad (3.4)$$

or

$$\Pi^{\text{RRF}}(\psi, t) \equiv P_X^{\text{RRF}}(\psi, t) + iP_Y^{\text{RRF}}(\psi, t), \quad (3.5)$$

with

$$\begin{aligned} P_X^{\text{RRF}}(\psi, t) &= P_R^{\text{RRF}}(t) \cos \psi - P_I^{\text{RRF}}(t) \sin \psi \\ P_Y^{\text{RRF}}(\psi, t) &= P_R^{\text{RRF}}(t) \sin \psi + P_I^{\text{RRF}}(t) \cos \psi \end{aligned} \quad (3.6)$$

where ψ is a phase which accounts for spin rotation during the muon’s time of flight and

$$\begin{aligned} P_R^{\text{RRF}}(t) &= \int_{-\infty}^{\infty} n_\nu(\nu) \cos[2\pi(\nu - \nu_r)t] d\nu \\ P_I^{\text{RRF}}(t) &= \int_{-\infty}^{\infty} n_\nu(\nu) \sin[2\pi(\nu - \nu_r)t] d\nu. \end{aligned} \quad (3.7)$$

The real and imaginary portions of the complex polarization function in the rotating reference frame are $P_X^{\text{RRF}}(\psi, t)$ and $P_Y^{\text{RRF}}(\psi, t)$ in the case of arbitrary phase ψ and are $P_R^{\text{RRF}}(t)$ and $P_I^{\text{RRF}}(t)$ in the case $\psi = 0$, which, when fitting data taken in the RRF, may be more convenient to calculate. This is rigorously valid only if the local field is strictly parallel to the average field (see Sec. 3.3.2 for a discussion of the more general case). The projections of the polarization onto the \hat{X} and \hat{Y} directions are indicated by X and Y in the subscripts. (Note that these equations are equivalent to Eqs. 2.69 and 2.71.)

The relationship between the theoretical lab-frame polarizations [$P_X(t)$, $P_Y(t)$], the theoretical real and imaginary RRF polarizations [$P_R^{\text{RRF}}(t)$, $P_I^{\text{RRF}}(t)$] and the theoretical lab-frame RRF polarizations [$P_X^{\text{RRF}}(t)$, $P_Y^{\text{RRF}}(t)$] is expressed by

$$\begin{aligned}
 P_X(\psi, t) &= P_R^{\text{RRF}}(t) \cos(2\pi\nu_r t + \psi) - P_I^{\text{RRF}}(t) \sin(2\pi\nu_r t + \psi) \\
 &= P_X^{\text{RRF}}(\psi, t) \cos(2\pi\nu_r t) - P_Y^{\text{RRF}}(\psi, t) \sin(2\pi\nu_r t) \\
 P_Y(\psi, t) &= P_R^{\text{RRF}}(t) \sin(2\pi\nu_r t + \psi) + P_I^{\text{RRF}}(t) \cos(2\pi\nu_r t + \psi) \\
 &= P_X^{\text{RRF}}(\psi, t) \sin(2\pi\nu_r t) + P_Y^{\text{RRF}}(\psi, t) \cos(2\pi\nu_r t)
 \end{aligned} \tag{3.8}$$

and conversely

$$\begin{aligned}
 P_X^{\text{RRF}}(\psi, t) &= P_X(\psi, t) \cos(2\pi\nu_r t) + P_Y(\psi, t) \sin(2\pi\nu_r t) \\
 P_Y^{\text{RRF}}(\psi, t) &= -P_X(\psi, t) \sin(2\pi\nu_r t) + P_Y(\psi, t) \cos(2\pi\nu_r t).
 \end{aligned} \tag{3.9}$$

where $P_X(\psi, t) = P_X(t)$ and $P_Y(\psi, t) = P_Y(t)$ is the polarization observed in the laboratory frame (from Eq. 3.3). The RRF is only useful as a fitting device when the local field inhomogeneity is much smaller than the average field ($\delta B \ll B_o$ and therefore $\delta\nu \ll \nu_o$), in which case Eq. 3.7 is approximately correct even if the local fields are not all perfectly parallel.

Thus to transform the experimental asymmetry $\vec{A}_{\text{lab}}(t)$ into the RRF we simply substitute the experimental asymmetry functions $A_X(t)$ and $A_Y(t)$ for the theoretical asymmetry functions $A_o P_X(\psi, t)$ and $A_o P_Y(\psi, t)$, giving

$$\begin{aligned}
 A_X^{\text{RRF}}(t) &= A_X(t) \cos(2\pi\nu_r t) + A_Y(t) \sin(2\pi\nu_r t) \\
 A_Y^{\text{RRF}}(t) &= -A_X(t) \sin(2\pi\nu_r t) + A_Y(t) \cos(2\pi\nu_r t).
 \end{aligned} \tag{3.10}$$

Due to tight geometries, some μ SR experiments have only two counters (usually $+\hat{X}$ and $-\hat{X}$ or $+\hat{Y}$ and $-\hat{Y}$) instead of four, giving only one polarization projection [$P_X(\psi, t)$ or $P_Y(\psi, t)$]. Moreover, this four counter treatment is only valid when the applied field is along the \hat{Z} direction; if that is not the case, only two counters may be used in the Fourier transform. One can show that the theoretical rotating reference frame signal for the two-counter data

$$\vec{P}_2^{\text{RRF}}(\psi, t) = P_{X_2}^{\text{RRF}}(\psi, t)\hat{X} + P_{Y_2}^{\text{RRF}}(\psi, t)\hat{Y} \quad (3.11)$$

can be expressed in terms of Eq. 3.4 for the four-counter signal as

$$\begin{aligned} P_{X_2}^{\text{RRF}}(\psi, t) &= +\cos^2\varphi P_X^{\text{RRF}}(\psi, t) - \sin\varphi\cos\varphi P_Y^{\text{RRF}}(\psi, t) \\ P_{Y_2}^{\text{RRF}}(\psi, t) &= -\sin\varphi\cos\varphi P_X^{\text{RRF}}(\psi, t) + \sin^2\varphi P_Y^{\text{RRF}}(\psi, t), \end{aligned} \quad (3.12)$$

where $\varphi = 2\pi\nu_r t$. Although P_X^{RRF} and P_Y^{RRF} are slowly varying functions of time, $P_{X_2}^{\text{RRF}}$ and $P_{Y_2}^{\text{RRF}}$ oscillate rapidly (through φ) for reasonable choices of the RRF frequency ν_r near the mean frequency ν_o . In effect, if there is only one polarization projection available (or even just a single spectrum), we cannot distinguish whether the muon is precessing clockwise or counterclockwise and hence terms involving both $\nu - \nu_r$ (desired) and $\nu + \nu_r$ (not desired) appear when the RRF transformation is performed.

However, if we rebin the RRF polarization functions using a time bin size equal to $\Delta t = m/\nu_r$ where m is an integer, the spurious high frequency component (the term involving φ) is avoided in the final RRF spectrum. This is seen by averaging φ over a time period ($1/\nu_r$), which gives

$$\begin{aligned} \langle \cos^2\varphi \rangle_{1/\nu_r} &= \frac{1}{2} + \frac{1}{2}\langle \cos(2\varphi) \rangle_{1/\nu_r} = \frac{1}{2}, \\ \langle \sin^2\varphi \rangle_{1/\nu_r} &= \frac{1}{2} - \frac{1}{2}\langle \cos(2\varphi) \rangle_{1/\nu_r} = \frac{1}{2} \end{aligned} \quad (3.13)$$

and

$$\langle \cos\varphi\sin\varphi \rangle_{1/\nu_r} = \frac{1}{2}\langle \sin(2\varphi) \rangle_{1/\nu_r} = 0. \quad (3.14)$$

Therefore, the theoretical two counter RRF polarization functions simplify to

$$\begin{aligned} \langle P_{X_2}^{\text{RRF}}(\psi, t) \rangle_{1/\nu_r} &= \frac{1}{2}P_X^{\text{RRF}}(\psi, t) \\ \langle P_{Y_2}^{\text{RRF}}(\psi, t) \rangle_{1/\nu_r} &= \frac{1}{2}P_Y^{\text{RRF}}(\psi, t). \end{aligned} \quad (3.15)$$

When the same ‘‘RRF transformation’’ is applied to the experimental asymmetry spectra $\vec{A}_{\text{lab}}(t)$, a similar averaging of the real and imaginary asymmetries occurs. If there are no counters along the \hat{Y} axis (*e.g.*, no $+Y$ or $-Y$ counters), then $A_o^Y = 0$ and we can set $A_o = A_o^X$, giving

$$\langle \vec{A}_{\text{RRF}}^{\text{exp}}(\psi, t) \rangle_{1/\nu_r} \approx \frac{1}{2} A_o (\langle P_X^{\text{RRF}}(\psi, t) \rangle_{1/\nu_r} \hat{X} + \langle P_Y^{\text{RRF}}(\psi, t) \rangle_{1/\nu_r} \hat{Y}). \quad (3.16)$$

If $A_o^X \neq 0$ and $A_o^Y \neq 0$, we can define $A_o = \frac{1}{2}(A_o^X + A_o^Y)$ and get

$$\langle \vec{A}_{\text{RRF}}^{\text{exp}}(\psi, t) \rangle_{1/\nu_r} \approx A_o (\langle P_X^{\text{RRF}}(\psi, t) \rangle_{1/\nu_r} \hat{X} + \langle P_Y^{\text{RRF}}(\psi, t) \rangle_{1/\nu_r} \hat{Y}). \quad (3.17)$$

In sufficiently large applied fields, the only qualitative difference between two-counter and four-counter data in the RRF is that the fitted amplitude of the former will be one half of the latter. One-counter data looks the same as two-counter data.

If there are two or more frequencies which are well separated, *e.g.*, $\nu_r - \nu_1 \ll \nu_r$ but $\nu_r - \nu_2 \sim \nu_r$, then the signal due to frequencies far away from the chosen RRF frequency will likely be ‘‘averaged away’’ in the rebinning. The case of several well separated frequencies may arise when there are several muon signals from a strong antiferromagnet in ZF or a sample in a low transverse field with both muonium and μ^+ signals ($\gamma_{\text{Mu}} \approx 103\gamma_{\mu}$). Depending on the relevance of the multiple signals, ‘‘binning out’’ some of the signals may or may not be desirable. Simultaneous fits of the same spectrum in several different RRFs can also be used.

Using a discrete rather than an analog RRF transform complicates the choice of RRF frequency ν_r . The apparent frequency in the RRF frame ($\nu - \nu_r$) must be appropriate for fitting and visualization but at the same time it must allow for a convenient bin size ($\Delta t = m/\nu_r = n_p \delta t$).

3.2.2 RRF in high Fields

In very high fields, the choice of rotating reference frame (RRF) frequency becomes more difficult. Lecroy 4204 series ‘‘clocks’’ have time bin sizes $\Delta t = 2^q \times 0.078125$ ns for integer q . If, for example, we start with data stored with 0.3125 ns per bin, we must find integers m and n for a given RRF frequency ν_r (in MHz) such that the equation

$$\frac{m}{\nu_r} = n \times 0.0003125 = \frac{n}{2^7 5^2} \quad (3.18)$$

is satisfied. If no such values of m and n can be found or if smallest RRF bin size allowed m/ν_r is too large, then we have made a poor choice of RRF frequency. Moreover, the applied field should be chosen such that the lineshape in the Fourier transform does not overlap the RRF frequency if only two opposing counters are being used. For the high temperature superconductor $\text{YBa}_2\text{Cu}_3\text{O}_{7-\delta}$, an average frequency approximately 2 MHz higher than ν_r allows for some error in the setting of the experimental magnet. Appendix A shows good choices of RRF frequencies over all frequencies currently measurable in μ SR, assuming the 2 MHz difference and $\Delta t = 0.3125$ ns per bin.

The choice of RRF becomes less critical with increasing frequencies because the undesired frequency $\nu + \nu_r$ becomes large. Even if the number of oscillations per RRF bin (m) is no longer an integer, the number of oscillations is so large that any partial oscillation can be ignored with a correspondingly small miscalculation of the RRF asymmetry. With higher fields, rounding errors during the transformation become very important. For μ^+ data, fields above 1 T produce high precession frequencies, which yield a huge accumulated phase at late times. Single precision RRF transformations introduce significant errors so double precision calculations, even for single precision data, are absolutely necessary.

3.3 The Art of Fourier Transforms

3.3.1 The Fourier Transform in μ SR: $B_X(\vec{r}) = B_Y(\vec{r}) = 0$

The polarization vector $\vec{P}(t)$, which is proportional to the asymmetry, represents the time evolution of the ensemble muon polarization in the presence of local fields in the sample. In the case of $\vec{B} \parallel \hat{Z}$, the projection of the polarization onto counters along the \hat{X} axis is

$$P_X(t) = \frac{1}{V} \int_V \left\{ \frac{B_X^2(\vec{r})}{B^2(\vec{r})} + \frac{B_Y^2(\vec{r}) + B_Z^2(\vec{r})}{B^2(\vec{r})} \cos[\gamma_\mu B(\vec{r})t + \psi + \psi_X] \right\} d\vec{r}. \quad (3.19)$$

We can define $n_\nu(\nu)d\nu$ as the probability that a muon will precess at the frequency between $\nu - d\nu/2$ and $\nu + d\nu/2$ with $\nu = \frac{\gamma_\mu}{2\pi} B$, allowing the polarization projection to be written as

$$P_X(t) = \int_{-\infty}^{\infty} n_\nu(\nu) \cos(2\pi\nu t + \psi) d\nu \quad (3.20)$$

in the special case when the local fields are parallel to the \hat{z} axis [*i.e.*, when $B_X(\vec{r}) = 0$ and $B_Y(\vec{r}) = 0$ throughout the sample] and the muon spin is perpendicular to the average field ($\phi = \pi/2$). [See Eq. 2.69 in Sec. 2.6.5 for why this treatment is appropriate in the case of $B_X(\vec{r}) = B_Y(\vec{r}) = 0$ for all \vec{r} .] In this case, $P_X(t)$ is the Fourier transform of $n_\nu(\nu)$, to within the effects of the phase ψ . Extending this to $P_Y(t)$, the complex polarization is

$$\begin{aligned}\Pi(t) &= P_X(t) + iP_Y(t) \\ &= \int_{-\infty}^{\infty} n_\nu(\nu) e^{i(2\pi\nu t + \psi)} d\nu.\end{aligned}\quad (3.21)$$

Since $n_\nu(\nu)$ is a probability, it is strictly real and $\int_{-\infty}^{\infty} n_\nu(\nu) d\nu = 1$. If $n_\nu(\nu)$ is non-zero only for positive frequencies, then the above integrals may be restricted to positive frequencies.

Since μ SR measures the time evolution of the muon polarization from zero time, when the muon ensemble is fully polarized (since each muon stopping in the sample has the same initial spin direction), the muon polarization at negative times has no real meaning—reflecting the causal sequence inherent in implanting polarized muons which depolarize in the inhomogeneous fields present in the sample. This will be treated here briefly in the context of Fourier transforms by explicitly including the Heaviside function

$$H(t) = \begin{cases} 1 & t > 0 \\ \frac{1}{2} & t = 0 \\ 0 & t < 0 \end{cases} . \quad (3.22)$$

The complex polarization is then defined for all times ($-\infty < t < \infty$) by

$$\begin{aligned}\Pi(t) &= \left[\int_{-\infty}^{\infty} n_\nu(\nu) e^{i(2\pi\nu t + \psi)} d\nu \right] H(t) \\ &= G(t) H(t),\end{aligned}\quad (3.23)$$

where we will use $G(t)$ as an abbreviation for $\int_{-\infty}^{\infty} n_\nu(\nu) e^{i(2\pi\nu t + \psi)} d\nu$. The Fourier transform of $\Pi(t)$ is the convolution of the transforms of $G(t)$ and $H(t)$ (this is discussed further in Sec. 3.4):

$$\int_{-\infty}^{\infty} \Pi(t) e^{-i(2\pi\nu t + \psi_c)} dt = e^{-i\psi_c} \int_{-\infty}^{\infty} g(\nu') h(\nu - \nu') d\nu', \quad (3.24)$$

where

$$g(\nu) = \int_{-\infty}^{\infty} G(t) e^{-i2\pi\nu t} dt$$

$$\begin{aligned}
&= \int_{-\infty}^{\infty} \left[\int_{-\infty}^{\infty} n_{\nu}(\nu') e^{i(2\pi\nu't + \psi)} d\nu' \right] e^{-i2\pi\nu t} dt \\
&= e^{i\psi} \int_{-\infty}^{\infty} n_{\nu}(\nu') \delta(\nu - \nu') d\nu \\
&= e^{i\psi} n_{\nu}(\nu)
\end{aligned} \tag{3.25}$$

and

$$h(\nu) = \int_{-\infty}^{\infty} H(t) e^{-i2\pi\nu t} dt. \tag{3.26}$$

The extra phase ψ_c in Eq. 3.24 has been added to correct for the initial phase ψ of the polarization function.

The Heaviside function can be expressed as

$$H(t) = \begin{cases} \lim_{c \rightarrow 0} e^{-ct} & t > 0 \\ \frac{1}{2} & t = 0 \\ 0 & t < 0 \end{cases}, \tag{3.27}$$

which has as its Fourier transform

$$\begin{aligned}
h(\nu) &= \lim_{c \rightarrow 0} \frac{i}{2\pi\nu + ic} \\
&= \lim_{c \rightarrow 0} \frac{i(2\pi\nu) + c}{(2\pi\nu)^2 + c^2} \\
&= \frac{1}{2}\delta(\nu) + \frac{i}{2\pi\nu}.
\end{aligned} \tag{3.28}$$

When the initial phase ψ is equal to the phase correction ψ_c used in the Fourier transform, the convolution can be expressed in terms of its real and imaginary parts

$$\begin{aligned}
\int_{-\infty}^{\infty} \Pi(t) e^{-i(2\pi\nu t + \psi_c)} dt &= e^{-i\psi_c} \int_{-\infty}^{\infty} g(\nu') h(\nu - \nu') d\nu' \\
&= \frac{1}{2}g(\nu) e^{-i\psi_c} + i \int_{-\infty}^{\infty} e^{-i\psi_c} g(\nu') \frac{1}{2\pi(\nu - \nu')} d\nu' \\
&= \frac{1}{2}n_{\nu}(\nu) + i \int_{-\infty}^{\infty} n_{\nu}(\nu') \frac{1}{2\pi(\nu - \nu')} d\nu'.
\end{aligned} \tag{3.29}$$

The real portion of the Fourier transform is exactly the distribution of muon precession frequencies $n_{\nu}(\nu)$ multiplied by one-half to reflect the fact that the polarization $\Pi(t)$ is only defined for positive times. The imaginary portion is an odd function of $\nu - \nu_0$.

For example, an exponential depolarization

$$\Pi(t) = e^{-\Lambda t} e^{i(2\pi\nu t + \psi)} H(t) \quad (3.30)$$

has a Lorentzian frequency distribution

$$F_R(\nu) = \frac{1}{2} n_\nu(\nu) = \frac{1}{2} \frac{\Lambda}{\Lambda^2 + [2\pi(\nu_o - \nu)]^2} \quad (3.31)$$

as the real portion of the Fourier transform $F_R(\nu)$ and has

$$F_I(\nu) = \frac{2\pi(\nu_o - \nu)}{\Lambda} n_\nu(\nu) \quad (3.32)$$

as the imaginary portion of the Fourier transform.

From Eq. 3.23, the area under the real portion of the Fourier transform is equal to the polarization at plus zero time

$$\lim_{t \rightarrow 0^+} \Pi(t) = \int_{-\infty}^{\infty} n_\nu(\nu) d\nu, \quad (3.33)$$

The area under the imaginary portion A_I is exactly equal to zero, regardless of whether or not $n_\nu(\nu)$ is symmetric:

$$\begin{aligned} A_I &\equiv \int_{-\infty}^{\infty} F_I(\nu) d\nu \\ &= \int_{-\infty}^{\infty} \int_{-\infty}^{\infty} n_\nu(\nu') \frac{1}{2\pi(\nu - \nu')} d\nu' d\nu \\ &= \int_{-\infty}^{\infty} \left[\int_{-\infty}^{\nu'} n_\nu(\nu') \frac{1}{2\pi(\nu - \nu')} d\nu + \int_{\nu'}^{\infty} n_\nu(\nu') \frac{1}{2\pi(\nu - \nu')} d\nu \right] d\nu' \\ &= 0. \end{aligned} \quad (3.34)$$

This has a very useful application when the initial phase ψ of the polarization function is not known. The initial phase ψ can be calculated from the Fourier transform of the experimental data with $\psi_c = 0$ using the relation

$$\psi = \sin^{-1}(A_I). \quad (3.35)$$

If one then sets setting $\psi_c = \psi$ in Eq. 3.29, the Fourier transform of the experimental data will produce “phase corrected” real $\left[\frac{1}{2}n_\nu(\nu)\right]$ and imaginary $\left[\int_{-\infty}^{\infty} n_\nu(\nu') \frac{1}{2\pi(\nu - \nu')} d\nu'\right]$ spectra.

We are exclusively interested in the distribution of muon precession frequencies $n_\nu(\nu)$, so it is important to correctly calculate the phase-corrected real Fourier spectrum $F_R(\nu)$. The imaginary spectrum $F_I(\nu)$ is of no particular use. The “amplitude” Fourier spectrum $F_A(\nu)$

$$F_A(\nu) = \sqrt{F_R^2(\nu) + F_I^2(\nu)} \quad (3.36)$$

is strictly positive but is “contaminated” by the far-reaching “tails” in the $F_I(\nu)$ due to the $\frac{1}{2\pi(\nu-\nu')}$ term, so it is not a satisfactory alternative to phase corrected $F_R(\nu)$. All Fourier transforms used in this thesis give the phase-corrected real Fourier transform spectra.

Just as in the RRF, the Fourier transform of the complex polarization [involving $P_X(t)$ and $P_Y(t)$] is only valid when $\vec{B}_o \parallel \hat{Z}$. Otherwise, one may only take the Fourier transform of the the polarization projected along a single direction. Using, for example, $P_X(t)$ (formed from a histogram pair) instead of $\Pi(t)$ (formed from two orthogonal histogram pairs) when $n_\nu(\nu) = 0$ for all $\nu < 0$ and $n_\nu(\nu)$ is centered at ν_o introduces the following effects: the Fourier amplitudes are reduced by 1/2 and a mirror-image lineshape is introduced into the Fourier transform centered at $-\nu_o$. If the function $n_\nu(\nu)$ has long “tails” in the imaginary Fourier spectrum, the lineshape and its mirror-image may overlap significantly. The real Fourier spectrum, which is the important one, will be unaffected as long as $n_\nu(\nu)$ is non-zero only for $\nu > 0$. These effects reflect the fact that two opposite counters cannot detect whether the muons are precessing clockwise or counter-clockwise.

If $B_X(\vec{r}) \ll B_Z(\vec{r})$ and $B_Y(\vec{r}) \ll B_Z(\vec{r})$ when $\vec{B}_o \parallel \hat{Z}$, then the above treatment is approximately correct and the real portion of the Fourier transform is almost proportional to the distribution of local fields $n_\nu(\nu)$.

3.3.2 The Fourier Transform in μ SR: General Case

The Fourier transform of the ensemble muon polarization along a certain direction can be quite informative if it accurately reflects the distribution of local field magnitudes $n(B)$, which is the case in the previous section where it was assumed that local fields are all parallel. However, in general, there are components of the local field perpendicular to the average field and the real portion of the Fourier transform is only approximately proportional to $n(B)$. This section

discusses the general case of the Fourier transform quantitatively in light of the formulation of the muon polarization vector given in Sec. 2.6.3.

If the perpendicular field components $B_x(\vec{r})$ and $B_y(\vec{r})$ are appreciable then the treatment in the previous section is not complete. (In this section we will use the \hat{x} - \hat{y} - \hat{z} reference frame, which is defined in part by $\vec{B}_o = \hat{z}$, rather than the counter reference frame \hat{X} - \hat{Y} - \hat{Z} in order to emphasize the properties of various kinds of field distributions.) To summarize the results in Sec. 2.6.3, the muon-ensemble polarization vector as a function of time (Eq. 2.53) is

$$\vec{P}(t) = \sin \phi \cos \psi \vec{P}(t; \hat{P}_o = \hat{x}) + \sin \phi \sin \psi \vec{P}(t; \hat{P}_o = \hat{y}) + \cos \phi \vec{P}(t; \hat{P}_o = \hat{z}) \quad (3.37)$$

where $\vec{P}(t; \hat{P}_o = \hat{j})$ is the time-dependent polarization vector that would be observed if the initial polarization \hat{P}_o were exactly along the direction \hat{j} . The projection of $\vec{P}(t)$ onto the \hat{C} direction is given by (Eq. 2.51)

$$\begin{aligned} \vec{P}(t) \cdot \hat{C} = & \hat{P}(0) \cdot \left\{ \int \tilde{U}(B') dB' \right\} \cdot \hat{C} \\ & + \hat{P}(0) \cdot \hat{C} \left\{ \int n(B') \cos [\gamma_\mu B' t] dB' \right\} \\ & - \hat{P}(0) \cdot \left\{ \int \tilde{U}(B') \cos [\gamma_\mu B' t] dB' \right\} \cdot \hat{C} \\ & + \left(\hat{P}(0) \times \hat{C} \right) \cdot \left\{ \int \vec{V}(B') \sin [\gamma_\mu B' t] dB' \right\}, \end{aligned} \quad (3.38)$$

where $\hat{P}(0) = P_o$ is the direction of the polarization at time $t = 0$. The term

$$\vec{P}(t \rightarrow \infty) \cdot \hat{C} = \vec{P}_{||}(t) \cdot \hat{C} = \hat{P}(0) \cdot \left\{ \int \tilde{U}(B) dB \right\} \cdot \hat{C} \quad (3.39)$$

has no time dependence and therefore only produces amplitude in the Fourier transform at zero frequency.

The Fourier transform of the vector polarization projected along the \hat{C} direction is

$$F_R(\nu) + iF_I(\nu) = \int_{-\infty}^{\infty} H(t) \left[\vec{P}(t) \cdot \hat{C} \right] e^{-i(2\pi\nu t + \psi_c)} dt. \quad (3.40)$$

As discussed in the previous section, we are not particularly interested in the imaginary portion of the Fourier transform $F_I(\nu)$. If the local field were always parallel to the average field, the real portion of the Fourier transform $F_R(\nu)$ would be equal to one fourth of the probability

distribution of muon precession frequencies, which is proportional to the probability distribution of the magnitude of the local fields:

$$F_R(\nu) d\nu = \frac{1}{4} n_\nu(\nu) d\nu = \frac{1}{4} n(B) dB, \quad (3.41)$$

where $\nu = \frac{\gamma\mu}{2\pi} B$ and the factor of $\frac{1}{4}$ comes from using the Heaviside function $H(t)$ and using only two opposing counters [*i.e.* $\vec{P}(t) \cdot \hat{C}$ but not $\vec{P}(t) \cdot (\hat{C} \times \hat{z})$]. In the general case where $\vec{B}(\vec{r})$ is not necessarily parallel to \vec{B}_o ,

$$F_R(\nu) d\nu = S_C(\nu) d\nu, \quad (3.42)$$

where $S_C(\nu)$ is approximately equal to $\frac{1}{4} n_\nu(\nu)$ in the limit of high applied fields when the projection direction is perpendicular to the average field direction ($\hat{C} \cdot \vec{B}_o = 0$). We will refer to $S_C(\nu)$ as “the observed lineshape for the polarization projection in the \hat{C} direction.” We will now discuss in detail what $S_C(\nu)$ is and how it differs from $\frac{1}{4} n_\nu(\nu)$.

In practice, it is common to “flatten” the asymmetry signal by subtracting any constant terms before applying the Fourier transform. The “flattened” polarization is simply the oscillatory portion $\vec{P}_\perp(t)$ of the vector polarization defined in Eq. 2.43. The real portion of the Fourier transform of the flattened polarization projection $\vec{P}_\perp(t) \cdot \hat{C}$ is given by

$$\begin{aligned} S_{C,\perp}(\nu) &\equiv \text{Re} \int_{-\infty}^{\infty} H(t) [\vec{P}(t) - \vec{P}(t \rightarrow \infty)] \cdot \hat{C} e^{-i(2\pi\nu t + \psi_c)} dt \\ &= \text{Re} \int_{-\infty}^{\infty} H(t) [\vec{P}_\perp(t) \cdot \hat{C}] e^{-i(2\pi\nu t + \psi_c)} dt. \end{aligned} \quad (3.43)$$

The Fourier transform of the non-oscillatory portion is a delta function at zero frequency

$$\begin{aligned} S_{C,\parallel}(\nu) &\equiv \text{Re} \int_{-\infty}^{\infty} H(t) [\vec{P}(t \rightarrow \infty) \cdot \hat{C}] e^{-i(2\pi\nu t + \psi_c)} dt \\ &= [\vec{P}(t \rightarrow \infty) \cdot \hat{C}] \text{Re} \int_{-\infty}^{\infty} H(t) e^{-i(2\pi\nu t + \psi_c)} dt \\ &= [\vec{P}(t \rightarrow \infty) \cdot \hat{C}] \frac{1}{4} \delta(\nu - 0). \end{aligned} \quad (3.44)$$

The real Fourier transform of the projection of the complete (or “unflattened”) polarization is

$$S_C(\nu) = S_{C,\perp}(\nu) + S_{C,\parallel}(\nu) \quad (3.45)$$

In the special case of uniaxial local field distributions (Sec. 2.6.5), where there are no transverse components [$\vec{B}(\vec{r}) \cdot \hat{x} = 0$ and $\vec{B}(\vec{r}) \cdot \hat{y} = 0$ for all \vec{r} and $\vec{B}_o = B_o \hat{z}$], which is the case for anisotropic

superconductors with the applied field along a principal axis, the expression for the polarization is very simple (Eq. 2.68):

$$\vec{P}^{\text{ULF}}(t) = \hat{x} \sin \phi \int n(B) \cos[\gamma_\mu B t + \psi] dB + \hat{y} \sin \phi \int n(B) \sin[\gamma_\mu B t + \psi] dB + \hat{z} \cos \phi. \quad (3.46)$$

The lineshape is related to the distribution of local fields by

$$\begin{aligned} S_{C,\perp}^{\text{ULF}}(\nu) &= |\hat{P}(0) \times \hat{z}| \frac{1}{4} n_\nu(\nu) \quad \text{when } \vec{B}(\vec{r}) \parallel \hat{z} \forall \vec{r} \\ &= \sin \phi \frac{1}{4} n_\nu(\nu), \end{aligned} \quad (3.47)$$

where the normalization $|\vec{P}(0) \times \hat{z}|$ represents the portion of the initial polarization which is perpendicular to the average field. The phase correction is $\psi_c = \psi$ for the case of $\hat{C} \parallel \hat{P}(0)$, otherwise it will also include the angle of the counters (in the \hat{C} direction) relative to $\hat{P}(0)$.

In the case of a non-correlated field distribution with x and y components of the local field, the corrected phase will be the same, but the lineshape $S_{C,\perp}^{\text{nc}}(\nu)$ will not be exactly proportional to the distribution of local fields $n_\nu(\nu)$. For $\hat{C} \parallel \hat{P}(0)$ when $\hat{P}(0) \perp \hat{z}$,

$$S_{C,\perp}^{\text{nc}}(\nu; \hat{C} = \hat{P}(0) \perp \hat{z}) d\nu = \frac{1}{4} \left[n(B) - \hat{P}(0) \cdot \vec{U}(B) \cdot \hat{P}(0) \right] dB \quad (3.48)$$

using a phase correction $\psi_c = 0$. Remember that the muon precession frequency is proportional to the magnitude of the field: $\nu = \frac{\gamma_\mu}{2\pi} B$. For the case of $\hat{C} = \hat{z} \times \hat{P}(0)$ when $\hat{P}(0) \perp \hat{z}$,

$$S_{C,\perp}^{\text{nc}}(\nu; \hat{C} = \hat{z} \times \hat{P}(0) \perp \hat{z}) d\nu = \frac{1}{4} \hat{z} \cdot \vec{V}(B) dB \quad (3.49)$$

using $\psi_c = \pi/2$. In both cases, the smaller the transverse field components are relative to the average field, the closer the real portion of the Fourier transform $S_{C,\perp}^{\text{nc}}(\nu)$ will be to the distribution of local fields $\frac{1}{4} n_\nu(\nu)$.

For arbitrary (*i.e.* correlated) field distributions, not only will the the lineshape not be exactly proportional to the distribution of local fields, but the corrected phase ψ_c used in the Fourier transform may not be equal to ψ , due to correlations in the x , y and z field distributions. The \hat{z} direction in the \hat{x} - \hat{y} - \hat{z} reference frame is defined by the average field's direction. For example, for a TF experiment, $\hat{x} \cdot \vec{P}(t; \hat{P}_o = \hat{x})$ (see Eq. 2.51) will have an oscillatory component which is

completely in phase ($\psi_c = 0$)

$$\begin{aligned}\hat{x} \cdot \vec{P}_\perp(t; \hat{P}_o = \hat{x}) &= \hat{x} \cdot \vec{P}(t; \hat{P}_o = \hat{x}) - \hat{x} \cdot \vec{P}_\parallel(t; \hat{P}_o = \hat{x}) \\ &= \int \{1 - \tilde{U}_{xx}(B)\} \cos[\gamma_\mu B t] dB\end{aligned}\quad (3.50)$$

and the real portion of the Fourier transform will simply become

$$S_x(\nu) = 1 - \tilde{U}_{xx}(B). \quad (3.51)$$

On the other hand, $\hat{y} \cdot \vec{P}(t; \hat{P}_o = \hat{x})$ will have oscillatory components

$$\begin{aligned}\hat{y} \cdot \vec{P}_\perp(t; \hat{P}_o = \hat{x}) &= \hat{y} \cdot \vec{P}(t; \hat{P}_o = \hat{x}) - \hat{y} \cdot \vec{P}_\parallel(t; \hat{P}_o = \hat{x}) \\ &= - \int \tilde{U}_{xy}(B) \cos[\gamma_\mu B t] dB + \int V_z(B) \sin[\gamma_\mu B t] dB\end{aligned}\quad (3.52)$$

which would be completely out of phase ($\psi_c = \pi/2$) if $\tilde{U}_{xy}(B) = 0$. Likewise, for a LF experiment, $\hat{x} \cdot \vec{P}(t; \hat{P}_o = \hat{z})$ and $\hat{y} \cdot \vec{P}(t; \hat{P}_o = \hat{z})$ may have oscillatory components (instead of being zero as in the case of a non-correlated distribution):

$$\begin{aligned}\hat{x} \cdot \vec{P}_\perp(t; \hat{P}_o = \hat{z}) &= \hat{x} \cdot \vec{P}(t; \hat{P}_o = \hat{z}) - \hat{x} \cdot \vec{P}_\parallel(t; \hat{P}_o = \hat{z}) \\ &= - \int \tilde{U}_{zx}(B) \cos[\gamma_\mu B t] db + \int V_y(B) \sin[\gamma_\mu B t] d\vec{r}. \\ \hat{y} \cdot \vec{P}_\perp(t; \hat{P}_o = \hat{z}) &= \hat{y} \cdot \vec{P}(t; \hat{P}_o = \hat{z}) - \hat{y} \cdot \vec{P}_\parallel(t; \hat{P}_o = \hat{z}) \\ &= - \int \tilde{U}_{zy}(B) \cos[\gamma_\mu B t] db - \int V_x(B) \sin[\gamma_\mu B t] d\vec{r}.\end{aligned}\quad (3.53)$$

Since this is quite a bit more complicated than the non-correlated case, it is even more dubious to identify the real portion of the Fourier transform of the projection of the polarization as “approximately the same as $n_\nu(\nu)$.” In the general case, the Fourier transform of a polarization projection contains only *part* of the information available in $\vec{P}(t)$. Therefore, with correlated field distributions, the straightforward approach is to fit $\vec{P}(t)$ (the method used in Ch. 5) rather than the Fourier transforms $S_{C,\perp}(\nu)$ of the different polarization projections ($\hat{C} = \hat{X}, \hat{Y}$ and \hat{Z})

The lineshape function $S_{C,\perp}(\nu)$ differs from the probability distribution of local field magnitudes $n_\nu(\nu)$ in that, by definition,

$$\int_{-\infty}^{\infty} n_\nu(\nu) d\nu \equiv 1 \quad (3.54)$$

while

$$\int_{-\infty}^{\infty} [S_{C,\perp}(\nu) + S_{C,\parallel}(\nu)] d\nu \leq \frac{1}{4}. \quad (3.55)$$

Note that applying the Fourier transform to the muon polarization projection along the \hat{C} direction, $[\vec{P}(t) - \vec{P}(t \rightarrow \infty)] \cdot \hat{C}$, results in a *weighted* probability density of muon precession frequencies $S_{C,\perp}(\nu)d\nu$ which is not necessarily proportional to the total probability density of the local field magnitudes $n_\nu(\nu) d\nu = n(B) dB$. The lineshape $S_{C,\perp}(\nu)$ is what is actually observed in the flattened Fourier transform of the polarization projected on the positron counter directions $\hat{C} = \hat{X}, \hat{Y}$ or \hat{Z} axis. The lineshape may be expected to be proportional to the total probability density $n_\nu(\nu)$ [and the zero frequency peak $S_{C,\parallel}(0)$ absent] *only* when all the local fields are along $\hat{z} \parallel \vec{B}_0$; they are *nearly* proportional when the applied field is very large [$B_x(\vec{r}), B_y(\vec{r}) \ll B_z(\vec{r})$]. For Chs. 6 and 7, in which the applied field is much larger than the local field inhomogeneity, the two are assumed to be proportional. For the cases discussed in Ch. 5, the two may be quite different and the presence of a large zero frequency peak [$S_{C,\parallel}(0) \gg 0$] is significant. Note that the decay positron emission asymmetry factor A_0 introduces an additional multiplicative factor in the Fourier transform of μ SR data.

Figs. 3.2.a, 3.2.c and 3.2.e show the polarization projections $P_C(t)$ for $\hat{C} = \hat{X}, \hat{Y}$ and \hat{Z} for an ensemble of muons in an anisotropic superconductor (see Chs. 4 and 5 for a discussion of the model used). The \hat{X} - \hat{Y} - \hat{Z} coordinate system is simply rotated from the \hat{x} - \hat{y} - \hat{z} system by an angle θ about the \hat{y} axis (Eq. 2.31). This is an example of a system which has a non-zero value for $\vec{P}(t \rightarrow \infty)$, and hence $S_{C,\parallel}(0)$ is also non-zero for one or more of the positron counter directions, $\hat{C} = \hat{X}, \hat{Y}$ and \hat{Z} . Note that at long times the average values for the projections of the ensemble polarization in the \hat{X} and \hat{Z} directions [$P_X(t), P_Z(t)$] are non-zero while the average value in the \hat{Y} direction [$P_Y(t)$] is nearly zero. Figs. 3.2.b, 3.2.d and 3.2.f show the real parts of the discrete Fourier transforms [$S_X\left(\frac{\gamma\mu}{2\pi}B\right), S_Y\left(\frac{\gamma\mu}{2\pi}B\right)$ and $S_Z\left(\frac{\gamma\mu}{2\pi}B\right)$] of the polarization projections. The average field is $B = 100$ G and the maximum probability amplitude is at about 65 G. The non-oscillatory portion is seen as a delta function at zero frequency. The polarization projection which has the largest amplitude is that in the \hat{Y} direction; correspondingly, its Fourier transform also has the largest amplitude.

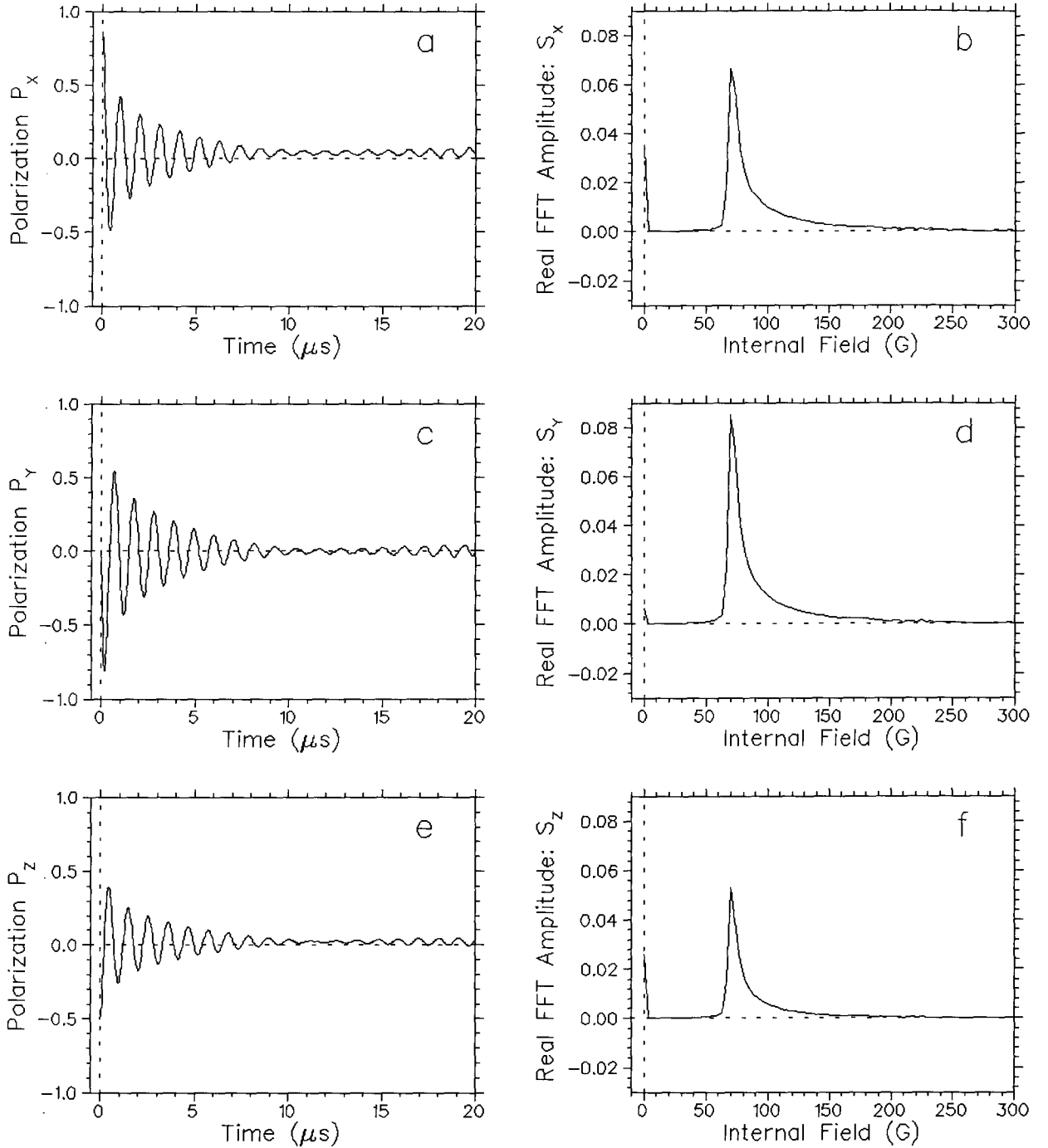


Figure 3.2: Figs. a, c and e show the polarization projections P_X , P_Y and P_Z respectively for an ensemble of muons in an anisotropic superconductor (chains model) with $\bar{\lambda}^{-2} = 20 \mu\text{m}^{-2}$ and $\Gamma = 5$ in a field of 100 G applied at an angle $\theta = 30^\circ$ with respect to $\hat{c} \parallel \hat{Z}$. The initial muon spin direction is in the \hat{X} - \hat{Z} plane (along \hat{x}) perpendicular to the average internal field: $\hat{P}(0) = \hat{x}$. Figs. b, d and f show the corresponding Fourier transforms (with the muon gyromagnetic ratio removed) S_X ($\frac{\gamma\mu}{2\pi}B$), S_Y ($\frac{\gamma\mu}{2\pi}B$) and S_Z ($\frac{\gamma\mu}{2\pi}B$). Notice that at long times the average values for $P_X(t)$ and $P_Z(t)$ are non-zero while S_X ($\frac{\gamma\mu}{2\pi}B$) and S_Z ($\frac{\gamma\mu}{2\pi}B$) have large zero-frequency peaks.

3.3.3 Basics of a μ SR FFT Program

I will not go into the details of the Fast Fourier Transform algorithm (for a complete description, see Ch. 12 of Ref. [54]). However, it is worthwhile to review a few features of discrete Fourier transforms as applied to μ SR. The experimental μ SR data is stored discretely, using time binning (δt) over a finite time range (0 to T_{\max}). This gives a resolution, or frequency bin size, of $\delta\nu = 1/(2T_{\max})$ and a maximum observable frequency of $\nu_{\max} = 1/(2\delta t)$ in the Fourier transform. Note that as the time bin size increases, the range of frequencies in the transform decreases.

The following is a list of features that all μ SR FFT programs should have:

Random background subtraction: Remove the random background obtained either from histogram bins at times less than $t = 0$ or by numerical analysis of the raw time spectrum.

Muon lifetime removal: Remove the muon lifetime from the single counter histograms either by forming a raw asymmetry with two single counter histograms (Eq. 2.18), or by multiplying each single counter histogram by e^{+t/τ_μ} after background subtraction (Eq. 3.2) where τ_μ is the muon lifetime.

Variable zero padding: Extend the time range of the asymmetry histogram by adding empty bins. FFT routines require an array size which is some power of two, so the asymmetry histogram must be padded until the next power of two is reached. If the asymmetry signal has fully relaxed by the end of the time range chosen, or if appropriate apodization is used, padding to an additional power of two has the effect (after overall renormalization) of smoothly interpolating between the Fourier amplitude points (because extending the time range [0 to T_{\max}] decreases the frequency bin size $\delta\nu$). The transform may look nicer, but there really is no additional information. In fact, when fitting the Fourier amplitude (with the error estimated by the standard deviation of the noise in the Fourier transform), the test for goodness of fit (χ^2) will increase artificially with increasing zero padding.

Flattening: Remove any constant and linear terms from the asymmetry histogram before transforming. A constant term represents both the inherent non-oscillatory signals (See Eqs. 3.43,

3.44 and 3.45) as well as the “ α term” or “baseline shift” calculated for a pair of single counter histograms. The α term represents mismatched counter sizes, tube efficiencies, *etc.*, (see Sec. 2.5.1). Removing the constant term reduces the amplitude and width of the spurious zero frequency peak in the Fourier transform. This is especially important for data taken in lower fields. Removing the linear term reduces the effects of “non-random” backgrounds (see Sec. 2.5.2) and helps remove slowly relaxing but non-oscillatory signals.

Phase correction: Correct the real $F_R(\nu)$ and imaginary $F_I(\nu)$ amplitude spectra Fourier transforms (defined in Sec. 3.3.1) for the initial phase ψ (see Eq. 3.24). This phase represents the muon’s precession during its time of flight before its arrival at the sample. Phase correction is essentially the inverse of Eq. 2.76. [$F_R(\nu)$ and $F_I(\nu)$ are related to the amplitude spectrum F_A by $F_A = \sqrt{F_R^2 + F_I^2}$ and to the power spectrum F_P by $F_P = F_R^2 + F_I^2$, which are both independent of ψ .] If the phase correction is done properly, then the real Fourier amplitude will be always positive, except for random noise in regions where the average amplitude is zero. The imaginary Fourier amplitude will be negative for frequencies less than the peak frequency and positive for frequencies greater than the peak frequency or *vice versa* but will have a total area of zero. If there are several frequencies, the imaginary amplitude may go through zero more than once. The phase correction is successful if the asymptotic values of the imaginary amplitude at very small and very large frequencies both go to the same absolute magnitude. The standard deviation of the noise for $F_R(\nu)$ is

$$e_R = \frac{1}{N} \sqrt{\sum_{j=1}^N [F_R(\nu_j) - \overline{F_R(\nu_j)}]^2} \quad (3.56)$$

where the range of N frequencies ν_j sampled excludes those within $\pm\Delta\nu$ (typically 2 MHz) of the peak frequency of the lineshape.

3.3.4 Apodization in FFTs

The “art” of the Fourier transform lies primarily in the choice of *time window* and *apodization*. Apodization (also known as data windowing) is done by multiplying the asymmetry spectrum by a weighting function which varies between one and zero. In this way one can remove early

or, more commonly, late portions of the asymmetry spectrum; this is useful if these portions are dominated by distortions or statistical noise or if the polarization has not completely dephased by the end of the time range. Simply selecting a time window is equivalent to selecting a square apodization function which is one inside the range and zero outside.

When fitting the asymmetry of a fast relaxing (depolarizing) signal directly, one should decrease the bin size and cut down the time window, thereby discarding the irrelevant and *noisy* later portion of the spectrum. Likewise, when performing a Fourier transform, one should cut down the time range either by selecting a smaller time window or by using an apodization function with average width near the size of the time window used when fitting the asymmetry. As the FFT is quite efficient, there is no need to speed it up by adjusting the time bin size. In fact, increasing the bin size reduces the frequency range found by the FFT, which risks inadvertently missing high frequency signals present in the experiment which have a period smaller than the new time bin size.

When a signal does not completely relax before the end of the spectrum's time range, the Fourier transform will exhibit "ringing." This is because discrete finite Fourier transforms presuppose that the spectrum has periodic boundary conditions. Zero padding the end of the spectrum will not fix the problem. Since the ringing is caused primarily by the discontinuity at the end of the time range, it can be greatly reduced by using an apodization function which smoothly changes from one (at $T = 0$) to zero. This forces the signal to be completely damped out by the end of the time range, albeit artificially, hence removing the troublesome discontinuity.

The theoretical polarization function shown in Fig. 3.2 has a time bin size of $\delta t = 0.04 \mu\text{s}$ which allows a maximum observable frequency $\nu_{\text{max}} = 12.5 \text{ MHz}$ (corresponding to a field of 922 G). The time range shown (0 to $t_{\text{max}} = 20 \mu\text{s}$) gives a frequency bin size of $\delta\nu = 0.05 \text{ MHz}$ (corresponding to 3.7 G). The effects of the finite bin size and finite time range are seen primarily as a small tail on the low side of the lineshape (at $\sim 60 \text{ G}$), which theoretically should be infinitely steep for this example. Since the polarization function is almost completely dephased at the end of the time range there is almost no ringing in the Fourier transform.

Apodization can also tame statistical noise. The Fourier transform completely ignores error

bars when calculating the transform, which means that the resulting experimental frequency spectrum is closest to the “true” frequency spectrum (which one would get if one could accumulate an infinite number of events) if the input data has the same statistical error for all points. This is never the case in μ SR due to the exponential decay of the muon. For the single counter histogram

$$N_j(t) = N_o^j e^{-t/\tau_\mu} [1 + A_j(t)] + B_j, \quad (3.57)$$

the statistical error is

$$e_N(t) = \sqrt{N_j(t) + 1} \approx \sqrt{N_o^j} e^{-\frac{1}{2}t/\tau_\mu}. \quad (3.58)$$

Since the asymmetry spectrum has the muon lifetime removed (Eq. 2.18 or Eq. 3.2), the statistical error increases exponentially in time according to

$$e_A(t) \approx \frac{\sqrt{N_o^j e^{-t/\tau_\mu}}}{e^{-t/\tau_\mu}} = \sqrt{N_o^j} e^{+\frac{1}{2}t/\tau_\mu}. \quad (3.59)$$

The asymmetry spectrum will reflect this increasing error with increasing scatter, consequently the Fourier transform will be unduly “noisy” if a long time range is used with no apodization. This suggests that one should apodize with either

$$Q_{\text{err}}(t) = e^{-\frac{1}{2}t/\tau_\mu}, \quad (3.60)$$

which approximately cancels this behavior, or

$$Q_{\text{err}}(t) = \sqrt{\frac{N_o^j + 1}{N_j(t) + 1}} \quad (3.61)$$

which cancels it exactly.

If all one needs from an FFT program are the average frequencies and approximate linewidths of one or more signals, it is not necessary to do anything more sophisticated than what has been presented so far. However, if the details of the lineshape are important, the choice of apodization function becomes very important. In particular, it is important to control the noise level in the Fourier transform. Note that the ratio of the signal to noise in the asymmetry signal at time t is important and not the ratio of the number of events—which is dominated by the muon lifetime—to noise (this will be demonstrated in Figs. 3.4 and 3.5). A single function $Q_{\text{err}}(t) = e^{-\frac{1}{2}t/\tau_\mu}$ will not be ideal for all depolarization rates or for runs with different total numbers of events.

The area under the polarization envelope determines the maximum amplitude of the Fourier lineshape. If the area is reduced by the application of an apodization function, then the amplitude too will be reduced or—from an alternative viewpoint—the linewidth will be increased. This is known as “an artificial broadening due to apodization.” For example, consider a Gaussian polarization function with $\sigma \gtrsim 1/\tau_\mu$ (so that the “signal” has fully decayed in the observable time range which is several times longer than the muon lifetime τ_μ and we can use an infinite-range Fourier transform):

$$\Pi(t) = e^{-\frac{1}{2}\sigma^2 t^2} \exp(i2\pi\nu_o t) H(t) \quad (3.62)$$

where $\nu_o = \frac{\gamma_\mu}{2\pi} B_o$ and $H(t)$ is the Heaviside function (see Sec. 3.3.1.) The polarization envelope $e^{-\frac{1}{2}\sigma^2 t^2}$ has an initial amplitude of 1.0 (at $t = 0$) and an area under the positive side of the envelope of $\sqrt{\pi/(2\sigma^2)}$. If we now apodize the function using a second Gaussian, $Q(t) = e^{-\frac{1}{2}\sigma_a^2 t^2}$, which starts at a value of one and decreases with time, the real portion of the Fourier transform of $\Pi(t)Q(t)$ becomes

$$S(\nu) = \frac{1}{2} n_\nu(\nu) = \sqrt{\frac{\pi}{2(\sigma^2 + \sigma_a^2)}} \exp\left[-\frac{(2\pi)^2(\nu - \nu_o)^2}{2(\sigma^2 + \sigma_a^2)}\right] \quad (3.63)$$

where $\int n_\nu(\nu) d\nu \equiv 1$ and the factor of $1/2$ arises from the use of the Heaviside function. [If the Fourier transform were performed on a projection of the polarization perpendicular to the average field direction, an additional factor of $1/2$ would appear: $S(\nu) = \frac{1}{4} n_\nu(\nu)$. The multiplicative factor is not a practical hindrance, since normalization of the Fourier transform is not generally important.] Note that the area under the envelope of $\Pi(t)Q(t)$ equals the amplitude of $1/2 n_\nu(\nu)$ and *vice versa*. The effect of the apodization is quite small as long as $\sigma_a^2 < \sigma^2$. In general, apodization will create a small distortion of the transform from its “true” lineshape. In the case of ringing, this information is already missing; the transform rings because the polarization is relaxing more slowly than the data’s finite storage time range. Ringing is only significant when the time range is about the same size or shorter as the inverse of the relaxation rate, σ^{-1} .

There is a special class of lineshapes which merits special apodization treatment: those consisting of more than one signal superimposed, where the peak which has the greatest height is both the sharpest and of the least interest. For this class, one should use apodization functions which minimize the distortion of the broad peak without regard to the effects on the sharp peak.

Weak Apodization	Medium Apodization	Strong Apodization
$c_{01} = 0.384093$	$c_{02} = 0.152442$	$c_{03} = 0.045335$
$c_{11} = -0.087577$	$c_{12} = -0.136176$	$c_{23} = 0.554883$
$c_{21} = 0.703484$	$c_{22} = 0.983734$	$c_{43} = 0.399782$

Table 3.1: Constants for Special Apodization

Norton and Beer[56] surveyed the effects of myriad apodization functions upon the first side lobe of the function $(\sin t)/t$ and found the set which caused minimal distortion for a given amount of apodization. Three functions from this set are “weak”, “medium” and “strong”, which use the constants in Table 3.1. For weak apodization the function is

$$Q_{\text{weak}}(t) = (c_{01} + c_{11} + c_{21}) - (c_{11} + 2c_{21})(t/t_{\text{max}})^2 + c_{21}(t/t_{\text{max}})^4, \quad (3.64)$$

where t_{max} is the time range of the spectrum. For medium apodization the function is

$$Q_{\text{medium}}(t) = (c_{02} + c_{12} + c_{22}) - (c_{12} + 2c_{22})(t/t_{\text{max}})^2 + (c_{22}(t/t_{\text{max}})^4. \quad (3.65)$$

For strong apodization the function is

$$\begin{aligned} Q_{\text{strong}}[t] = & (c_{03} + c_{23} + c_{43}) - (2c_{23} + 4c_{43})(t/t_{\text{max}})^2 + (c_{23} + 6c_{43})(t/t_{\text{max}})^4 \\ & - (4c_{43})(t/t_{\text{max}})^6 + c_{43}(t/t_{\text{max}})^8. \end{aligned} \quad (3.66)$$

Fig. 3.3 compares Norton’s and Beer’s apodization functions to Gaussians and exponentials.

At early times, the error bars for μ^+ SR data are small compared to the signal amplitude. At later times, the error bars increase while the signal amplitude decreases and problems with statistical noise arise. The exponential apodization function drops off rapidly at early times, so though it keeps the noise under control, it severely distorts the signal of interest. Of the Norton and Beer functions (strong, medium or weak), the best choice is the one which keeps the statistical scatter in the apodized asymmetry to less than about 10% of the signal amplitude. The ideal apodization function damps out the asymmetry signal just at the end of the time range, thereby avoiding ringing in the Fourier transform while minimizing the loss of signal.

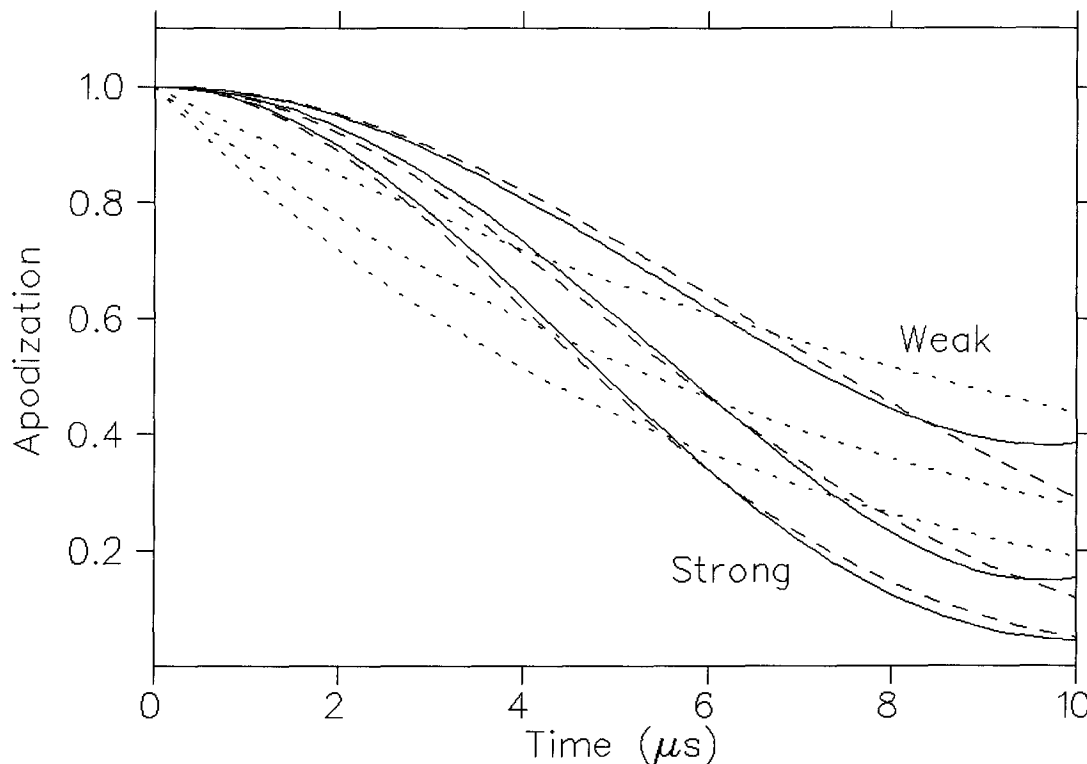


Figure 3.3: For a time range of $10 \mu\text{s}$, “weak”, “medium” and “strong” apodization functions (see Ref. [56]) are shown with solid lines, Gaussians with the same degree of apodization are shown with dashed lines and exponentials are shown with dotted lines.

Norton’s and Beer’s functions are surprisingly close to the versatile Gaussian. This means that we can apodize with Gaussians with very little additional degradation of the lineshape and thereby benefit from simplified interpretation of fits to the lineshape. In particular, Figs. 3.4 and 3.5 show an example of the effects of various Gaussian apodizations, going from too little apodization ($\sigma_a^{-1} = 4$ and $5 \mu\text{s}$) to too much ($\sigma_a^{-1} = 1 \mu\text{s}$). The choice of $\sigma_a^{-1} = 3 \mu\text{s}$ is the best shown.

Notice in Fig. 3.4 that there is a point in the asymmetry at about $7.5 \mu\text{s}$ which is visibly out of line from the rest of the data. This produces the oscillatory noise in the Fourier transform (with period 0.13 MHz) shown in Fig. 3.5. By apodizing with a Gaussian with $\sigma_a^{-1} \leq 3 \mu\text{s}$ the offending point is virtually eliminated from the asymmetry signal along with the corresponding oscillation in the Fourier transform. As the apodization decreases from $\sigma^{-1} = 3 \mu\text{s}$ to $2 \mu\text{s}$ to $1 \mu\text{s}$, oscillations in the tail of the Fourier transform have longer periods and lower amplitudes; this

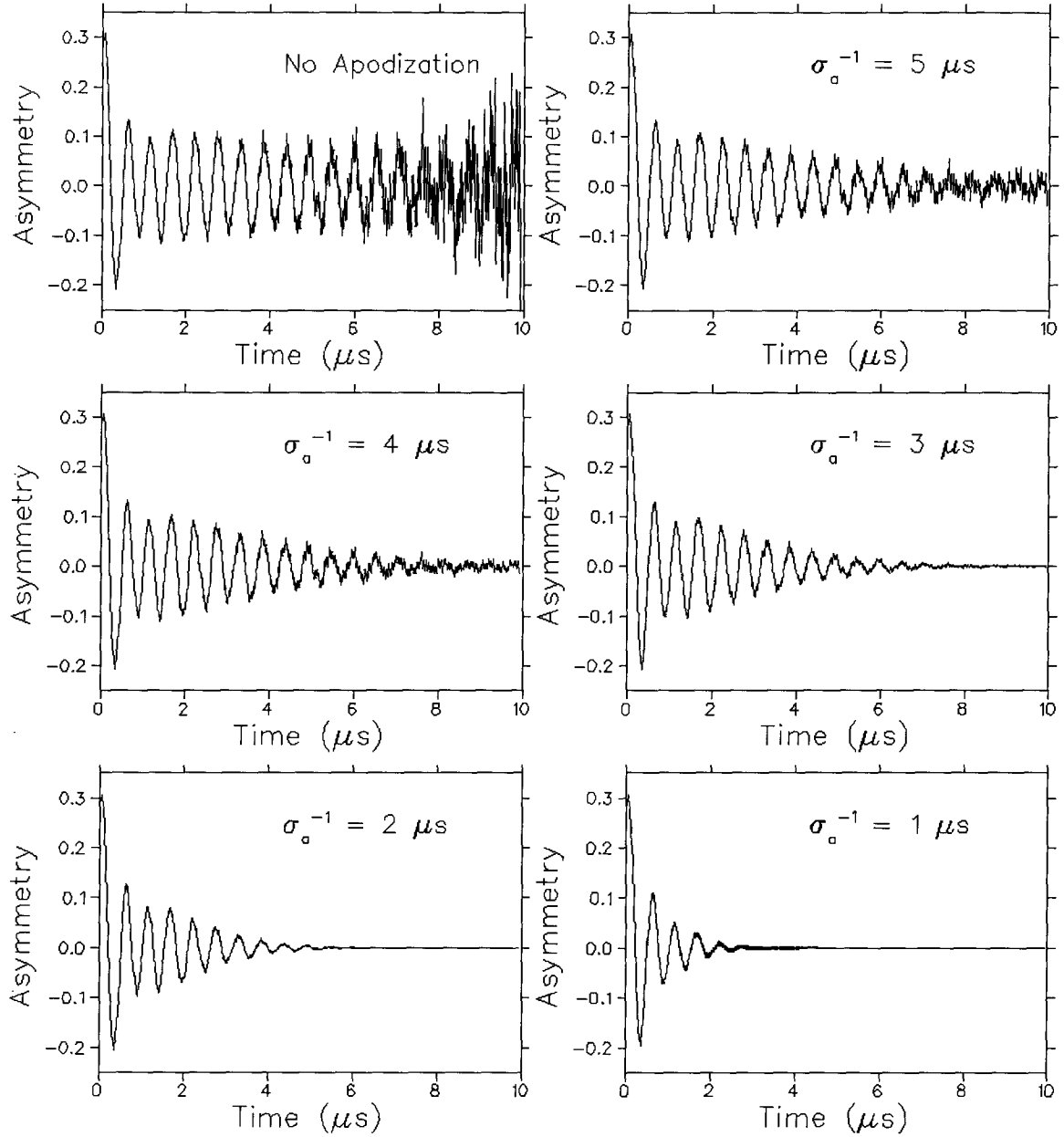


Figure 3.4: The experimental spectrum for YBa₂Cu₃O_{6.95} crystals mounted on silver with $\vec{B} \parallel \hat{c}$ in 0.25 T at 10 K in a RRF of 32.0 Mhz with Gaussian apodization σ_a^{-1} of 1, 2, 3, 4, and 5 μs .

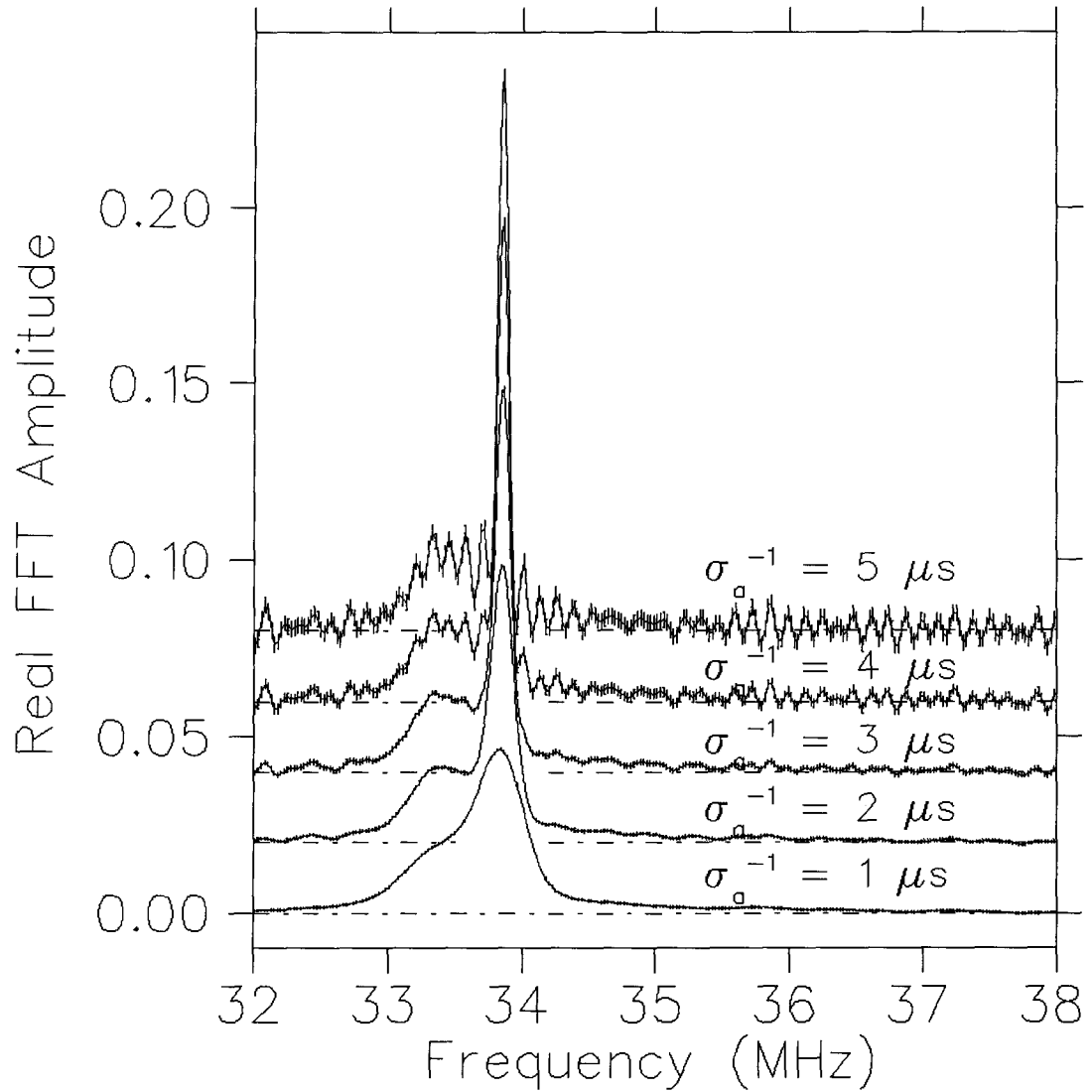


Figure 3.5: The real FFT amplitude for $\text{YBa}_2\text{Cu}_3\text{O}_{6.95}$ crystals mounted on silver with $\vec{B} \parallel \hat{c}$ in 0.25 T at 10 K with Gaussian apodization σ_a^{-1} of 1, 2, 3, 4, and 5 μs . The FFTs were performed over the first 8 μs of data.

reflects the smaller statistical fluctuations in the asymmetry at earlier times. Because apodization with $\sigma_a^{-1} \leq 3 \mu\text{s}$ reduces the amplitude of the asymmetry signal to zero by the end of the time range, the oscillations observed are entirely due to statistical noise and should not be confused with ringing caused by a time window which ends before the signal has gone to zero.

The point at $7.5 \mu\text{s}$ is *not* a “bad bin” due to, for example, the electronic’s histogramming memory mistakenly storing a very high number of events in one bin of the histogram. It is merely representative of the statistical scatter in the number of events recorded. In particular, it is expected that 32% of the points in the asymmetry plot will be more than one standard deviation [$e_A(t)$ in Eq. 3.59] from their expected position and that 5% will be more than two standard deviations away.

Because the statistical error $e_A(t)$ in the asymmetry spectra increases exponentially with time, the signal-to-noise ratio $A_o P_C(t)/e_A(t)$ decreases approximately exponentially with time. Consequently the noise in the Fourier transform will be dominated by oscillations with period ν_n

$$\nu_n = \frac{1}{t_n}, \quad (3.67)$$

where t_n are the times at which there is a data point in the asymmetry which is both more than one standard deviation away from the expected value and has a very low signal-to-noise ratio. (In contrast, a signal which has errors *independent* of time will produce random [or white] noise in its Fourier transform.) A single counter histogram, which is dominated by the muon lifetime, will have errors which decrease with longer times. Is the Fourier transform of a single histogram better in any sense than that of the asymmetry plot? No. The lineshape arising from the distribution of muon precession frequencies will be superimposed on the Lorentzian centered at zero frequency representing the muon lifetime. Phase correction cannot remove the effects of the Lorentzian. The Lorentzian may also be confused with any tail inherent in the lineshape. In addition, it does nothing to reduce the signal-to-noise ratio for the asymmetry signal’s contribution to the single counter histogram.

3.4 Convolution Versus Compounding

3.4.1 Convolution Theorem

In some systems, there may be many sources of local field inhomogeneity which act simultaneously everywhere. For instance, in superconductors there are both dipolar fields produced by the magnetic moments of the nuclei and field variations produced by the presence of a vortex lattice. To fit the data, one must combine the polarization functions for all sources of local field inhomogeneity. In the time domain, simple multiplication (called “compounding” herein) is all that is necessary. In the frequency domain, the corresponding muon frequency distributions must be convoluted.

Consider $\vec{P}(t) \cdot \hat{C}$, the projection of the ensemble muon polarization in the \hat{C} direction, where \hat{C} may be, for instance, \hat{X} , \hat{Y} or \hat{Z} . For the sake of convenience, let us momentarily neglect the fact that $\vec{P}(t)$ is only defined for positive times and that a cosine Fourier transform [to be used with single signal $\vec{P}(t) \cdot \hat{C}$] is more appropriate than a complex Fourier transform (to be used with two signals, the second one of which is $\vec{P}(t) \cdot [\hat{B}_o \times \hat{C}]$). This details of the correct treatment are discussed in great detail in Secs. 3.2.1, 3.3.1 and 3.3.2. The Fourier transform of $P_C(t) = \vec{P}(t) \cdot \hat{C}$ (from Sec. 3.3.2) is

$$S_C(\nu) = \int_{-\infty}^{\infty} [\vec{P}(t) \cdot \hat{C}] H(t) e^{-i2\pi\nu t} dt \quad (3.68)$$

and its inverse is

$$H(t)P_C(t) = \int_{-\infty}^{\infty} S_C(\nu) e^{+i2\pi\nu t} d\nu. \quad (3.69)$$

If the fields are high enough that the linewidth does not overlap zero frequency, the muons will always precess in the same direction (clockwise or counter-clockwise) and it would be legitimate to restrict the integral to positive frequencies.[†]

If one wishes to “smear” the frequency spectrum by some symmetric function $F_{\text{sym}}(\nu)$, one

[†]If the μ SR signal includes negative frequencies, whether due to a field distribution overlapping zero field or due to the inclusion of a muonium signal (which precesses in the opposite sense from the diamagnetic μ^+), the polarization function must include real and imaginary portions with at least two orthogonal counters to record it. The more general treatment (*i.e.*, integration over all frequencies) is necessary for a proper simultaneous Fourier transform—I will ignore such complications in this discussion.

can perform a convolution

$$\{S_C * F_{\text{sym}}\}(\nu) = \int_{-\infty}^{\infty} S_C(\nu') F_{\text{sym}}(\nu - \nu') d\nu'. \quad (3.70)$$

The convolution theorem[54] states that the Fourier transform of the convolution is given by

$$P_C(t) G_{\text{sym}}(t) = \int_{-\infty}^{\infty} \{S_C * F_{\text{sym}}\}(\nu) e^{+i2\pi\nu t} d\nu, \quad (3.71)$$

where $G_{\text{sym}}(t)$ is the Fourier transform of $F_{\text{sym}}(\nu)$. Multiplying the two polarization functions in Eq. 3.71 is known as ‘‘compounding.’’ This means that convolution of two functions in the frequency domain corresponds to simple multiplication in the time domain and *vice versa*. Multiplication is much faster than convolution so there is a preferred domain, ostensibly the time domain. However, when the number of data points is reduced by appropriate choice of binning and RRF frequency in the case of the time domain, or by fitting in a restricted range of frequencies in the frequency domain, the preferred domain depends on the particulars of the problem and the quality of software available. Note that the function which results from a convolution will always have a wider lineshape than either of the original functions. We will assume that a single symmetric function $G_{\text{sym}}(t)$ in the time domain or, alternatively, $F_{\text{sym}}(\nu)$ in the frequency domain, will be adequate for use with all polarization projections.

Consider the symmetric frequency probability distribution $F_{\text{sym}}(\nu)$ which has the property that the average frequency is zero and $F_{\text{sym}}(\nu) = F_{\text{sym}}(-\nu)$. The particular function

$$F_{\text{sym}}(\nu) = \sqrt{\frac{\pi}{2\sigma^2}} e^{-\frac{1}{2}\nu^2/\sigma^2}, \quad (3.72)$$

which has as its Fourier transform $G_{\text{sym}}(t) = e^{-\frac{1}{2}\sigma^2 t^2}$, will be of practical use in this thesis in describing effects such as nuclear dipolar moments and disorder in the flux line lattice. When convoluting lineshapes, it is sometimes useful to ignore the zero-frequency peak in $S(\nu)$ due to the non-oscillatory component $\hat{C} \cdot \vec{P}(t \rightarrow \infty)$. In the time domain this corresponds to compounding the polarization signal relative to the non-oscillatory portion of $P_C(t)$ (see Eq. 2.77)—that is, separating out the non-oscillatory portion of $P_C(t)$ and then compounding only the oscillatory portion with $G_{\text{sym}}(t)$:

$$\hat{C} \cdot \vec{P}^{\text{comp}}(t) = P_C(t \rightarrow \infty) + [P_C(t) - P_C(t \rightarrow \infty)] G_{\text{sym}}(t). \quad (3.73)$$

The alternative is to compound the entire polarization function

$$\hat{C} \cdot \vec{P}^{\text{comp whole}}(t) = P_C(t)G_{\text{sym}}(t), \quad (3.74)$$

in which case, the “non-oscillatory” portion

$$\vec{P}_{\parallel}^{\text{comp whole}}(t) = P_C(t \rightarrow \infty)G_{\text{sym}}(t) \quad (3.75)$$

is *no longer* independent of time and the compounded polarization function as a whole must have an asymptotic value of *zero*. Depending on the physical system being described, either one of these two approaches may be more appropriate. A preference for the first compounding approach (Eq. 3.73) within the context of this thesis is justified in Sec. 4.8.

Suppose that $S_C(\nu)$ is a lineshape which has non-zero values *only* for $\nu > 0$ with its lowest significant frequency component many times larger than $\sigma/(2\pi)$. From Eq. 2.76, the projection along \hat{C} of the compounded polarization vector $\vec{P}^{\text{comp}}(t)$ with phase ψ can be expressed in terms of the polarization functions $\vec{P}_{\parallel}(t; \hat{P}_o = \hat{x})$ and $\vec{P}_{\parallel}(t; \hat{P}_o = \hat{y})$ if the initial polarization is perpendicular to the average field ($\phi = \pi/2$):

$$\begin{aligned} P_C(t) &= \hat{C} \cdot \left[\vec{P}_{\parallel}(t; \hat{P}_o = \hat{x}) + \vec{P}_{\perp}(t; \hat{P}_o = \hat{x}) \right] \cos \psi \\ &\quad + \hat{C} \cdot \left[\vec{P}_{\parallel}(t; \hat{P}_o = \hat{y}) + \vec{P}_{\perp}(t; \hat{P}_o = \hat{y}) \right] \sin \psi \end{aligned} \quad (3.76)$$

From Eq. 2.77, the compound function $P_C^{\text{comp}}(t)$ for $P_C(t)$ and the symmetric function $G_{\text{sym}}(t)$ can be expressed relative to the non-oscillatory portion $P_C(t \rightarrow \infty)$ as

$$\begin{aligned} P_{C, \phi=\pi/2}^{\text{comp}}(t) &= \hat{C} \cdot \vec{P}_{\parallel}(t; \hat{P}_o = \hat{x}) \cos \psi + \hat{C} \cdot \vec{P}_{\parallel}(t; \hat{P}_o = \hat{y}) \sin \psi \\ &\quad + G_{\text{sym}}(t) \hat{C} \cdot \left\{ \vec{P}_{\perp}(t; \hat{P}_o = \hat{x}) \cos \psi + \vec{P}_{\perp}(t; \hat{P}_o = \hat{y}) \sin \psi \right\}. \end{aligned} \quad (3.77)$$

Fig. 3.6.a shows the polarization projection $P_X(t)$ for an ensemble of muons in an anisotropic superconductor. Fig. 3.6.b shows the Fourier transform $S_X(B)$ with the muon gyromagnetic ratio removed and with phase correction. In Fig. 3.6.c, $P_X(t)$ is compounded with a second function,

$$G_{\text{sym}}(t) = e^{-\frac{1}{2}(\gamma_{\mu}\delta_B t)^2} = e^{-\frac{1}{2}(2\pi\delta_{\nu} t)^2} = e^{-\frac{1}{2}(\sigma t)^2} \quad (3.78)$$

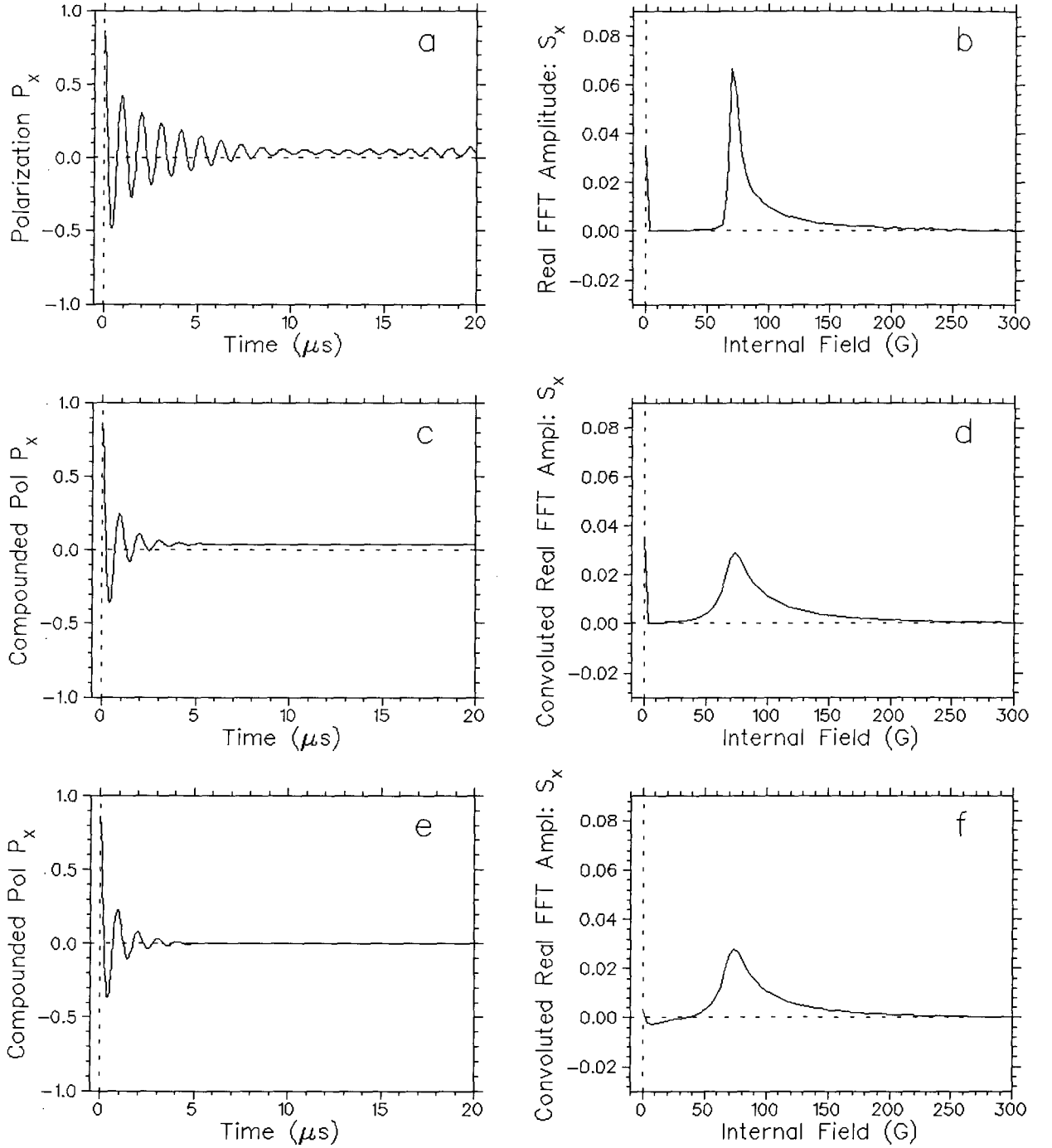


Figure 3.6: Fig. a shows the polarization projection $P_X(t)$ and Fig. b shows the corresponding Fourier transform $S_X(B)$ for an ensemble of muons in an anisotropic superconductor (chains model) with $\bar{\lambda}^{-2} = 20 \mu\text{m}^{-2}$ and $\Gamma = 5$ in a field of 100 G applied at an angle $\theta = 30^\circ$ with respect to $\hat{c} \parallel \hat{Z}$. The initial muon spin direction is in the \hat{X} - \hat{Z} plane (along \hat{x}) perpendicular to the average internal field: $\hat{P}(0) = \hat{x}$. Figs. c and d show the same pair with Gaussian smearing of the oscillatory portion only, while Figs. e and f show them with smearing of both the oscillatory and non-oscillatory signals.

where $\delta_B = 11$ G, $\sigma = 0.937 \mu\text{s}^{-1}$ and $\frac{\gamma_\mu}{2\pi} = 0.01355342$ MHz/G, relative to the non-oscillatory portion of the signal. The Fourier transform of this compounded signal is shown in Fig. 3.6.d; it is the convolution of the superconductor lineshape excluding the zero frequency peak with the function $F_{\text{sym}}(B) = \sqrt{\pi/(2\delta_B)} e^{-\frac{1}{2}(B/\delta_B)^2}$. [The transform could have been shown in terms of frequency using $F_{\text{sym}}(\nu) = \sqrt{\pi/(2\delta_\nu)} e^{-\frac{1}{2}(\nu/\delta_\nu)^2}$ by changing the values and units displayed on the internal field axis.] Fig. 3.6.e shows the same compounding relative to zero and Fig. 3.6.f shows the same convolution including the zero-frequency peak.

Compounding relative to the non-oscillatory signal is legitimate when the rms deviation δb_{sym} of the local field produced by the symmetric frequency distribution,

$$\delta b_{\text{sym}} = \frac{2\pi}{\gamma_\mu} \sqrt{\frac{\int_{-\infty}^{\infty} \nu^2 F_{\text{sym}}^2(\nu) d\nu}{\int_{-\infty}^{\infty} F_{\text{sym}}(\nu) d\nu}}, \quad (3.79)$$

is much smaller than both the average field B_o of the asymmetric distribution,

$$B_o = \frac{2\pi}{\gamma_\mu} \frac{\int_{-\infty}^{\infty} \nu n_\nu(\nu) d\nu}{\int_{-\infty}^{\infty} n_\nu(\nu) d\nu}, \quad (3.80)$$

and the rms deviation δb_a of the local field of the asymmetric frequency distribution

$$\delta b_a = \frac{2\pi}{\gamma_\mu} \sqrt{\frac{\int_{-\infty}^{\infty} (\nu - \frac{\gamma_\mu B_o}{2\pi})^2 n_\nu(\nu) d\nu}{\int_{-\infty}^{\infty} n_\nu(\nu) d\nu}}. \quad (3.81)$$

Remember that the component frequency distributions $S_X(\nu)$, $S_Y(\nu)$ and $S_Z(\nu)$ describe the probabilities of *observing* a muon precession frequency ν in the counters along the \hat{X} , \hat{Y} or \hat{Z} axis; in general, they are *not* proportional to the probability $n_\nu(\nu)$ of there being a local field magnitude B which produces a muon precession frequency of $\nu = \frac{\gamma_\mu}{2\pi} B$. See Secs. 2.6.4, 2.6.5 and 3.3.2 for a detailed discussion of when they are proportional to $n_\nu(\nu)$ or nearly so.

To reduce the cost of convoluting two functions, one can transform them into the time domain, multiply and transform the result back into the frequency domain. To avoid “wrap around pollution” from the periodic boundary conditions assumed by the Fourier transform, one should zero pad each of the original functions to at least the sum of their number of bins beforehand (see Ref. [54, Sec. 12.4]). If the numbers of bins for the two functions are not comparable, it may be cheaper to convolute directly.

Chapter 4

Anisotropic London Theory

4.1 Treatment of Anisotropy

The copper-oxide based high temperature superconductors have a layered structure, with planes of copper and oxygen separated by other atoms. (See Ch. 4 in Ref. [57] for an overview of the chemical structure of copper-oxide based high temperature superconductors.) The superconducting carriers move easily within a copper-oxygen plane but they have difficulty moving from one plane to the next. This accounts for the highly anisotropic behavior of the high- T_c superconductors.

If the separation of superconducting layers (*e.g.*, the copper oxygen planes in high T_c superconductors) is smaller than the coherence length ξ_c of the Cooper pairs in that direction, the superconductor can be treated as an anisotropic 3-dimensional superconductor. The Ginzburg-Landau (GL) formalism remains similar to that described in Sec. 1.1 but with the electron mass replaced by a mass tensor describing the ‘degree of difficulty’ with which the superconducting carriers move in different directions within the superconductor. When one uses a mass tensor, both the magnetic penetration depth and the coherence length become tensors as well. If the inter-layer separation is larger than the coherence length in the \hat{c} direction, the superconductor is more accurately described as a series of weakly coupled 2-dimensional superconducting layers. A generalization of the GL formalism to this situation was obtained by Lawrence and Doniach.[58] They treated the superconductor as a stack of Josephson-coupled superconducting layers. More precisely, the use of a mass tensor is valid in a layered superconductor which has an interlayer spacing of s when the coherence length perpendicular to the layers (ξ_c) exceeds $s/\sqrt{2}$. [58,59] In pre-high T_c studies,[60] NbSe₂, which has a layered chemical structure, was shown to act as an anisotropic 3-D superconductor while TaS₂ intercalated with aniline acted 3-dimensionally near

T_c but showed evidence of 2-D behavior at lower temperatures.

Many of the copper oxide-based high temperature superconductors, such as $\text{Bi}_2\text{Sr}_2\text{CaCu}_2\text{O}_{8+\delta}$ and $\text{Tl}_2\text{Ba}_2\text{CaCu}_2\text{O}_8$, are extremely anisotropic and probably meet the criterion for the applicability of the Lawrence-Doniach description for all temperatures below a small range of temperatures near T_c . However, $\text{YBa}_2\text{Cu}_3\text{O}_{7-\delta}$, which has an anisotropy in the magnetic penetration depth of approximately 5, is likely to be in the 3-D regime for all or almost all temperatures. The chemical unit cell height is 11.7 \AA and the distance between copper-oxide planes on either side of the yttrium layer is 3.9 \AA [61] in $\text{YBa}_2\text{Cu}_3\text{O}_{7-\delta}$. Using an anisotropy of 5 found in Ch. 5 and $\xi_{ab} = 19 \text{ \AA}$ found in Ch. 7, I estimate $\xi_c \simeq 3.8 \text{ \AA}$ at 10 K which just barely places it in the 3-D regime for all temperatures. On the other hand, torque measurements of $\text{YBa}_2\text{Cu}_3\text{O}_{7-\delta}$ [62] suggest that there is a crossover from 3-D to 2-D behavior roughly 10 K below T_c . Lawrence-Doniach theory for Josephson-coupled layered superconductors, being more complicated than anisotropic London theory, has only been developed for fields applied along one of the crystallographic axes of the sample; in the absence of a complete theory and with uncertainty in the temperature at which it would come into effect, this thesis assumes that the 3-D effective mass tensor applies for $\text{YBa}_2\text{Cu}_3\text{O}_{6.95}$.

4.2 Derivation of the Anisotropic London Model

In this section, I present a derivation published by V.G. Kogan[63] for a uniaxial anisotropic superconductor, with a few of the omitted steps filled in.

In the London approximation, the total energy of an anisotropic superconductor * is given by

$$8\pi E = \int \left[B^2 + \lambda^2 m_{ij} (\nabla \times B)_i (\nabla \times B)_j \right] d\vec{r}, \quad (4.1)$$

where λ is the average London penetration depth

$$\lambda = \sqrt{\frac{\bar{M}c^2}{4\pi n_s e^2}}, \quad (4.2)$$

*Eq. 4.1 can be derived from the Ginzburg-Landau equations by assuming that the magnitude of the order parameter is constant but the phase depends on position. Although Ginzburg-Landau theory is valid only near T_c , the London approximation is valid over a much wider range of temperatures and fields.

\bar{M} is the average mass of the charge carrier, with its anisotropy given by the normalized effective mass tensor of the carriers, m_{ij} :

$$M_{ij} = \bar{M} m_{ij} = \bar{M} \begin{vmatrix} m_{xx} & m_{xy} & m_{xz} \\ m_{xy} & m_{yy} & m_{yz} \\ m_{xz} & m_{yz} & m_{zz} \end{vmatrix}, \quad \text{where } Tr(m_{ij}) = 1 \quad (4.3)$$

and M_{ij} is the carrier mass tensor itself. In the crystal frame of the superconductor \hat{a} - \hat{b} - \hat{c} , the mass tensor is given by

$$m_{ij} = \begin{vmatrix} m_1 & 0 & 0 \\ 0 & m_2 & 0 \\ 0 & 0 & m_3 \end{vmatrix}. \quad (4.4)$$

Our model uses a layered superconductor in which the \hat{a} and \hat{b} crystal directions are equivalent ($m_1 = m_2$) and the \hat{c} axis is the hard direction ($m_3 \gg m_1$). The ratio of the magnetic penetration depths for the principal axes is

$$\Gamma \equiv \frac{\lambda_c}{\lambda_{ab}} = \sqrt{\frac{m_3}{m_1}} \quad (4.5)$$

Let us assume that the average field \vec{B}_o is along the \hat{z} axis, which makes an angle θ with the \hat{c} axis (see Fig. 4.1). Since we are considering a uniaxial superconductor, we can take the \hat{y} axis as fixed relative to one of the crystal axes (\hat{b}). Therefore, the rotation matrix is

$$R(\theta) = \begin{vmatrix} \cos \theta & 0 & \sin \theta \\ 0 & 1 & 0 \\ -\sin \theta & 0 & \cos \theta \end{vmatrix}. \quad (4.6)$$

The rotated mass tensor is

$$m_{ij}(\theta) = R^{-1} m_{ij}(0) R \quad (4.7)$$

or, more explicitly,

$$m_{ij}(\theta) = \begin{vmatrix} m_1 \cos^2 \theta + m_3 \sin^2 \theta & 0 & (m_1 - m_3) \sin \theta \cos \theta \\ 0 & m_1 & 0 \\ (m_1 - m_3) \sin \theta \cos \theta & 0 & m_3 \cos^2 \theta + m_1 \sin^2 \theta \end{vmatrix}. \quad (4.8)$$

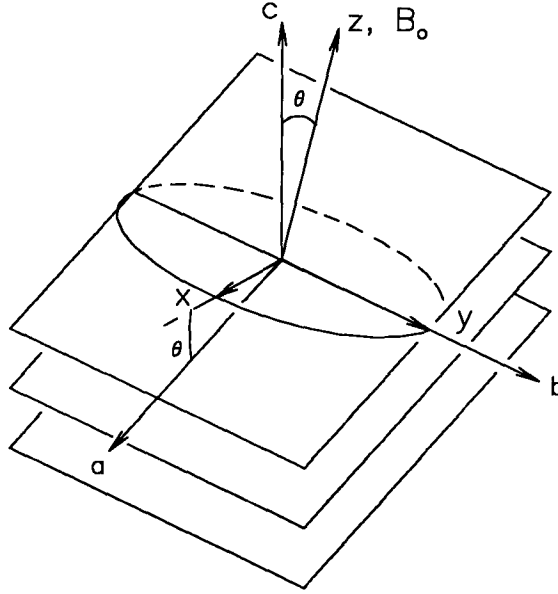


Figure 4.1: Coordinate and crystal axes; θ is the rotation of the crystal's hard axis \hat{c} with respect to the coordinate axis \hat{z} .

Minimizing the energy gives the London equations

$$B_i - \lambda^2 \sum_{jklst} m_{kl} \epsilon_{lsi} \epsilon_{ktj} \frac{\partial^2 B_j}{\partial x_s \partial x_t} = \begin{cases} \phi_o \sum_v \delta(\vec{r} - \vec{r}_v) & H_{c1}(T, \theta) < B_o < H_{c2}(T, \theta) \\ 0 & B_o < H_{c1}(T, \theta) \end{cases}, \quad (4.9)$$

where the penetration depth is defined by $\lambda_{ij}^2 = \lambda^2 m_{ij}$ and the sum over v is restricted to a unit area ($1 \mu\text{m}^2$ if ϕ_o is in units of $\text{G}\mu\text{m}^2$) to ensure normalization in this choice of units. The constant ϕ_o is the flux quantum for a Cooper pair of two carriers each with charge $q = e$

$$\phi_o = \frac{c(2\pi\hbar)}{2q} = 20.6785 \text{ G}\mu\text{m}^2, \quad (4.10)$$

where \hbar is Planck's constant. In a type II superconductor above $H_{c1}(T)$, the magnetic field penetrates partially inside the superconductor by forming vortices (or flux lines). These vortices correspond to locations in the material where the magnitude of the order parameter vanishes but the phase varies by 2π along a closed contour encircling the vortex. As a result, the "charge" carried by each singularity in the order parameter is quantized, *i.e.*, each vortex carries exactly one flux quantum, ϕ_o . Because the London approximation averages over the spatial variations of the magnitude of the order parameter, the size of the vortex core is effectively zero, *i.e.*, the

vortex is reduced to a point singularity described by the delta function on the right hand side of Eq. 4.9. The energy of the superconductor is minimized when the vortices form a regular triangular lattice.[64]

Whether the superconductor is type I (no singularities) or type II (with singularities when $H_{c1}(T) < B_o < H_{c2}(T)$) depends upon its lowest energy state — more specifically, whether

$$\kappa \equiv \lambda/\xi \begin{cases} \leq 1/\sqrt{2} & \text{type I} \\ > 1/\sqrt{2} & \text{type II.} \end{cases} \quad (4.11)$$

The symbol ξ stands for the coherence length, which is the typical length scale over which the superconducting Cooper pairs of electrons or holes are correlated. The high temperature superconductor $\text{YBa}_2\text{Cu}_3\text{O}_{7-\delta}$ has κ of the order of 55[5] to 77,[6] which is well within the type II regime.

Ultimately, we would like to determine the distribution of the magnetic field in type II superconductors (isotropic and anisotropic) from the spectral distribution of the muon precession frequencies and thus determine the magnetic penetration depth λ . With the goal of calculating the field everywhere in the superconductor (neglecting edge effects), we apply the Fourier transform to the London equation for a superconductor in the type II state (Eq. 4.9). The Fourier transform is continuous, but the result will be a discrete summation due to the lattice of singularities on the right hand side of Eq. 4.9. Assuming that the flux lines are along the \hat{z} direction,

$$\begin{aligned} B_x(\vec{r}) &= \lambda^2 \left[m_{zz} \left(\frac{\partial^2 B_x}{\partial y^2} - \frac{\partial^2 B_y}{\partial x \partial y} \right) - m_{xz} \left(\frac{\partial^2 B_z}{\partial y^2} \right) \right] \\ B_y(\vec{r}) &= \lambda^2 \left[m_{xz} \left(\frac{\partial^2 B_z}{\partial x \partial y} \right) + m_{zz} \left(\frac{\partial^2 B_y}{\partial x^2} - \frac{\partial^2 B_x}{\partial x \partial y} \right) \right] \\ B_z(\vec{r}) &= \lambda^2 \left[m_{11} \left(\frac{\partial^2 B_z}{\partial x^2} \right) + m_{xx} \left(\frac{\partial^2 B_z}{\partial y^2} \right) + m_{xz} \left(-\frac{\partial^2 B_x}{\partial y^2} + \frac{\partial^2 B_y}{\partial x \partial y} \right) \right] \\ &\quad + \phi_o \sum_v \delta(\vec{r} - \vec{r}_v). \end{aligned} \quad (4.12)$$

Using $\nabla \cdot \vec{B}(\vec{r}) = 0$ and assuming that $\partial B_z(\vec{r})/\partial z = 0$, this can be rewritten as

$$\begin{aligned} B_x(\vec{r}) &= \lambda^2 \left[m_{zz} \Delta B_x - m_{xz} \left(\frac{\partial^2 B_z}{\partial y^2} \right) \right] \\ B_y(\vec{r}) &= \lambda^2 \left[+m_{zz} \Delta B_y + m_{xz} \left(\frac{\partial^2 B_z}{\partial x \partial y} \right) \right] \end{aligned}$$

$$B_z(\vec{r}) = \lambda^2 \left[m_1 \left(\frac{\partial^2 B_z}{\partial x^2} \right) + m_{xx} \left(\frac{\partial^2 B_z}{\partial y^2} \right) + m_{xz} \Delta B_x \right] + \phi_o \sum_v \delta(\vec{r} - \vec{r}_v), \quad (4.13)$$

where $\Delta \equiv \partial^2/\partial x^2 + \partial^2/\partial y^2$.

Let us suppose that there is a regular flux line lattice with the v^{th} vortex at position \vec{r}_v in the \hat{x} - \hat{y} plane. In the course of taking the Fourier transform we remove the term $e^{i\vec{k} \cdot \vec{r}_v}$ by only allowing $\vec{k} \in \{\vec{K}\}$, where $\{\vec{K}\}$ is the set of reciprocal lattice vectors for \vec{r}_v . The number of flux tubes per unit area in the \hat{x} - \hat{y} plane is defined as n_f . The anisotropic treatment produces the following Fourier components of the local field (*i.e.* the spatial Fourier transforms of the three components in Eq. 4.13),

$$\begin{aligned} B_x(\vec{K}) &= n_f \phi_o (\lambda^2 m_{xz} K_y^2) / d \\ B_y(\vec{K}) &= -n_f \phi_o (\lambda^2 m_{xz} K_x K_y) / d \\ B_z(\vec{K}) &= n_f \phi_o (1 + \lambda^2 m_{zz} K^2) / d \end{aligned} \quad (4.14)$$

where

$$d = (1 + \lambda^2 m_{yy} K_x^2 + \lambda^2 m_{xx} K_y^2)(1 + \lambda^2 m_{zz} K^2) - (\lambda^2 m_{xz} K_x K_y)^2 \quad (4.15)$$

and

$$K^2 = K_x^2 + K_y^2. \quad (4.16)$$

Here n_f is the areal density of vortex cores. Since each vortex carries a flux quantum $\phi_o = 20.7 \text{ G}\mu\text{m}^2$, the average internal field is $B_o = n_f \phi_o$ and B_o is equal to the applied field (H_o) in the absence of any flux exclusion. The total local field at a point $\vec{r} = (x, y)$ is

$$\vec{B}(\vec{r}) = \text{Re} \sum_{\vec{K}} \vec{B}(\vec{K}) e^{-i\vec{K} \cdot \vec{r}} \quad (4.17)$$

where $\vec{B}(\vec{K}) = B_x(\vec{K})\hat{x} + B_y(\vec{K})\hat{y} + B_z(\vec{K})\hat{z}$.

In the case of an isotropic superconductor, $m_{kl} = \delta_{kl}$ and Eq. 4.14 reduces to

$$\begin{aligned} B_x(\vec{K}) &= 0 \\ B_y(\vec{K}) &= 0 \\ B_z(\vec{K}) &= \frac{n_f \phi_o}{(1 + \lambda^2 K^2)}. \end{aligned} \quad (4.18)$$

If there were only a single, isolated flux line at the origin ($\vec{r}_o = 0$), there would be no restriction on \vec{k} since

$$e^{i\vec{k}\cdot\vec{r}_o} = e^0 \equiv 1. \quad (4.19)$$

In this case, all the summations would be replaced with integrals, giving a modified Bessel function for the local field as an approximate solution

$$\vec{B}(\vec{r}) \approx B(\vec{r})\hat{z} \propto K_0 \left(\left\{ \frac{x}{\lambda\sqrt{m_{yy}}} \right\}^2 + \left\{ \frac{y}{\lambda\sqrt{m_{xx}}} \right\}^2 \right). \quad (4.20)$$

Fig. 4.2 shows a single vortex for $\theta = 90$ and $\theta = 0$. Note that the subscripts of the penetration depth are defined by the direction of the superconducting current, *i.e.*, the exponential decay of the magnetic field in the \hat{y} direction is produced by supercurrents in the \hat{x} direction (j_{xx}) and the decay constant is given by the penetration depth λ_{xx} . In these two cases, the supercurrents are only in the x - y plane; when the average field is not along one of the crystalline axes, the supercurrents are in a plane which is tilted relative to x - y . [65]

Notice that in the isotropic case the local field is parallel to the applied field, while in the anisotropic case there are transverse components of the local field which can be quite substantial. Physically this is because the screening currents, discouraged by the poor carrier coupling along the \hat{c} axis, tend to flow in the \hat{a} - \hat{b} planes rather than always perpendicular to the applied field.

4.3 Choice of Reciprocal Lattice

The tensor behavior of the effective mass tensor also gives rise to the effect that for a single vortex, the \hat{z} component of the local field will be *negative* at certain positions far from the vortex core [66,67] when the applied field is not along one of the crystal's principal axes. If a second vortex is added, [67,68,69] the two will mutually repel if both are placed along the \hat{y} axis as they both have positive values for $B_z(\vec{r})$. The second one will prefer to situate itself along the \hat{x} direction in the position of the maximum negative value of single vortex's $B_z(\vec{r})$. This is essentially an angular dependent attractive force between vortices along certain directions that is not present in the isotropic case. At very high vortex densities, this attractive effect along \hat{x} becomes negligible

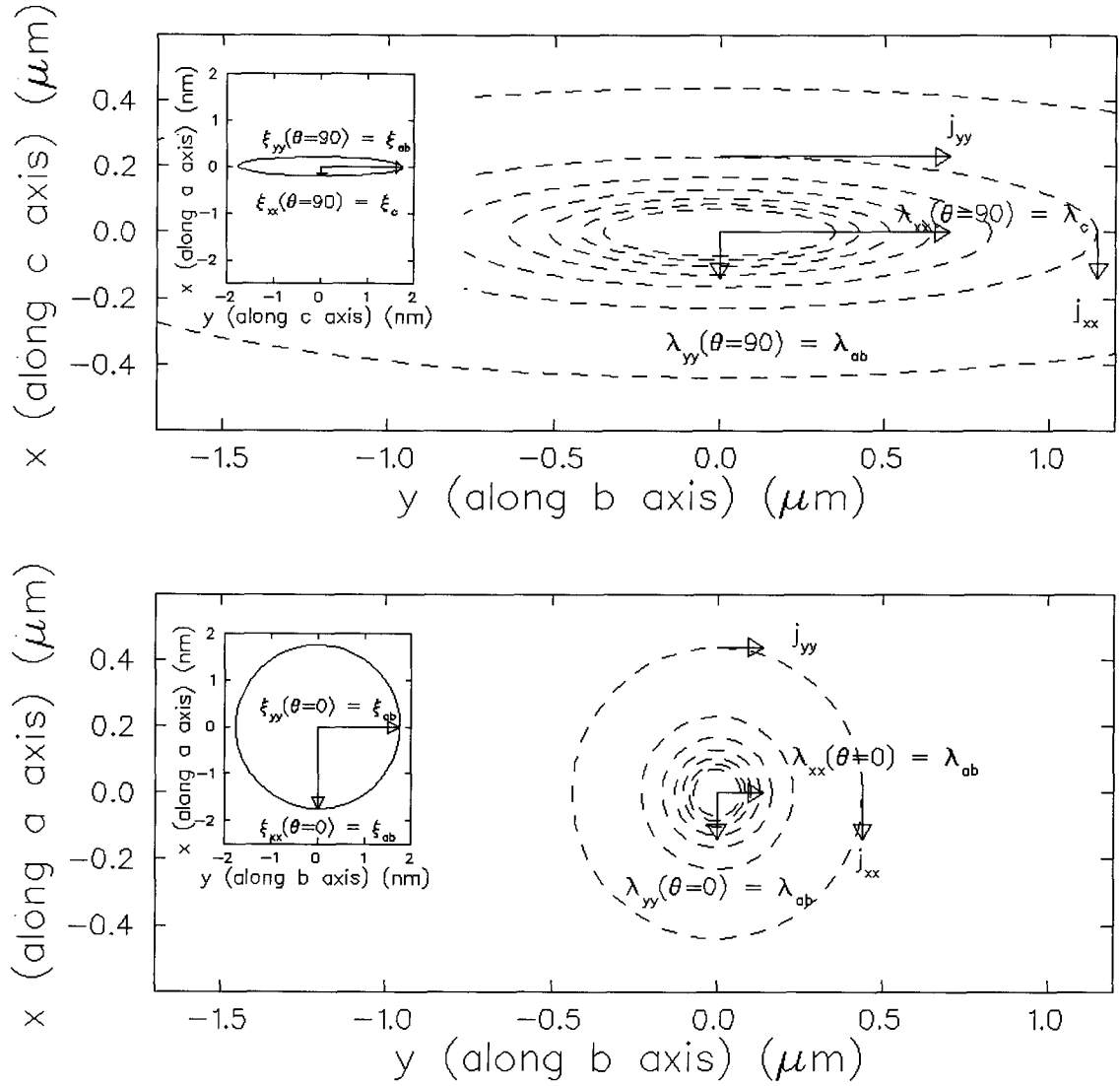


Figure 4.2: Magnetic penetration depths are shown in the \hat{x} - \hat{y} plane, for $\theta = 90^\circ$ (top) and $\theta = 0^\circ$ (bottom). The direction of the local current is indicated by j_{xx} and j_{yy} . The case shown corresponds to a magnetic penetration depth in the \hat{a} - \hat{b} plane of $\lambda_{ab} = 0.1400 \mu\text{m}$ and a ratio of $\lambda_c/\lambda_{ab} = 5.0$. The inserts show the approximate size of vortex core, which is an ellipse with axes given by the coherence length. If $\kappa_{ab} = \lambda_{ab}/\xi_{ab} = 80$, then $\xi_{ab} = 1.75 \text{ nm}$ and $\xi_c = 0.305 \text{ nm}$.

and the flux line lattice geometry becomes constant. However, at lower fields, the energy of flux line lattice must be minimized in order to calculate the correct lattice geometry \vec{r}_v .

4.3.1 High Field Limit

In this section, I will discuss the vortex geometry in the high field limit, *i.e.*, when the spatial variation in vortex-vortex attraction/repulsion due to the off-diagonal elements of the effective mass tensor becomes negligible. It is reasonable to assume that the flux tube lattice will be a non-equilateral (*i.e.* isosceles) triangular array. The lowest energy solution has the following set of anisotropic primitive vectors:[70,71]

$$\begin{aligned}\hat{r}_1 &= L_x \hat{x} \\ \hat{r}_2 &= L_x \frac{1}{2} \hat{x} + L_y \frac{\sqrt{3}}{2} \hat{y}.\end{aligned}\quad (4.21)$$

The number of flux tubes per unit area is

$$n_f = \frac{B_o}{\phi_o} = \frac{2}{\sqrt{3}} \frac{1}{L_x L_y} \quad (4.22)$$

for an average internal magnetic field B_o , which equals the applied field H_o in the absence of overall flux exclusion. The distances L_x and L_y are determined by

$$L_x L_y = \frac{2}{\sqrt{3}} \frac{\phi_o}{B_o} \quad (4.23)$$

and by

$$\frac{L_x}{L_y} = \sqrt{\frac{m_{zz}}{m_3}}, \quad (4.24)$$

giving

$$\begin{aligned}L_x &= \left(\frac{2}{\sqrt{3}} \frac{\phi_o}{B_o} \right)^{1/2} \left(\frac{m_{zz}}{m_3} \right)^{1/4} \\ L_y &= \left(\frac{2}{\sqrt{3}} \frac{\phi_o}{B_o} \right)^{1/2} \left(\frac{m_3}{m_{zz}} \right)^{1/4}.\end{aligned}\quad (4.25)$$

If \hat{r}_1 , \hat{r}_2 and \hat{r}_3 are a set of primitive vectors for a Bravais lattice, then the reciprocal lattice vectors \hat{k}_1 , \hat{k}_2 and \hat{k}_3 are generated by[72]

$$\hat{k}_i = \epsilon_{ijk} 2\pi \frac{\hat{r}_j \times \hat{r}_k}{\hat{r}_i \cdot (\hat{r}_j \times \hat{r}_k)}. \quad (4.26)$$

From this, we conclude that the reciprocal lattice's primitive vectors are

$$\begin{aligned}\hat{k}_1 &= 2\pi \left(\frac{1}{L_x} \hat{x} - \frac{1}{L_y} \frac{1}{\sqrt{3}} \hat{y} \right) \\ \hat{k}_2 &= 2\pi \left(\frac{1}{L_y} \frac{2}{\sqrt{3}} \hat{y} \right) \\ \hat{k}_3 &= 2\pi \hat{z}.\end{aligned}\tag{4.27}$$

An arbitrary reciprocal lattice vector \vec{K} is

$$\vec{K} = n\hat{k}_1 + m\hat{k}_2,\tag{4.28}$$

where n and m are integers.

4.3.2 Vortex Chains for Low Fields

The attraction of vortices to each other's minima in $B_z(\theta)$ along the \hat{x} axis[65] gives rise to the formation of "chains"[67,68,69] when a low field is applied at an angle to the superconductor's principal axes. Since the magnetic field due to each vortex adds vectorially, this effect is reduced at higher fields where the high density of vortices washes out the variation of $\vec{B}(\vec{r})$ in the \hat{x} - \hat{y} plane. Calculating the correct flux lattice geometry involves minimizing the energy e (per unit cell of the FLL F_o)

$$e = \frac{1}{8\pi F_o} \sum_{\vec{K}} \left\{ |\vec{B}(\vec{K})|^2 + \lambda^2 [\vec{K} \times \vec{B}(\vec{K})]_i m_{ij} [\vec{K} \times \vec{B}(\vec{K})]_j \right\}\tag{4.29}$$

as a function of $\rho = r_1/r_2$. [67] The sides of the FLL's isosceles triangle of three vortices are defined by

$$\begin{aligned}r_1 &= \left(\frac{\phi_o}{B_o} \frac{\rho}{\sqrt{1 - (\rho/2)^2}} \right)^{1/2} \\ r_2 &= \left(\frac{\phi_o}{B_o} \frac{1}{\rho \sqrt{1 - (\rho/2)^2}} \right)^{1/2}.\end{aligned}\tag{4.30}$$

Fig. 3 in Ref. [67] shows the angular dependence of ρ as a function of angle (0° to 90°) and applied field for an anisotropy of $\Gamma = \lambda_c/\lambda_{ab} = \sqrt{m_3/m_1} = 5$. The average field B in the figure is expressed in the reduced units of $\phi_o/(2\pi\bar{\lambda}^2)$, where $\lambda = (\lambda_{ab}^2\lambda_c)^{1/3}$. Reduced units B of 1.5, 5.0, 10.0, and 50.0 correspond to fields of 86.22, 287.4, 574.8, and 2874.2 G for $\lambda_{ab} = 1400 \text{ \AA}$, $\Gamma = 5$ and $\bar{\lambda} = 2394 \text{ \AA}$.

4.4 Effect of Vortex Core

London theory can be modified to take into account the finite size of the vortex core by cutting off the infinite sum over the reciprocal lattice vectors \vec{K} at values equal to the inverse of the coherence length ($|K_{\max}| \approx 2\pi/\xi$) which gives[73]

$$\vec{B}(\vec{r}) = Re \sum_{\vec{K}} \vec{B}(\vec{K}) \exp(-i\vec{K}\cdot\vec{r}) \exp \left\{ - \left[\xi_{ab}^2 (\vec{K} \times \hat{c})^2 + \xi_c^2 (\vec{K} \cdot \hat{c})^2 \right] \right\}. \quad (4.31)$$

For straight vortices this can be expressed as

$$\vec{B}(\vec{r}) = Re \sum_{\vec{K}} \vec{B}(\vec{K}) \exp(-i\vec{K}\cdot\vec{r}) \exp \left\{ - \left[K_x^2 \xi_{xx}^2 + K_y^2 \xi_{yy}^2 \right] \right\}, \quad (4.32)$$

where the coherence length is given by

$$\xi_{xx} = \xi_{ab} \sqrt{m_{zz}(\theta)/m_3} = \lambda_{zz}/(\kappa_{ab} \sqrt{m_3}) = \xi_c \sqrt{m_{zz}(\theta)/m_1}, \quad (4.33)$$

and

$$\xi_{yy}^2 = \xi_{ab} = \lambda_{ab}/\kappa_{ab} \quad (4.34)$$

where $\kappa_{ab} = \lambda_{ab}/\xi_{ab}$ is the Ginzburg-Landau parameter in the \hat{a} - \hat{b} plane.

The coherence length in the \hat{a} - \hat{b} plane (ξ_{ab}) is a factor of $\sqrt{m_3/m_1} = \Gamma$ larger than the coherence length along the \hat{c} axis (ξ_c) (see Fig. 4.2). The exponential $\exp \left\{ - \left[K_x^2 \xi_{xx}^2 + K_y^2 \xi_{yy}^2 \right] \right\}$ produces a field which smoothly reaches a finite value at the center of the vortex, whereas the unmodified London model diverges logarithmically. This modified London model is valid for $B_o = n_f \phi_o \ll 0.25 H_{c2}$. [74,75]

4.5 The Magnetic Field Distribution and the μ SR Lineshape

4.5.1 Isotropic Case

A triangular FLL for an isotropic superconductor in low field and its corresponding lineshape are shown in Fig. 4.3. The minimum field occurs at the point at the center of the triangle formed by three adjacent vortices. The midpoint between two adjacent vortices is a saddle point in

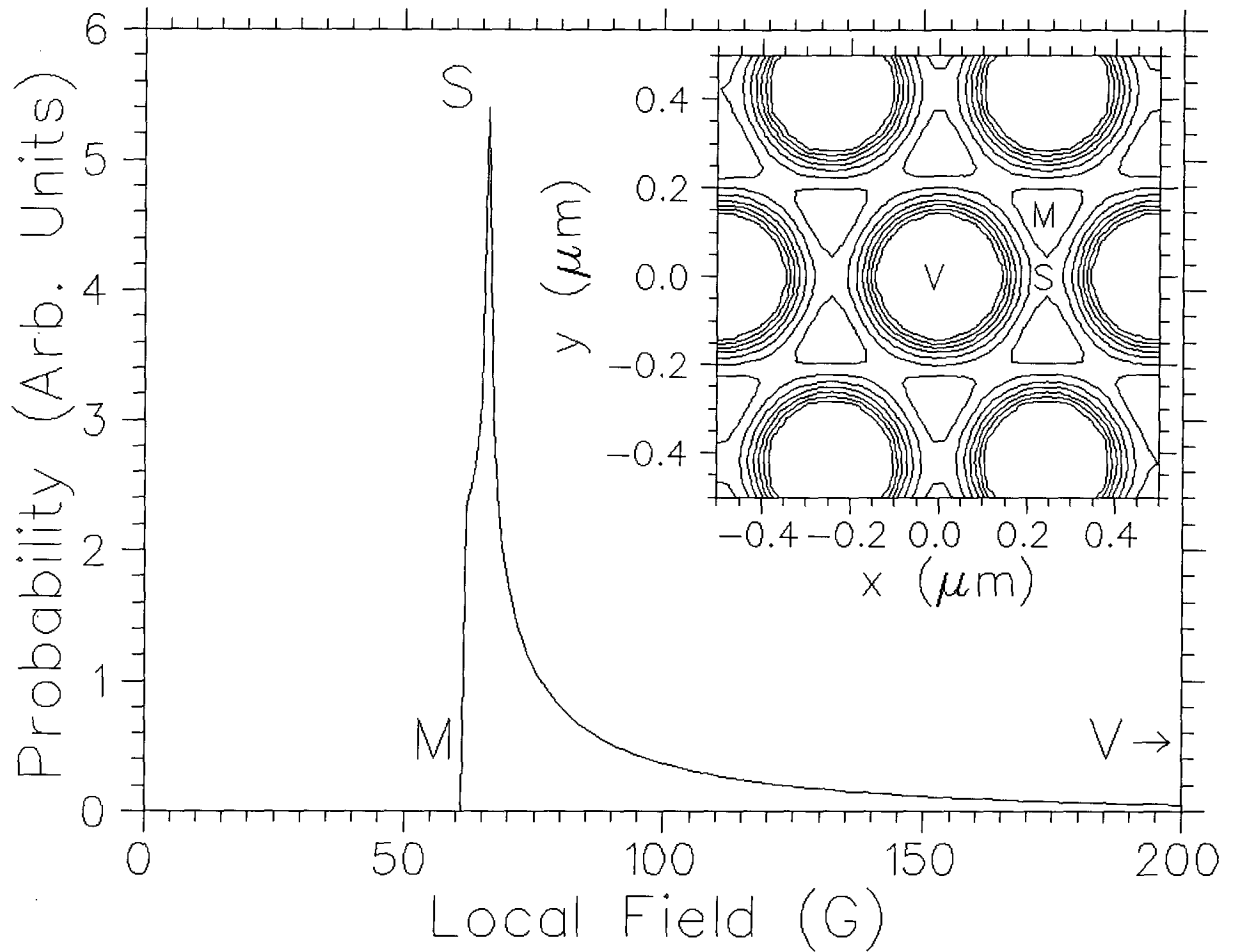


Figure 4.3: The insert shows the FLL unit cell for an isotropic superconductor in the modified London model (Eq. 4.32) with $\kappa = 60$, $\lambda = 0.1318 \mu\text{m}$ and an average field of 100 G, which produces an intervortex spacing of $L = 0.4889 \mu\text{m}$. The contour lines are from 65 G to 100 G. Contours for local fields above 100 G have been left out for clarity. The minimum field (marked “M”) is at the center of the triangle formed by three adjacent vortices. The maximum field (marked “V”, 1037 G) is at the center of the vortex. The saddle point (marked “S”) has the greatest amplitude in the lineshape. The corresponding μSR lineshape is shown in the main figure.

the local field distribution. Because the London equations are linear, the spatial magnetic field distributions due to each of the vortices in the flux line lattice (FLL) can be summed. The probability amplitude for a given field $B \pm \delta B$ in the μ SR lineshape is directly proportional to the area within δB of that field in the FLL, so the density of the field contours about a given field is inversely proportional to the amplitude for that field. The minimum and saddle point fields (B_M and B_S) are in the region where the contour lines are sparse, so they both have a large amplitude in the lineshape. The saddle point field has the largest area within δB so it appears as a cusp (or van Hove singularity) in the lineshape.[75] Both the minimum and maximum fields (B_M and B_V) are seen as vertical cut-offs in the lineshape, reflecting the fact that they are present in the FLL but there is no field beyond. At the minimum field, this cut-off is seen as a “shoulder” since it is in a high amplitude region. From Eq. 4.20 one can see that the field increases rapidly near a vortex core hence the contours are close together. This leads to a high field “tail” in the lineshape which can be easily lost in experimental noise.[76,77] Even though the rate of field change decreases to zero at the vortex core, this region is so small for moderate applied fields that the maximum field has negligible amplitude in the lineshape.

4.5.2 Anisotropic Case

For an anisotropic superconductor with a field applied at an arbitrary angle, the vortices form isosceles triangles rather than equilateral triangles. The field at the saddle point on the short side is different from that on the long sides, which leads to two separate cusps in the lineshape (see Ref. [65] and Figs. 5.2 and 4.4).

Fig. 4.4 shows the total field and the \hat{x} , \hat{y} and \hat{z} components of the local field in an anisotropic superconductor ($\Gamma = 5$, frozen model which assumes Eq. 4.25 rather than Eq. 4.30) with the applied field at an angles of 60° to the crystal’s \hat{c} axis. Note that the components B_x and B_y are non-zero, in contrast to the isotropic case or the anisotropic case with $\theta = 0^\circ$ or 90° . Moreover, the maximum negative value of B_x is associated with the vortex cores [$\vec{r} = (x, y, z) = (0, 0, z)$, etc.] and the maximum positive value of B_x is associated with the region between the \hat{x} -axis “chains” of vortices where there is a relatively low value for the local field’s magnitude $B(\vec{r})$. In contrast,

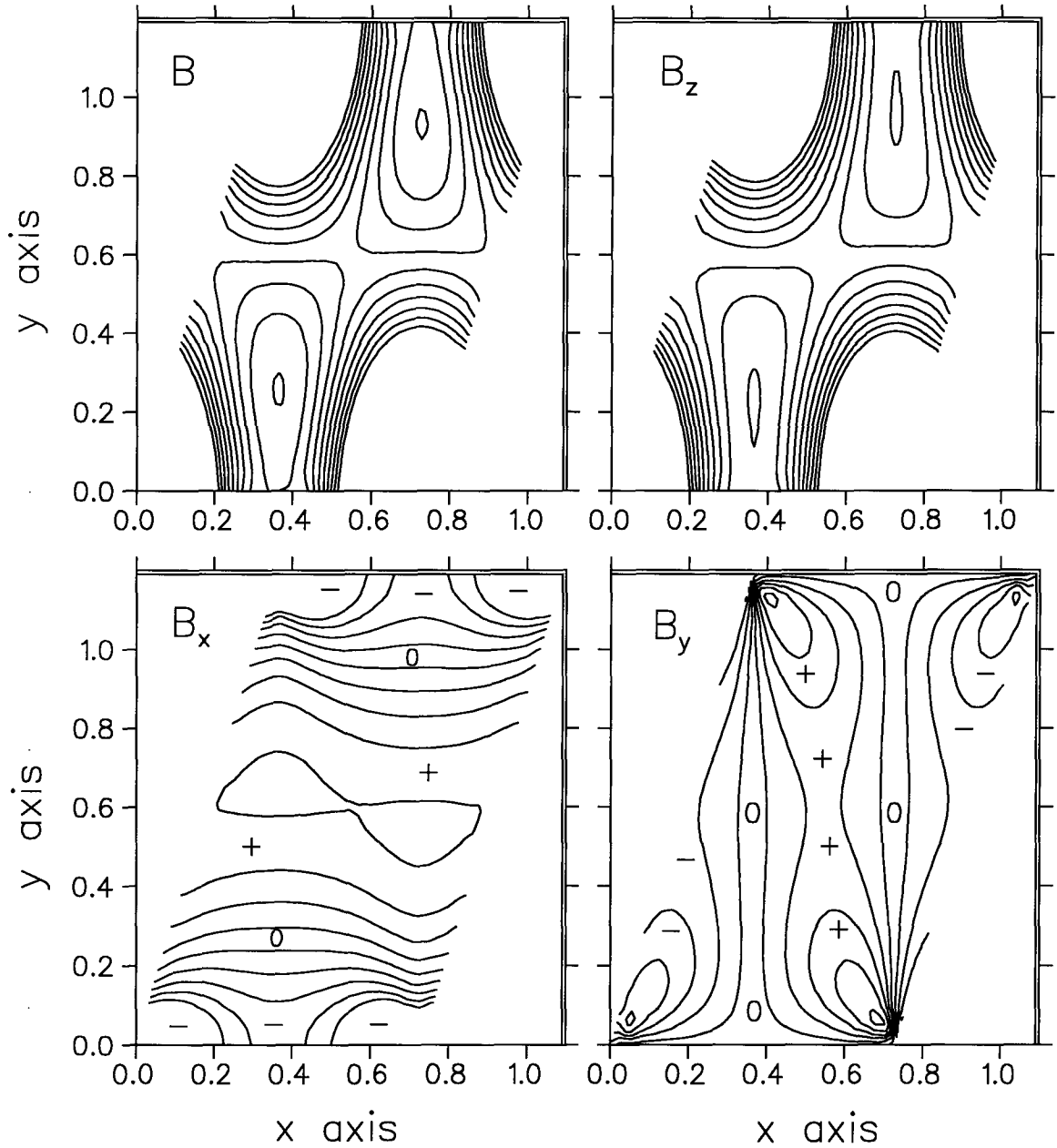


Figure 4.4: The spatial magnetic field distribution B and the field components B_x , B_y and B_z (where \hat{z} is parallel to the average field direction \vec{B}_0) in an anisotropic superconductor with the applied field at an angle $\theta = 60^\circ$ to the \hat{c} axis, in the frozen model. The average field is 100 G, $\lambda_{ab} = 0.1754 \mu\text{m}$ and $\Gamma = \lambda_c/\lambda_{ab} = 5$. The \hat{x} and \hat{y} axes have been normalized by $L = \sqrt{L_x L_y} = 0.4889 \mu\text{m}$ (see Eq. 4.25) so that the centers of the vortices are at $(x, y) = (0, 0)$, $(0.727, 0)L$, $(0.364, 1.190)L$, $(1.091, 1.190)L$, etc. For B and B_z , the contour lines shown have values between 86.5 G and 100.0 G, differ by 1.5 G and are omitted for local fields above 100 G for the sake of clarity. For B_x , the contours shown vary between -18 G and 14 G, differ by 4 G and are omitted for values between -108 G (at the vortex core) and -20 G for the sake of clarity. For B_y , the contours shown vary between -18 G and 18 G and differ by 4 G. For B_x and B_y , the signs $+$ and $-$ indicate the regions which have positive and negative values and zero (0) indicates where the component is zero.

for every point $\vec{r} = (x, y, z)$, the point $\vec{s} = (L_x - x, y, z)$ has the property that $B_y(\vec{s}) = -B_y(\vec{r})$. Therefore, by inspection, for an anisotropic superconductor, two out of three of the correlation parameters (see Eq. 2.48) are zero:

$$\tilde{U}_{x,y}(B') dB' = \frac{1}{V} \int_{\left| |\vec{B}(\vec{r})| - B' \right| < \frac{dB'}{2}} \left[\hat{x} \cdot \hat{B}(\vec{r}) \right] \left[\hat{B}(\vec{r}) \cdot \hat{y} \right] d\vec{r} \equiv 0 \quad (4.35)$$

$$\tilde{U}_{y,z}(B') dB' = \frac{1}{V} \int_{\left| |\vec{B}(\vec{r})| - B' \right| < \frac{dB'}{2}} \left[\hat{y} \cdot \hat{B}(\vec{r}) \right] \left[\hat{B}(\vec{r}) \cdot \hat{z} \right] d\vec{r} \equiv 0, \quad (4.36)$$

while

$$\tilde{U}_{x,z}(B') dB' = \frac{1}{V} \int_{\left| |\vec{B}(\vec{r})| - B' \right| < \frac{dB'}{2}} \left[\hat{x} \cdot \hat{B}(\vec{r}) \right] \left[\hat{B}(\vec{r}) \cdot \hat{z} \right] d\vec{r} \neq 0, \quad (4.37)$$

where the integrals are restricted to those positions \vec{r} such that the magnitude of the local field is within $\pm dB'$ of a particular value B' . Likewise, the components of the vector (Eq. 2.49) are

$$\hat{x} \cdot \vec{V}(B') dB' = \hat{x} \cdot \left\{ \frac{1}{V} \int_{\left| |\vec{B}(\vec{r})| - B' \right| < \frac{dB'}{2}} \hat{B}(\vec{r}) d\vec{r} \right\} \neq 0 \quad (4.38)$$

while

$$\hat{y} \cdot \vec{V}(B') dB' = \hat{y} \cdot \left\{ \frac{1}{V} \int_{\left| |\vec{B}(\vec{r})| - B' \right| < \frac{dB'}{2}} \hat{B}(\vec{r}) d\vec{r} \right\} = 0. \quad (4.39)$$

Therefore, by the definition in Sec. 2.6.4, this field distribution is definitely correlated. Because $\tilde{U}_{x,z} \neq 0$, the non-oscillatory portion of the polarization $\vec{P}(t \rightarrow \infty)$ (Eq. 2.42) will have a component in the direction of the applied field (\hat{z}) and will not be exactly parallel to the initial muon polarization direction, if $\hat{P}(0)$ is not in the \hat{y} - \hat{z} plane (see Fig. 5.6 in Sec. 5.3.1).

The London model (Eqs. 4.14 and 4.17) has a singularity in the field at the center of the vortex ($B_{\text{core}} \rightarrow \infty$) because it assumes $\kappa \gg 1$ and $\xi \approx 0$. The modified London model (Eq. 4.32) makes the field finite at the vortex core by introducing the coherence length ξ . In low ($\lambda < L$) and moderate ($\lambda > L$) fields, this does not change the lineshape significantly because the amplitude at the maximum field is negligible. Fits to data taken in low and moderate fields all assume $\kappa = 60$ in this thesis. In high fields ($\lambda \gg L > \xi$), the maximum field becomes observable as a cut-off in the lineshape. The London model must be further modified to take into account the upper critical field H_{c2} (Eq. 7.7).

4.6 The Effect of Non s -Wave Pairing on the Lineshape

As discussed in Ch. 1, one goal of this investigation is to determine whether $\lambda(T)$ in $\text{YBa}_2\text{Cu}_3\text{O}_{6.95}$ is consistent with s -wave superconductivity or with another pairing state such as d -wave. A feature of non s -wave superconductors is that the binding energy for the Cooper pairs [twice the superconducting gap $\Delta(\vec{k})$] is no longer isotropic, but rather has nodes in momentum space. Since quasi-particle excitations can only be produced with energy greater than 2Δ , quasi-particle excitations due to phonons are more common at low temperatures in superconductors with nodes in the gaps compared to s -wave superconductors which have isotropic gaps. The formal treatment in this chapter is based on the premise of anisotropic s -wave superconductivity. The question of utmost importance is that of the validity of fitting experimental data with results from s -wave theory if the sample (*e.g.* $\text{YBa}_2\text{Cu}_3\text{O}_{6.95}$) happens not to be an s -wave superconductor.

It is reasonable to assume for simplicity that $\text{YBa}_2\text{Cu}_3\text{O}_{6.95}$ has a single scalar order parameter, since it shows no signs of split transition peaks, *etc.*, reflective of multiple order parameters such as in UPt_3 .^[11] A single order parameter is appropriate when the superconductor has orthorhombic symmetry;^[11] in the superconducting state, $\text{YBa}_2\text{Cu}_3\text{O}_{7-\delta}$ has an orthorhombic crystallographic structure, although in the insulating state ($\delta \gtrsim 0.65$) it is tetragonal. On the basis of the AFM spin fluctuations, the candidate spin-singlet state $d_{x^2-y^2}$ has been proposed, in which the excitation gap vanishes along the positions $|\hat{k}_x| = |\hat{k}_y|$ in momentum space.^[23] In this case, it is possible that the vortex core may be rosette-shaped rather than elliptical,^[78] which may in turn affect the “tail” of the μSR lineshape, in which case the s -wave equation for the local field distribution (Eq. 4.32 for intermediate fields, Eq. 7.7 for high fields) is not valid. However, calculations of the local field distribution in the high field range in various d -wave states are not available at this time, which makes it difficult to assess the size of the error introduced by using only s -wave predictions of the μSR lineshape. This should not be a problem in low and moderate fields (such as in Chapters 5 and 6) because the size of the core is negligible and the spatial field distribution should be nearly identical in both s - and d -wave models.

4.7 Disorder in the Flux Line Lattice

If the flux line lattice (FLL) deviates from its ideal configuration (a perfect triangular array) due to dislocations, microscopic disorder, variations in the macroscopic average field, *etc.*, the theoretical μ SR lineshape will lose its sharp features at the minimum, cusp and maximum fields. This means that the lineshape of the experimental data cannot be adequately fitted by the theoretical lineshape for the ideal FLL alone.

Brandt[79] determined that μ SR data taken in Nb *can* be fit to a theoretical lineshape convoluted with a Gaussian distribution of fields and that this convolution is consistent with how disorder in the FLL due to flux pinning modifies the lineshape from the ideal case.[75] When fitting μ SR data, convolution with a square function works nearly as well as a Gaussian function with the same second moment. In fact, almost any symmetric convolution function will fit well, while many asymmetric functions fit poorly. The experimental data can only roughly determine the relative appropriateness of convolution functions for use with a given ideal theoretical function.

The width of the ideal μ SR lineshape is roughly proportional to λ^{-2} . If the variation of the magnetic penetration depth within the sample is negligible, we can relate the degree of “smearing” to the degree of disorder in the FLL. The drawback is that one cannot *a priori* determine the cause of the smearing from μ SR data alone. On the macroscopic scale, the density of vortices may vary from the center to the edge of a superconducting crystal due to imperfect flux expulsion in the presence of pinning. On a smaller scale, vortices may be preferentially pinned at twin boundaries and other structural defects in the sample, causing an increase of the average local field at these defects. On a microscopic scale, individual vortices may be pinned multiple times along their length, in which case the pinning forces may pull them individually out of alignment relative to the ideal FLL.

Most sources of smearing (*e.g.*, pinning, uneven doping leading to a distribution of penetration depths and inhomogeneities in the applied magnet field) can be represented by a symmetric distribution. An exception is the smearing caused by the gradient in the average local field from the center to the edges of a platelet-shaped superconducting sample due to the interaction of flux

expulsion and vortex pinning, which according to the Bean critical state model requires a right-triangular convolution function with the maximum amplitude on the low field side. (Actually, the Bean model usually is in reference to an external field which is changed while the sample is in the superconducting state (see Chapter 11 in Ref.[8] and reference within), but it is plausible to extend it to the case of increasing flux expulsion as the superconductor is cooled in a static applied field.) Ref. [80] used the Bean model in this way to analyze μ SR data taken in an unoriented powder of $\text{YBa}_2\text{Cu}_3\text{O}_{7-\delta}$ with platelet-shaped crystallites cooled in a static applied field. Since the ideal unoriented powder lineshape is much more symmetric than the single crystal lineshape,[53,81] the experimental data can be fit adequately using the right-triangular smearing alone. This does not prove that right-triangular smearing is the primary source, since a symmetric smearing function will fit the data equally well. The rounded cusp in the experimental lineshape for a mosaic of large oriented crystals with $\vec{B} \parallel \hat{c}$ (see Fig. 5.7) forces the use of a symmetric smearing function. The theoretical lineshape has a skewness similar to that of the right-triangular smearing function produced by the Bean model, so the resulting convolution alone would not fit the data well. This suggests that while there could be some macroscopic field inhomogeneity due to flux expulsion, it cannot be easily distinguished from the ideal lineshape unless the applied field is high enough that the high field cut-off due to the vortex core is observable (Figs. B.11 through B.18). The upper limit to the size of the field inhomogeneity from the flux expulsion interacting with the pinning may be estimated by the size of the observed *average* flux expulsion, which is less than the observed Gaussian smearing in $\text{YBa}_2\text{Cu}_3\text{O}_{6.95}$. In fact, given the large size of the crystals and the mosaic, and hence the small size of the flux expulsion before pinning sets in (as determined from magnetization measurements), the Bean model does not predict significant smearing, compared to the observed symmetric smearing presumably due to pinning. In light of this, convoluting the theoretical lineshape with a Gaussian is quite appropriate.

Brandt (see Ref. [75] and references therein) has calculated the elastic moduli for the flux line lattice of the isotropic superconductor and the elastic energy of an arbitrarily distorted FLL. If random pinning produces an approximately Gaussian distribution of distortions in the FLL, the size of the distortions can be estimated with the following treatment.

The vortex displacement is given by

$$\vec{s}_v(z) = \vec{r}_v(z) - \vec{r}_v^o \quad (4.40)$$

where \vec{r}_v^o is the location of the v^{th} flux line in the ideal FLL. The Fourier transform of Eq. 4.40 is

$$\vec{\zeta}(\vec{k}) = \zeta_x(\vec{k})\hat{x} + \zeta_y(\vec{k})\hat{y} \quad (4.41)$$

$$\vec{s}_v(z) = \int e^{i\vec{k}\cdot\vec{r}_v^o} \vec{\zeta}(\vec{k}) \frac{d\vec{k}}{8\pi^3} \quad (4.42)$$

$$\vec{\zeta}(\vec{k}) = n_f \sum_v \int e^{-i\vec{k}\cdot\vec{r}_v^o} \vec{s}_v(z). \quad (4.43)$$

Brandt[75] calculated the smearing width by shear and compression in the presence of an approximately Gaussian distribution of FLL distortions as

$$\sigma_s^2 \approx B_o^2 \int_{\text{B.Z.}} (\zeta_x k_y - \zeta_y k_x)^2 \frac{d\vec{k}}{8\pi^3} \quad (\text{shear}) \quad (4.44)$$

$$\sigma_c^2 = B_o^2 \int_{\text{B.Z.}} \frac{(\zeta_x k_x + \zeta_y k_y)^2}{(1 + k^2/k_h^2)^2} \frac{d\vec{k}}{8\pi^3} \quad (\text{compression}) \quad (4.45)$$

where $k_h^2 = [1 - B_o/H_{c2}(T)]/\lambda^2$. The integrals are over the first Brillouin zone (B.Z.), which includes k from 0 to $2\pi/L$, where L is the intervortex spacing. Eq. 4.44 would become a proper equality with the addition of a constant of order 1.[75]

I will make the simplifying assumption that the vortices are stiff, *i.e.*, $\vec{s}_v(z) \equiv \vec{s}_v$. By substituting Eq. 4.43 into Eq. 4.45 and noting that the integrals of the exponentials are Dirac delta functions, we see that the degree of lineshape smearing in the case of random compression (Eq. 4.45) can be rewritten as

$$\sigma_c^2 = B_o^2 \frac{\langle s^2 \rangle}{2} \sum_{\vec{k} \in \vec{K}_{BZ}} \frac{k_x^2 + k_y^2}{(1 + k^2/k_h^2)^2}, \quad (4.46)$$

where $\langle s^2 \rangle^{1/2}$ is the root mean square of the vortices' displacements from their ideal positions in the FLL. The reciprocal lattice vectors of the ideal FLL which are within the first Brillouin zone are indicated by \vec{K}_{BZ} . Likewise, the degree of lineshape smearing in the case of random shear (Eq. 4.44) can be rewritten as

$$\sigma_s^2 = B_o^2 \frac{\langle s^2 \rangle}{2} \sum_{\vec{k} \in \vec{K}_{BZ}} k_x^2 + k_y^2. \quad (4.47)$$

Brandt[75] estimates that the smearing width of the μ SR lineshape is

$$\sigma_1 \approx (\sigma_s^2 + \sigma_c^2)^{1/2} \quad (4.48)$$

at the minimum and cusp fields and is

$$\sigma_2 \approx \sigma_c \quad (4.49)$$

at the maximum field (the lineshape's cutoff). I have calculated that for the fields (100 G, 0.25 T and 1.9–6.5 T) and magnetic penetration depths present in my experiments, the smearing width due to random shear is much smaller than that due to random compression. Therefore, I use only the expression for random compression (Eq. 4.46) to estimate the degree of disorder present in the sample:

$$\langle s^2 \rangle^{1/2} \approx \frac{\sigma_c}{B_o} \sqrt{2} \left(\sum_{\vec{k} \in \vec{K}_{BZ}} \frac{k_x^2 + k_y^2}{(1 + k^2/k_h^2)^2} \right)^{-\frac{1}{2}}. \quad (4.50)$$

Note that because each muon is a local probe which responds only to the local magnetic field where it stops in the sample, μ SR cannot distinguish between short range disorder and long range disorder in the FLL. In contrast, neutron scattering off the FLL[82] and magnetic decoration experiments[32] can determine the degree to which the FLL maintains its long range hexagonal order in the presence of pinning.

For an anisotropic superconductor, I estimate $\langle s^2 \rangle^{1/2}$ by using an effective penetration depth $\lambda_{\text{eff}} = \bar{\lambda}(m_{xx}m_{yy})^{1/4}$ and vortex separation $L = (L_{xx}L_{yy})^{1/2}$ in the above isotropic equations. This should be accurate in high fields where the inter-vortex attraction along the \hat{x} axis is negligible (see Sec. 4.3.2). In low fields, there is currently no expression in the literature for $\langle s^2 \rangle^{1/2}$ so this simple-minded approximation will have to suffice.

4.8 Discussion of Non-oscillatory Amplitude

When the non-oscillatory signal is appreciable, we must determine the physical cause of both the “smearing” and the polarization function for the ideal FLL. Can we assume that the non-oscillatory portion of the theoretical polarization is unaffected by the smearing function? Regardless, we must keep track of the non-oscillatory portion if we wish to fit in the time domain. The

non-oscillatory portion of the polarization $\vec{P}(t \rightarrow \infty)$ will be parallel to the initial muon polarization direction $[\vec{P}(0)]$ if the local field distribution is symmetric (see Sec. 2.6.4).

For the flux line lattice in an anisotropic superconductor, the non-oscillatory signal is entirely due to components of the local field perpendicular to the average field which arise from the tensor nature of the anisotropic magnetic penetration depth when the applied field is not along one of the principal axes of the superconductor (see Sec. 4.2). Because the local field distribution is not symmetric (see Sec. 2.6.4), $\vec{P}(t \rightarrow \infty)$ is not parallel to $\vec{P}(0)$, unless the angle θ between the average field and the crystal's \hat{c} axis is 0° or 90° .

Disorder in the flux line lattice (FLL) will smear the lineshape.[75,74] In the case of an isotropic superconductor or an anisotropic superconductor with the applied field along a principal axis, *i.e.*, 0° or 90° , the local fields vary in magnitude as a function of position in the FLL but are all parallel to the average field direction (\hat{z}). Assuming that the vortices are stiff (*i.e.*, each vortex is parallel to \hat{z} throughout its entire length), disorder in the FLL (in the \hat{x} - \hat{y} plane) will cause variations in the local average field but the local fields will still be aligned with \hat{z} . As there are no components of the field perpendicular to the applied field, there will be no non-oscillatory signal if the initial muon polarization is perpendicular to the average field [$\vec{P}(t \rightarrow \infty; \hat{P}_o = \hat{x}) \equiv 0$ and $\vec{P}(t \rightarrow \infty; \hat{P}_o = \hat{y}) \equiv 0$].

An anisotropic superconductor with an applied field *not* along one of the principal axes of the crystal has local fields with components *perpendicular* to the average field direction. An increase in the density of vortices due to an increased field reduces these perpendicular components as the vortices increasingly overlap and the perpendicular components cancel out. Even in a moderate field of 720 G with the applied field at an angle of $\theta = 70^\circ$ with respect to the hard axis (\hat{c}), $\lambda_{ab} = 1400 \text{ \AA}$ and $\lambda_c = 7000 \text{ \AA}$, the amplitude of the non-oscillatory signal $P(t \rightarrow \infty)$ has dropped to approximately 6×10^{-6} times that of the oscillatory signal $P_\perp(t=0)$. Only at fields comparable to the lower critical field $H_{c1}(T) = \frac{\phi_o}{2\pi\lambda^2(T)}$ will the non-oscillatory signal be significant.

The perpendicular field components, which are significant in low fields, will be reduced where the FLL is compressed and increased where it is stretched out. Still, the average perpendicular

field and the resulting non-oscillatory asymmetry $\vec{P}_{||}(t \rightarrow \infty)$ should be about the same for a mildly disordered FLL as for a perfect FLL. It is reasonable to compound the polarization function representing the FLL [$\vec{P}_1(t)$] with that representing the disorder [$G_{\text{sym}}(t)$] relative to the non-oscillatory amplitude (Eq. 3.77). In the frequency domain, this is like convoluting the oscillatory signals (centered about $\nu_o = \frac{\gamma}{2\pi} B_o$) while ignoring the non-oscillatory signal (a delta function at zero frequency). Note that flattening in the Fourier transform (see Sec. 3.3.3) removes both the non-oscillatory signal and the effects of mismatched counters (α), so one cannot tell *a priori* what is happening to the non-oscillatory signal.

If the smearing function is chosen to represent nuclear dipole fields, which are randomly oriented, the effects are different.[†] For an isotropic superconductor, this introduces components of the local field which are perpendicular to the applied field, some of which cause a non-oscillatory signal. If the size of nuclear fields are small compared to average field, the non-oscillatory signal will be small. One generally ignores the small non-oscillatory portion introduced in TF experiments; in this case, Eqs. 2.77 and 3.77 are only approximate.

For an anisotropic superconductor with its own perpendicular fields, the dipolar fields may change the size of the non-oscillatory signal. If the dipolar fields are small compared to both the total field and the perpendicular components, then the change in the non-oscillatory signal will be negligible and one can compound the two polarization functions relative to the non-oscillatory amplitude.

Because dipolar fields are generally much smaller than the fields produced by the superconductor in $\text{YBa}_2\text{Cu}_3\text{O}_{7-\delta}$, we can be confident in the approximation that magnetic field distributions from superconductivity and nuclear dipole fields can be reasonably modeled by the convolution of the oscillatory signals in the frequency domain or by compounding of the polarization functions for the FLL [P^{sc}] and the dipolar fields ($P^{\text{DP}} = e^{-\frac{1}{2}\sigma^2 t^2}$) relative to the non-oscillatory signal in the time domain. Since disorder in the flux lattice can be modelled in the same way, the Gaussian convolution in practice represents both the FLL disorder and the dipolar fields. Moreover,

[†]I presume that the finite superconducting currents prevent the nuclear dipole fields from being screened out completely on a microscopic or nearest-neighbors level.

since the experimental μ SR lineshapes were produced by calculating the real Fourier transform of the experimental asymmetry signal using Gaussian apodization to control statistical noise (see Sec. 3.3.4), the Gaussian convolution also includes the degree of apodization in those cases where the lineshape was fitted rather than the asymmetry.

It must be noted that this treatment is predicated on the assumption that each muon precesses in a static magnetic field arising from the somewhat disordered FLL and nuclear dipolar fields. If the field distribution changes (*e.g.*, if the FLL moves due to the Lorentz force because an electric field is applied) or if the muons move within the sample, the observed lineshape will be qualitatively different—in particular, it will be narrower. Fortunately, muons, which form hydrogen-like bonds with oxygen in copper-oxide based high temperature superconductors,[34,35,36,37,38] show no evidence of diffusing in $\text{YBa}_2\text{Cu}_3\text{O}_{7-\delta}$ below 150 K.[39]

4.9 The Demagnetizing Factor

For a magnetic material, the internal field B_{int} can be expressed in terms of the applied field H_{ext} and the magnetization M , assuming uniform M and all vectors parallel:

$$B_{\text{int}} = H_{\text{ext}} + 4\pi(1 - N)M \quad (4.51)$$

where N is the demagnetization factor, due to the shape of the sample. The magnetization M will be uniform throughout the sample if it has the shape of an ellipsoid. The muon precesses in the internal field B_{int} with frequency ν ,

$$\nu = \frac{\gamma_{\mu}}{2\pi} B_{\text{int}}. \quad (4.52)$$

Assuming no sources of paramagnetism or diamagnetism exist in the sample other than that produced by the superconducting state, the internal field in the sample is equal to the applied field $H_{\text{ext}} = B_{\text{int}}$ at $T > T_c$. When the sample is cooled below T_c the superconductor will expel magnetic flux, which means that the superconductor has become diamagnetic; that is, the magnetization M will have a negative value. This results in a lower muon precession frequency

below T_c . With 100% flux expulsion ($B_{\text{int}} = 0$), the magnetization is given by

$$4\pi M = -\frac{1}{1-N} H_{\text{ext}}. \quad (4.53)$$

and the demagnetization factor is

$$N = 1 + \frac{H_{\text{ext}}}{4\pi M} < 1. \quad (4.54)$$

For an infinitely long cylinder, the demagnetization factor N is zero when the field is applied axially. For an infinitely large slab, N is one when the field is applied normal to the surface, which means that the internal field is always equal to the applied field ($H_{\text{ext}} = B_{\text{int}}$). For a very flat oblate spheroid (an ellipsoid with semi-axes a, b, c with $a = b$ and $m = a/c \gg 1$), [83] N is

$$N_{\parallel} \approx 1 - \frac{\pi}{2m} + \frac{2}{m^2} \quad (4.55)$$

when the field is applied in the \hat{c} direction and

$$N_{\perp} \approx \frac{\pi}{4m} \left(1 - \frac{4}{\pi m}\right). \quad (4.56)$$

when the field is applied perpendicular to the \hat{c} direction. $\text{YBa}_2\text{Cu}_3\text{O}_{6.95}$ grows in platelet-shaped crystals, so the expressions for the oblate spheroid should approximate the demagnetizing factors quite well.

When the superconductor has no vortex pinning, it responds reversibly to the applied field,

$$M(H_{\text{ext}}) \approx \begin{cases} -H_{\text{ext}} & \text{when } H_{\text{ext}} \leq H_{c1} \\ -\frac{1}{2\kappa^2}(H_{c2} - H_{\text{ext}}) & \text{when } H_{c1} \ll H_{\text{ext}} < H_{c2}, \end{cases} \quad (4.57)$$

where $\kappa = \lambda/\xi$ is the Ginzburg-Landau parameter. However, vortex pinning, which prevents flux from being expelled as the superconductor is cooled below the pinning temperature $T_{\text{irr}} < T_c$, occurs in experimental situations. The total flux expulsion at low temperature is reduced compared to that in the absence of pinning, $4\pi(1-N)M[H_{c2}(T_{\text{irr}})] < 4\pi(1-N)M$. Note that if κ , H_{c1} and H_{c2} are anisotropic, the magnetization will also be anisotropic. For $\text{YBa}_2\text{Cu}_3\text{O}_{6.95}$ the magnetization M is smallest when the applied field is in the $\hat{a}\text{-}\hat{b}$ direction ($\theta = 90^\circ$). For $H_{\text{ext}} \gg H_{c1}(\theta)$, the ratio of the magnetizations will be

$$\frac{M(0^\circ)}{M(90^\circ)} \approx \Gamma = \left(\frac{\lambda_c}{\lambda_{ab}}\right). \quad (4.58)$$

In platelet-shaped samples, the term $(1 - N)$ acts in the opposite way (with a ratio of $\approx 2m/\pi$), with the result that flux expulsion should show relatively little angular dependence. This is experimentally important in Ch. 5, where angular dependence of the lineshape is investigated and the internal field B_{int} is difficult to determine.

Two samples of the same material but with different ratios of the semi-axes m_1 and m_2 will have different demagnetization factors N_1 and N_2 and therefore will have different internal fields for the same applied field,

$$M = \frac{B_{\text{int},1} - H_{\text{ext}}}{4\pi(1 - N_1)} = \frac{B_{\text{int},2} - H_{\text{ext}}}{4\pi(1 - N_2)}. \quad (4.59)$$

Therefore, one can estimate the flux expulsion $4\pi(1 - N)M$ for a sample too large to fit in the magnetometer (like the mosaics used in the μSR experiments) by scaling the size of the flux expulsion from a smaller sample as determined from magnetization measurements.

Because of pinning, the amount of flux expulsion cannot be calculated so it must be measured. Having said that, using $m = 75$ I estimate the demagnetization factor N_{\parallel} at 0.98 for a 15 mm diameter mosaic with crystal thickness ranges between 100 μm and 300 μm when $\vec{H}_{\text{ext}} \parallel \hat{c}$. For an 8 mm diameter mosaic, using $m = 40$ I estimate N_{\parallel} at 0.96.

Magnetization measurements were made by Ruixing Liang on a single crystal of $\text{YBa}_2\text{Cu}_3\text{O}_{6.95}$ from the mosaic used in the μSR measurements reported on in this thesis. The crystal was 1.68 mm by 1.80 mm square with a thickness of 0.12 mm, with a triangular corner of size 0.75 mm by 0.65 mm missing. It had a weight of 2.04 ± 0.02 mg and a theoretical density of 6.366 g/cm³. The demagnetization factor N_{\parallel} was measured to be 0.8769 ± 0.0015 by zero field cooling the crystal to 5 K and applying fields of 5–50 G parallel to the \hat{c} axis, assuming that the flux pinning provides 100% shielding (Eq. 4.53). Estimating N_{\parallel} from the dimensions of the crystal results in a similar value. The low temperature magnetization was -0.68 emu/cm³ in 100 G, -2.5 emu/cm³ in 0.3 T, -7.5 emu/cm³ in 1.9 T and -21 emu/cm³ in 4.1 T. The flux expulsion should be -0.19 G in $H_{\text{ext}} = 100$ G and -0.65 G in $H_{\text{ext}} = 0.25$ T from the 15 mm diameter mosaic and -3.6 G in $H_{\text{ext}} = 1.9$ T and -10 G in $H_{\text{ext}} = 4.1$ T from the 8 mm diameter mosaic.

Chapter 5

Anisotropy of $\lambda(\theta)$ as Measured in Low Fields

5.1 Introduction and Motivation

This chapter describes measurements of the angular dependence of the magnetic penetration depth λ taken with an applied field of 100 G. The first goal was to simply observe the degree of anisotropy in λ using a method which is more consistent than that used in previous μ SR experiments.[84,28] The second and more ambitious goal was to observe features in the data (either in the frequency domain or in the time domain) which are indicative of the geometry of the flux line lattice (FLL) in low fields (see Sec. 4.3.2). While the first goal was easily achieved, the second proved more elusive.

Luke Daemen of Los Alamos National Lab provided the theoretical calculations of the field distributions used in this chapter to make the corresponding magnetic polarization functions.

In the experiment described in this chapter, the sample used was a 1.5 cm diameter mosaic of $\text{YBa}_2\text{Cu}_3\text{O}_{6.95}$ crystals mounted on a silver disk, with the \hat{c} axis normal to the plane of the disk. See Sec. 1.7 for a more detailed description.

5.2 Apparatus

This experiment was done using the M15 beamline at TRIUMF. The muon spin rotator was used to select a spin direction from 165° to 90° relative to the muon momentum—muons are produced with spins antiparallel to their momentum. The Omni Prime μ SR spectrometer (see Fig. 2.2) was used to apply a field of 100 G orthogonal to the spin direction in the plane of rotation. See Fig. 5.1 for a schematic. Omni Prime was outfitted with positron detection counters forming a six-sided

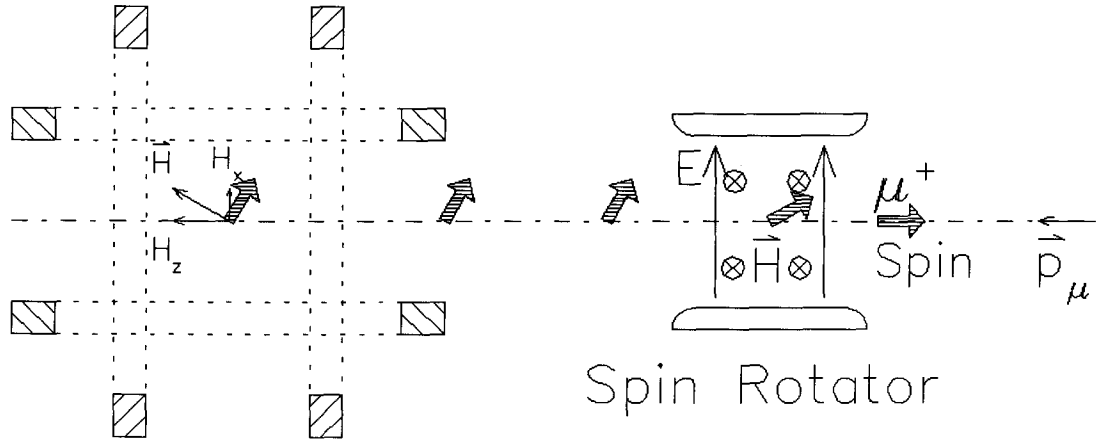


Figure 5.1: Schematic of side view of spin rotator (with orthogonal electric and magnetic fields) and experimental magnets (shown as two sets of Helmholtz coils). The muon enters from the right and stops in the sample at the center of the Helmholtz coils (left). The arrow marked \vec{p}_μ indicates the muon momentum direction. The large arrows are the muon spin direction at different locations. The thin arrows are magnetic fields produced by the vertical Helmholtz coils (H_x) and the horizontal Helmholtz coils (H_z) and the total applied field (\vec{H}).

box about the sample location, as pictured in Fig. 2.2. (For most experiments, only a subset of these counters would be used.) The RIGHT and LEFT counters had rectangular scintillators ($\frac{1}{4} \times 4 \times 6 \text{ in}^3$) with vertical light guides. The UP and DOWN counters had Y-shaped scintillators ($\frac{1}{4} \times 6 \times 2 \text{ in}^3$) which allowed vertical mounting of the light guides hence avoiding conflict with RIGHT and LEFT. The BACK counter had a square scintillator ($\frac{1}{4} \times 7 \times 7 \text{ in}^3$) with a hole (1 in diameter) for the beam to enter. Between the BACK counter and the cryostat there was a muon counter with a square scintillator ($1 \times 1 \text{ in}^2$). A single FORWARD signal was produced in the electronics by combining two counters with rectangular scintillators ($\frac{1}{4} \times 3.5 \times 7 \text{ in}^3$) with a semi-circular notch (2 in diameter) removed from each to make room for a horizontal gas flow cryostat. Together the scintillators form a square ($\frac{1}{4} \times 7 \times 7 \text{ in}^3$). The FORWARD and BACK counters were pulled away from the RIGHT and LEFT counters so that there was no overlap of solid angles. The tips of the “Y” in the UP and DOWN counters were allowed to overlap slightly with the FORWARD and BACK counters to maximize the solid angle subtended by the UP-DOWN-RIGHT-LEFT box.

The box of counters defines the laboratory reference frame, with UP-DOWN defining the \hat{X}

axis, RIGHT-LEFT defining the \hat{Y} axis and FORWARD-BACK defining the \hat{Z} axis (see Fig. 2.10). The projection of the decay positron asymmetry (proportional to the muon polarization) onto the plane normal to each axis of the coordinate system is recorded by the corresponding pair of positron counters. The theory or sample reference frame (\hat{x} - \hat{y} - \hat{z}) is defined by the angle of the average field ($\vec{B}_o \parallel \hat{z}$) relative to the \hat{c} axis of the anisotropic superconductor. If the direction of the magnetic field were fixed relative to the laboratory frame, the sample would have to be rotated for each desired θ . This would limit the number of angles available because at extreme angles the disk-shaped sample would subtend very little of the muon beam spot. Instead, the sample was fixed with $\hat{c} \parallel \hat{Z}$ and we rotated the applied field (using two orthogonal Helmholtz coils) and the initial muon spin direction (using a muon spin rotator).

In this experiment, our choice of collimation inadvertently stopped many muons in the final collimator. The resulting γ -ray shower (from decay positrons travelling through the lead shielding) produced a large unexpected “random” background which *decreased* with time. However, we estimate the random background for a given counter by counting the events which occur within a fixed time interval (250 ns) prior to the muon entering the muon counter. Subtracting this over-estimated random background from the counter histogram distorted the “background corrected” data, culminating in the number of events actually going *negative* at long times! This produced a resonance-like distortion in the asymmetry (see Sec. 2.5.2) at approximately 11 μ s, which is why the representative data shown in Fig. 2.6 has the asymmetry cut off prematurely at 8 μ s.

5.3 The Chains Model Versus the Frozen Model

As discussed briefly in Sec. 4.3, a single vortex has local fields with components B_z which are *negative* along the \hat{x} axis (see Fig. 1 of Ref. [67]) when the applied field ($\vec{B}_o \parallel \hat{z}$) is not along one of the principal crystallographic axes. Since the vortex-vortex interaction is proportional to B_z , this gives rise to an attractive force between vortices in the \hat{x} direction, whereas in an isotropic superconductor the force is always repulsive. According to the “chains model,” chains of vortices tend to form along the \hat{x} direction, with the density in the \hat{y} direction reduced accordingly so that the average field is maintained.[67,69] The preferred chain spacing is equal to the distance from

the center of a single vortex to the minimum in $B_z(\vec{r})$. In high fields, the distance between vortices is much smaller than the preferred chain spacing, so the effect is reduced. In the limit of very high fields, the ratio ρ of the sides of the isosceles triangle forming the unit cell is a function of the angle θ and the anisotropy $\Gamma = \lambda_c/\lambda_{ab}$, but is independent of the average field (see Sec. 4.3.1). In low fields, ρ also depends on the average field (see Sec. 4.3.2).

In low fields, the penetration depth near T_c is so large that the the superconductor must be operating in the “high field limit” [$\lambda(\theta, T \lesssim T_c) \gg L_x, L_y$, where L_x and L_y are defined in Eq. 4.25.] As it is cooled down and enters the “low field limit” [$\lambda(\theta, T \ll T_c) < L_x, L_y$], the FLL will rearrange itself into the configuration predicted by the chains model only if the attractive force along \hat{x} is strong enough to overcome other microscopic forces such as pinning which may keep the vortices in their original high field configuration. Pinning comes in two varieties—individual pinning in which a single vortex occupies each pinning site and collective pinning in which a bundle of vortices cluster near each pinning site. With collective pinning, the FLL might be able to rearrange itself when the applied field is not along a principal axis. However, collective pinning is only expected in those superconductors with low values for the Ginzburg-Landau parameter ($\kappa = \lambda/\xi \approx 1/\sqrt{2}$), such as niobium; in high temperature superconductors, the value of κ is much too high. With individual pinning, the FLL geometry should be frozen in at the irreversibility temperature.[85]

In $\text{YBa}_2\text{Cu}_3\text{O}_{7-\delta}$, the irreversibility temperature T_{irr} is very close to T_c , especially in large single crystals. (Refs. [86], [87] and [88] show the relative effect of morphology on the pinning for $\text{Bi}_2\text{Sr}_2\text{CaCu}_2\text{O}_8$ as measured by μSR .) Rather than presume $T_{\text{irr}}(\theta)$ for an applied field of 100 G, we assumed that the FLL structure at the irreversibility temperature is identical to that in the high field limit; we refer to this model as the “frozen model”.

5.3.1 A Pictorial Exposé of the Chains Model and the Frozen Model

The chains model and the frozen model produce distinctly different FLL geometries and consequently different theoretical μSR lineshapes.[65] (Furthermore, the frozen model for low fields

looks very different from that for high fields.) In both models, the triangle formed by three adjacent vortices in the FLL is an isosceles triangle. This gives rise to two distinct cusp fields with different amplitudes in the ideal μ SR lineshape, corresponding to the matching saddle points on the matching edges of the isosceles triangle and the third saddle point on the shorter third edge. Fig. 5.2 shows the lineshapes for an applied field of 100 G at $\theta = 37.8^\circ$, for $\bar{\lambda}^{-2}$ between 5 and 70 for both the chains and frozen models. (The bulk average of the magnetic penetration depth is $\bar{\lambda} = [\lambda_{ab}^2 \lambda_c]^{\frac{1}{3}}$. For $\Gamma = 5$ and $\bar{\lambda}^{-2} = 20 \mu\text{m}^{-2}$, $\lambda_{ab} = 0.1220 \mu\text{m}$.) For the chains model, the minimum field is nearly identical with the field at the matching saddle points (which lie halfway between the chains). The third saddle point (which lies halfway between the vortices along the \hat{x} axis) produces only a small bump in the lineshape. If that bump is ignored, the lineshape is reminiscent of the isotropic lineshape, though it is hard to see the shoulder between the minimum field and the first cusp. For the frozen model, the lineshape resulting from the FLL is striking—there are two pronounced cusps, and the minimum field extends much lower than in the chains model. With an applied field along a principal axis of the superconductor, the two models produce the same lineshape, with only one cusp. When the applied field is small, the lineshape is extremely sensitive to its value. Even in an isotropic superconductor (or an anisotropic superconductor with $\theta = 0^\circ$), the shoulder becomes more pronounced in low fields as the one in the denominator of Eq. 4.18 becomes significant.

Because the field is applied at an angle of θ from the \hat{Z} axis in the \hat{Z} - \hat{X} plane of the laboratory reference frame, the polarization projection is $\approx 100\%$ in the \hat{Y} direction but reduced by a factor of $\approx \cos \theta$ in the \hat{X} direction and $\approx \sin \theta$ in the \hat{Z} direction, when the initial polarization is along the \hat{x} direction. Polarization projections in the \hat{X} , \hat{Y} and \hat{Z} directions are shown in Fig. 5.3 for the chains model with $\theta = 37.8^\circ$ and in Fig. 5.4 for the frozen model with $\theta = 37.8^\circ$. Note that the polarization at later times appears to be more uniform in the frozen model than in the chains model. This is because the frozen model produces a wider lineshape (Fig. 5.2), which reflects the more rapidly dephasing polarization. The asymptotic values at long times seen in Figs. 5.3 and 5.4 are exactly equal to the projections of the non-oscillatory portion of the polarization $\vec{P}(t \rightarrow \infty)$ introduced in Eq. 2.42. Fig. 5.5 shows the angular dependence of the calculated polarization projections in the \hat{X} , \hat{Y} and \hat{Z} directions for the chains model when $\bar{\lambda}^{-2} = 20.0 \mu\text{m}$. Note that

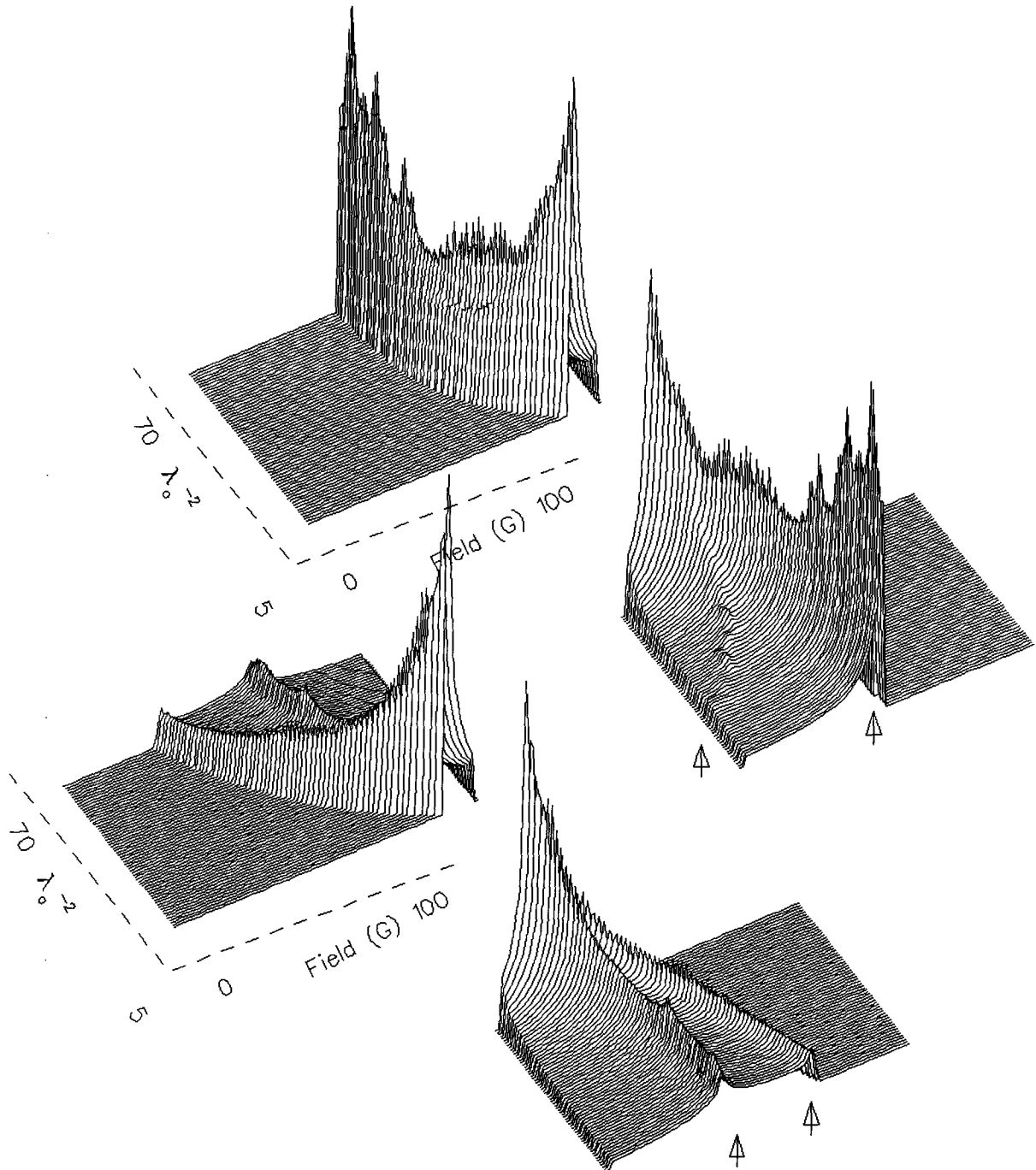


Figure 5.2: Theoretical field distribution $[n(B)]$ in a field of 100 G applied at $\theta = 37.8^\circ$ to a crystal with anisotropy of $\Gamma = \lambda_c/\lambda_{ab} = 5$ for the chains model (with no pinning) [top] and the frozen model (with pinning near T_c as the crystal is field cooled) [bottom]. The portion of the lineshapes above 100 G has been discarded for clarity. The range shown for the “scaling factor” $\bar{\lambda}^{-2}$ is 5.0 to 70.0 μm^{-2} . The vertical axis is the probability density (or lineshape) $n(B)$. The arrows point out the two cusp fields (for the chains model, the second cusp bump is so tiny that it is hardly visible). The figures on the right are the figures on the left rotated by 180° . Note that the jaggedness of the cusps is merely an artifact of discrete calculations.

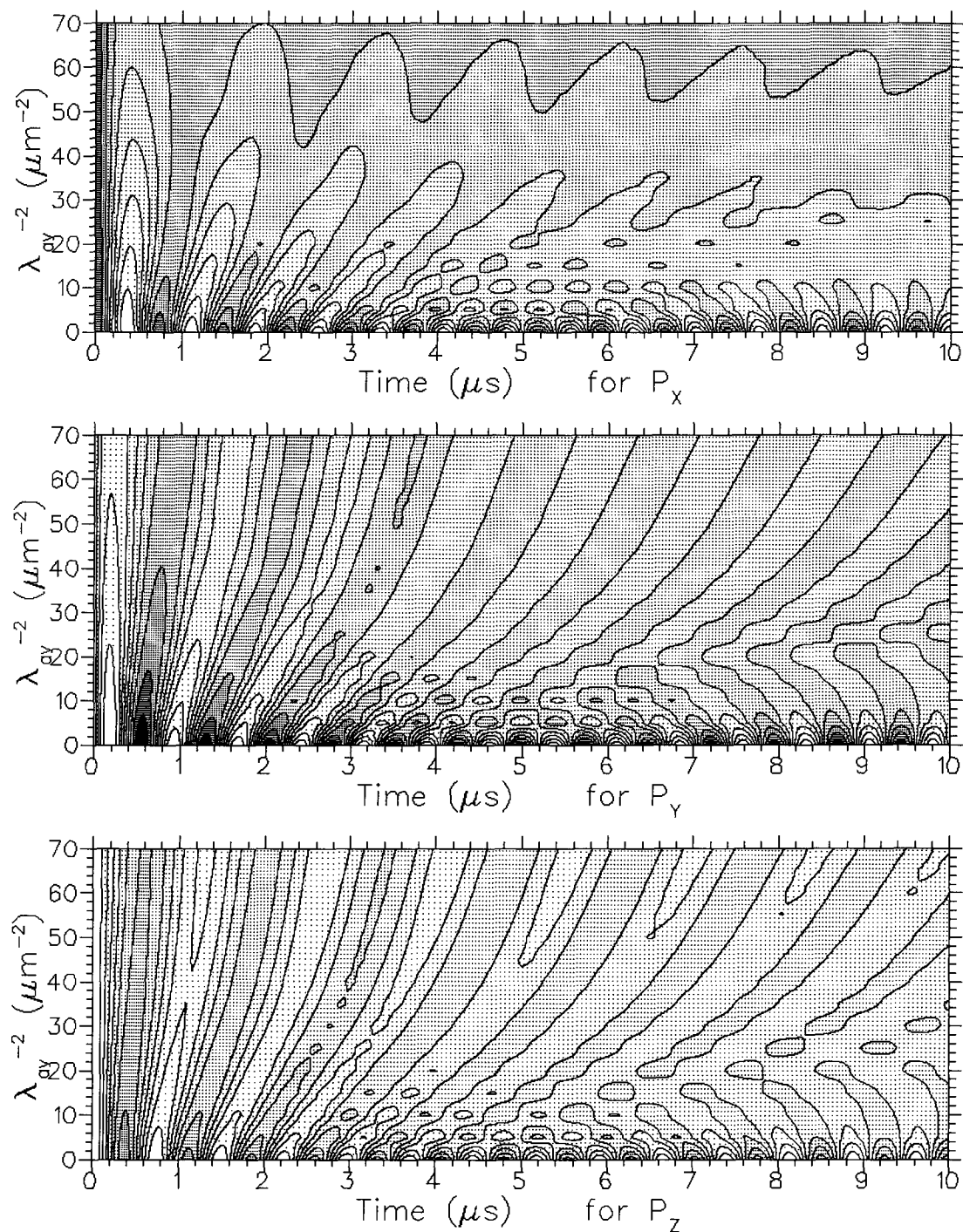


Figure 5.3: Polarization projections $[P_X(T), P_Y(T), P_Z(T)]$ as a function of $\bar{\lambda}^{-2}$ for $B_o = 100$ G and $\theta = 37.8^\circ$ in the chains model with no pinning. There are 10 grey scales, ranging from black for polarization parallel to that axis [$P_i(T) = 1$] to white for polarization antiparallel to that axis [$P_i(T) = -1$]. The initial polarization is along \hat{x} , $\vec{P}(0) = \hat{x}$.

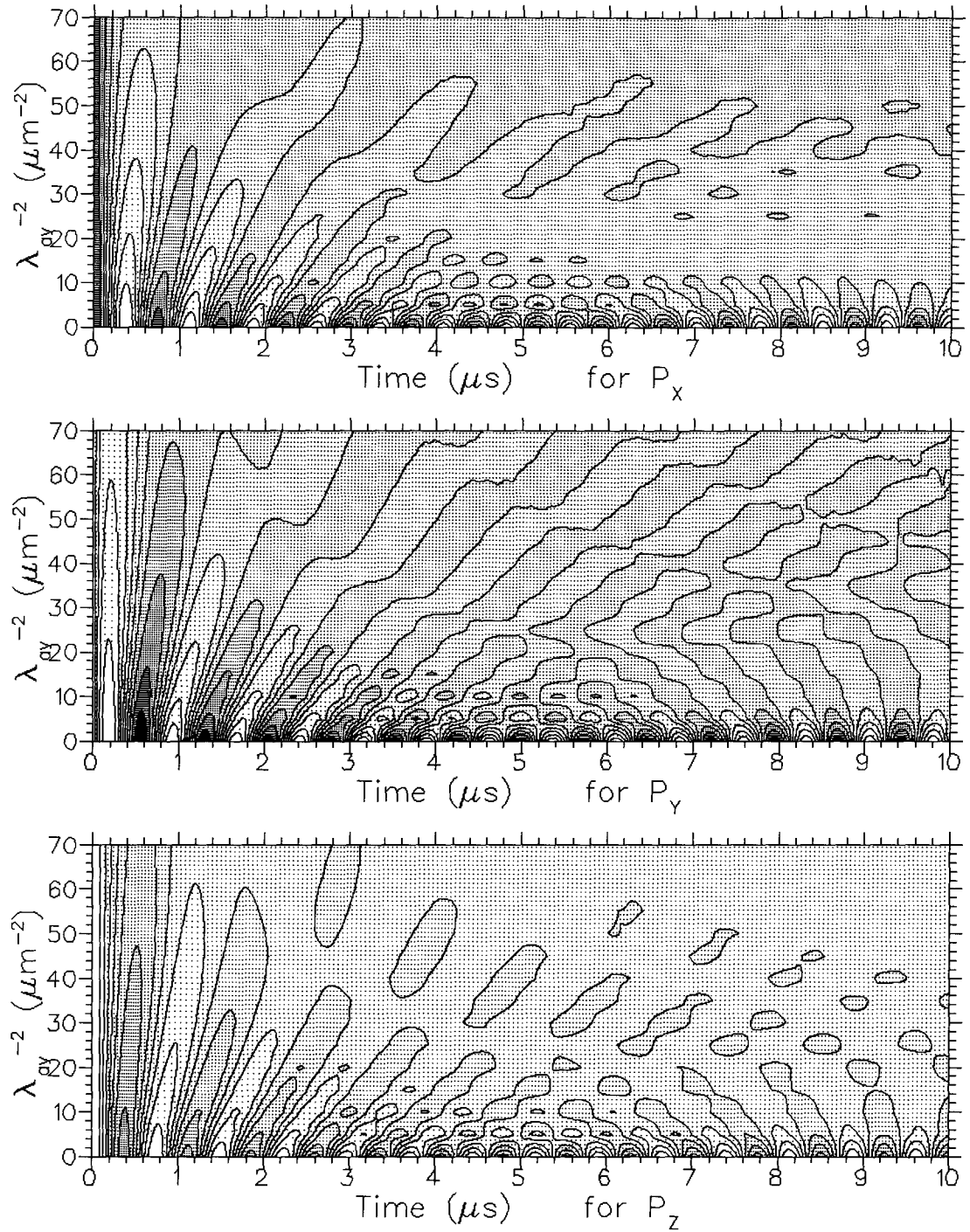


Figure 5.4: Polarization projections $[P_X(T), P_Y(T), P_Z(T)]$ as a function of $\bar{\lambda}^{-2}$ for $B_o = 100$ G and $\theta = 37.8^\circ$ in the frozen model with pinning near T_c as the crystal is field cooled. There are 10 grey scales, ranging from black for polarization parallel to that axis [$P_i(T) = 1$] to white for polarization antiparallel to that axis [$P_i(T) = -1$]. The initial polarization is along \hat{x} , $\vec{P}(0) = \hat{x}$.

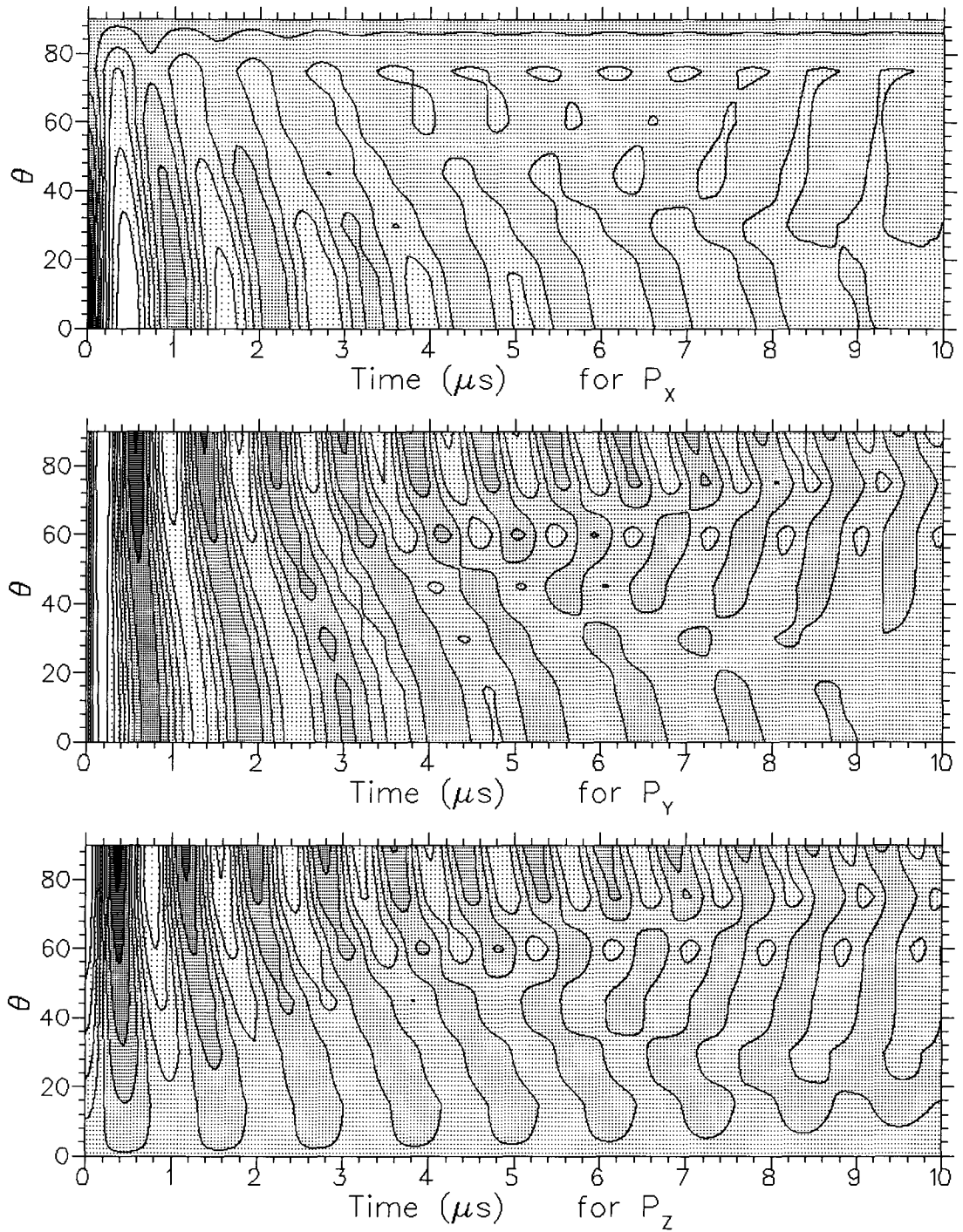


Figure 5.5: Polarization projections $[P_X(T), P_Y(T), P_Z(T)]$ as a function of θ (from 0° to 90°) for $B_o = 100$ G and $\bar{\lambda}^{-2} = 20.0 \mu\text{m}$ and $\Gamma = 5$ in the chains model with no pinning. There are 10 grey scales, ranging from black for polarization parallel to that axis [$P_i(T) = 1$] to white for polarization antiparallel to that axis [$P_i(T) = -1$]. The initial polarization is along \hat{x} , $\vec{P}(0) = \hat{x}$.

as θ progresses from 0° to 90° , the polarization dephases less rapidly reflecting the increase of the effective penetration depth $\lambda(\theta)$ from λ_{ab} to $\sqrt{\lambda_{ab}\lambda_c}$.

Fig. 5.6 shows the polarization $\vec{P}(t; \hat{P}_o = \hat{x})$ (from Eq. 2.45) projected along the axes associated with the $\hat{x}-\hat{y}-\hat{z}$ and $\hat{X}-\hat{Y}-\hat{Z}$ reference frames at times $t = 0$ and $t = \infty$. Note that the polarization projection $P_x(t)$ along the direction of the original polarization [$\hat{P}(0) = \hat{x}$] is non-zero, reflecting the presence of transverse components of the local field. Also, for $\theta \neq 0$ or 90 degrees, $P_z(t \rightarrow \infty)$ is non-zero due to the fact that the field distribution is “correlated” (see Secs. 2.6.4 and 4.5.2).

5.4 Experimental Results

5.4.1 Fourier Transforms of RIGHT/LEFT Counters

The motivation of this experiment was to verify the existence of chains by direct inspection of the lineshape or by detailed fits of the angular dependence of the lineshape. Fig. 5.7 shows the Fourier transforms of the projection of the muon asymmetry along the \hat{Y} axis (RIGHT-LEFT counters). Because the \hat{Y} axis is perpendicular to the applied field, the envelope function for the \hat{Y} axis projection of the muon asymmetry $A_o P_Y(t)$ (which is proportional to the muon polarization) is maximal, while envelope functions for the projections along the \hat{X} and \hat{Z} directions are reduced by factors of $\cos \theta$ and $\sin \theta$, where θ is the angle of the applied field. As discussed extensively in Sec. 3.3.2, the “flattened” real Fourier transform amplitude $S_{Y,\perp}(\nu)$ is only roughly equal to the probability distribution of local fields $n_\nu(\nu) d\nu = n(B) dB$ where $\nu = \frac{\gamma\mu}{2\pi} B$. The flattened real Fourier transform amplitude $S_{\perp,Y}(\nu)$ should be equal to the unflattened $S_Y(\nu)$ because $P_Y(t \rightarrow \infty)$ is predicted to be zero in Sec. 4.5.2. Unfortunately, the degree of disorder in the FLL washes out the details of the lineshape so the two cusps are indistinguishable. As well, the background signal is quite large and sits about where the second cusp for the chains model might be. However, the general characteristics of the angular dependence of the penetration depth can be observed. Both the overall linewidth and the shift of the cusp relative to the background signal ($\approx B_o$) are proportional to the inverse square of the effective magnetic penetration depth (see

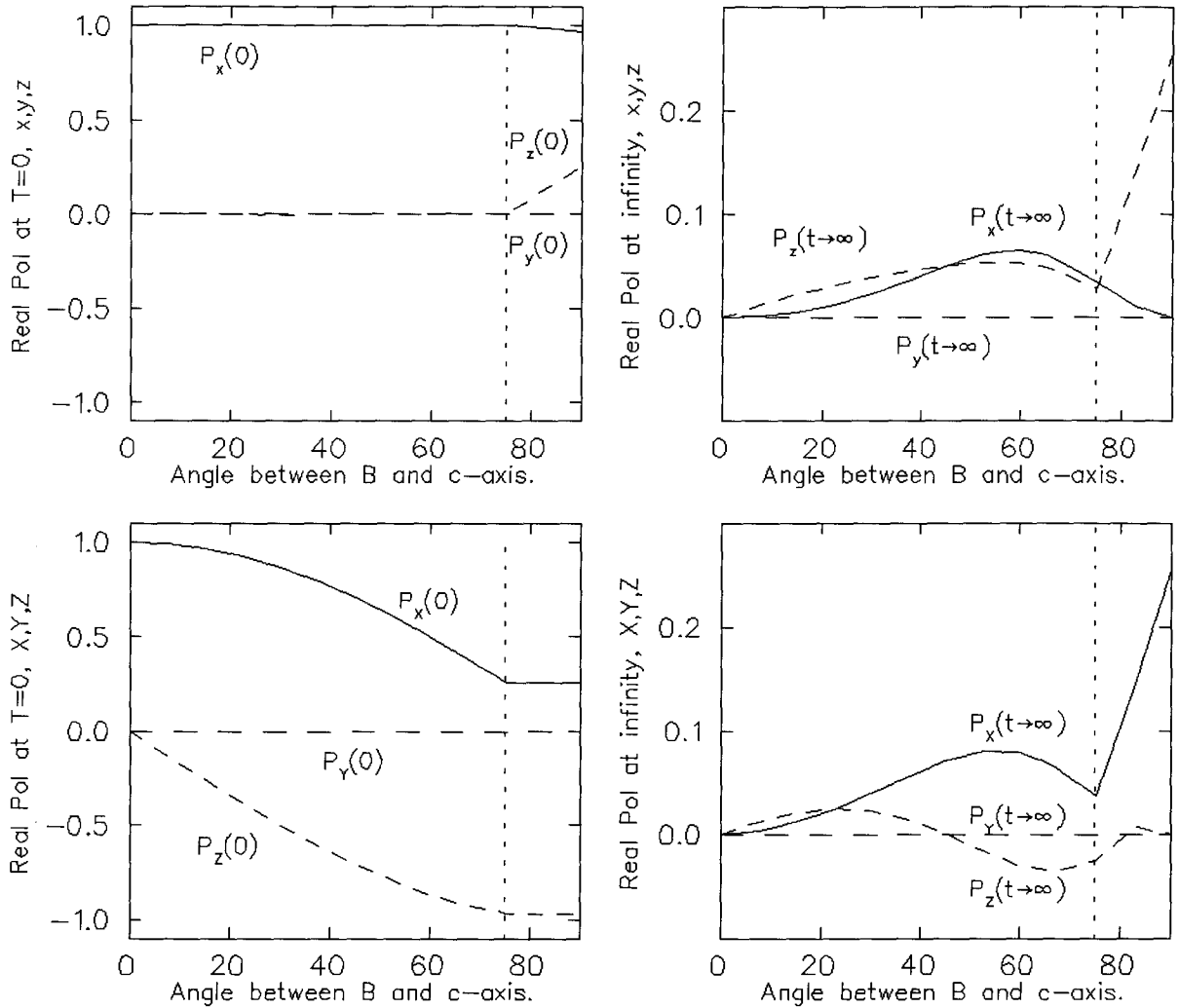


Figure 5.6: The muon polarization $\vec{P}(t)$ projections on the \hat{X} , \hat{Y} and \hat{Z} axes and the \hat{x} , \hat{y} and \hat{z} axes at time $t = 0$ and as time $t \rightarrow \infty$ as a function of angle θ between the average field \vec{B} and the $\hat{Z} = \hat{c}$ directions. The value as $t \rightarrow \infty$ represents the non-oscillatory portion of the muon polarization. These values are used in the fitting tables. The angle between the original muon spin direction and the \hat{Z} direction is $\phi = 90^\circ + \theta$ for θ between 0° and 67.5° ; that is, the initial polarization is along \hat{x} , $\vec{P}(0) = \hat{x}$. The angle ϕ is restricted to a maximum value of $\leq 165^\circ$ because the spin rotator cannot filter out beam line positrons at larger angles. In this case, when θ is between 75° and 90° (separated by the vertical dashed line), ϕ is fixed at $= 165^\circ$ and the muon spin direction and the magnetic field direction are not perpendicular. If they were, the asymptotic value for the polarization projections $P_x(t)$, $P_z(t)$, $P_X(t)$ and $P_Z(t)$ would decrease smoothly to zero as θ goes to 90° .

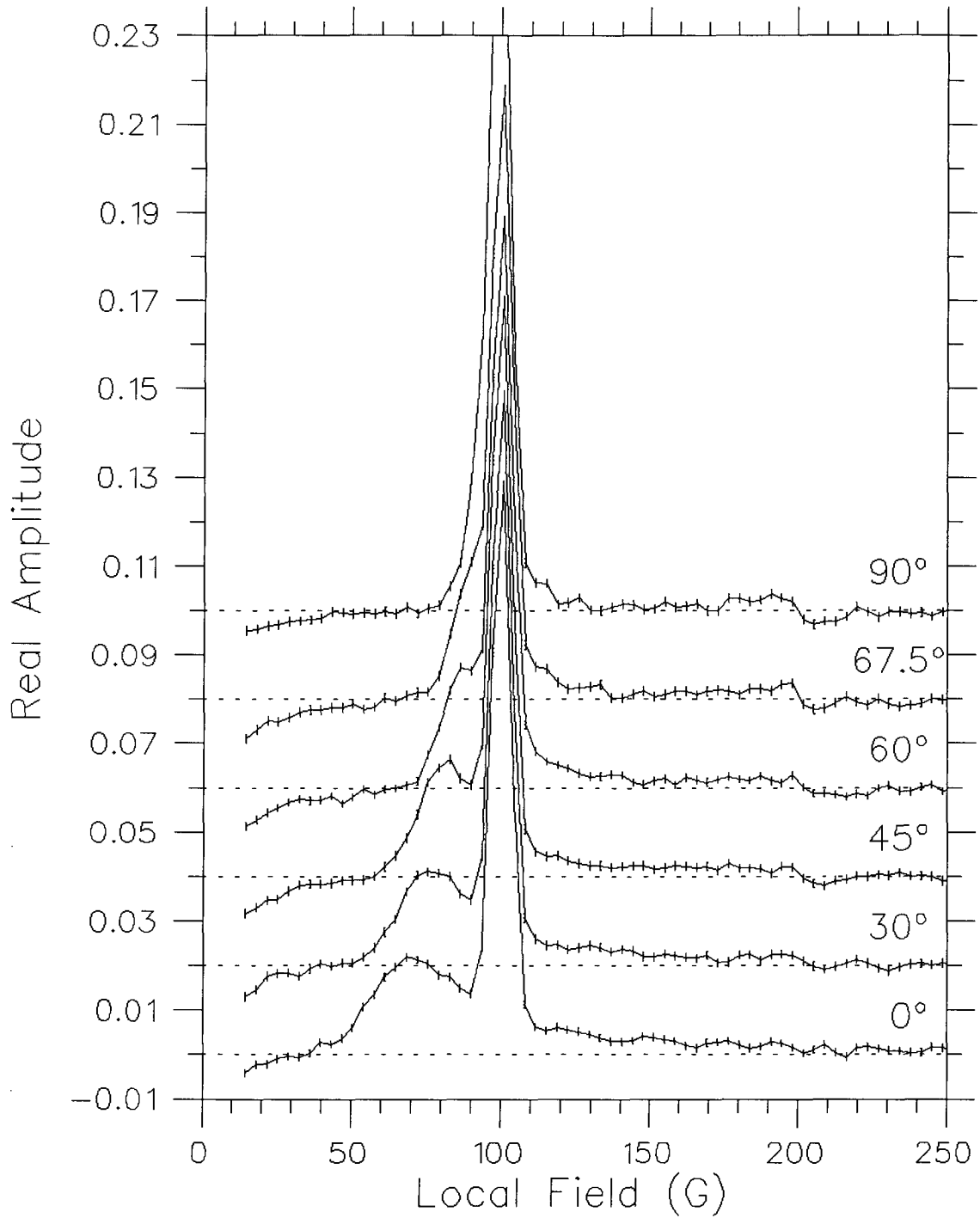


Figure 5.7: The μ SR lineshape $S_{Y,\perp}(\nu) d\nu = S_{Y,\perp}(\frac{\gamma_{\mu} B}{2\pi}) \frac{\gamma_{\mu}}{2\pi} dB$ [the real FFT of the LEFT-RIGHT counters] in 100 G as a function of the angle θ between the applied field and the \hat{c} axis of a mosaic of $\text{YBa}_2\text{Cu}_3\text{O}_{6.95}$ crystals. (The muon gyromagnetic ratio γ_{μ} has been removed.)

Eq. 4.8)

$$\lambda^{-2}(\theta) = \frac{\bar{\lambda}^{-2}}{(m_1 \cos^2 \theta + m_3 \sin^2 \theta)^{1/2} (m_3 \cos^2 \theta + m_1 \sin^2 \theta)^{1/2}}. \quad (5.1)$$

As the angle θ between the average field and the \hat{c} axis is increased (up to $\pi/2$), the whole lineshape shrinks.

Note the “glitch” at twice the average field, 200 G, the amplitude of which increases with increasing angle. It appears because the counters are not exactly centered about the sample (see Sec. 2.5.3 on the problems due to the relative phase of counters). The LEFT and RIGHT counters extend symmetrically in the \hat{X} and $-\hat{X}$ directions but are offset in the $+\hat{Z}$ direction (upstream) to minimize air gaps between the cryostat window, the muon counter, the BACK counter and the beam pipe’s window.* (Since the beam spreads by multiple scattering in air, it is best to minimize the amount of air through which the beam must travel.) As θ increases, the placement of the RIGHT-LEFT counters becomes more asymmetric with respect to the muon precession cone.

In this chapter, all errors bars shown for fits of individual experimental runs are returned from MIGRAD, a χ^2 minimization routine in the CERN fitting package MINUIT which is used in the μ SR fitting program MSRFIT. The fit parameters and errors quoted for the curves through the data were calculated using a weighted least squares fit (also known as χ^2 minimization) using the Gauss-Newton method, as implemented in TRIUMF’s PLOTDATA program. In Fig. 5.7, the FFT errors are estimated by the standard deviation of the noise in the real Fourier transform. All errors quoted are statistical errors and do not include any systematic errors.

5.4.2 Simple Gaussian fits

To quantify the anisotropy of the penetration depth, the low field data taken at a temperature of 10 K were fit to two Gaussians in the time domain, one fitting the cusp region and the other the background signal. No attempt was made to introduce an additional Gaussian for the tail region. All three pairs of counters were fit simultaneously. The non-oscillatory asymmetry, which is small compared to the oscillatory asymmetry, was ignored in the fits by allowing it to be absorbed

*For safety reasons, the μ SR apparatus is not allowed to share the same vacuum as the muon beam line.

into the α parameter. (This simple method of fitting was intended to demonstrate the general tendencies in the data; in no way was it intended to be a high precision fitting method.) Fig. 5.8.a shows the oscillatory asymmetry as a function of angle for all sets of counters. Note that the \hat{Y} projection of the asymmetry is roughly independent of angle, the \hat{X} projection of the asymmetry shows a $\cos \theta$ dependence and the \hat{Z} projection of the asymmetry shows a $\sin \theta$ dependence. Fig. 5.8.c shows the angular dependence of the background signal at 10 K and the total signal (superconductor plus background) at 100 K. The difference between these two signals (about 0.3 G) may reflect the flux expulsion. Magnetization measurements taken in a single crystal with $\vec{B} \parallel \hat{c}$ suggest that the flux expulsion should be about 0.2 G in this mosaic (see Sec. 4.9), which is close to the observed 0.3 G.

The expected angular dependence of the effective penetration depth in the \hat{x} - \hat{y} plane is given by Eq. 5.1. In high fields [$\lambda(\theta) > L_x, L_y$], the angular dependence of the lineshape's second moment relative to the average field B_o is

$$\delta B(\theta) = \sqrt{\langle (B(\vec{r}) - B_o)^2 \rangle_{\vec{r}}} = \delta B_{\max} (\Gamma^{-2} \sin^2 \theta + \cos^2 \theta)^{1/2} \quad (5.2)$$

and the shift of the cusp field from the average field is

$$B_{\text{cusp}}(\theta) - B_o = -\Delta B (\Gamma^{-2} \sin^2 \theta + \cos^2 \theta)^{1/2}, \quad (5.3)$$

with the anisotropy ratio Γ defined by $\Gamma = \lambda_c / \lambda_{ab}$. The second moment is essentially the lineshape's width which is proportional to the relaxation rate in the time domain. These formulas should not be valid in low fields, since both $B_{\text{cusp}} - B_o$ and the linewidth $\delta B(\theta)$ are no longer independent of the applied field B_o because the ones in the denominator of Eq. 4.14 are not negligible.

Fig. 5.9 shows the angular dependence of the second moment and the cusp field in the chains model with $\lambda_{ab} = 0.1220 \mu\text{m}$, field $B_o = 100$ G and anisotropy ratio $\Gamma = 5$. For the sake of comparison, the second moment of the field distribution has been fit to Eq. 5.2 with $\delta B_{\max} = 70.20 \pm 0.44$ G and a fixed anisotropy ratio $\Gamma = 5$. The shift of the cusp field from the average field has been fit to Eq. 5.3 with $\Delta B = 36.73 \pm 0.44$ G and a fixed anisotropy ratio $\Gamma = 5$. These equations are only valid when the spacing between vortices L is much smaller than the

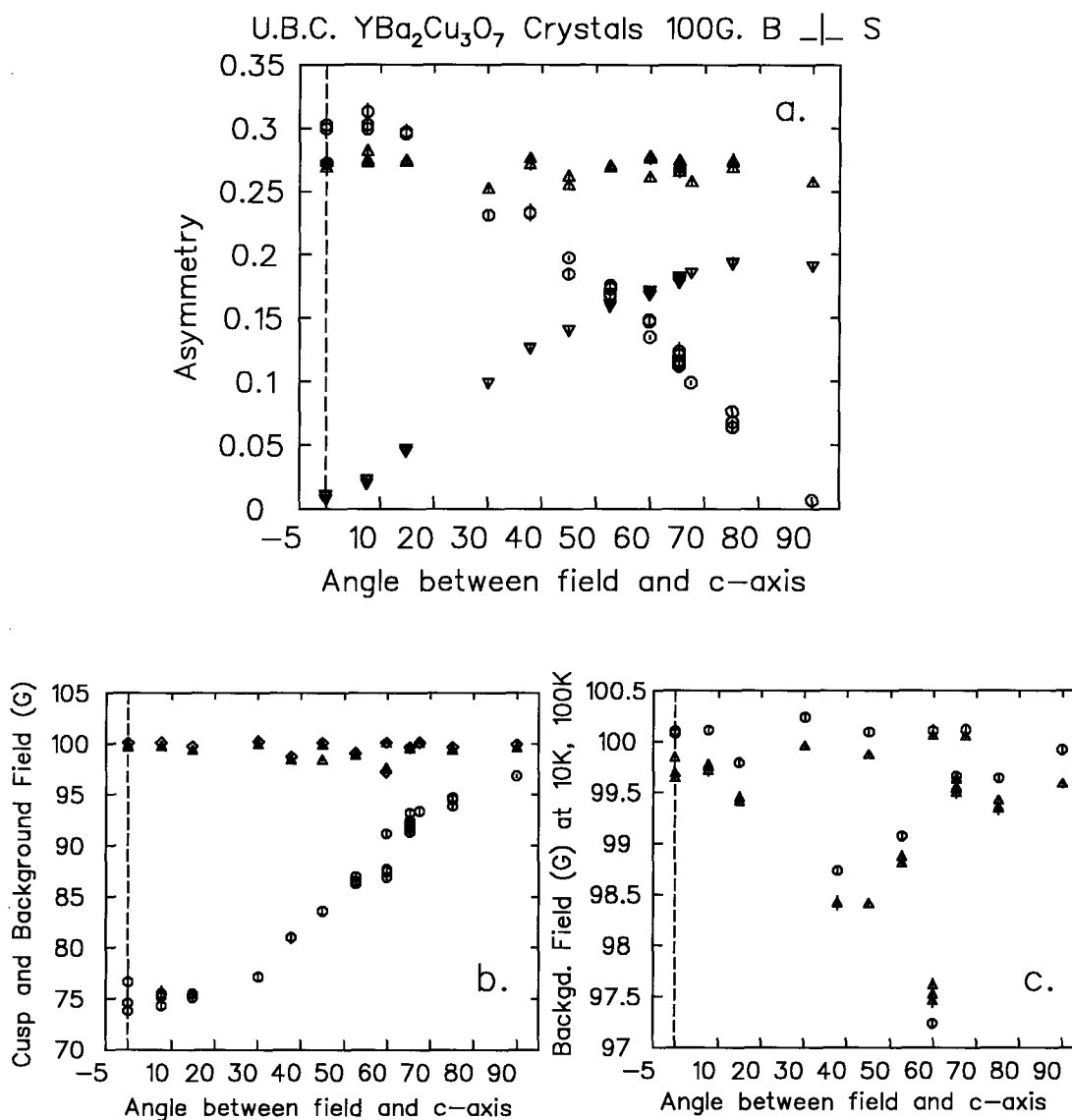


Figure 5.8:

a. Angular dependence of the asymmetry at 100 G, in the \hat{X} counters (circles), in the \hat{Y} counters (triangles) and in the \hat{Z} counters (upside-down triangles). Notice that the asymmetry in the in the \hat{Y} counters is constant, to within our ability to apply fields orthogonal to the muon spin directions.

b. Angular dependence of the average magnetic field in the silver background at 10 K (triangles), the combined superconductor and silver signal at 100 K (diamonds) and the cusp fields in the superconductor at 10 K (circles).

c. Blowup of the angular dependence of the silver background at 10 K (triangles) and the combined superconductor and silver signal at 100 K (circles).

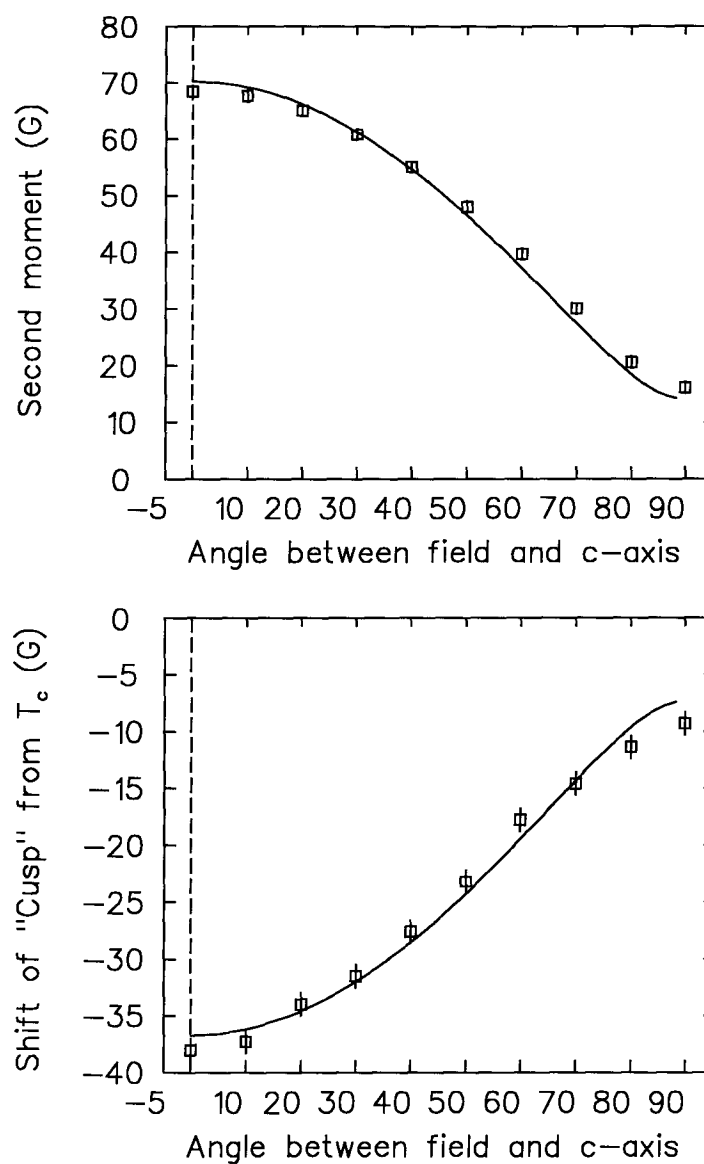


Figure 5.9: The angular dependence of the second moment and the cusp field expected from the chains model (squares) with $\lambda_{ab} = 1220 \text{ \AA}$, field $B_o = 100 \text{ G}$ and anisotropy ratio $\Gamma = \lambda_c/\lambda_{ab} = 5$. Curves show the behavior expected in high applied fields (Eqs. 5.2 and 5.3), so they are not strictly correct in this case.

average penetration depth, which is definitely not the case here. However, they provide a guide for comparison between the theory and the experimental results.

Fig. 5.10 shows the fit of the shift of the experimental cusp field from the average field to the formula in Eq. 5.3 with the addition of a constant c . With the anisotropy ratio fixed at $\Gamma = 5$, the fit results are $\Delta B_{\text{exp}} = 28.760 \pm 0.065$ G and a constant $c = 4.755 \pm 0.035$ G. If c were negative, it might represent flux expulsion. By scaling the chains model results,

$$\Delta B_{\text{exp}} \lambda_{\text{exp}}^2 = \Delta B_{\text{th}} \lambda_{\text{th}}^2, \quad (5.4)$$

the estimated magnetic penetration depth of the sample is between $0.1380 \mu\text{m}$ (using $\Delta B_{\text{exp}} = 28.760$ G) and $0.1510 \mu\text{m}$ (using $\Delta B_{\text{exp}} = 28.760 + 4.755$ G). The odd result of the constant c being positive may simply reflect the results of neglecting a possible angular dependent flux expulsion and the shift of the cusp due to “smearing” from disorder in the FLL. The results of these simple Gaussian fits should be regarded as purely qualitative. From Sec. 4.9, the anisotropy of the magnetization of $\text{YBa}_2\text{Cu}_3\text{O}_{6.95}$ [$\frac{M(\theta=0)}{M(\theta=\pi/2)} \approx \Gamma = (\lambda_c/\lambda_{ab}) = 5$] partially cancels out the angular dependence of the shape factor [$\frac{N(\theta=0)}{N(\theta=\pi/2)} = \frac{N_{\parallel}}{N_{\perp}} \approx 0.0208$ for an ellipsoid with a ratio of sides $m = 75$], which suggests that a flux expulsion of 0.19 G when the applied field is parallel to the \hat{c} axis (based on magnetization measurements in Sec. 4.9) will be no more than a factor of ten higher (1.8 G) when $\vec{H} \perp \hat{c}$ in this sample. This estimate assumes that there is no angular dependence to the strength of the pinning or the irreversibility temperature, which is not the case. Regardless, the flux expulsion in this sample is probably quite small, less than one or two gauss, at all angles.

Fig. 5.10 also shows the angular dependence of the field inhomogeneity estimated by the Gaussian relaxation rate for a Gaussian fit to the superconductor signal. This does not follow the expected angular dependence for the second moment seen in Eq. 5.2 and Fig. 5.9, but instead appears to be linear, with [in gauss]

$$B_o - B_{\text{cusp}}(\theta) = (19.55 \pm 0.44) + (-0.1617 \pm 0.0067)\theta. \quad (5.5)$$

Qualitatively, the deviations from the high field formula for the shift of the cusp field (Eq. 5.3) are similar for both the chains model and the experimental data. In both, the field is lower than

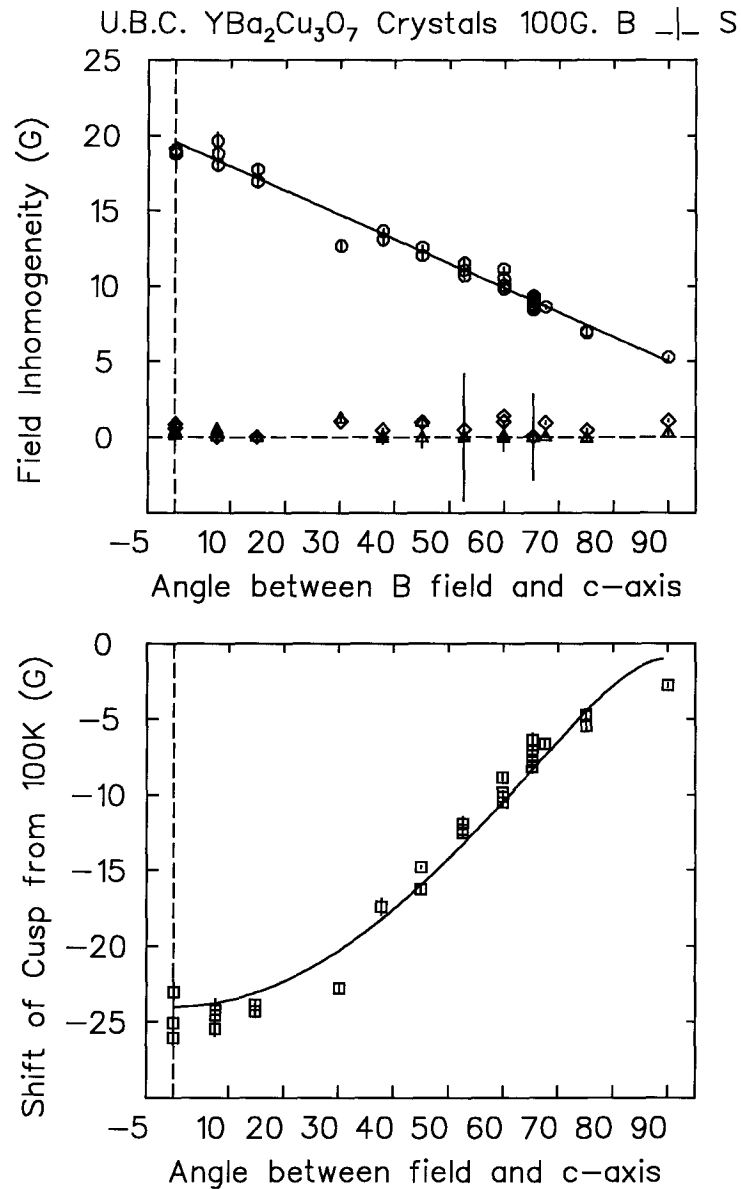


Figure 5.10: The angular dependence of the field inhomogeneity (as estimated by the width of a Gaussian fit) and the cusp field measured in a mosaic of $\text{YBa}_2\text{Cu}_3\text{O}_{6.95}$ crystals in 100 G. The asymmetry signals were fit with two Gaussians, one representing the silver background signal and the second the “smeared” cusp region of the superconducting signal. (Some asymmetry was lost since the fast relaxing portion was not explicitly fit.) For the field inhomogeneity, the superconducting signal at 10 K (circles), the background signal at 10 K (triangles), and the combined superconducting and background signals at 100 K (diamonds) are shown. The superconducting signal’s inhomogeneity (circles) in the upper frame is shown with a straight line as a guide to the eye. The curve in the lower frame shows the behavior expected in high applied fields (Eq. 5.3), so it is not strictly correct in this case.

the high field formula at low and high angles. The pronounced cusp in the chains model falls approximately halfway between the two cusps in the frozen model, so one might expect similar behaviour with a convolution that smears the two cusps into one. Since an anisotropy ratio $\Gamma = 5$ was assumed in the fit to the *Ansatz* formula, it is fair to say that the experimental results are *consistent* with $\Gamma = 5$, especially since the estimated value of the penetration depth in the \hat{a} - \hat{b} plane ($0.1380 \mu\text{m} < \lambda_{ab} < 0.1510 \mu\text{m}$) is consistent with values from other measurements (such as $0.1405 \mu\text{m}$ in Ch. 6 and $0.1491 \mu\text{m}$ in Ch. 7). The lineshape is also affected by the degree of disorder in the FLL but the angular dependence of this disorder is not fully known, so it is not possible to fit Γ directly using this data.

Another μSR group [28,84] obtained similar results by rotating a mosaic of crystals relative to a fixed applied field. However, in the paper which shows the full angular dependence,[28] they give results for a field of 3500 G with angles θ between 0° and 45° and for a field of 220 G with angles θ between 45° and 90° which are consistent with an anisotropy of $\Gamma = 5$ or 5.5. But a field of 220 G is a little too low for the high field limit to be in effect, and the ramifications of this point are not discussed in the papers.

While the range of relaxation rates reported by Pümpin *et al.*[28] is almost identical with the values measured here (expressed as the second moment of magnetic field in Fig. 5.10), they observed the expected angular dependence for the field inhomogeneity as estimated by the gaussian relaxation rate while we observe it only for the cusp field and not for the inhomogeneity. This is especially puzzling since both experiments fit the data to Gaussians. The ideal μSR experiment would measure the complete angular dependence of λ in a single high field, such as 0.2 T. Unfortunately, our spectrometer is not capable of producing fields greater than 100 G in arbitrary directions.

5.4.3 Fits to the Chains and Frozen Models

5.4.3.1 Data Analysis

In order to fit the chains and frozen models, the TRIUMF solid state group's μ SR fitting program (MSRFIT) was altered to use look-up tables for the \hat{X} , \hat{Y} and \hat{Z} projections of the theoretical polarization, with \hat{X} , \hat{Y} and \hat{Z} defined by the position of the counters (see Fig. 2.10). The tables, indexed by time ($t = 0$ to $20 \mu\text{s}$) and scaling factor ($\bar{\lambda}_{\text{th}}^{-2} = 0.1, 5, 10, 15, \dots, 55, 60, 65, 70, 80, 90, 100, 150$ and $5000 \mu\text{m}^{-2}$), contain both "real" and "imaginary" polarization values [$P_i(t, B, \bar{\lambda}^{-2}, \theta; \hat{P}_o = \hat{x})$ and $P_i(t, B, \bar{\lambda}^{-2}, \theta; \hat{P}_o = \hat{y})$ for $i = X, Y,$ and Z] calculated from an applied field $\vec{B}_{\text{th}} = 100 \text{ G}$ at an angle of θ from the \hat{Z} axis in the \hat{X} - \hat{Z} plane. The initial muon spin direction is assumed to be orthogonal to the applied field in the \hat{X} - \hat{Z} plane ($\psi = \pi/2$ in Fig 2.11), except for when θ is greater than 75 degrees, in which case $\psi + \theta$ is restricted to 165 degrees so that the separators will be effective in separating out positron contamination. The anisotropic superconductor is assumed to have $\hat{c} \parallel \hat{Z}$. A complete set of tables was constructed for each angle θ required. The theory values given $B_o, \bar{\lambda}^{-2}$ and initial phase ψ are read from the tables as follows:

1. The time index t and the scale index $\bar{\lambda}^{-2}$ are multiplied by B_o/B_{th} , giving

$$P_i^{\text{exp}} \left(t_{\text{exp}}, \bar{\lambda}_{\text{exp}}^{-2}, \theta, \psi; B_{\text{exp}} \right) = P_i^{\text{th}} \left(t_{\text{exp}} \frac{B_{\text{exp}}}{B_{\text{th}}}, \bar{\lambda}_{\text{exp}}^{-2} \frac{B_{\text{th}}}{B_{\text{exp}}}, \theta, \psi; B_{\text{th}} = 100\text{G} \right) \quad (5.6)$$

for $i = X, Y,$ and Z .

2. A 2-D bi-cubic spline is used to interpolate between points.
3. Both the smearing (compounding in the time domain) due to disorder in the FLL and nuclear dipole moments and the experimental initial phase ψ are accounted for using Eq. 2.77, that is the oscillatory portion of the resulting polarization function is multiplied by the Gaussian $e^{-\frac{1}{2}(\gamma\mu\sigma_B t)^2}$ corresponding to the Gaussian convolution $e^{-\frac{1}{2}(B/\sigma_B)^2}$ of the field distribution reflecting disorder in the FLL due to pinning.

For each angle θ , a global fit was performed using a run with a temperature $T = 10$ K as well as the run above T_c (approximately $T = 100$ K). The run above T_c was fit with $\bar{\lambda}^{-2}$ fixed to the small value ($0.15 \mu\text{m}^{-2}$); since it contained no significant field components perpendicular to the applied field, it could provide values for $A_i(0)$ and α_i which should hold for all runs at that angle θ . (Because the size of the flux expulsion could not be accurately determined, though it appears to be small, the background signal and the superconducting signal were constrained to share the same average field in the fits for all temperatures below T_c .) Because fits to runs below T_c could confuse $A_i(0)$ and α_i with the relative size of the oscillatory and non-oscillatory asymmetries for different values of $\bar{\lambda}^{-2}$, the runs were assumed to share a common initial asymmetry $A_i(0)$ and normalization α_i (see Eq. 2.16) for each set of counters ($i = X, Y, Z$). In principle, this procedure should determine $A_i(0)$, α_i and $\bar{\lambda}^{-2}$ uniquely. Also, by using the run above T_c we absorb any small errors in the angles of the applied field and the muon spin (relative to the values assumed in the tables) into the fitted values of $A_i(0)$ and α_i .

Since the tables contain the *full* time dependent polarization function, including both oscillatory and non-oscillatory portions, the fitted asymmetry $A_i(0)$ for all the counters is independent of the angle θ .

The program MSRFIT performs χ^2 -minimization fitting of the data to the models using various routines in the MINUIT package. The MIGRAD routine is generally used to find the best fit and a crude error estimate. More accurate (and usually larger) estimates of the parameter errors are produced by the MINOS routine, which defines the error in a parameter as the deviation which increases χ^2 by one while all other parameters are free to vary. For this data, two parameters (λ^{-2} and σ) determine the linewidth, rather than just one, and the high field tail is unaffected by smearing (σ), so the convergence was slow even with MIGRAD. Given that MINOS requires considerably more computational effort than MIGRAD, its use was not practical. This is regrettable—it is precisely in cases like this that MINOS may yield a more accurate, albeit usually larger, estimate of the error. The scatter in the data is also somewhat larger than the statistical error alone because of systematic errors in setting the muon spin direction and magnetic field direction—the data were taken on two separate occasions.

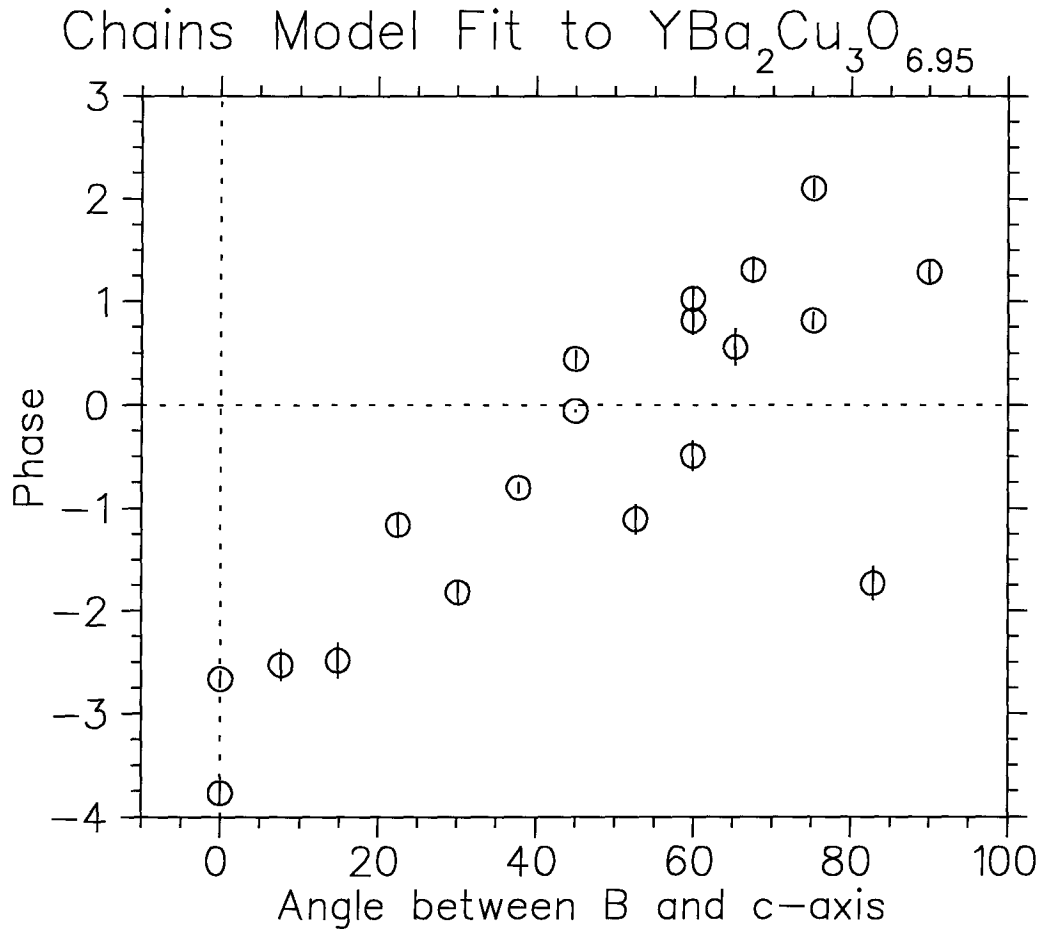


Figure 5.11: Initial phase obtained by fitting the data to the chains model in an applied field of 100 G.

5.4.3.2 Results of Fits to the Chains Model

Fig. 5.11 shows the angular dependence of the initial phase which is produced by muon rotation in flight through the fringe fields produced by Omni Prime's magnets and by the TRIUMF cyclotron.

Fig. 5.12 shows the angular dependence of λ_{ab} ($\lambda_{ab} = \Gamma^{-1/3}\bar{\lambda}$), which must be constant if $\Gamma = 5$ as was assumed and if the chains model used to calculate theoretical polarizations was correct. The penetration depth varies $\pm 0.0058 \mu\text{m}$, with an apparent period of approximately 66° . If the anisotropy ($\Gamma = 5$) were grossly underestimated, one would expect that $\lambda_{ab}(\theta)$ would show a clear increase with increasing angle. It is not clear how the apparent behavior of $\lambda_{ab}(\theta)$ relates to any possible deficiencies in the model used.

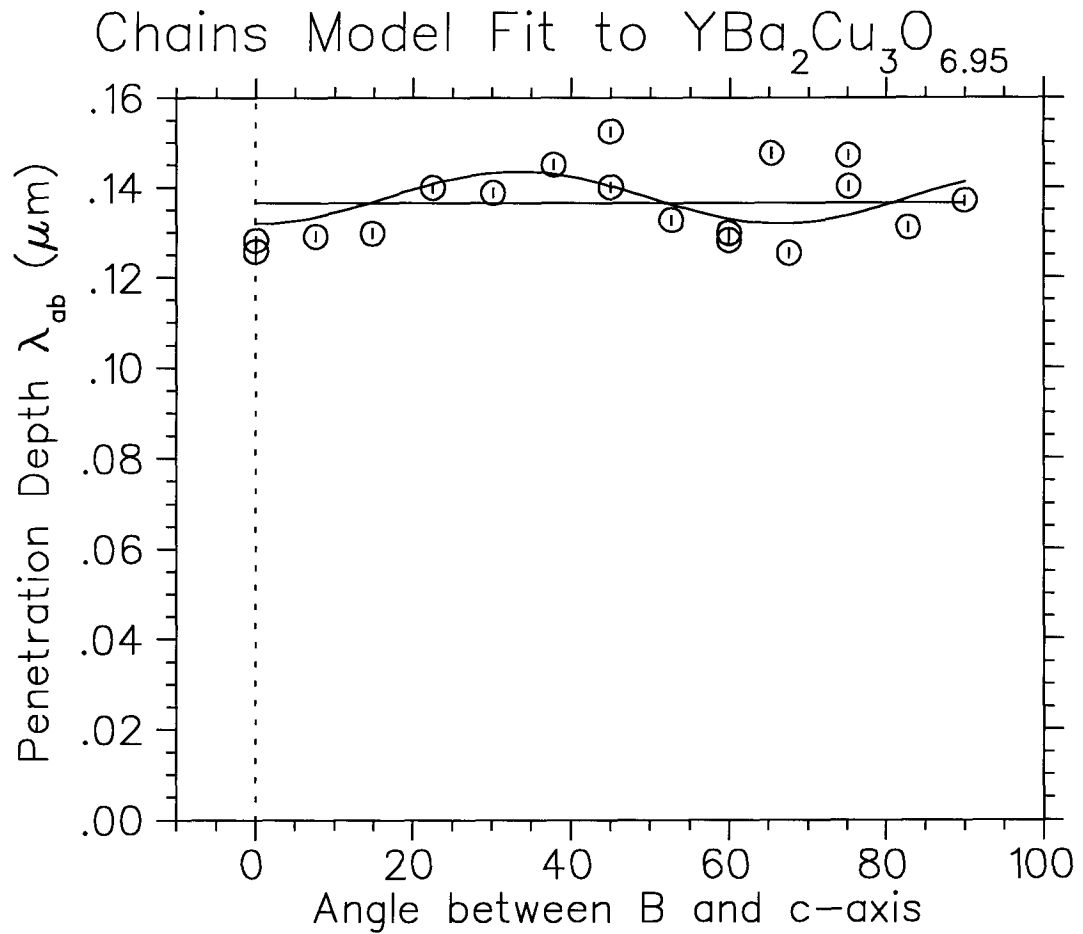


Figure 5.12: λ_{ab} obtained from fits to the chains model assuming $\Gamma = 5$ with an applied field of 100 G. The straight line is a fit to a constant $\lambda_{ab} = 0.1345 \pm 0.0019 \mu\text{m}$. The curve shows the function $\lambda_{ab} = \langle \lambda_{ab} \rangle + \delta \lambda_{ab} \sin(c\theta + \phi_{\text{wig}})$ with ϕ_{wig} fixed to -90° , $\langle \lambda_{ab} \rangle = 0.1377 \pm 0.0019 \mu\text{m}$, $\delta \lambda_{ab} = 0.0058 \pm 0.0025 \mu\text{m}$ and $c = 5.42 \pm 0.91$ (corresponding to one oscillation every 66.44°).

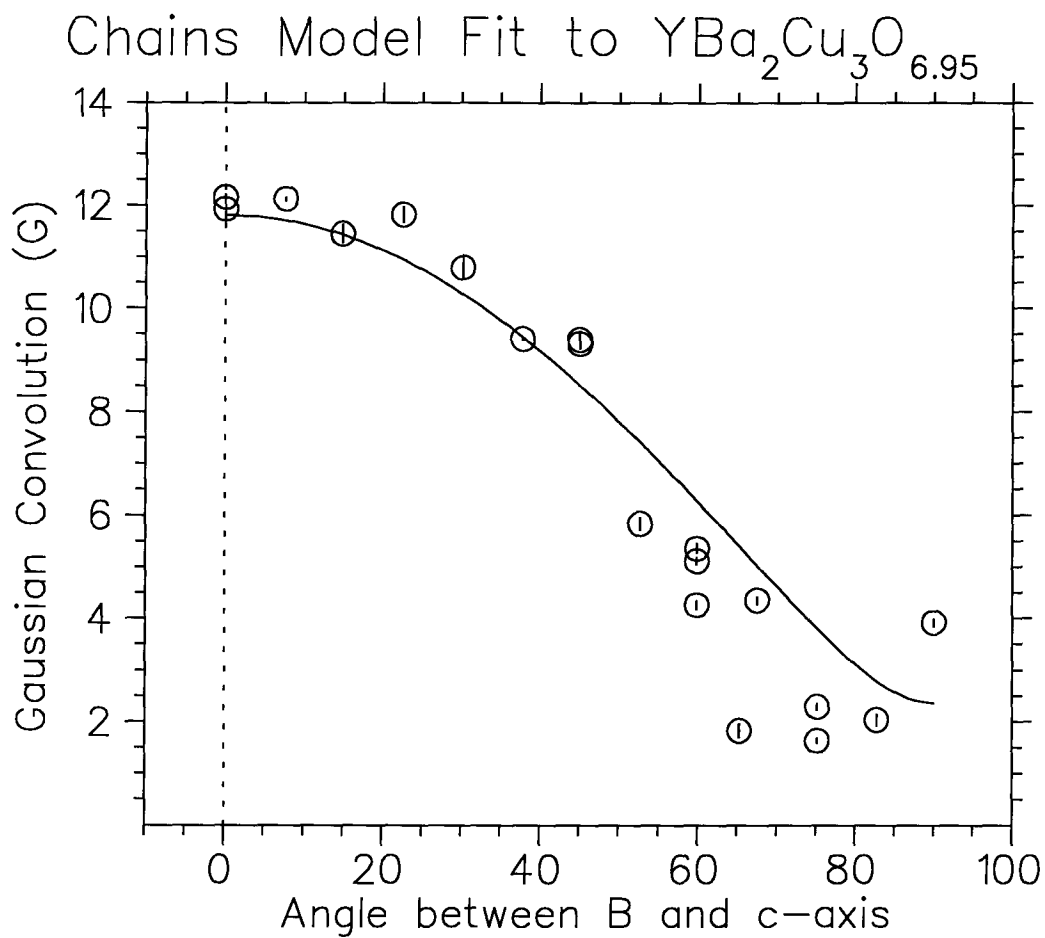


Figure 5.13: The width of the Gaussian convolution obtained from fits in the chains model assuming $\Gamma = 5$ with an applied field of 100 G. The curve shows the function $\sigma = \sigma_o[\Gamma^{-2} \sin^2(\theta) + \cos^2(\theta)]^{1/2}$, with $\sigma_o = 11.805 \pm 0.052$ G.

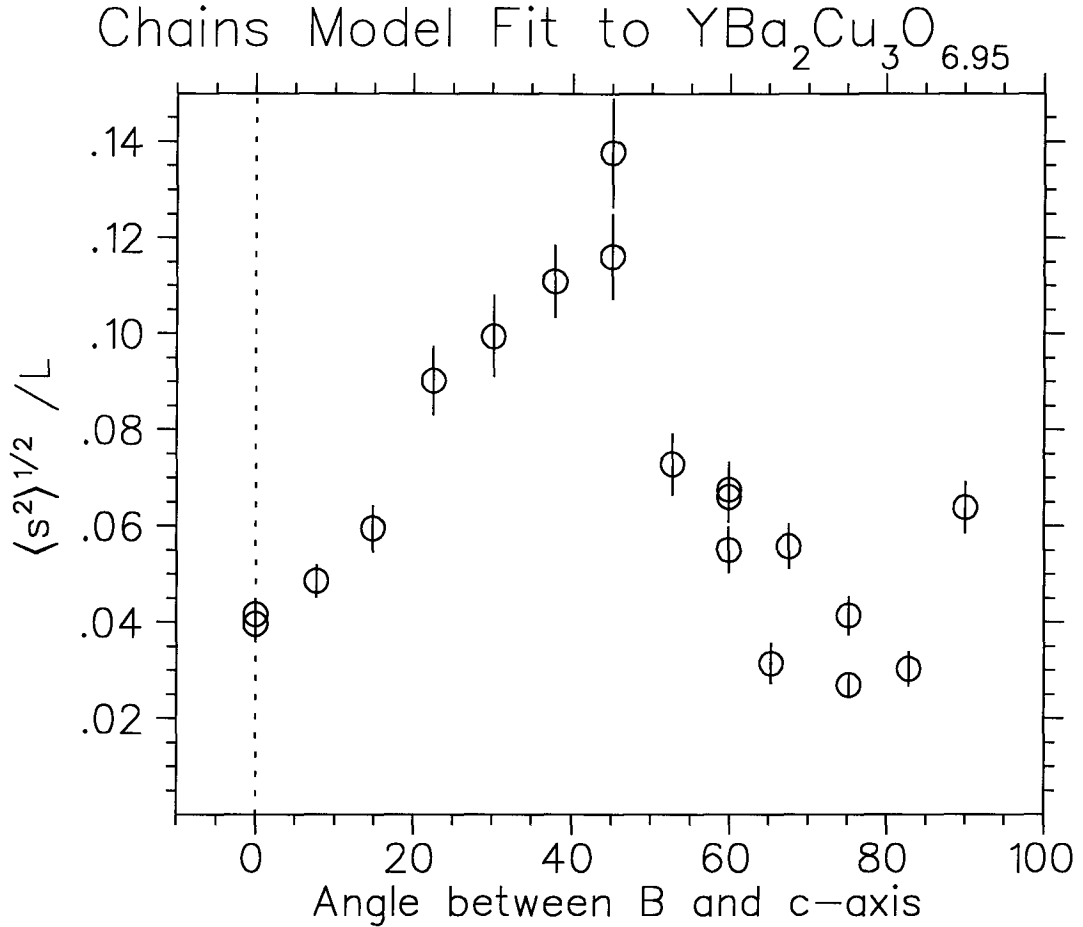


Figure 5.14: Deviation of vortices from their ideal positions in the FLL ($\langle s^2 \rangle^{1/2} / L$) as calculated from fits to the chains model with an applied field of 100 G.

Fig. 5.13 shows the angular dependence of the the width of the Gaussian convolution obtained from the fit to the chains model. Notice that the fit to the *Ansatz*

$$\sigma = \sigma_0 [\Gamma^{-2} \sin^2(\theta) + \cos^2(\theta)]^{1/2}, \quad (5.7)$$

assuming that $\Gamma = 5$ is not a particularly good one. A higher anisotropy ratio would fit somewhat better. Fig. 5.14 shows the deviation of vortices from their ideal positions in the FLL ($\langle s^2 \rangle^{1/2} / L$) as calculated from fits to the chains model. While $\langle s^2 \rangle^{1/2} / L$ is only about 4% at the lowest and highest angles, it leaps up to 12% at $\theta = 45^\circ$. The Lindemann criterion for a “melting transition” (for unpinned vortices) or a “glassy state” (for pinned, static vortices) is that the disorder exceeds about 10%.[89] It is also possible that the vortices are kinked, zig-zagging from one copper-oxygen layer to the next or from one twinning plane to the next; only at angles of $\theta = 0^\circ$ and 90° would

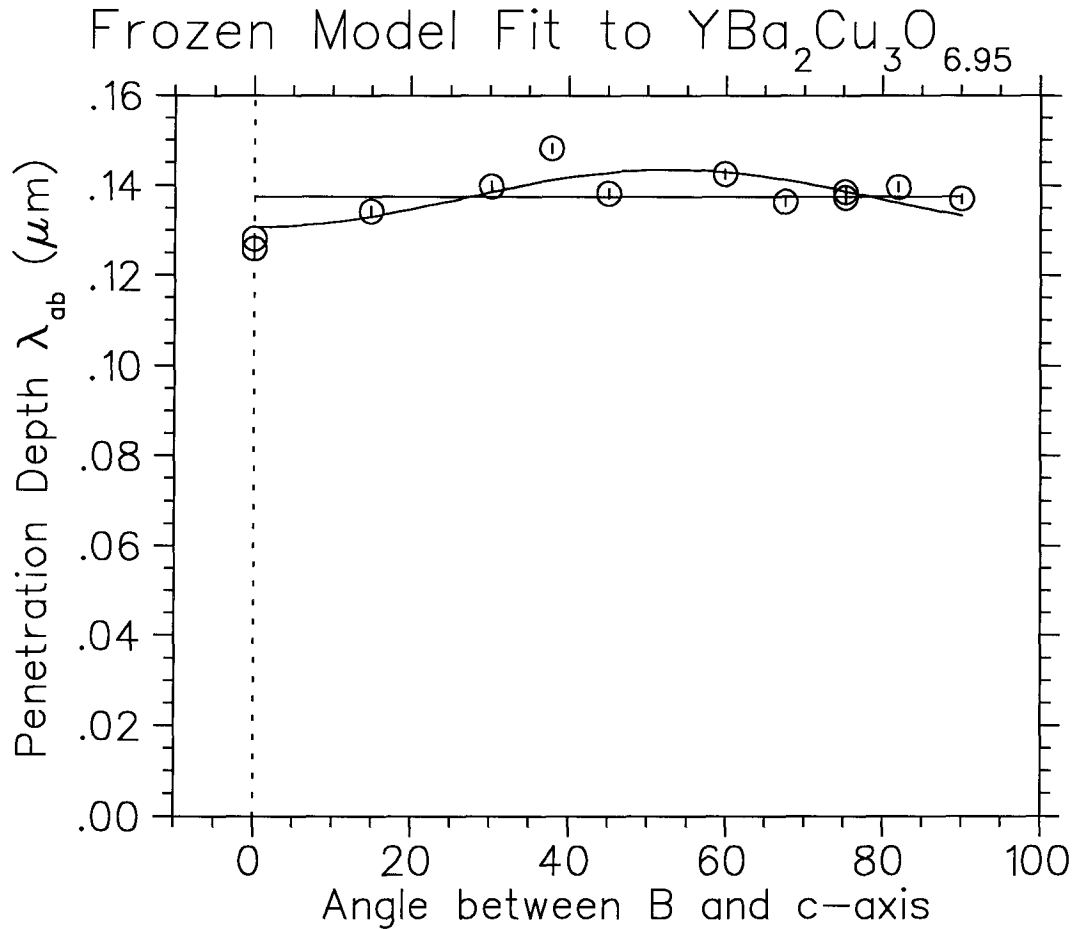


Figure 5.15: λ_{ab} obtained from fits to the frozen model assuming $\Gamma = 5$ with an applied field of 100 G. The straight line is a fit to a constant $\lambda_{ab} = 0.1376 \pm 0.0017 \mu\text{m}$. The curve shows the function $\lambda_{ab} = \langle \lambda_{ab} \rangle + \delta \lambda_{ab} \sin(c\theta + \phi_{\text{wig}})$ with ϕ_{wig} fixed to -90° , $\langle \lambda_{ab} \rangle = 0.1371 \pm 0.0014 \mu\text{m}$, $\delta \lambda_{ab} = 0.0064 \pm 0.0019 \mu\text{m}$ and $c = 3.41 \pm 0.26$ (corresponding to one oscillation every 105.7°).

they be relatively straight. Of course, the effect could be caused by misalignment of crystals in the mosaic or it could be that the model used is completely inappropriate. If the FLL is frozen in at a temperature close to T_c , the overall linewidth at a given angle θ that is not parallel to one of the principal axes will be wider (see Fig. 5.2); in that case, the apparent increased disorder occurs because the chains model ignores pinning.

5.4.3.3 Results of Fits to the Frozen Model

For the frozen model, fewer tables were made. Fig. 5.15 shows the angular dependence of the

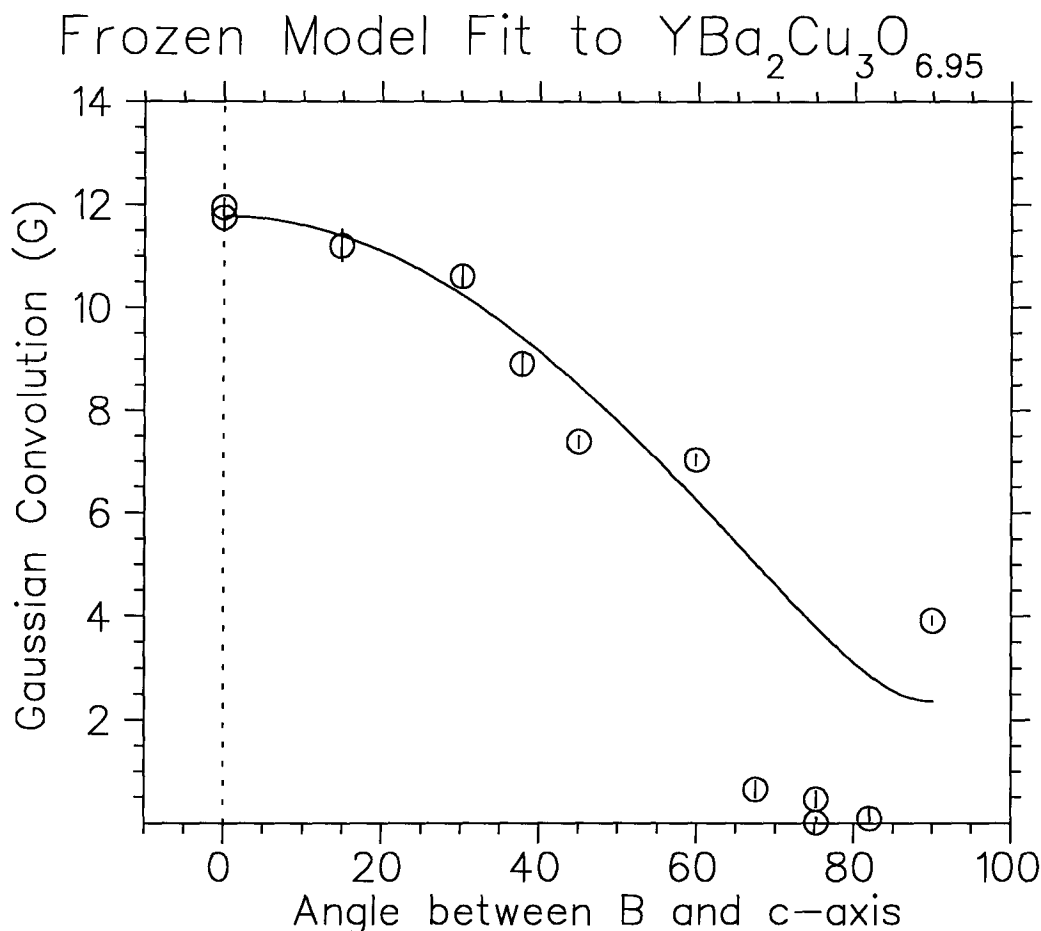


Figure 5.16: The width of the Gaussian convolution obtained from fits to the frozen model assuming $\Gamma = 5$ with an applied field of 100 G. The curve shows the function $\sigma = \sigma_o[\Gamma^2 \sin^2(\theta) + \cos^2(\theta)]^{1/2}$, with $\sigma_o = 11.77 \pm 0.31$ G.

penetration depth λ_{ab} in the frozen model assuming $\Gamma = 5$. Any apparent deviations from a constant $\lambda_{ab}(\theta)$ are somewhat smaller and have a longer period than those from fits to the chains model.

Fig. 5.16 shows the angular dependence of the width of the Gaussian convolution obtained from the fit to the frozen model. The width drops to zero for angles between 65° and 85° , which is an unphysical result, suggesting that either the effective angular dependence of the penetration depth is underestimated at these angles (implying that $\Gamma > 5$) or that the frozen model is inappropriate. The lineshape is relatively narrow at these angles (see Fig. 5.7), which means that there may not be enough information available to find both $\bar{\lambda}$ and the convolution width σ . Therefore, there is no

reason to take seriously the surprising result that the convolution width (and therefore $\langle s^2 \rangle^{1/2}/L$) goes to zero at high angles.

5.5 Discussion

The qualitative effects of the penetration depth anisotropy are clearly observable both in Fourier transforms and in simple gaussian fits. An anisotropy of 5 is consistent with the data.

Originally, we hoped to determine the geometry of the FLL by observing two cusps in the lineshapes, but disorder in the FLL (at least 4%) smeared the lineshape so much that most of the detail was lost.

We then tried to fit the data using polarization functions corresponding to models for the two extremes: the chains model in which the FLL is able to rearrange itself as the penetration depth decreases with decreasing temperature and the frozen model in which the FLL is fixed near T_c as pinning sets in. Gammel *et al.*[85] published flux decoration experiments on $\text{YBa}_2\text{Cu}_3\text{O}_{7-\delta}$ crystals in low field which showed that the FLL geometry was consistent with the FLL being frozen at about $T_{\text{irr}}/T_c = 0.92$. (Note that here T_{irr} corresponds to the average temperature at which the bulk of the FLL freezes. Other measurements, such as magnetization, define T_{irr} as the temperature at which irreversibility first sets in.) This suggests that the frozen model (for which we assume $T_{\text{irr}} = T_c$) should be closer than the chains model to the true situation. The bizarre results we obtained from fits to the frozen model at the higher angles may have occurred because the irreversibility temperature is a function of angle, decreasing with increasing θ or we may have assumed too small a value for Γ . Ideally, the frozen model should be modified to fix the geometry at $T_{\text{irr}}(\theta)$.

Fits to both the chains model and the frozen model were difficult and time consuming because both $\bar{\lambda}^{-2}$ and σ contribute to the linewidth of the superconducting signal. Fits at angles above $\theta = 60^\circ$ are particularly difficult due to the narrowness of the lineshape. Analysis with an improved model would be circuitous since that would require data for T_{irr} from flux decoration experiments which already purport to measure what we are looking for. However, the existence

of transverse field components in the superconducting state could be confirmed by μ SR by inspecting the angular dependence of the asymptotic polarization projections $P_x(t \rightarrow \infty; \hat{P}_o = \hat{x})$ and $P_z(t \rightarrow \infty; \hat{P}_o = \hat{x})$ in the case of an TF experiment or by looking for an oscillatory signal in the projections $P_x(t; \hat{P}_o = \hat{z})$ and $P_y(t; \hat{P}_o = \hat{z})$ which is not present above T_c in the case of a LF experiment (see Sec. 4.5.2.)

While the fits of $\text{YBa}_2\text{Cu}_3\text{O}_{6.95}$ data in low fields to the full theoretical polarization functions are quantitatively inconclusive beyond confirming the degree of anisotropy, they do serve as a proof of principle: one can indeed use a full vectorized treatment of the muon polarization with nonsymmetric field distributions. Perhaps this technique could be used to identify muon sites in magnetically ordered systems (antiferromagnetic or ferromagnetic) or to study other systems with distinctive local field distributions. Qualitatively, the Fourier transforms of this data (Fig. 5.7) show an asymmetric lineshape characteristic of the field distribution in a FLL and have minimum fields which are distinctly larger than zero gauss, which demonstrates that the FLL is *not* completely random at low fields due to strong pinning, as suggested by Gorbunov and Smilga.[90]

Chapter 6

Intermediate Fields

6.1 Introduction

The London model (Ch. 4) is in the “high field” limit when the magnetic penetration depth λ is greater than the distance between vortices $L = \sqrt{2\phi_o/\sqrt{3}B_o}$. Because the anisotropy in the \hat{a} - \hat{b} plane in $\text{YBa}_2\text{Cu}_3\text{O}_{6.95}$ is relatively small, the isotropic equations (Eqs. 4.17 and 4.18) can be used when the applied field \vec{B} is parallel to \hat{c} . In the high field limit, this produces a μSR lineshape in which “horizontal scale” parameters, such as the distance from the cusp field to the average field and the square root of the second moment, are independent of field and proportional to λ^{-2} . At lower fields ($\lambda < L$) the linewidth is smaller, as described in Ch. 5.

In the experiments and calculations discussed in this chapter, the applied field is always parallel to the superconductor’s \hat{c} axis. The anisotropic London model that is used assumes that there is no anisotropy in this configuration, *i.e.* $m_1 \equiv m_2$ in Sec. 4.2; therefore the isotropic treatment is sufficient when $\vec{H} \parallel \hat{c}$. In fact, there is a small anisotropy in the \hat{a} - \hat{b} plane, approximately 1.15 in the magnetic penetration depth in $\text{YBa}_2\text{Cu}_3\text{O}_{6.95}$. [91] However, since the applied field is along one of the superconductor’s principal axes, the lineshape has very nearly the same shape for either an isotropic or an anisotropic penetration depth and μSR is sensitive to only the average magnetic penetration depth (see Ref. [65].)

The London model assumes that the Ginzburg–Landau parameter $\kappa = \lambda/\xi$ is much larger than one. It treats the vortex core as a singularity ($B_{\text{core}} \rightarrow \infty$) in the local magnetic field. This breaks down when the spacing between vortices is within one or two orders of magnitude of the coherence length ξ , which is approximately the radius of the vortex core. While modifying the London model with Eq. 4.32 partly compensates for the fact that the field is physically finite at the vortex core,

Ch. 7 provides a more complete treatment. The general result is a decrease in the linewidth of the μ SR lineshape. However, Ref. [92] shows that the linewidth is approximately constant when $\ln(B/H_{c2})$ lies in the range of -9 to -4 for $\kappa = 70$, so this range is more appropriately referred to as the “intermediate field regime” ($\lambda > L$ and $\xi \ll L$).

This chapter presents data taken in a mosaic of \hat{c} -axis aligned crystals of $\text{YBa}_2\text{Cu}_3\text{O}_{6.95}$ over a temperature range from 5 K to 120 K in a field of 0.25 T applied parallel to \hat{c} .* If we assume that $dH_{c2}/dT|_{T_c} = -1.65$ T/K,[5] then the sample is in the intermediate regime at this field below approximately 87 K. The mosaic, with an onset T_c of 93.5 K as measured by specific heat, was mounted with Apiezon N grease on a 99.9985% pure disk of silver, with the \hat{c} -axis perpendicular to the disk. The crystals covered an area 1.5 cm in diameter. (See Sec. 1.7 for a more detailed description of the sample.) A magnetic field of 0.25 T was applied parallel to the the \hat{c} -axis of the crystals. The muons stopped in the bulk of the sample with their spins perpendicular to the applied field and precessed at a rate proportional to the local field.

6.2 Analysis and Results

The error bars shown in the figures are MINOS errors for the superconducting signal and MIGRAD errors for the background signal, where MINOS and MIGRAD are χ^2 minimization routines in CERN’s fitting package used in the μ SR program MSRFIT. As discussed in Sec. 5.4.3.1, the MIGRAD error estimates are based on the correlation between parameters, whereas MINOS error estimates are determined for each parameter by stepping its value along, allowing all other parameters to vary in a new χ^2 minimization at each position, and defining one standard deviation as the change in value that increases the otherwise minimal χ^2 by one. The fit parameters and errors quoted for the curves through the data were calculated from a weighted least squares fit (also known as χ^2 minimization) using the Gauss-Newton method, as implemented in TRIUMF’s PLOTDATA program.

In a real superconductor, imperfections in the vortex lattice “smear” the ideal lineshape. One

*The data in this chapter was originally presented in Ref. [93].

can directly fit the experimental μ SR lineshape to a range of ideal lineshapes (as a function of λ_{ab}) convoluted with a range of Gaussians (as a function of width σ). The best fit for a high statistics run at 10 K (Fig. 3.5) with the average internal field fixed to $B_o = 2494.7$ G (3.8 G less than the applied field) has $\lambda_{ab} = 0.1405 \pm 0.0092$ μm and $\sigma = 17.7 \pm 2.4$ G. (The corresponding asymmetry spectrum for the 10 K run is shown in Fig. 3.4.) Assuming a flux expulsion of only 0.5 G reduces the penetration depth by one-half of its uncertainty, to $\lambda_{ab} = 0.1352 \pm 0.0088$ μm with $\sigma = 18.1 \pm 2.4$ G. Magnetization measurements (Sec. 4.9) in a single crystal from the mosaic suggest that the flux expulsion from the mosaic as a whole should be 0.65 G. The ideal superconducting lineshape has a cusp at a field lower than the applied field (see Fig. 4.3). After convoluting, the distance from the average field to the cusp field is reduced by 25%. If the convolution truly reflects the disorder in the vortex lattice due to pinning and the disorder is frozen in place as the sample is field-cooled through the irreversibility temperature (a few degrees below T_c), one would expect σ to have the same temperature dependence as $\lambda^{-2}(T)$.

6.2.1 Fits to Exponentials

Because the high field tail stretches to an extremely high field, it is very difficult to fit the London lineshape with the average field as a free parameter; nevertheless, it can be done for runs with high statistics. Since only the 10 K and 70 K runs have high statistics, another method for estimating the temperature dependence of the penetration depth was required for the bulk of the data. I have adopted the following empirical approach: The μ SR data, representing the muon polarization as a function of time, were fit using a pair of exponentials sharing the same phase:

$$A(t) = A_1 e^{-\Lambda_1 t} \cos(2\pi\nu_1 t + \phi) + A_2 e^{-\Lambda_2 t} \cos(2\pi\nu_2 t + \phi) \quad (6.1)$$

where the average field B_i is given by $\nu_i = \frac{\gamma_\mu}{2\pi} B_i$ and the exponential relaxation rate Λ_i is proportional to the spread of the local fields: $\Lambda_i = \gamma_\mu (\delta B_i)$. This is equivalent to fitting a pair of Lorentzians centered about ν_1 and ν_2 to the Fourier transform (which corresponds to a probability distribution of local fields). One Lorentzian represents the background signal from muons stopping in the silver disk rather than in the crystals. The other Lorentzian represents the cusp region of the superconducting signal, with the average field reflecting the experimental cusp field and the

full width at half maximum reflecting both the intrinsic linewidth of the ideal lineshape and the “smearing” due to imperfections in the vortex lattice. A pair of Gaussians was also tried,

$$A(t) = A_1 e^{-\frac{1}{2}(\sigma_1 t)^2} \cos(2\pi\nu_1 t + \phi) + A_2 e^{-\frac{1}{2}(\sigma_2 t)^2} \cos(2\pi\nu_2 t + \phi) \quad (6.2)$$

where the Gaussian relaxation rate σ_i is proportional to the spread of local fields $\sigma_i = \gamma_\mu(\delta B_i)$, but the fits were much worse and the average field of the “superconducting” Gaussian did not correspond to the experimentally observed cusp field. Neither empirical function accurately describes the “tail” region corresponding to the logarithmic increase of the local field at the vortex core, so this empirical method is used only to reveal the qualitative temperature dependence and should not be considered a valid means of determining λ quantitatively.

The exponential fit values for superconducting signal are shown in Fig. 6.1 as a function of temperature. The temperature dependence of the exponential’s average field (Fig. 6.1.a) was fit to

$$B_c(T) - B_{\text{ap}} = \Delta B_c \left[1 - \left(\frac{T}{T_c} \right)^p \right] + c_B \frac{2}{\pi} \arctan \left(\frac{T - T_c}{c_T} \right) \quad (6.3)$$

between $T = 0$ and $T = 87$ K, the range over which the lineshape width (measured here by the shift of the cusp field from the average field) should be proportional to λ^{-2} . The arctangent approximately represents the expected temperature dependence of the flux expulsion, with c_T fixed to a value of -1.378 K (from magnetization measurements) and c_B varying. The critical temperature T_c was fixed to its onset value of 93.5 K. Since only the points with temperatures below 87 K were considered for the fit, details of how the flux is expelled are unimportant; only the total flux expulsion c_B affects the fit. In Fig. 6.1.a the average magnetic field of the exponential fit to the the cusp field is fairly well described by a power law with $p = 2.61 \pm 0.13$ and a flux-expulsion constant $c_B = -3.68 \pm 0.64$ G. Weak coupling s -wave BCS theory fits the temperature dependence of the cusp frequency almost as well,

$$B_c(T) - B_{\text{ap}} = \Delta B_{\text{BCS}}(T) + c_B \frac{2}{\pi} \arctan \left(\frac{T - T_c}{c_T} \right) \quad (6.4)$$

with $c_B = -6.07 \pm 0.47$.

If flux expulsion c_B is fixed to the value of -0.65 G inferred from magnetization measurements (see Sec. 4.9), the exponent of the temperature dependence of the cusp field is increased to

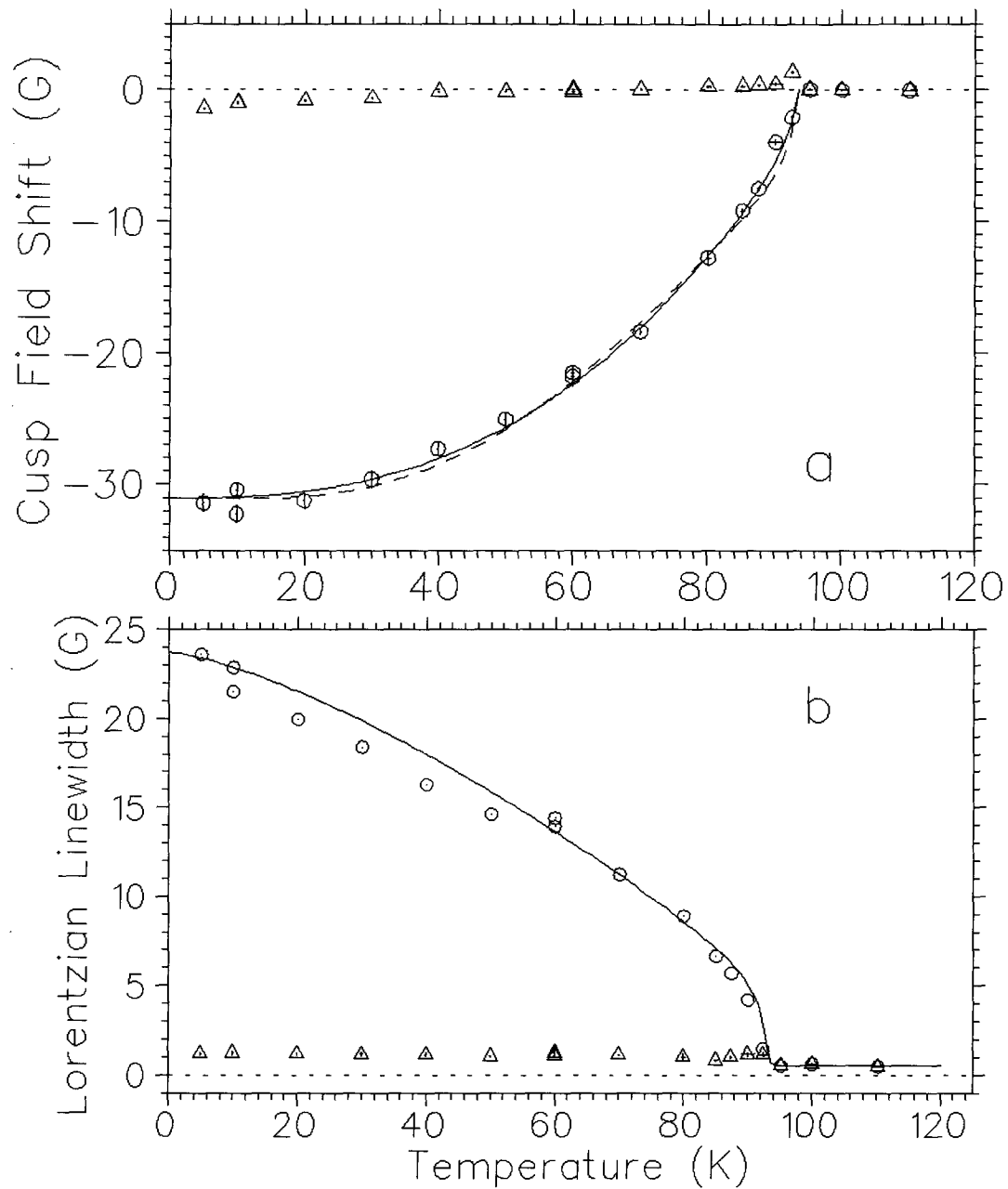


Figure 6.1: Results of fitting μ SR data taken at 2498.5 G with two exponentials.

(a) Shift of the average field of the two exponentials (triangles: background signal; circles: cusp region of superconducting signal) relative to the applied field. The solid line is a least squares fit to Eq. 6.3 with $\Delta B_c = -27.39 \pm 0.64$ G, $p = 2.61 \pm 0.13$, and $c_B = -3.68 \pm 0.64$ G. The dashed line is a fit to a weak-coupling s-wave BCS model, with $\Delta B_{\text{BCS}}(0) = -24.967 \pm 0.76$ G, $c_B = -6.07 \pm 0.47$ G. For both fits, c_T is fixed to -1.378 K.

(b) Lorentzian linewidths; (triangles: background signal; circles: cusp region of superconducting signal). The solid line is a fit to Eq. 6.5 with $\Delta B_c = 17.93 \pm 0.70$ G, $p = 1.38 \pm 0.17$ and $c_G = -4.74 \pm 0.60$ G, with c_T fixed to -1.378 K.

$p = 3.14 \pm 0.14$ G (see Fig. 6.2). If flux expulsion c_B is fixed to the value of 0.0 G, *i.e.*, no flux expulsion, the temperature dependence increases to $p = 3.26 \pm 0.17$ G (see Fig. 6.3). Note that results shown in Figs. 6.2 and 6.3 are nearly indistinguishable.

It is reasonable to assume that the field gradient produced across the sample when pinning interferes with flux expulsion should be no greater than the size of the flux expulsion. Therefore, the linewidth should be fitted with an expression similar to Eq. 6.3, namely

$$\Lambda(T) = \Delta B_c \left[1 - \left(\frac{T}{T_c} \right)^p \right] + c_G \frac{2}{\pi} \arctan \left[\frac{T - T_c}{c_T} \right]. \quad (6.5)$$

Note that the effective Lorentzian linewidth shown in Fig. 6.1.b has an almost linear temperature dependence, with $p = 1.38 \pm 0.17$ when c_G is allowed to vary. The term $c_G = 4.74 \pm 0.60$ G may represent a field gradient due the effects of pinning on the flux expulsion process; it is of the same order of magnitude as the flux expulsion seen in Fig. 6.1.a. A pair of exponentials was chosen over a pair of Gaussians because they fit the cusp region better; however, the temperature dependence of the local field inhomogeneity due to the FLL and disorder is surprisingly linear. The temperature dependence of the field inhomogeneity and cusp field position for an ideal FLL will be identical in this field regime. If the disorder in the FLL is strongly temperature dependent, one might expect that the field inhomogeneity for the disordered FLL to have a somewhat weaker temperature than the cusp position, but not as much as implied by these exponential fits. Moreover, the field inhomogeneity is inconsistent with the temperature dependence of the Gaussian convolution, which represents the additional field inhomogeneity produced by disorder in the FLL, used in the fits to the proper lineshape reported in Chapter 7 (see Fig. 7.15).

As seen in Fig. 6.2.b, assuming the field inhomogeneity produced by flux expulsion and pinning (c_G) is equal to the size of the flux expulsion $c_B = -0.65$ G produces poor results. This suggests the possibility that the flux expulsion may be greater than the -0.65 estimated from the magnetization of a single crystal, perhaps because the sample is a mosaic with some holes rather than a single crystal.

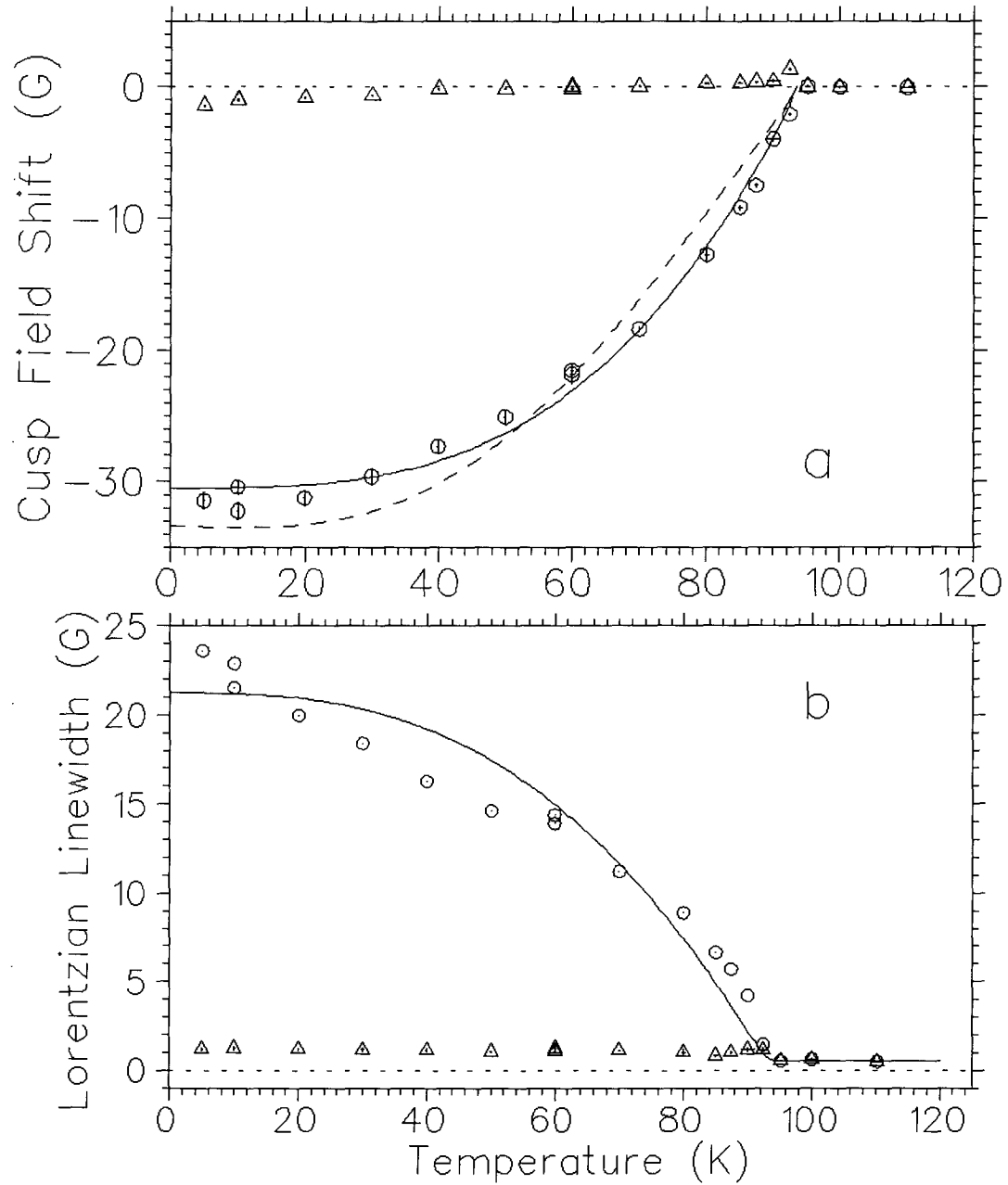


Figure 6.2: Results of fitting μ SR data taken at 2498.5 G with two exponentials.

(a) Shift of the average field of the two exponentials (triangles: background signal; circles: cusp region of superconducting signal) relative to the applied field. The solid line shows Eq. 6.3 with $\Delta B_c = -29.83 \pm 0.59$ G, $p = 3.14 \pm 0.14$ as determined by least squares fitting. The dashed line shows a weak-coupling *s*-wave BCS temperature dependence with $\Delta B_{\text{BCS}}(0) = -32.7 \pm 1.3$ G. For both curves, c_T is fixed to -1.378 K and c_B is fixed to -0.65 G.

(b) Lorentzian linewidths; (triangles: background signal; circles: cusp region of superconducting signal). The solid line shows Eq. 6.5 with $\Delta B_c = 21.3 \pm 1.1$ G, $p = 2.76 \pm 0.33$ with c_T fixed to -1.378 K and c_G fixed to -0.65 G.

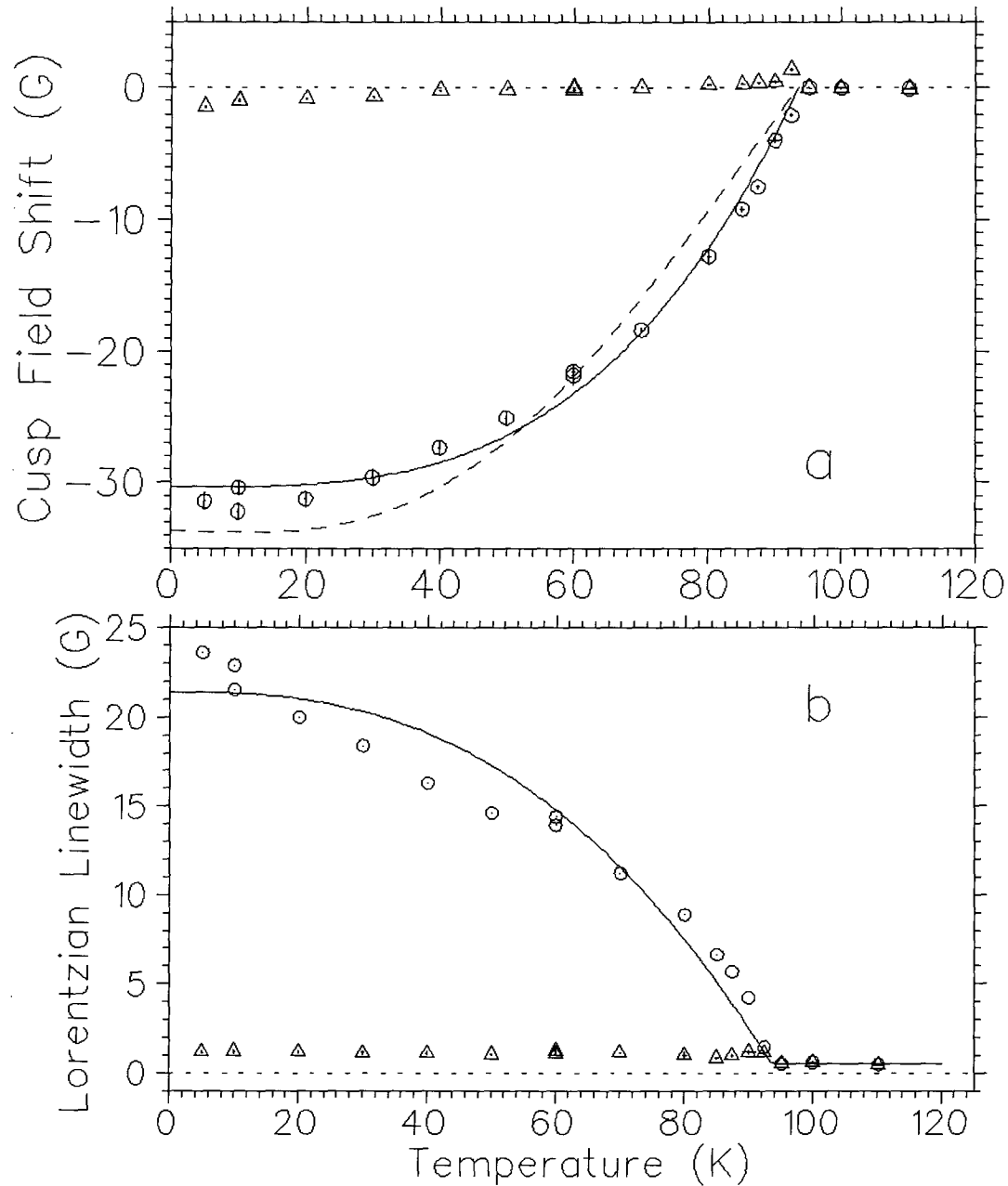


Figure 6.3: Results of fitting μ SR data taken at 2498.5 G with two exponentials.

(a) Shift of the average field of the two exponentials (triangles: background signal; circles: cusp region of superconducting signal) relative to the applied field. The solid line shows Eq. 6.3 with $\Delta B_c = -30.35 \pm 0.67$ G, $p = 3.26 \pm 0.17$ as determined by least squares fitting. The dashed line shows a weak-coupling *s*-wave BCS temperature dependence with $\Delta B_{\text{BCS}}(0) = -33.6 \pm 1.4$ G. For both curves, c_T is fixed to -1.378 K and c_B is fixed to 0.0 G.

(b) Lorentzian linewidths; (triangles: background signal; circles: cusp region of superconducting signal). The solid line shows Eq. 6.5 with $\Delta B_c = 20.9 \pm 1.0$ G, $p = 2.58 \pm 0.29$ with c_T fixed to -1.378 K and c_G fixed to 0.0 G.

6.2.2 Fits to Gaussians

While the fits to two exponentials (Eq. 6.1) produce better fits to the high statistic runs at 10 K and 70 K than do fits to two Gaussians (Eq. 6.2), it is important to present the Gaussian results for comparison purposes with previously reported μ SR results,[29,28,24,26,27] which used Gaussians to fit both unoriented and oriented samples. Fig. 6.4 shows the results of fitting the 2.5 kG data with two Gaussians, one representing the background signal and the other the cusp region. In this case, no fits are shown since a single power law (see Eqs. 6.3 and 6.5) cannot adequately fit the entire temperature range. In particular, both the field inhomogeneity as estimated by the Gaussian relaxation rate and the cusp field shift have a T^2 behavior over the temperature range 25 K to 80 K while they are approximately linear below 25 K.

6.3 Discussion and Conclusions

Since a power law such as that used in Eqs. 6.3 and 6.5 has no known theoretical basis, we should briefly consider a power law approximation to BCS[94] (see Fig. 6.5). The exponent $p = 2.27$ obtained by fitting the BCS temperature dependence with a power law is very close to the exponent $p = 2$ found for $\lambda^{-2}(T)$ by non- μ SR techniques.[95] Although the power law does not replicate the BCS plateau at low temperatures, the error in the values for $\lambda^{-2}(T)$ never exceeds 3%. In the low temperature region ($T < 0.2T_c$), μ SR may help to answer the following question about the behavior of $\lambda^{-2}(T)$: [96,11]

- Is the sample an s -wave superconductor, with

$$1 - \frac{\lambda^2(0)}{\lambda^2(T)} \sim e^{-\Delta_0/k_b T} (2\pi\Delta_0/k_b T)^{1/2}, \quad (6.6)$$

- or does it have a superconducting ground state with low-lying excitations so that

$$1 - \frac{\lambda^2(0)}{\lambda^2(T)} \sim T^p? \quad (6.7)$$

Some possibilities which produce low lying excitations that are frequently discussed are triplet p -wave, d -wave with point or line nodes and magnetic impurities.[96,11] In particular line nodes

will produce a linear temperature dependence. Moreover, often many more than one possibility can produce identical behavior. Impurity effects are expected to change the temperature dependence towards T^2 at the lower temperatures for both d -wave (normally T^1) and s -wave (normally exponential behavior) superconductors. This may explain the T^2 behavior observed in Ref. [95], where the sample was a thin film.

Neither empirical function (two exponentials or two Gaussians) could be expected to fit all features of the experimental data accurately since both have symmetric field distributions while the FLL produces a very asymmetric distribution. It is rather surprising, however, that they produce such different results when all features of the disorder FLL's lineshape are expected to have the same temperature dependence below the irreversibility temperature in the intermediate field of 2.5 kG. Except for the cusp field in the case of the exponential fits, the *ad hoc* analyses seems to suggest a linear temperature dependence at low temperatures, which has been confirmed by more accurate microwave measurements[97,98] and by very recent high statistics μ SR measurements.[99] In the present data, the scatter at lower temperatures is too large to confidently determine the exact temperature dependence, and hence the general characteristics of the gap (uniform, line nodes or point nodes, *etc.*) cannot be unambiguously determined.

In the μ SR literature, unoriented sintered powders of $\text{YBa}_2\text{Cu}_3\text{O}_{7-\delta}$ [24,25] are fit to Gaussians over the entire temperature range and the temperature dependence of the Gaussian relaxation rate is typically fitted with the Gorter-Casimir version of the two-fluid model (a power law with exponent $p = 4$). The Gorter-Casimir behavior is an *ad hoc* description which only comes close to BCS predictions for strong-coupling s -wave superconductors. If the exponent p in Eq. 6.3 is allowed to float, it typically varies between 3.2 and 3.5 for unoriented powders for fits over the *entire* range. Fig. 6.6 shows two unoriented sintered powder samples of $\text{YBa}_2\text{Cu}_3\text{O}_x$, one with an oxygen concentration of $x = 6.556$ (originally published in Ref. [26]) and the other with $x = 6.95$ (originally published in Ref. [100]). They show a power law temperature dependence with exponents $p = 3.33 \pm 0.37$ and $p = 3.40 \pm 0.24$ respectively, assuming no additional inhomogeneity due to partial flux expulsion. Note that in the higher quality experiments on unoriented powders, such as in Ref. [26], the low temperature points deviate from the fits in a way which suggests

a small linear temperature dependence. In particular, no μ SR experiment on high temperature superconductors with sufficient number of data points shows completely flat behavior at low temperatures.

In our mosaic of oriented single-crystal $\text{YBa}_2\text{Cu}_3\text{O}_{6.95}$, the temperature dependence of $\lambda^{-2}(T)$ inferred from the cusp frequency (from exponential fits) was found to fit Eq. 6.3 with an exponent p varying between 2.61 ± 0.13 and 3.26 ± 0.17 depending on the amount of flux expulsion assumed. If these data were treated the same way as published data on the linewidth of unoriented sintered powders (*i.e.*, ignoring the flux expulsion and including the points near T_c where the London model breaks down) the exponent $p = 3.26 \pm 0.17$ from fits to exponentials would still be somewhat lower than that observed in the unoriented powders fit with Gaussians. Using the results from Gaussian fits or the field inhomogeneity from the exponential fits would give a decidedly weaker temperature dependence. Therefore, the temperature dependence seen in the oriented single crystals ($\vec{B} \parallel \hat{c}$) is inconsistent with that seen in unoriented sintered powders. It is not clear whether this difference is due to the effects of morphology (mm^2 -sized platelet-shaped crystals *vs.* ≈ 50 micron sintered crystallites and different filling factors) on the pinning behavior or weak links, or due to a temperature dependent anisotropy factor which affects the powder averaged linewidth for the unoriented samples.[101] The data presented here certainly do not exhibit the plateau at low temperatures characteristic of weak-coupling BCS *s*-wave superconductivity. However, since this analysis does not unambiguously show the temperature dependence of the magnetic penetration depth, we must turn to high field lineshapes and a less empirical treatment.

Certainly, single crystals are preferable over unoriented powders for measuring the temperature dependence of magnetic penetration depth because the issue of the anisotropy is less important, the lineshape is more distinctive, and the crystals are freer of impurities and microscopic defects. Neither fits with exponentials nor fits with Gaussians provide consistent results. Even when taken at face value, the temperature dependence determined can be strongly influenced by assumptions such as the amount of flux expulsion. Full fits were not feasible due to low statistics, but even with high statistics, full fits are difficult to do and produce results with a certain amount of scatter due to the increase in the number of variables which change the fitting function in a similar

fashion. The lesson here is that *even* when dealing with single crystal data, the details of how the temperature dependence of magnetic penetration depth is inferred must be carefully examined for unintentional biases, and conclusions regarding the temperature dependence must be made conservatively.

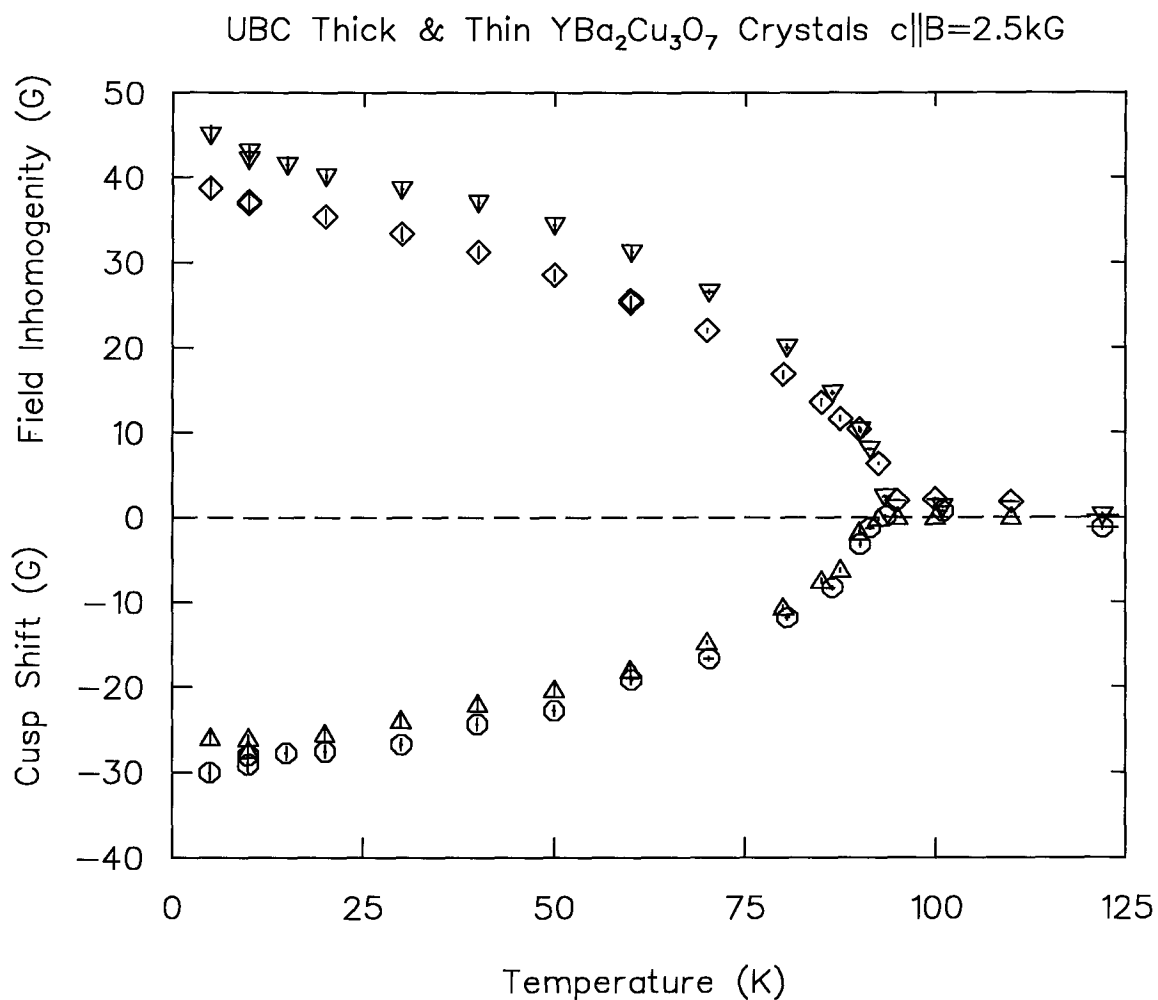


Figure 6.4: Results of fitting μSR data taken at 2498.5G with two Gaussians. The top shows temperature dependence of the Gaussian field inhomogeneity (thin sample [diamonds] and thick sample [upside down triangles]) and the bottom shows the cusp field (thin sample [triangles] and thick sample [circles]). The “thin” sample is the same one used in Chapters 5 and 7 and in Figs. 6.1 through 6.3 in this chapter. The “thick” sample differs in containing crystals with thickness 300 to $500\ \mu\text{m}$ rather than 200 to $300\ \mu\text{m}$.

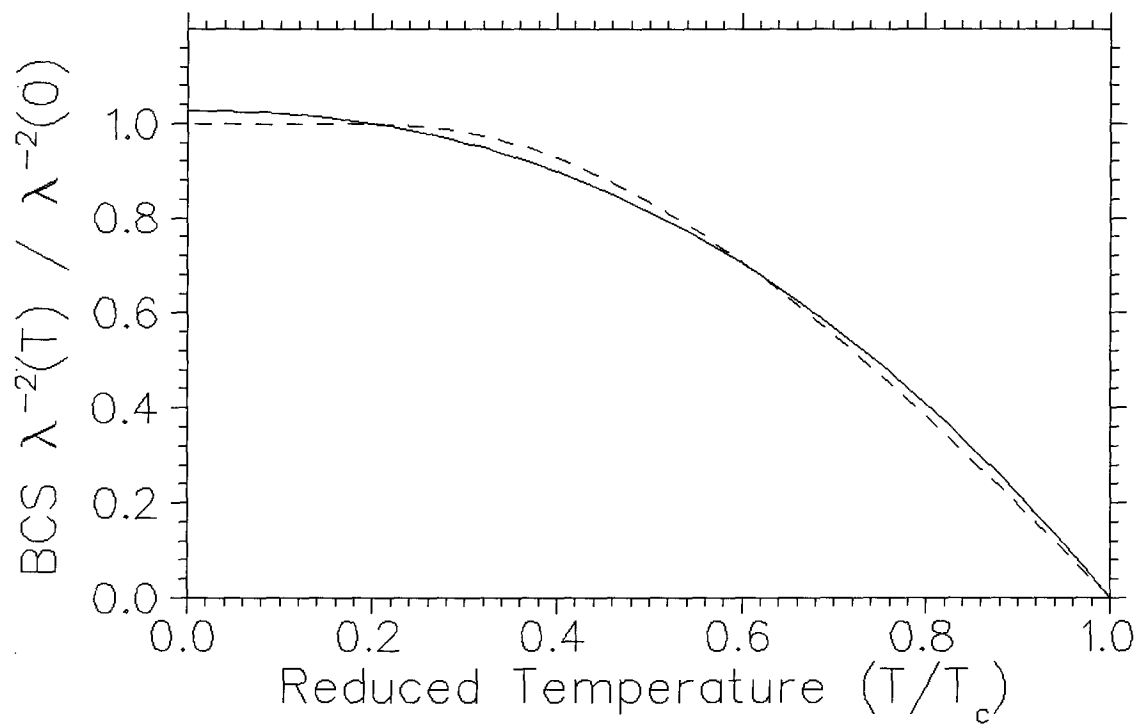


Figure 6.5: Fit of the BCS dependence of $[\lambda(0)/\lambda(T)]^2$ (dashed line) to a power law (solid line), The exponent is 2.2685 ± 0.0385 and the normalization is 1.0270 ± 0.0056 .

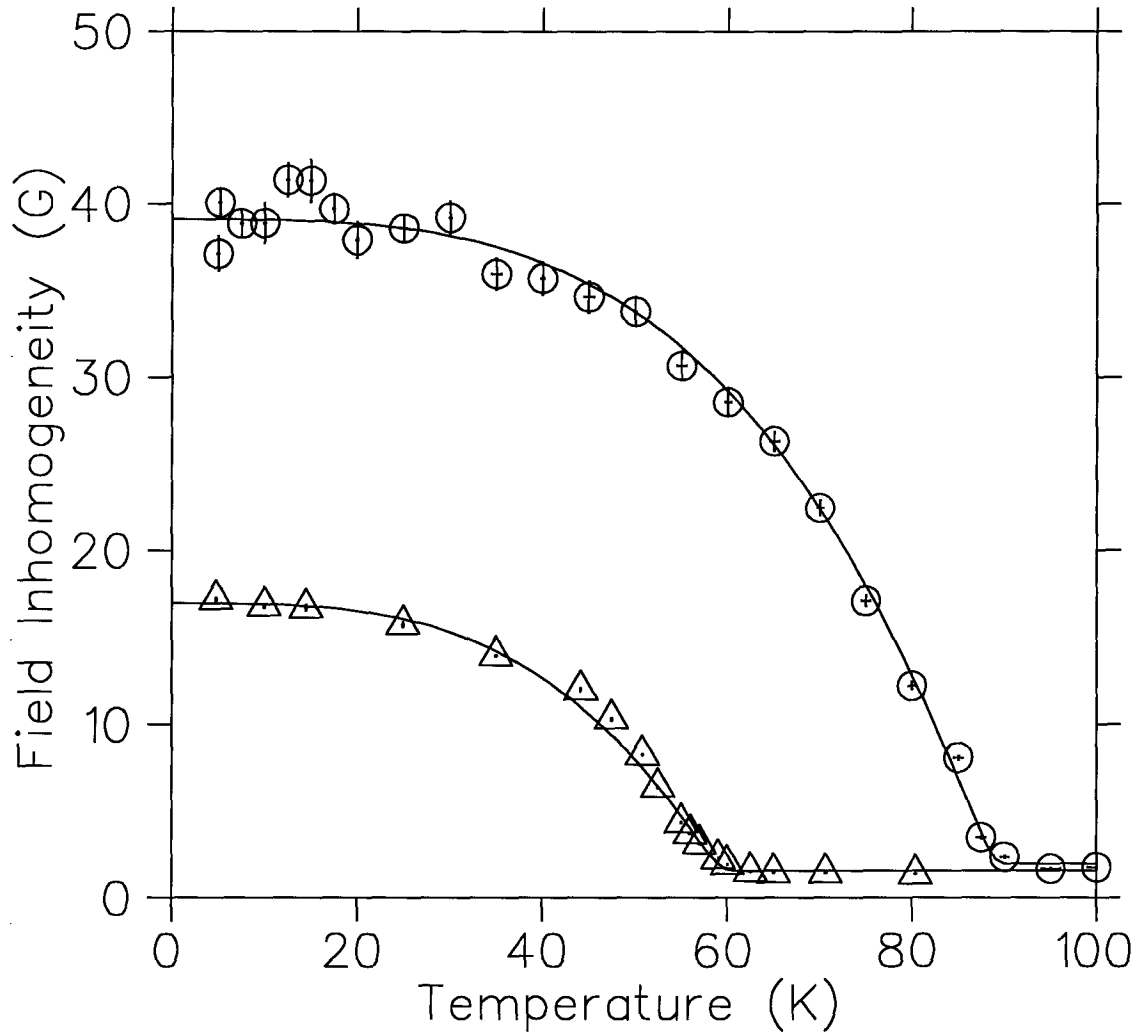


Figure 6.6: Field inhomogeneity (as estimated by Gaussian fits) in unoriented sintered powder samples of $\text{YBa}_2\text{Cu}_3\text{O}_{6.556}$ (triangles) and $\text{YBa}_2\text{Cu}_3\text{O}_{6.95}$ (circles). The fits are to a power law temperature dependence with exponents $p = 3.33 \pm 0.37$ and $p = 3.40 \pm 0.24$ respectively.

Chapter 7

High Field Lineshapes; Determination of H_{c2} and κ

7.1 Introduction

At higher fields ($B \gtrsim 0.05H_{c2}$, where H_{c2} is the upper critical field), the area occupied by the vortex core, which has a radius of approximately the coherence length ξ , becomes significant relative to the unit cell of the flux line lattice (FLL). This means the maximum field in the vortex core has a non-negligible amplitude in the μ SR lineshape; this shows up as an upper field cutoff when $B \gtrsim 0.05H_{c2}$. In such high fields, the lineshape is determined by ξ as well as by the magnetic penetration depth λ (see Fig. 7.1).

This chapter presents μ SR data taken in fields of 1.9 T, 4.1 T, 4.7 T and 6.5 T, between temperatures of 10 K and 75 K. An extensive analysis is presented using a modified London model, which introduces a cutoff in the reciprocal lattice vectors (\vec{K}) to make the field finite at the vortex core and introduces a term $(1 - B_o/H_{c2})$ to take into account the field dependence of the superconducting order parameter. When the applied field is below about 25% of H_{c2} , the lineshape produced by this model matches the features of the exact theoretical lineshapes produced from Gorkov's equations[31,75] while being relatively easy to express mathematically. The Gorkov treatment requires assumptions about the Fermi surface and the degree of strong coupling in order to calculate the field distribution. The effects of faulty assumptions must be disentangled from the temperature dependence found for λ and ξ . On the other hand, the modified London model, being phenomenological, needs no such assumptions in order to calculate the field distribution. The effects of the Fermi surface, strong coupling and so on may be inferred from the temperature dependence found for λ and ξ . The simplicity of the modified London model allows the recasting of results presented here in terms of other models, be they conventional or exotic.

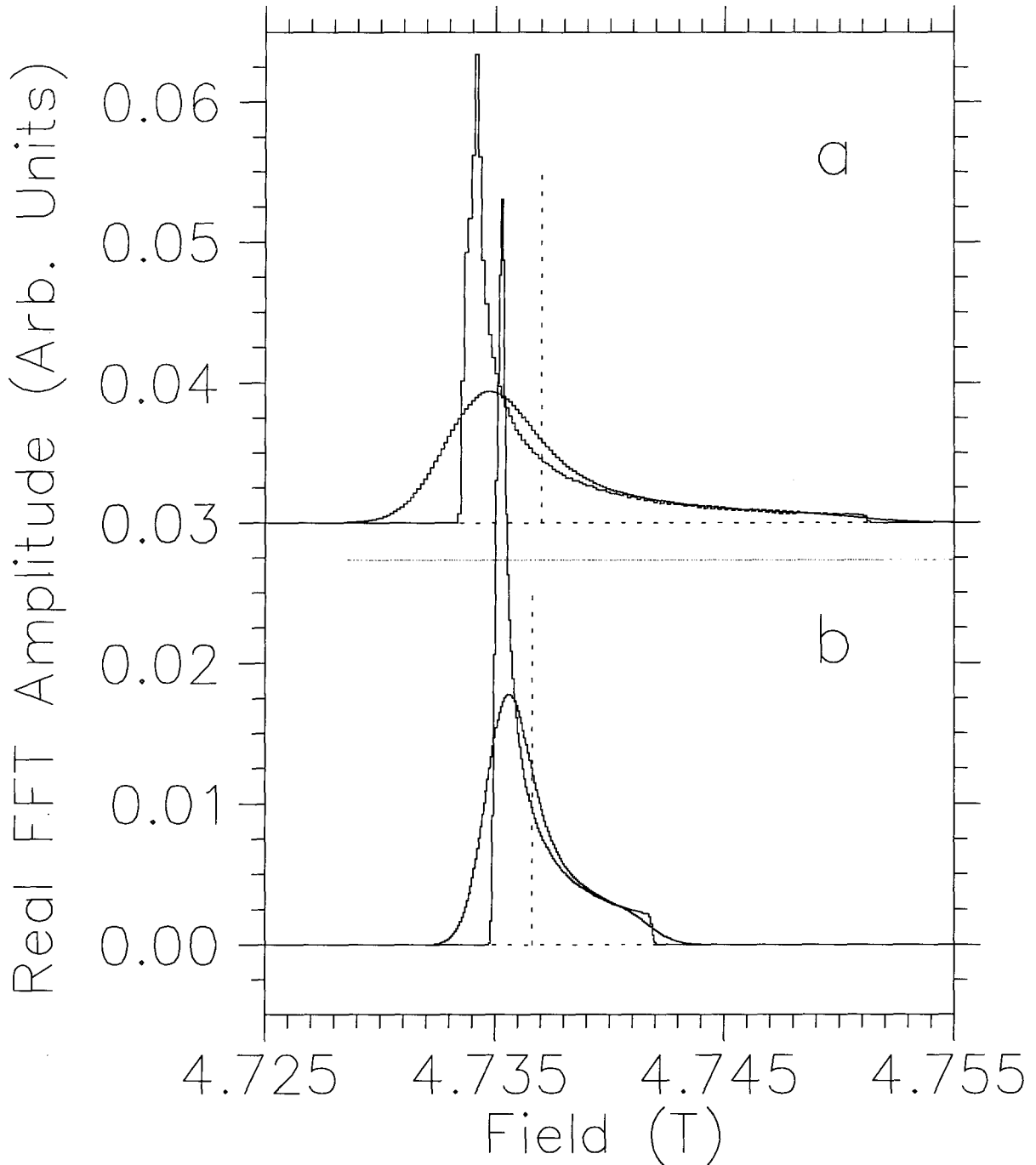


Figure 7.1: Lineshape as calculated by the modified London model (Eq. 7.7) for an isotropic superconductor with

(a) $H_{c2} = 90$ T (or $\xi_{ab} = 0.0019 \mu\text{m}$), $\lambda_{ab}^{-2} = 45.0 \mu\text{m}^{-2}$ (or $\lambda_{ab} = 0.1491 \mu\text{m}$), average field $B_o = 4.7370$ T (indicated by the dashed vertical line) and convolutions of width 16.64 G (corresponding to data taken at 10 K in $\text{YBa}_2\text{Cu}_3\text{O}_{6.95}$) and 0.74 G.

(b) $H_{c2} = 47$ T (or $\xi_{ab} = 0.0026 \mu\text{m}$), $\lambda_{ab}^{-2} = 25.75 \mu\text{m}^{-2}$ (or $\lambda_{ab} = 0.1971 \mu\text{m}$), average field $B_o = 4.7363$ T (indicated by the dashed vertical line) and convolutions of width 8.51 G (corresponding to data taken at 70 K in $\text{YBa}_2\text{Cu}_3\text{O}_{6.95}$) and 0.74 G.

In isotropic BCS theory, the coherence length can be related to the upper critical field (see Eq. 175 on p. 860 of Ref. [102]) by

$$H_{c2} = \frac{\phi_0}{2\pi\xi^2}, \quad (7.1)$$

where ϕ_0 is the magnetic flux quantum. The horizontal scale and high-field cutoff of the μ SR lineshape are determined by λ and ξ coherence length respectively, or alternatively by λ^{-2} and H_{c2} . Since the lineshape is more sensitive to λ than to ξ it would be convenient to assume the temperature dependence of ξ or H_{c2} from other experiments, but no reliable values exist in the literature. The high temperature superconductor $\text{YBa}_2\text{Cu}_3\text{O}_{7-\delta}$ has a very high $H_{c2}(T=0)$; reported values for H_{c2} vary from 40 T (from pulsed fields[103]) to 130 T (from de Haas-van Alphen oscillations using explosively-driven pulsed magnets[104]) to 190 T (from resistivity using explosively-driven pulsed magnets[105]) when $\vec{B} \parallel \hat{c}$. Its tremendously high value makes it quite difficult to measure. Lower bounds for $dH_{c2}/dT|_{T_c}$ can be made from AC and DC resistivity measurements using conventional static magnets, but measurements of H_{c2} near T_c are complicated by flux flow, flux creep and glassy vortex phase transitions. Perhaps the most reliable estimates of $dH_{c2}/dT|_{T_c}$ have been made using magnetization measurements in the reversible regime near T_c , giving values of dH_{c2}/dT ranging from -1.65 T/K[5] in a single crystal of $\text{YBa}_2\text{Cu}_3\text{O}_7$ to -1.90 T/K[6] in an aligned $\text{YBa}_2\text{Cu}_3\text{O}_{7-\delta}$ powder suspended in epoxy. Extrapolating $H_{c2}(T)$ over the whole temperature range from values close to T_c is risky since it requires assumptions about the temperature dependence of H_{c2} . A consensus on $H_{c2}(T)$ well below T_c is certainly lacking, so we cannot assume values for $H_{c2}(T)$ in μ SR fits.

7.2 Apparatus for High Timing Resolution in High Fields

7.2.1 Motive

We set out to take μ SR data in $\text{YBa}_2\text{Cu}_3\text{O}_{6.95}$ with applied fields high enough that the effects of the finite vortex core become observable. Specifically, when the magnetic penetration depth is one to two orders of magnitude larger than the spacing between vortices (L) and the coherence length is only one order of magnitude smaller than L , the maximum field at the vortex core is

seen as a distinct cutoff in the μ SR lineshape. In $\text{YBa}_2\text{Cu}_3\text{O}_{6.95}$, the upper critical field is so high that, with temperatures from 50 K to 75 K, fields from 2 T to 6.5 T are needed to observe this, so extraordinary μ SR equipment with superior timing resolution must be used.

7.2.2 Apparatus

Most μ SR spectrometers are built with “traditional” paddle-shaped counters which have a rectangular piece of scintillator (*e.g.*, $\frac{1}{4} \times 3.5 \times 7$ in³) glued to a Lucite light guide with a rectangular cross section which is subsequently fluted and contorted into a cylinder with a 1.75 in diameter. A photomultiplier tube (PMT), which converts the light into an electrical pulse, is attached to the cylinder end of the light guide. The problem with this design is that every light ray from the same event (*i.e.*, a charged particle passing through the scintillator) follows a different path in the light guide. For a given length light guide, the path length (and hence the time of transit) for a given ray is determined by the angle at which the ray reflects off the rectangular sides of the light guide. The larger the angle, the larger the number of reflections and the longer the path length. The spread of angles determines the spread of transit times, and hence the timing resolution.

Our spectrometer used one muon counter and two positron counters with parabolic surfaces designed to give all light rays roughly the same transit time.* Combined with the TRIUMF μ SR User Facility’s 7 T warm bore superconducting magnet, these counters comprise a high field, high timing resolution spectrometer. Fig. 7.2 shows the portion of the apparatus (counters, cryostat and beam pipe) which lie within the bore of the magnet. Fig. 7.3 shows the whole counters. The positron and muon scintillators are placed at the foci of the first parabolic surfaces of their respective counters. The counters are designed so that all the light is totally internally reflected from the parabolic surfaces. After the first parabolic surface, the light travels parallel to the sides of the counters. Just outside the magnet bore the counters have a 45° reflective surface which turns the light path 90° and directs the light onto a second parabolic surface. At the 45° turn, the muon counter splits into two focusing parabolas with semi-circular cross sections 180°

*The counter design was conceived by Robert Kiefl of U.B.C. Christoff Neidermayer of Universität Konstanz finalized the design and oversaw construction. Robert Kiefl, Andrew MacFarlane and Kim Chow of U.B.C. tested the counters before use in the experiment.

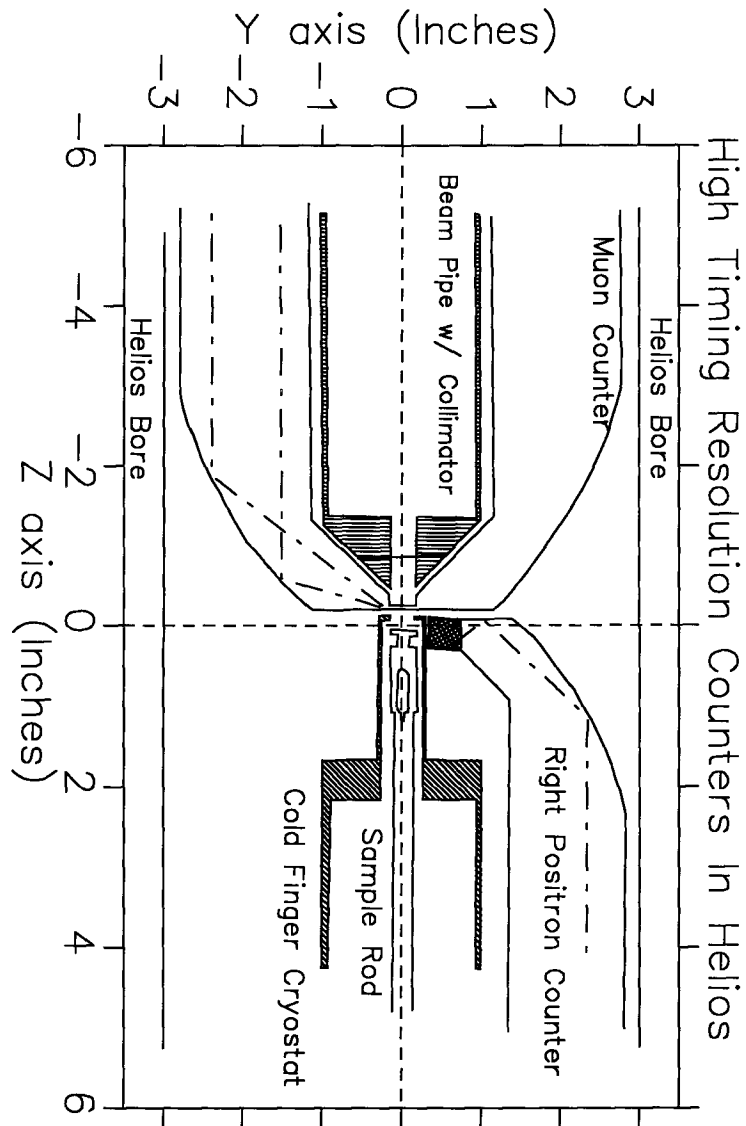


Figure 7.2: High timing resolution apparatus. Several light paths are indicated by the dot-dashed lines. The cross hatched area is the scintillator for the right positron counter. The source of light rays for the muon counter is the 1 cm diameter by $500 \mu\text{m}$ thick scintillator. The roughly capsule-shaped groove near the end of the sample rod is the location of a carbon glass thermometer. Helios is a 7 T superconducting magnet with a six inch warm bore.

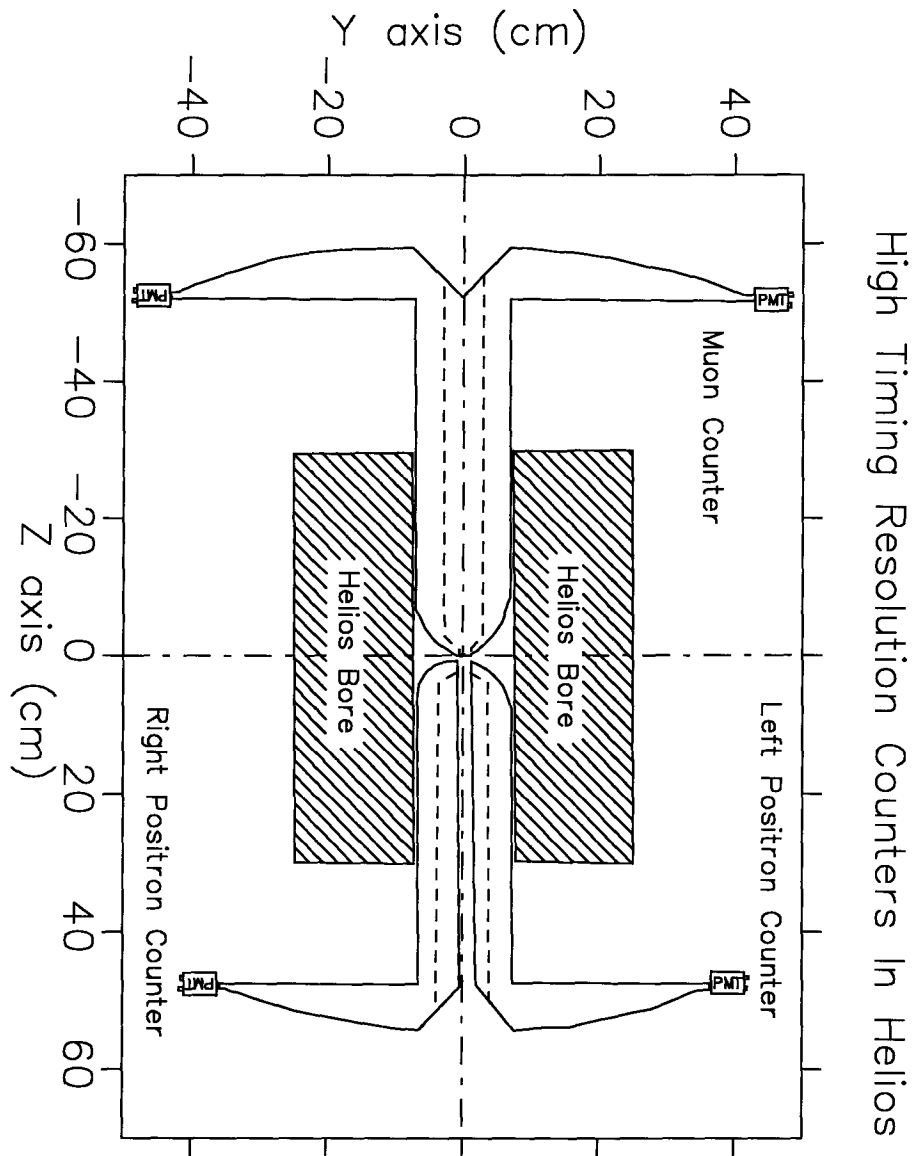


Figure 7.3: High timing resolution counters. The dashed lines indicate the hollowed-out portions in the interiors of the counters.

apart which focus the light onto two photomultiplier tubes (PMTs). Inside the magnet, the muon counter has an annular cross section and the positron counters have semi-annular cross sections for both the collecting parabolas and the straight portions. Because the light from the scintillating portion is only transmitted to the portion of the parabolic reflective surfaces which lie behind the focal points, the center-most portion of the light guide cross section is optically dead; when it is removed, there is room for the cryostat and the beam pipe.

The second parabolic surface uses total internal reflection to focus the light upon on a mesh dynode PMT (also known as a transmissive dynode tube). Conventional dynode tubes contain a series of staggered cups relatively far apart—unfortunately Lorentz forces from stray magnetic fields can deflect the electrons away from the next stage. Transmissive dynode tubes contain a series of closely spaced wire meshes, so that even large stray fields cannot deflect the electrons away from the next stage, especially if the tube is parallel to the field. The lengths of the two legs of the counters were chosen such that each PMT is placed in a field parallel to its axis. In a 7 T field, the fringe field is approximately 350 G at the muon counter PMTs and less than 700 G at each positron counter PMT. The fringe field scales with the applied field. Using mesh dynode PMTs allows shorter and therefore lighter and more efficient counters because larger fringe fields can be tolerated; this compensates for the thicker cross-section required by the parabolic design. Since internal reflection is not 100% efficient, the small number of reflections ensures a more efficient light collection compared to traditional counters. This in turn compensates for the lower gain of the mesh-dynode PMTs. The scintillators were made out of “Pilot U” material, which is one of the faster scintillating materials available.

The size of the scintillators (10 mm diameter by 500 μm thick for the muon counter and approximately a 1 cm cube for each positron counter) was chosen as a compromise. Bigger scintillators produce more light, which produces a stronger signal in the PMT that allows for better timing resolution. However, the counters work best if the light is a point source at the focus of the parabolic reflector; the timing resolution becomes worse as the scintillator size increases relative to the parabolic reflector because of extra reflections, unequal path lengths and even some absorption of off-focus light rays. The sizes of the sample (8 mm diameter) and cryostat (14 mm

wide at the sample) were minimized in order to maximize the size of the counter parabolas, since larger parabolas are less sensitive to machining errors and to the size of the scintillators. A new 20 cm long sample rod, a longer radiation shield and a 2 in diameter, extra long vacuum snout were made for an existing cold finger cryostat. The additional length was necessary to allow the cryostat to reach into the Helios magnet and the high timing resolution counters. The snout narrowed from 2 inches in diameter down to a rectangular ending (14 mm by 1.5 in) for the last 2 inches. It has a 7 mm diameter Kapton window through which the muons entered. The radiation shield ended just before the snout narrowed and single sided aluminized Mylar took its place as a radiation shield for the sample rod. The sample was a mosaic of $\text{YBa}_2\text{Cu}_3\text{O}_{6.95}$ crystals mounted with Apiezon N grease on an 8 mm disk of pure silver with their \hat{c} axes normal to the disk (see Sec. 1.7). It was attached to the sample rod using Apiezon N grease and covered with thin aluminum foil for radiation shielding and thermal connectivity. X-ray Mylar ($3.5 \mu\text{m}$ thick) was used as a final covering for the sample to prevent an accidental thermal short between the sample rod and the snout, which was at room temperature. The sample was 3–5 mm from the Kapton window inside the cryostat. A carbon glass resistor (CGR) thermometer was attached approximately 1 cm behind the sample. A second CGR thermometer was on the cold finger's copper block, which was cooled with liquid helium. The thermal gradient between the two thermometers (approximately 19 cm apart) varied between 0.5 K and 2 K.

Pre-experimental tests of the counters suggested a timing resolution of 600 ps. We expected something like 300 ps from consideration of the finite scintillator size. The remaining 300 ps may be due to insufficient light for optimal timing resolution from the PMT signal.

Under experimental conditions, the μSR asymmetry in the rotating reference frame decreased with increasing applied field (see Fig. 7.4). Asymmetry may be lost due to the intrinsic timing resolution δt of the counters, the PMTs and electronics, which becomes comparable to the period of the muon precession as the applied field is increased. The field dependence of this effect is given by (from Eq. 7 in Ref. [106])

$$\begin{aligned} A_o(B) &= A_o(B=0) e^{-\left(\frac{1}{4}\gamma_\mu B \delta t\right)^2 / \ln 2} \\ A_o(\nu) &= A_o(\nu=0) e^{-\left(\frac{1}{2}\pi\nu \delta t\right)^2 / \ln 2} \end{aligned} \quad (7.2)$$

where the muon gyromagnetic ratio is $\frac{\gamma_\mu}{2\pi} = 135.5342$ MHz/T. Asymmetry may also be lost due to the range of flight times ($t \pm \Delta t$) through the fringe field of the experimental magnet since muons with different momenta precess by different amounts. Since the fringe field scales with the applied field, the net depolarization due to this phenomenon is linear with applied field:

$$\begin{aligned} A_o(B) &= A_o(B=0) \left(1 - C\Delta t \frac{\gamma_\mu}{2\pi} B\right) \\ A_o(\nu) &= A_o(\nu=0) (1 - C\Delta t \nu) \end{aligned} \quad (7.3)$$

where C is the ratio of the average field the muons experience during their time of flight (both inside and outside the magnet) to the applied field B and ν is the muon precession frequency in the applied field. Eq. 7.3 arises from the fact that the muons will be completely depolarized (and the observable asymmetry will be zero) *before* they are implanted in the sample when the spread of transit times Δt is approximately equal to the muon precession period,

$$\Delta t = \left(C \frac{\gamma_\mu}{2\pi} B\right)^{-1}. \quad (7.4)$$

For muons with a mean momentum of 26.2 MeV/c and a momentum spread of 3%, the spread of transit times is 240 ps for a path length of 30 cm. (The sample was at the center of the Helios magnet, so the muons must travel through 30 cm of the magnet's bore. The fringe field outside of the magnet is much smaller than that inside so it can be ignored.) If a field of 30.7 T were applied, it would completely depolarize the muons in flight. (The maximum field Helios can produce is 7.0 T so this is not possible.)

Regardless of the cause, the loss of asymmetry places a practical limit on the choice of magnitude for the applied field. Combining these effects gives an asymmetry with a field dependence of

$$A_o(\nu) = A_o(\nu=0) e^{-\left(\frac{1}{2}\pi\nu\delta_t\right)^2 / \ln 2} (1 - C\Delta t \nu). \quad (7.5)$$

Fig. 7.4 shows the results of fits to the asymmetry loss. The solid lines show the field dependence of the asymmetry assuming that the decrease is due to timing resolution alone (Eq. 7.2), which gives $\delta_t = 796 \pm 22$ ps and $A_o(\nu=0) = 0.0983 \pm 0.0036$, and depolarization alone (Eq. 7.3), which gives $C\Delta t = 971 \pm 21$ ps and $A_o(\nu=0) = 0.1091 \pm 0.0037$. The dashed line shows the asymmetry assuming loss due to both effects together (Eq. 7.5), which gives $\delta_t = 748 \pm 25$ ps and

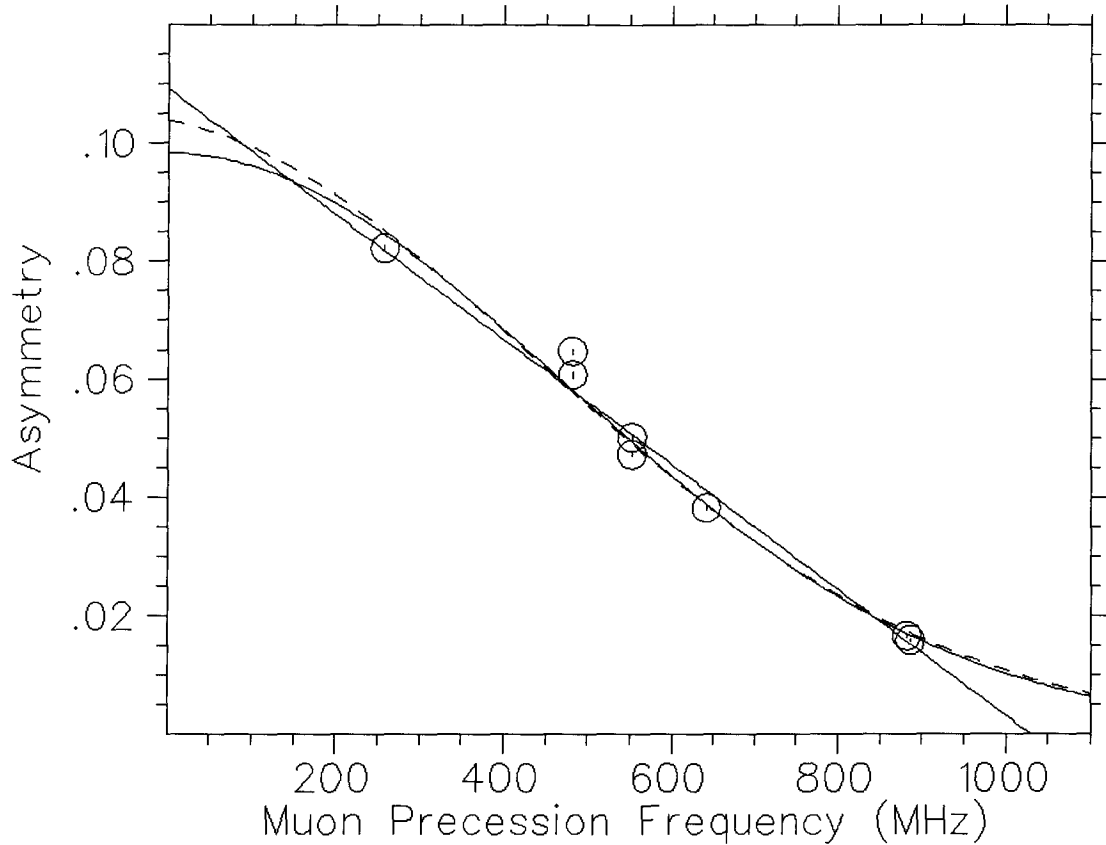


Figure 7.4: The solid lines show the results of fits to the field dependence of the observed asymmetry assuming that the decrease is due to (a) timing resolution alone [Eq. 7.2 with $\delta_t = 796 \pm 22$ ps and $A_o(\nu=0) = 0.0983 \pm 0.0036$] and (b) muon depolarization alone [Eq. 7.3 with $C\Delta t = 971 \pm 21$ ps and $A_o(\nu=0) = 0.1091 \pm 0.0037$]. Clearly, more data points are required to distinguish the two effects. The dashed line shows the results assuming both effects together [Eq. 7.5 with $\delta_t = 748 \pm 25$ ps and $A_o(\nu=0) = 0.1037 \pm 0.0047$] using $\Delta t = 240$ ps and $C \approx 1$.

$A_o(\nu=0) = 0.1037 \pm 0.0047$ using $\Delta t = 240$ ps and $C \approx 1$. If the estimate of 3% for the muon momentum spread is correct, this suggests that the timing resolution obtained for the counters, PMTs and electronics ($\delta t \approx 750$ ps) is comparable to the value obtained from pre-experimental tests ($\delta t = 600$ ps).

7.2.3 Muon Beam Oscillations

The muon beam line can be thought of as an optical system, with an image of the production target being brought into focus approximately one meter from the end of the beam line where the

sample is mounted. When there are large stray fields produced by the experimental magnet, the muon beam delivery system and the μ SR spectrometer cannot generally be treated as independent subsystems. At low fields (< 0.5 T), the two systems are essentially independent. At moderate fields (0.5 T to 1 T), the beam is narrowed in the center of the magnet for a long distance, so exact placement of the sample is of less importance than at very low fields. At higher fields (> 1 T), the beam envelope has nodes and antinodes within the magnet, with the distance between nodes decreasing with increasing field and/or decreasing muon velocity (see Fig. 7.5 and Ref. [107]). A momentum spread smears out the nodes and increases the minimum beam spot size. Worse, it results in a spread of transit times through the fringe field and the magnet itself, which in turn results in a spread in the amount of muon spin rotation. This causes a loss of muon polarization before the muon is even implanted in the sample (see Eq. 7.3). For high fields, a tight muon momentum bite is *very* important.

The node and anti-node behavior is, in part, caused by the fact that muons will spiral in a magnetic field which has components perpendicular to their momentum. The appreciable fringe field of the Helios magnet flares away from end of the magnet, which means that there are perpendicular components of the field off the beam's axis.

The envelope is estimated to have a maximum amplitude of about 9 mm above 1.5 T.[107] This means that a sample of 4 mm radius must be placed at a node in order to have a small background signal (see Fig. 7.5). In general there will be quite a large background signal.

We used the small muon scintillator (1 cm diameter) to detect the luminosity of the beam after final collimation as a function of field and momentum (see Fig. 7.6). When a node is at the muon counter, the rate is maximum. When an anti-node is at the muon counter, the beam spot is wider than the size of the muon scintillator and not all the muons are detected. The sample is about 24 mm downstream from the midpoint of the final collimator; the ideal situation is to have the node centered on the sample rather than on the collimation. The data taken at 4.1 T seem to have been very close to this arrangement as the non-superconducting background signal has a very small amplitude (see Fig. B.12). The worst case is when the node is a little upstream of the muon counter, so that the beam is blowing up at the sample. In this case, many muons

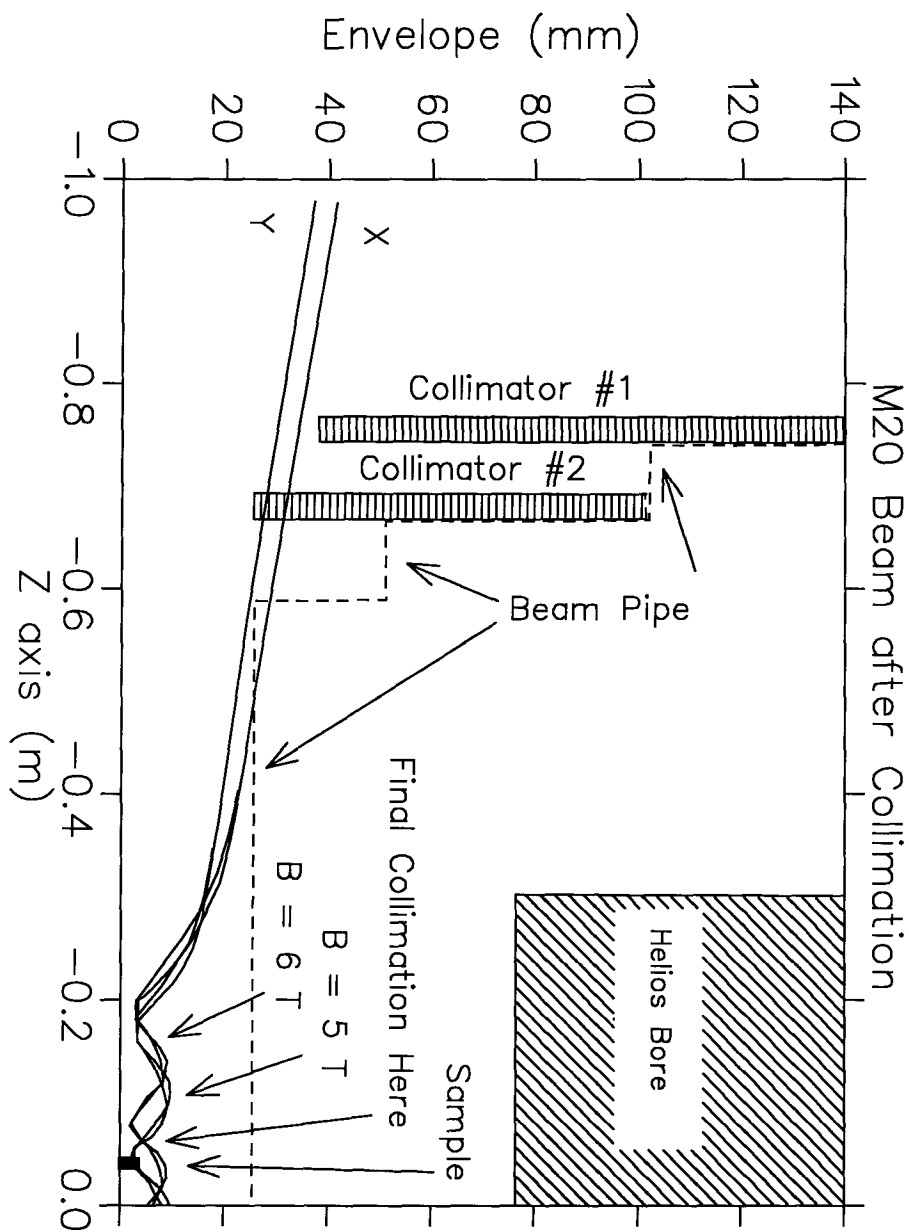


Figure 7.5: Calculated beam envelope oscillations (\hat{X} and \hat{Y} directions) for magnetic fields of 5 T and 6 T in the the TRIUMF M20 beam line. The beam envelopes shown are for the beam which survives collimation by the upstream collimators #1 and #2. A schematic 8 mm diameter sample is shown in a position where the beam is optimally focused on the sample at 5 T and is poorly focused at 6 T. (Adapted from Ref. [107].)

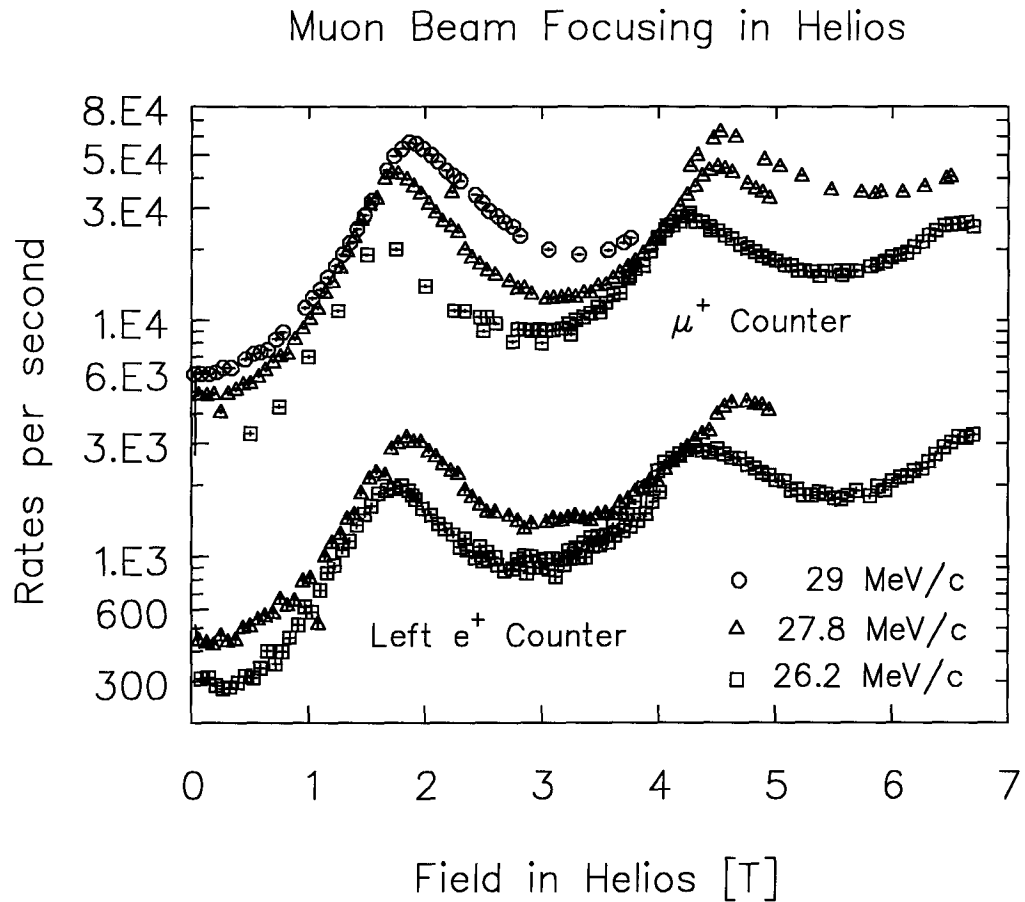


Figure 7.6: Muon beam focusing in the 7 T superconducting magnet Helios on TRIUMF's M20 beam line, as seen by the high timing resolution muon and left positron counters, at three different muon momenta.

TRIUMF Beam Line	B (T)	ΔN (m) (for $p = 29$ MeV/c)	$\Delta N/\Delta D$ (for $p = 29$ MeV/c)	$\Delta N/\Delta D$ (for $p = 26.2$ MeV/c)
M15	0.5	0.0	n.a.	n.a.
M15	2.5	0.254	0.095	0.105
M15	4.0	0.154	0.156	0.173
M15	6.5	0.0975	0.25	0.28
M20	4.0	0.154	0.156	0.173
M20	5.0	0.132	0.182	0.201
M20	6.0	0.1073	0.224	0.248

Table 7.1: Distance between beam oscillation nodes as calculated in TRIUMF design note TRI-DN-92-1 (Ref. [107]), for beam lines M20 and M15. The distance between beam oscillation nodes is ΔN . The distance between the center of the built-in collimator and the sample is $\Delta D \approx 24$ mm, since the sample is 12 mm from the beam pipe and 24 mm from the beam pipe's built-in collimator. The ratio of $\frac{\Delta N}{\Delta D}$ for $p = 26.2$ MeV/c is linearly scaled from $p = 29$ MeV/cm. At very low fields, no nodes are produced and the beam focus point is at the center of the magnet.

will stop in the aluminum cryostat rather than going through the 7 mm window and hitting the 8 mm sample. Table 7.1 lists the approximate spatial distance between nodes at several fields, the approximate ratio of the distance from node to node and the distance from the collimator to the sample, using the calculations in [107]. As one cannot easily move the sample, cryostat and counters within the magnet, one must change the field in order to minimize the background signal. For a given muon momentum, the optimal field will be somewhat lower than the field which gives the maximum rate. The spacing of the nodes as a function of field is inversely proportional to the muon momentum. Table 7.2 shows the optimal fields estimated by

$$B_{\text{opt}} = B_{\text{max}} - 2 \frac{\Delta N}{\Delta D} (B_{\text{max}} - B_{\text{min}}), \quad (7.6)$$

using the ratios calculated in Table 7.1.

In order to improve the quality of the data one could do the following:

1. Make the sample and cryostat window larger. Preferably the sample should be 18 mm in diameter, so that problems of nodes and antinodes are moot. However, the positron counters will have to be moved apart, which reduces their solid angle and exacerbates the loss of rate as lower energy positrons spiral in high fields, missing the positron counters.

Min. Rate at B_{\min} (T)	Max. Rate at B_{\max} (T)	p (MeV/c)	$\Delta N/\Delta D$	Optimal Focusing B_{opt} (T)
0.0	1.6	26.2	0.067	1.4
2.9	4.2	26.2	0.182	3.7
5.3	6.6	26.2	0.273	5.9
0.0	1.7	27.8	0.067	1.47
3.0	4.5	27.8	0.183	3.95
6.0	–	27.8	–	–
0.0	1.9	29.0	0.072	1.63
3.3	–	29.0	–	–

Table 7.2: Estimated optimal focusing fields for a sample which is 24 mm from the collimator, using observed maximum and minimum fields from Fig. 7.6. The optimal field for focusing is estimated using $B_{\text{opt}} = B_{\max} - 2\frac{\Delta N}{\Delta D}(B_{\max} - B_{\min})$.

2. Make the muon scintillator smaller so that it is closer in size to the sample, preferably smaller, so that all muons hitting the muon scintillator will also stop in the sample. This acts like collimation.
3. Use a thicker sample so that higher momentum (up to about 29 MeV/c) muons may be used. Increasing the momentum decreases the node separation so that more “ideal” fields are available. Alternatively, the momentum could be tuned to suit the applied field.
4. Take care with the size and placement of the upstream “stripper” collimators (#1 and #2 in Fig. 7.5) as these somewhat affect the envelope amplitude in the magnet (see Figs. 6 and 7 in [107]). Effective collimation near the sample is very difficult in the presence of nodes and anti-nodes.
5. Introduce a veto counter behind the sample.

Since there are additional constraints on the choice of applied field, such as compatibility with a “good” RRF frequency and the physics of the experiment, one cannot completely pander to the nodes. Given that, the first two suggestions are the best.

7.3 Modified London Model

Brandt[75,74,108] states that in fields less than approximately $(1/4)H_{c2}$, the field distribution in an isotropic superconductor as predicted by Ginzburg-Landau theory can be phenomenologically approximated by modifying the London model (Eqs. 4.17 and 4.18) as follows:

$$B(\vec{r}) = B_o \sum_{\vec{K}} \frac{\exp[-i\vec{K} \cdot \vec{r}] \exp\left[-\frac{\xi^2 K^2}{2(1-b)}\right]}{1 + \frac{K^2 \lambda^2}{1-b}}, \quad (7.7)$$

where \vec{K} are the reciprocal lattice vectors of the FLL, $\xi = \xi(T)$ is the coherence length, $\lambda = \lambda(T)$ is the magnetic penetration depth and $b = B_o/H_{c2}(T)$ is the reduced magnetic field. The exponential involving the coherence length serves as a cutoff for the reciprocal lattice vectors at $K \approx 2\pi/\xi$, which yields a finite value of the magnetic field at the vortex core (see Sec. 4.4). The term $1 - b$ approximately reflects the field dependence of the superconducting order parameter[108, Eq. 28a] which causes a reduction in the width of the lineshape at higher temperatures where the upper critical field $H_{c2}(T)$ is relatively close to the applied field. (This effect is discussed in Ref. [92].)

The above equation can be rewritten in terms of the dimensionless quantities $\lambda_r = \lambda/L$, $\xi_r = \xi/L$, $\vec{x} = \vec{r}/L$, $\vec{q} = \vec{K}L$, where

$$L = \sqrt{\frac{2\phi_o}{\sqrt{3}B_o}} \quad (7.8)$$

is the spacing between vortex cores. Using the relation between H_{c2} and ξ ,

$$H_{c2} = \frac{\phi_o}{2\pi\xi^2}, \quad (7.9)$$

the reduced field can be expressed as

$$b = \frac{4\pi}{\sqrt{3}}\xi_r^2 \quad (7.10)$$

and the fractional field difference for the modified London model is, in dimensionless quantities,

$$\frac{B(\vec{r}) - B_o}{B_o} = \sum_{\vec{q} \neq 0} \frac{\exp[-i\vec{q} \cdot \vec{x}] \exp\left[-\frac{\xi_r^2 q^2}{2(1 - \xi_r^2 4\pi/\sqrt{3})}\right]}{1 + \frac{q^2 \lambda_r^2}{1 - \xi_r^2 4\pi/\sqrt{3}}}. \quad (7.11)$$

Contour plots of the fractional field difference $[B(\vec{r}) - B_o]/B_o$ at the vortex core, at the saddle point and at the minimum are shown in Fig. 7.7 as functions of λ_r and ξ_r and in Fig. 7.8 as functions of λ_r^{-2} and H_{c2}/B_o .

7.4 Ambiguity in the Determination of λ and ξ

Note that in Fig. 7.7 while field contour lines for the saddle point and minimum are curved in the opposite sense from the field contour lines for the vortex core, the curvature is mild considering the large range for λ_r and ξ_r . If one uses the modified London model to fit data taken at a particular field and temperature, one will find that many values of λ and ξ along a particular field contour for the vortex core will all fit the data equally well. Fitting multiple runs taken at different fields but the same temperature with common values for λ and ξ will reduce the degeneracy because the curvature and slope of the contour lines changes with the average field B_o . Note that this discussion neglects uncertainties in determining the average internal field and the effects of pinning on the lineshape. If one knows the value of $\xi(T)$ accurately, say from measurements of $H_{c2}(T)$, one can uniquely determine $\lambda(T)$ and therefore $\kappa(T)$. Conversely, if one knows the value of $\lambda(T)$ accurately, one can uniquely determine $\xi(T)$ and therefore $\kappa(T)$ and $H_{c2}(T)$. This degeneracy is starkly portrayed in Fig. 7.8, which also demonstrates how the lineshape becomes independent of the upper critical field H_{c2} , known as the London limit, when λ_r^{-2} is small and H_{c2}/B_o is large.

7.5 Data Analysis

A special fitting program called FIT-GLOBAL-HC2, which uses the fitting package MINUIT, was written to fit the lineshapes without the use of pre-existing tables. Since the field cutoff at the core is observable in the high field data, no simple scaling of a single representative lineshape is possible. Directly calculating the lineshape was simpler and more direct than interpolation using a series of representative lineshapes.

The parameters for the fit were λ^{-2} and $H_{c2} \propto \xi^{-2}$, because they behave with the same “dimensionality” as others such as the convolution σ and the linewidth of the background signal

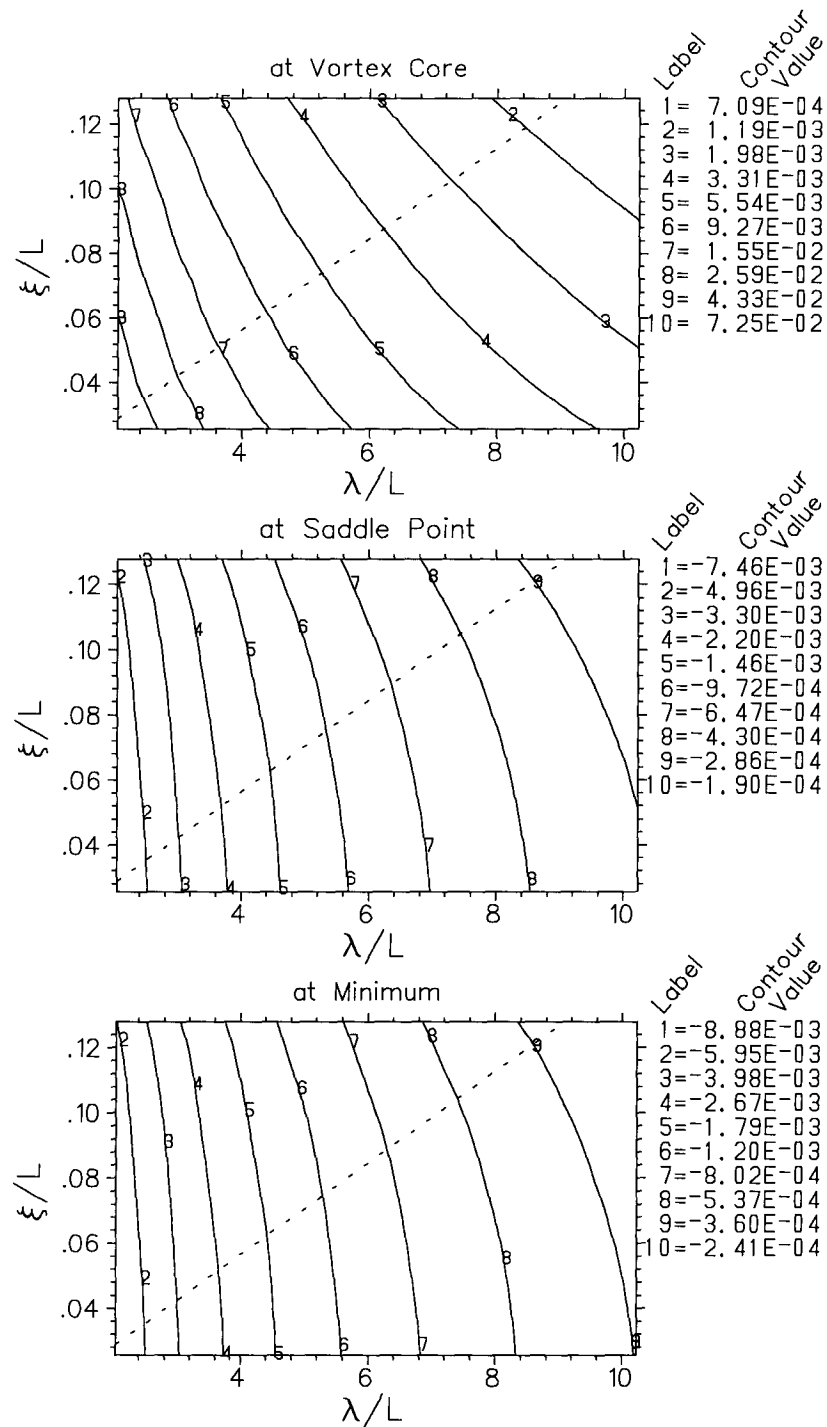


Figure 7.7: Contour plots of the fractional field difference $[B(\vec{r}) - B_0]/B_0$ (solid lines) at the vortex core, at the saddle point and at the minimum are shown spaced logarithmically as functions of λ_r and ξ_r . The dashed line is $\kappa = \lambda/\xi = 71.0$.

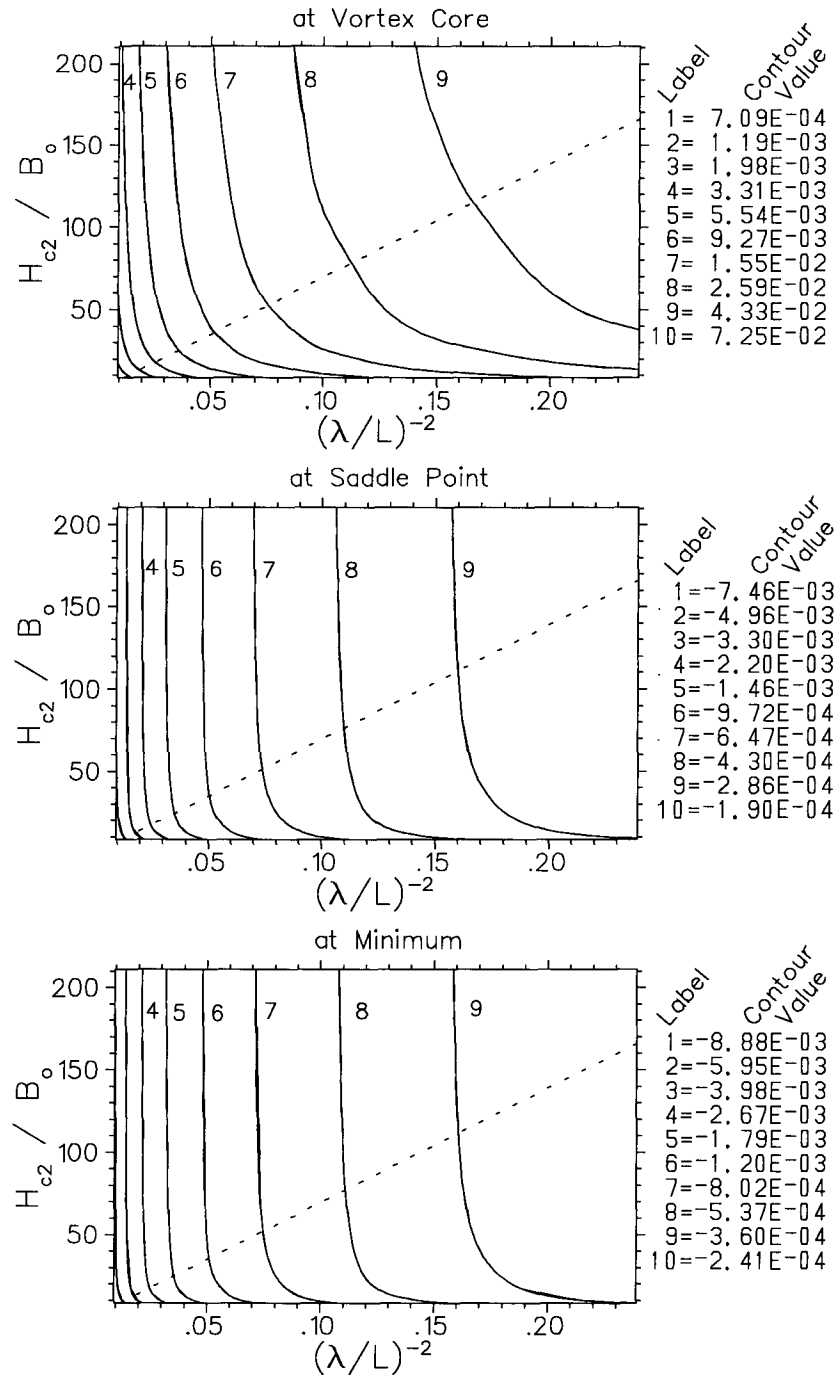


Figure 7.8: Contour plots of the fractional field difference $[B(\vec{r}) - B_0]/B_0$ (solid lines) at the vortex core, at the saddle point and at the minimum are shown as functions of λ_r^{-2} and H_{c2}/B_0 . The dashed line is $\kappa = \lambda/\xi = 71.0$.

δ_b . For example, if λ^{-2} is doubled the superconductor's lineshape will double in width. If H_{c2} is increased, the cutoff field increases and the overall width of the lineshape increases as well. MINUIT works best under these circumstances.

For given values of the parameters λ^{-2} , H_{c2} and B_o , the spatial distribution of the local magnetic field is calculated for an array of positions within the FLL unit cell and then interpolated to increase the effective number of points. From this, a probability distribution of local fields (also known as the theoretical lineshape) is calculated.[†] This is convoluted by a Gaussian of width σ , to mimic the effects of nuclear dipolar fields, disorder in the flux line lattice and the Gaussian apodization used in the Fourier transform of the data. (The convolution can be done using Eq. 3.71 since the applied field is high enough that components of the local field which are perpendicular to the applied field are negligible.) Finally, this "smeared" theoretical lineshape is multiplied by a normalization n_s . In addition, a simple Gaussian with width δ_b , average field B_b and normalization n_b is added to mimic the background signal due to muons stopping in the sample mounting or the cryostat itself rather than in the sample. In summary, FIT-GLOBAL-HC2 uses a total of five parameters for the superconductor lineshape:

1. the inverse square of the penetration depth λ^{-2} ,
2. the upper critical field H_{c2} ,
3. the average internal field B_o ,
4. a Gaussian convolution of width σ and
5. a normalization n_s ,

and three for the background signal $n_b e^{-\frac{1}{2}(B-B_o)^2/\delta_b^2}$ due to muons stopping in the cryostat:

1. a Gaussian width δ_b ,
2. the average background field B_b and

[†]The routines used to interpolate between calculated points in the spatial distribution and to calculate the lineshape were adapted from code written by Josef Rammer.

3. a normalization n_b .

The MINUIT package from CERN is a collection of routines which call a user-provided function for χ^2 given the current parameter values. MINUIT changes the parameter values until χ^2 is minimized. To speed up the fit, the “unsmeared” theoretical lineshape is only re-calculated when the parameters λ^{-2} or H_{c2} are changed. If the superconducting average field B_o is changed while λ^{-2} and H_{c2} remain the same, the previous lineshape is translated along the field axes by an amount equal to the change of field.

The sizes of arrays, the number of points calculated within the FLL unit cell and other numbers related to the discretization of the numerical calculation were chosen to reduce the time of calculation. Because the time is proportional to the square of the number of reciprocal lattice vectors, $q_{\max}^2/(2\pi)^2 = \xi_r^{-2} = (\xi/L)^{-2}$, analyzing $\text{YBa}_2\text{Cu}_3\text{O}_{6.95}$ data taken at fields below about 1 T becomes impractical with this program since the distance between vortices is very much larger than the size of the vortex core.

The program FIT-GLOBAL-HC2 allows several runs to be fitted at the same time with shared parameters. This feature was used to fit with the same values of the parameters λ^{-2} and H_{c2} all the runs which share approximately the same temperature (within one degree) but have different applied fields. Upon finishing, it produces several quantities in addition to the parameters corresponding to the best fit. It calculates the minimum, cusp and maximum fields for the unsmeared theoretical lineshape for the best fit. It also calculates the convolution width corrected for both the degree of apodization in the Fourier transform and the nuclear dipolar fields as observed above T_c in the same applied field. Using this corrected convolution width, it calculates the estimated mean deviation of the vortices from their ideal position in the FLL ($\langle s^2 \rangle^{1/2}/L$) for both random compression and random shear. The Ginzburg-Landau parameter $\kappa = \lambda/\xi$ is produced. And finally, both the χ_R^2 for individual runs and χ_T^2 for the fit as a whole are recorded.

The data was difficult to analyze because *three* parameters, λ^{-2} , H_{c2} and σ , all contribute to the width of the μSR lineshape. In order to get some leverage upon this problem, I made preliminary fits assuming that the magnetic penetration depth has the following temperature

dependence

$$\lambda^{-2} = \lambda(0)^{-2} [1 - (T/T_c)^p], \quad (7.12)$$

with a zero temperature penetration depth of $\lambda(0) = 0.1405 \mu\text{m}$ and an exponent of $p = 2.37$, values estimated from data taken in a 0.25 T field[93]. Since the lineshape varies slowly with H_{c2} , it was necessary to fit a series of runs with fixed H_{c2} for each temperature. This resulted in κ decreasing with decreasing field. A separate round of fitting assuming a BCS temperature dependence of H_{c2} using $dH_{c2}/dT_c|_{T_c} = -1.9 \text{ T/K}$ [6] resulted in κ increasing with decreasing temperature.

Because there is a range of values for λ^{-2} and H_{c2} which give nearly the same lineshape, both cannot be fitted at the same time. In fact, the lineshape is so weakly dependent upon H_{c2} at the lower temperatures that the fits do not converge if its value is allowed to float. To compensate, FIT-GLOBAL-HC2 was made to loop through a grid of the fixed parameters λ^{-2} and H_{c2} (FIT-GLOBAL-HC2-LOOP). With each change in λ^{-2} and H_{c2} , λ^{-2} and H_{c2} were fixed, the superconducting average field B_o for each run was scanned[†] between plus and minus five times the estimated error in B_o and, using MIGRAD in MINUIT, χ^2_T was minimized. Scanning B_o before minimization was necessary because the average field is very sensitive to the maximum field cutoff (determined largely by H_{c2}) which is not always a distinctive feature.

The results of the preliminary analysis [assuming $\lambda(T)$] were used as the initial guess in the program FIT-GLOBAL-HC2-LOOP. In order to keep the computation time reasonable, the convolution width σ was fixed to that from the preliminary analysis. The remaining parameters n_s , B_o , δ_b , B_b and n_b are all comparatively cheap to calculate. Because the unsmeared theoretical lineshape is infinitely steep at the minimum field, the slope at half amplitude on the low field side of the experimental lineshape determines the size of the convolution. Since χ^2 minimization finds the biggest, most distinct features (the low field shoulder), the fits will estimate the minimum field (location) and the convolution (slope) more accurately than features such as the maximum field. Even though σ was fixed using values from an incomplete series of fits, it should be fairly accurate.

[†]The SCAN command in MINUIT minimizes χ^2 by varying only the specified parameter.

7.6 Results

7.6.1 Sample

A mosaic of $\text{YBa}_2\text{Cu}_3\text{O}_{6.95}$ single crystals (see Sec. 1.7) was mounted on an 8 mm diameter pure silver disk using Apiezon N grease, with the crystals' hard axes (\hat{c}) perpendicular to the disk's face. The sample was mounted in a helium-cooled cold finger cryostat inside the warm bore of TRIUMF's 7 T magnet called Helios (see Sec. 7.2). The magnetic field, between 1.9 T and 6.5 T, was applied parallel to the mosaic's common \hat{c} axis. All the following results are for $\vec{B} \parallel \hat{c}$ for which the isotropic treatment in Sec. 7.3 is appropriate: λ refers to the magnetic penetration depth in the copper oxide planes (λ_{ab}); H_{c2} refers to $\vec{H}_{c2} \parallel \hat{c}$ and so on.

7.6.2 Intermediate Results

To avoid burying this chapter in figures, the intermediate results are presented in Appendix B. For each target temperature ($T = 10, 20, \dots, 60, 70, 75$ K) runs with different fields ($B_o = 1.9, 4.1, 4.7, 6.5$ T) within $\pm 1^\circ$ of that temperature were fit (together) using FIT-GLOBAL-HC2-LOOP sharing only the parameters $\lambda^{-2}(T)$ and $H_{c2}(T)$. FIT-GLOBAL-HC2-LOOP produces a grid of results ($\chi_R^2, \chi_T^2, B_o, \text{etc.}$) as a function of λ^{-2} and H_{c2} . Fig. B.1 through B.8 show the test of goodness-of-fit χ_R^2 as a function of λ^{-2} and H_{c2} for the individual runs. The best (lowest) χ_R^2 for each run is highlighted by a solid square and increasing values of χ_R^2 are indicated by smaller and smaller boxes, thereby roughly indicating values of λ^{-2} and H_{c2} which give contours of similar fit quality. If λ^{-2} and H_{c2} were completely independent variables, one would expect an elliptical shape for contours of constant χ_R^2 near the minimum. Instead there are curved "troughs," which show the high degree of correlation between λ^{-2} and H_{c2} . The troughs in χ_R^2 tend to follow the contours of constant average field extracted from the fits with the lowest χ_R^2 for the individual runs (marked "R" in the figures) and constant average field extracted from the fits with the lowest total χ_T^2 for all the runs at different fields at that temperature (marked "T"). This suggests that along the contour, the lineshapes are nearly identical (see Fig. 7.8).

Figs. B.9 and B.10 show the combined goodness-of-fit $\chi_T^2 = \sum_{\text{all fields}} \chi_R^2$ as a function of λ^{-2} and H_{c2} for all runs at each temperature. Because the individual χ_R^2 contours are curved troughs which have different slopes at different fields, the total χ_T^2 contours tend to have deeper and less trough-like minima. In other words, by fitting to a common λ^{-2} and a common H_{c2} for runs of different fields at a given temperature, both λ^{-2} and H_{c2} can be determined from the μSR lineshapes. The uncertainties in the best values of λ^{-2} and H_{c2} were estimated in terms of the distance from the χ_T^2 minimum in $\chi_{T,\text{min}}^2$ to $\chi_{T,\text{min}}^2 + 1$ (highlighted by a solid diamond). If there were no points within 2 of $\chi_{T,\text{min}}^2$, then the uncertainties were estimated to be the step size in the grid of λ^{-2} and H_{c2} over which χ_T^2 was evaluated. Due to the relatively coarse step size, the error estimates for λ^{-2} and H_{c2} are sometimes rather rough.

The errors quoted for the remaining parameter of importance, the Gaussian convolution width σ , are MIGRAD errors. The calculated quantities ξ , λ , κ and $\langle s^2 \rangle^{1/2}/L$ for both random compression and random shear are reported with propagated errors. When MIGRAD returned an unreasonably large error for the average field B_o (sometimes as large as B_o itself), the error was set to 2 G for the purposes of estimating the error in the maximum, cusp and minimum fields. The curves shown in Figs. 7.9 through 7.16 are the result of a weighted least squares fit using the Gauss-Newton method as implemented in TRIUMF's PLOTDATA program. The parameter errors quoted for these curves represent statistical error only.

Figs. B.11, B.12, B.13 and B.14 show the experimental lineshapes and fits with all measured temperatures shown for each applied field. The lineshapes are all shown relative to the background signal (centered at 0 G), the values of which are listed in table B.1. The linewidth increases with decreasing temperature, reflecting the temperature dependence of λ . Figs. B.15, B.16, B.17 and B.18 show the same lineshapes and fits for selected temperatures with all applied fields shown for each temperature. Because the μSR signal amplitude is reduced with increasing applied field due to loss of timing resolution and muon dephasing (see Sec. 7.2), the Fourier amplitudes have been re-normalized so that the superconducting lineshapes all have the same area. These figures demonstrate that the lineshape narrows slightly and the maximum local field is reduced with increasing applied field. These changes in the lineshape are most dramatic at 70 K (Fig. B.18)

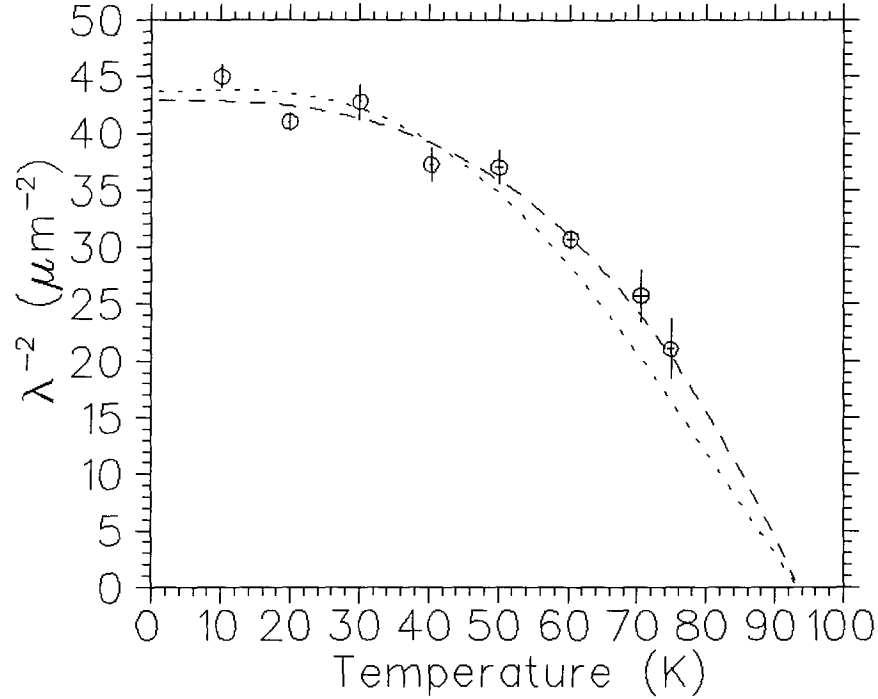


Figure 7.9: $\lambda_{ab}^{-2}(T)$ from global fits of the high field data. The dashed line is a fit to $\lambda_{ab}^{-2}(T) = c(1 - \{T/T_c\}^p)$ with $c = 42.90 \pm 0.88 \mu\text{m}^{-2}$, $p = 2.89 \pm 0.23$ and T_c fixed to 93.5 K. The dotted line is a fit to BCS s -wave theory, with a normalization of $43.6 \pm 1.0 \mu\text{m}^{-2}$.

where the available fields cover the largest range of reduced fields $B_o/H_{c2}(T)$. Here the lineshape shows a very distinct high field cutoff at the highest measured field of 6.5 T, while at the lowest field the lineshape looks almost London-like with the cutoff field nearly lost in the noise.

7.6.3 $\lambda_{ab}^{-2}(T)$, $H_{c2,\parallel,\hat{c}}(T)$ and $\kappa_{ab}(T)$

Fig. 7.9 shows the temperature dependence of the best-fit values of the inverse square of the the penetration depth in the copper oxide planes (λ_{ab}^{-2}). Fitting to a power law yields an exponent of $p = 2.89 \pm 0.23$. The results do not support the Gorter-Casimir version of the two-fluid temperature dependence ($\lambda^{-2} \propto 1 - \{T/T_c\}^p$ with $p = 4$) reported in sintered powder samples.[100,24] The BCS weak coupling s -wave temperature dependence does not fit as well as the power law.

Fig. 7.10 shows the temperature dependence of the upper critical field H_{c2} . Since H_{c2} has relatively little influence on the lineshape at lower temperature, results below 30 K are not well

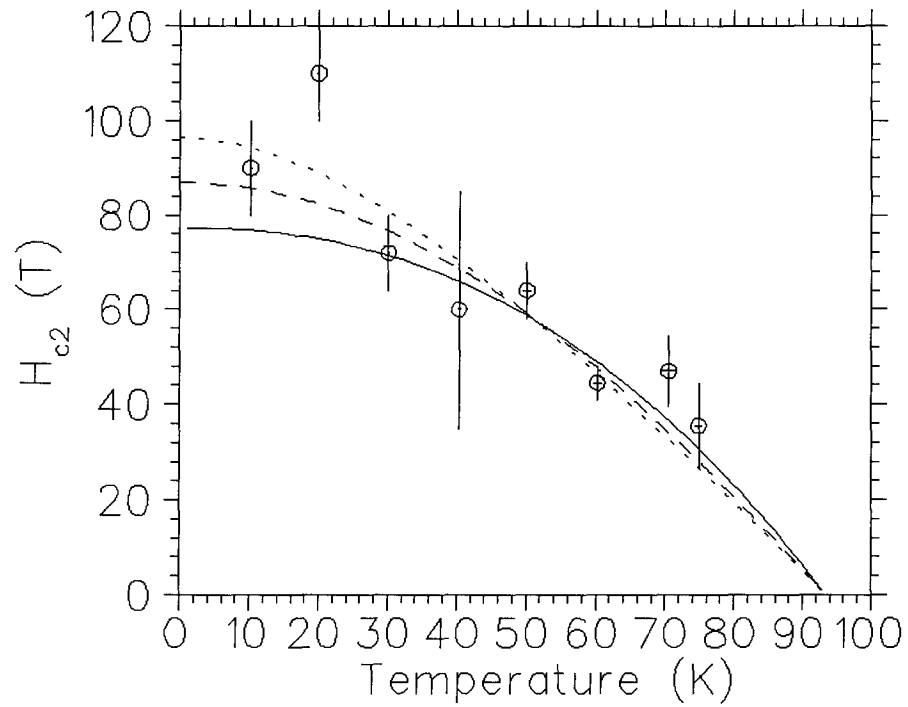


Figure 7.10: $H_{c2}(T)$ for $B_o \parallel \hat{c}$ from global fits of the high field data. The low temperature runs at 10 K and 20 K were excluded from the fits. The solid line is a fit to $H_{c2}(T) = c(1 - \{T/T_c\}^p)$ with $c = 77 \pm 13$ T, $p = 2.28 \pm 0.76$ and T_c fixed to 93.5 K. The dotted line is a fit to the temperature dependence of H_{c2} for an s -wave BCS weak coupling isotropic superconductor, with $dH_{c2}/dT = -1.429 \pm 0.083$ T/K. The dashed line is a fit to the temperature dependence of H_{c2} for a superconductor with a cylindrical Fermi surface (*i.e.*, 2-D), with $dH_{c2}/dT = -1.511 \pm 0.078$ T/K. Since H_{c2} has relatively little influence on the lineshape at lower temperature, results below 30 K are not well determined, and so were excluded from the fits to the various models.

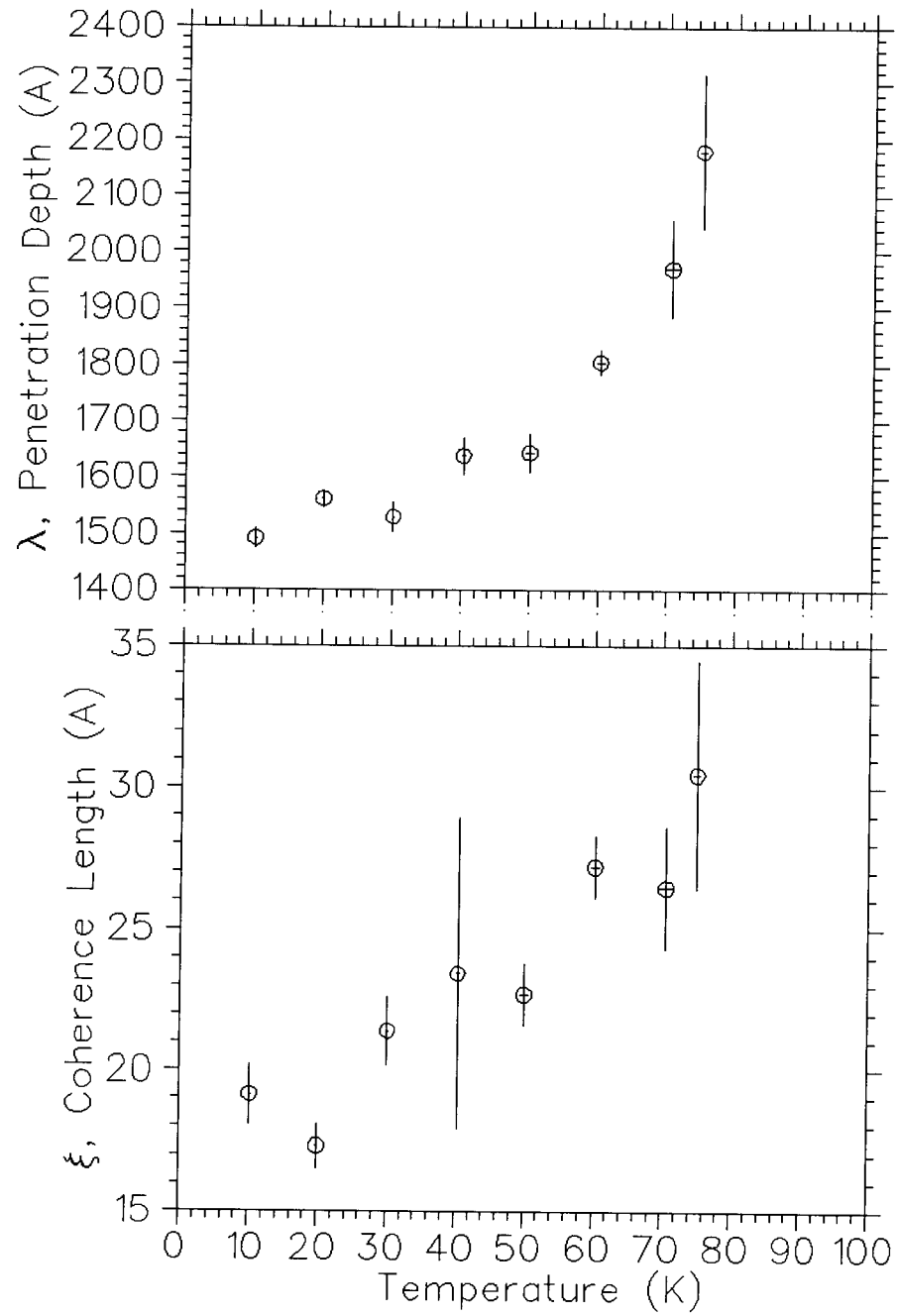
determined, and so were excluded from the fits to the various models. The weak-coupling s -wave BCS temperature dependence for H_{c2} in an isotropic superconductor cannot be distinguished in Fig. 7.10 from that in a 2-D superconductor with a cylindrical Fermi surface (see Ref. [31] and references therein). Fitting to a power law yields an exponent close to two. Fig. 7.11 shows the parameters λ^{-2} and H_{c2} recast as λ and ξ .

The Ginzburg-Landau parameter κ (Fig. 7.12) essentially shows no temperature dependence, if one ignores the points below 30 K where the values of H_{c2} are less reliable. The fit to a constant gives the Ginzburg-Landau parameter $\kappa = 69.6 \pm 1.4$. The value for κ should be independent of temperature if $\text{YBa}_2\text{Cu}_3\text{O}_{6.95}$ is a weak-coupling s -wave BCS superconductor. There could be a weak temperature dependence for κ which is unnoticeable beneath the large error bars for the measured values $\kappa(T)$, in which case $\text{YBa}_2\text{Cu}_3\text{O}_{6.95}$ could not be a weak-coupling superconductor. Linear regression produces a line with a slope smaller than its error bar, so a linear fit is no better than a fit to a constant. However, the linear fit gives a more generous error of 6.0 for the value of κ . The value of 70 ± 6 is consistent with the average value of 72 found by Gohng and Finnemore[6] using reversible magnetization in the temperature range between T_c and the irreversibility temperature.

The non-monotonic behavior of H_{c2} and κ (seen as a maximum at 20K) is likely spurious, reflecting the uncertainty of determining H_{c2} at lower temperatures. The error bars at 10K and 20K are probably underestimated due to the course step size used in the fitting method.

7.6.4 The Local Fields Versus Temperature

Fig. 7.13 shows the temperature and field dependence of the maximum B_V , cusp B_C and minimum B_M fields. These fields are all relative to the average field B_o of the superconducting signal. They are not the parameters used in the calculation of the lineshape, but rather they are features of the *unsmearred* theoretical lineshape which fit the experimental data best when $\lambda^{-2}(T)$ and $H_{c2}(T)$ are shared for all fields at a given temperature T . The curves shown are the result of fits to B_M , B_C or $B_V = c(1 - \{T/T_c\}^p)$, individual values of which are listed in Table 7.3. Note

Figure 7.11: λ and ξ from global fits of high field data.

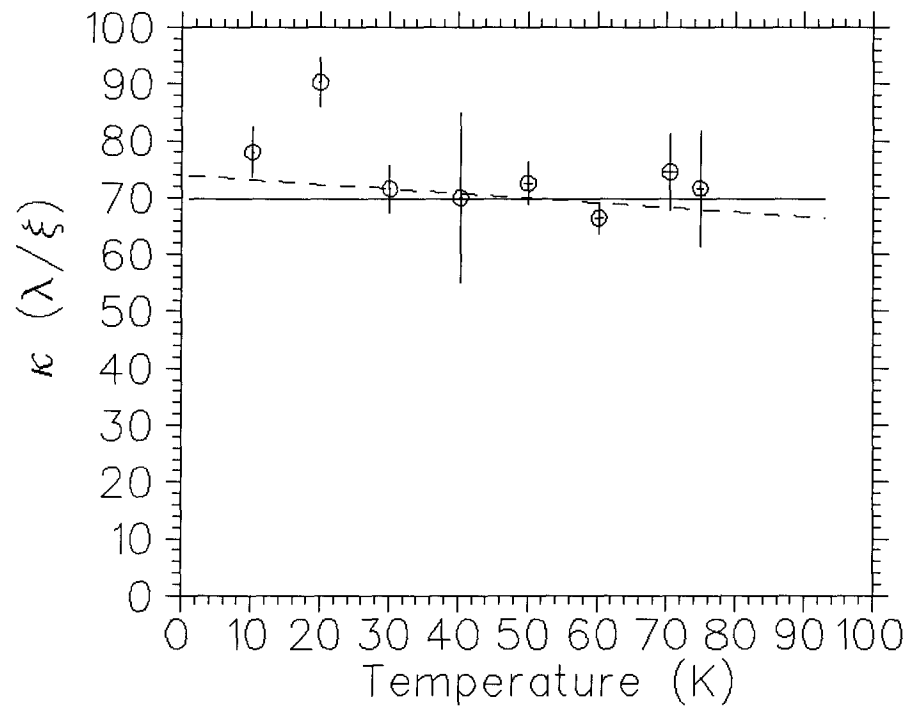


Figure 7.12: κ from global fits of high field data. The solid line is a fit over the range 30 K to 75 K for a constant κ , with $\kappa = 69.6 \pm 1.4$. The dashed line is a fit to a linear temperature dependence, with $\kappa(0) = 74.0 \pm 6.0$ and a slope of $s = -0.08 \pm 0.11 \text{ K}^{-1}$. Since H_{c2} has relatively little influence on the lineshape at lower temperature, results below 30 K are not well determined, and so were excluded from the fits to the various models.

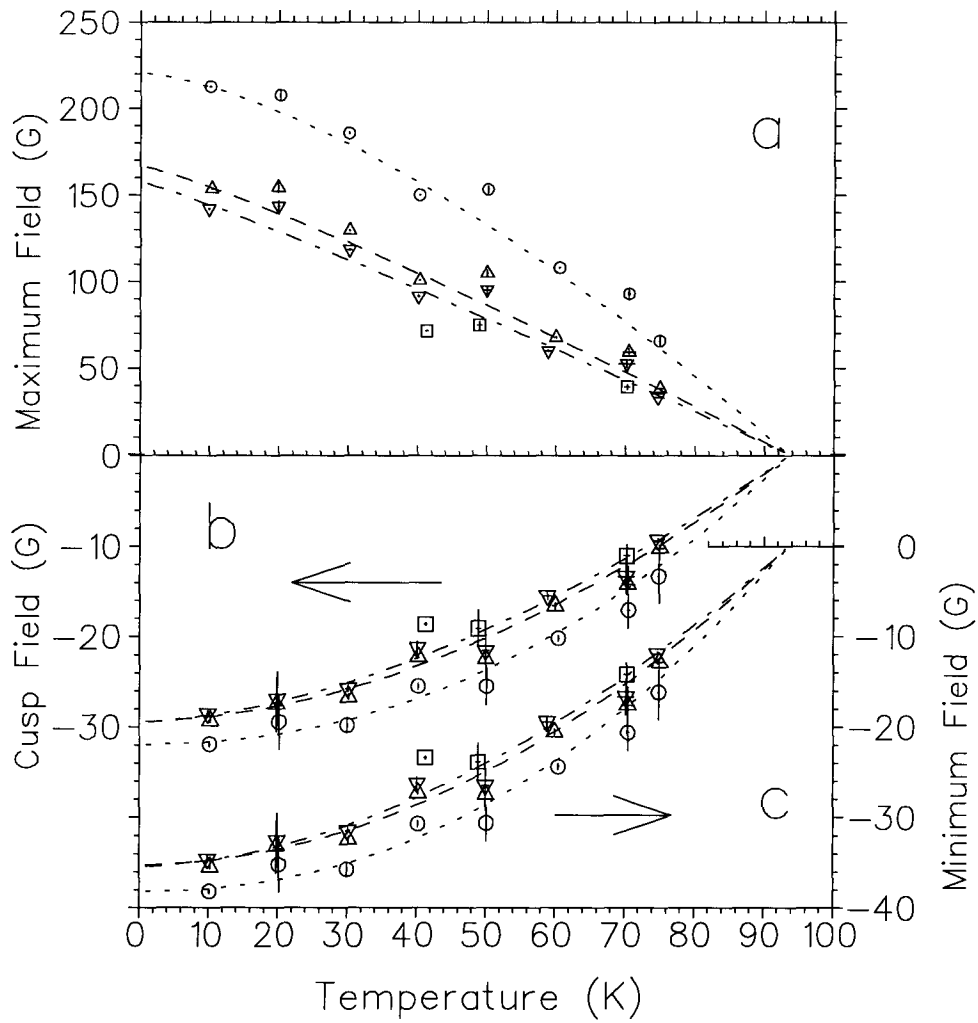


Figure 7.13: Maximum (a), cusp (b) and minimum (c) fields relative to the average field in the superconductor from global fits for applied fields of 1.9 T (circles, dotted curve), 4.1 T (triangles, dashed curve), 4.7 T (upside-down triangles, dotted-dashed curve) and 6.5 T (squares, without curve). See Table 7.3 for the parameters used in the curves.

Applied Field (T)	Minimum Field	Cusp Field	Maximum Field
1.9 T	$c = -38.18 \pm 0.66$ (G) $p = 2.20 \pm 0.13$	$c = -31.91 \pm 0.55$ (G) $p = 2.16 \pm 0.13$	$c = 220.6 \pm 4.1$ (G) $p = 1.471 \pm 0.078$
4.1 T	$c = -35.22 \pm 0.90$ (G) $p = 1.97 \pm 0.12$	$c = -29.35 \pm 0.71$ (G) $p = 1.85 \pm 0.10$	$c = 166.9 \pm 4.9$ (G) $p = 1.163 \pm 0.066$
4.7 T	$c = -35.39 \pm 0.46$ (G) $p = 1.812 \pm 0.055$	$c = -29.39 \pm 0.42$ (G) $p = 1.693 \pm 0.056$	$c = 157.6 \pm 5.2$ (G) $p = 1.100 \pm 0.076$

Table 7.3: Fits to minimum, cusp and maximum fields in Fig. 7.13 using B_M , B_C or $B_V = c(1 - \{T/T_c\}^p)$. (Since the errors are underestimated for the maximum field, the errors for the parameters c and p are likely to be underestimated as well.)

that B_C and B_M have exponents p close to 2, while B_V has an exponent p between 1.5 and 1.0. In all cases, the exponent (which is always smaller than that for λ^{-2}) is reduced when the applied field is increased, with the strongest effect for B_V . The reduction is due to the term $(1 - b)$ in Eq. 7.7 which represents the field dependence of the superconducting order parameter.

The errors in B_V , B_C and B_M have been estimated by adding in quadrature the errors for B_o and the width σ of the Gaussian convolution. If the theoretical lineshape is too wide or too narrow due to a poor choice of λ^{-2} or H_{c2} , the fit will match the cusp and shoulder regions where the amplitude is high and concentrate the mismatches in the tail region where the amplitude is low. Therefore, good error estimates for B_M and B_C can be produced from the error estimates for B_o and σ alone. The error in H_{c2} and λ^{-2} will affect B_V much more than B_M and B_C . Since the error in H_{c2} was not taken into account, the error has been grossly underestimated for B_V .

The Meissner effect is not well determined by the μ SR data. At 70–75 K, the average internal field in the superconductor relative to the applied field (as determined by runs taken above T_C) is about -1 G for 1.9 T, -2 G for 4.1 T, -3 G for 4.7 T and -2 G for 6.5 T. However, as the temperature decreases, the average field in the superconductor *increases* approximately linearly, which is not consistent with flux expulsion. Over the temperature range measured, the runs at 1.9 T are within ± 2 G of the applied field, the runs at 4.1 T are within ± 3 G and the runs at 4.7 T are within ± 4 G. These results should not be taken too seriously; the average field is strongly influenced by the maximum field at the vortex core and this is poorly determined at

the lower temperatures. Using μ SR, it is impossible to determine the temperature dependence of the average field with enough accuracy to distinguish the effects of the flux expulsion from other effects such as paramagnetism and muon Knight shifts. From magnetization measurements (Sec. 4.9), the amount of flux expulsion for this 8 mm sample is predicted to be ≈ 3.6 G in an applied field of 1.9 T and ≈ 10 G in 4.1 T, which is too large to fit the μ SR data with.

It is curious to note that above T_c the μ SR linewidth for our $\text{YBa}_2\text{Cu}_3\text{O}_{6.95}$ mosaic (presumably due to nuclear dipolar fields) and the bulk magnetization for a single crystal of that mosaic show a very similar linear dependence on the applied field. Fig. 7.14 shows the root mean square field inhomogeneity in Gauss above T_c in μ SR data at $T = 95\text{--}120$ K, which fits well to

$$\delta(T > T_c) = \delta_o + SB_o \quad (7.13)$$

with a slope of $S = (0.1798 \pm 0.0074) \times 10^{-4}$ and an offset of $\delta_o = 0.158 \pm 0.027$ G. This field dependent inhomogeneity was not observed in silver (which has no dipolar moments) so it is not due to a spatial inhomogeneity of the magnet. The magnetization at $T = 100$ K fits well to

$$(B - H) = H_0 + sH \quad (7.14)$$

with a slope of $S = (0.1936 \pm 0.0048) \times 10^{-4}$ and an offset of $H_0 = 0.011 \pm 0.14$ G.

7.6.5 Degree of Disorder in the FLL

The experimental lineshapes show appreciable ‘‘smearing’’ relative to the theoretical lineshapes. To mimic the effects of the nuclear dipolar fields, the apodization in the Fourier transform and the inherent disorder in the FLL, the theoretical lineshapes were convoluted with a Gaussian. Fig. 7.15 shows the convolution width (σ) after correction for the nuclear dipolar fields (estimated from above T_c) and the apodization used in the Fourier transform. Note that σ is about one half the difference between the cusp field and the average field. The convolution also shows an exponent ≈ 2 in its temperature dependence.

Fig. 7.16 shows an estimate of $\langle s^2 \rangle^{1/2}/L$, the square root of the mean square of the deviation of each vortex from its ideal position in the FLL normalized by the distance L between vortices,

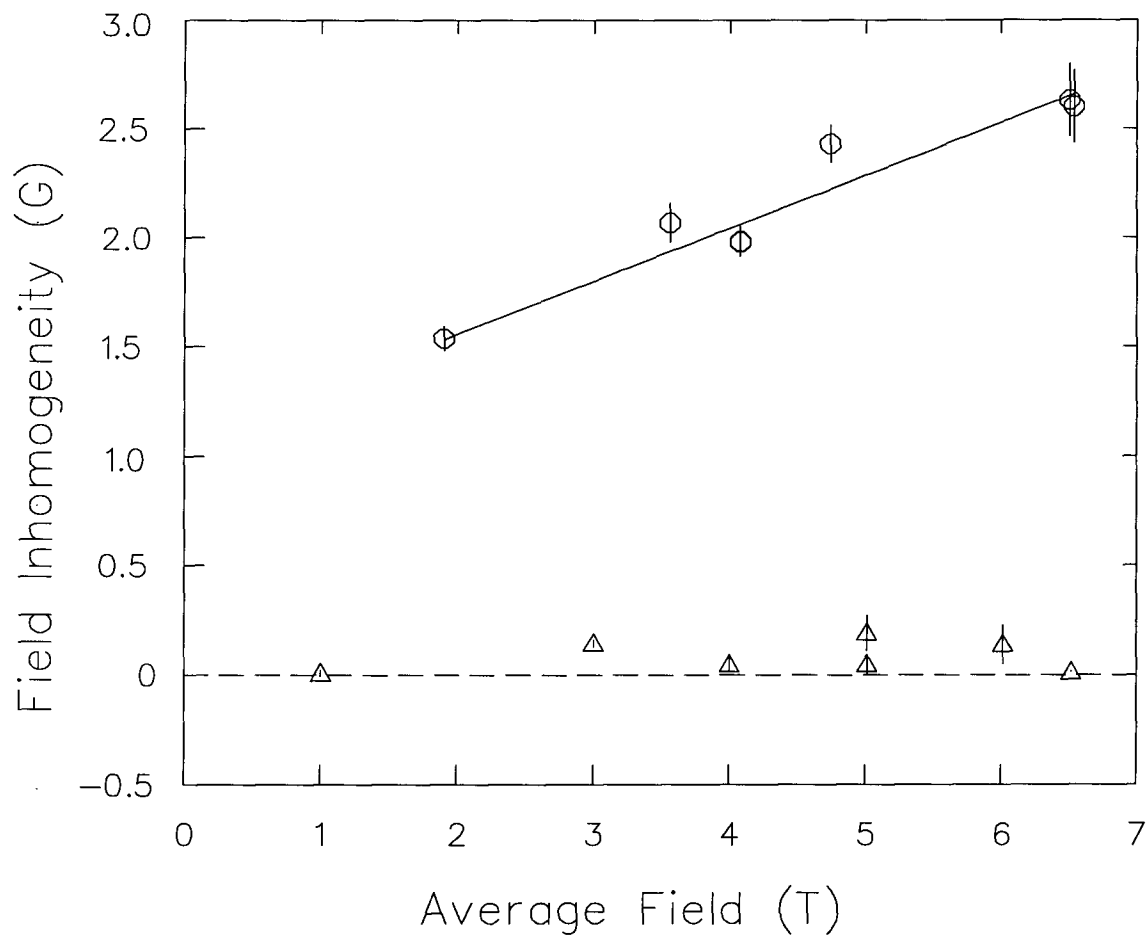


Figure 7.14: Local field inhomogeneity from nuclear dipole moments above T_c , determined by Gaussian fits to $\text{YBa}_2\text{Cu}_3\text{O}_{6.95}$ at temperatures between 95 K and 120 K (circles). Triangles show fits to silver at room temperature, which should show the magnet's inhomogeneity alone since there are no nuclear dipole moments in silver.

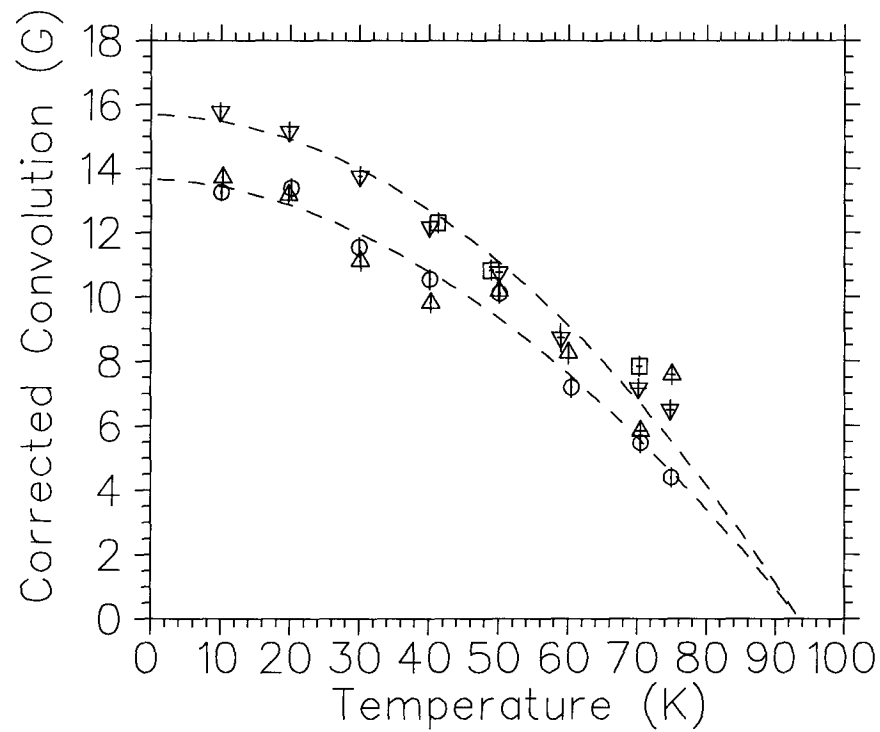


Figure 7.15: The convolution width (σ) in gauss from global fits, after correction for the Gaussian apodization used in the Fourier transform and width of the nuclear dipolar field distribution as measured above T_c for fields of 1.9 T (circles), 4.1 T (triangles), 4.7 T (upside-down triangles) and 6.5 T (squares). The dashed lines are fits to $\sigma = c(1 - \{T/T_c\}^p)$ with T_c fixed to 93.5 K, $c = 13.66 \pm 0.37$ G and $p = 1.84 \pm 0.13$ for the 1.9 T data and $c = 15.68 \pm 0.44$ G and $p = 1.96 \pm 0.15$ for the 4.7 T data.

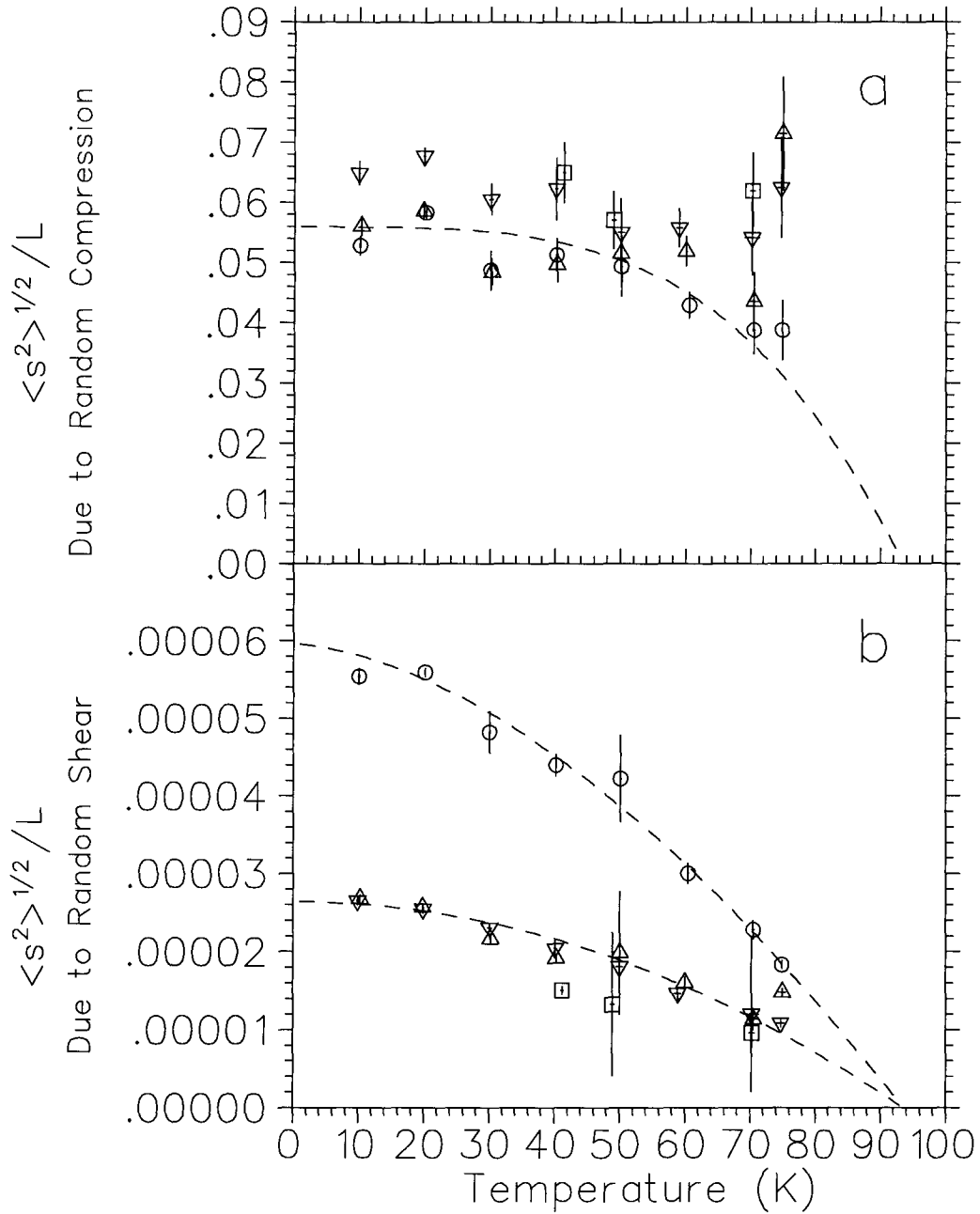


Figure 7.16: Calculated values of $\langle s^2 \rangle^{1/2}/L$, the square root of the mean square of the deviation of each vortex from its ideal position in the FLL normalized by the distance L between vortices, due to random compression (a) and random shear (b), for fields of 1.9 T (circles), 4.1 T (triangles), 4.7 T (upside-down triangles) and 6.5 T (squares). For random compression (a), the dashed line shows $c(1 - \{T/T_c\}^p)$ with T_c fixed to 93.5 K, $c = 0.0559 \pm 0.0015$ and $p = 3.69 \pm 0.63$ for the 1.9 T data. For random shear (b), the dashed lines show $c(1 - \{T/T_c\}^p)$ with T_c fixed to 93.5 K, $c = (5.96 \pm 0.11) \times 10^{-5}$ and $p = 1.681 \pm 0.087$ for the 1.9 T data and $c = (2.642 \pm 0.063) \times 10^{-5}$ and $p = 2.02 \pm 0.17$ for the 4.7 T data.

using the corrected convolution values, the average field B_o , λ^{-2} and H_{c2} . In particular, both random compression and random shear of the FLL should contribute to the smearing observed (see Eqs. 4.48 and 4.49), though random compression contributes much more in this experiment. This suggests that a single Gaussian can be used to convolute the entire theory lineshape. So, when estimating the degree of disorder in the FLL, only the $\langle s^2 \rangle^{1/2}/L$ estimated from the expression for random compression will be used. From Fig. 7.16, the degree of disorder lies between about 5% and 6.5%. The highest values occur in runs with an applied field of 4.7 T, all of which have a rather large background signal (see Fig. B.13). This makes fitting more difficult and leads to an artificially large convolution. In the narrowed lineshapes (those at the higher temperatures and higher fields), the fits tend to misplace the cusp region because the cusp contains very few points in the discrete FFT. This also leads to an artificially large convolution. One should trust the results for 1.9 T, which show a slight reduction in $\langle s^2 \rangle^{1/2}/L$ at larger temperatures, more than those for higher fields, which show a slight reduction followed by a large increase with increasing temperature. Other factors can contribute to the smearing, such as macroscopic field gradients due to the interaction of flux expulsion with pinning and different geometric factors due to the range of crystals sizes and shapes in the mosaic. Since we cannot separate the various causes of smearing, the mean deviation of the vortices from their ideal positions in the FLL in the bulk of $\text{YBa}_2\text{Cu}_3\text{O}_{6.95}$ has an upper limit of 5.5% below 60 K and is nearly constant. Above 60 K, there may be a small decrease in $\langle s^2 \rangle^{1/2}/L$ with increasing temperature.

7.7 Discussion and Conclusions

The simplest yet perhaps most important result from the high field experiments is that the Ginzburg-Landau parameter $\kappa \equiv \lambda/\xi$ is measured to be roughly constant with a value of 70 ± 6 over the majority of the temperature range for $\text{YBa}_2\text{Cu}_3\text{O}_{6.95}$. If we presume that the $\text{YBa}_2\text{Cu}_3\text{O}_{6.95}$ is a weak coupling s -wave superconductor, this result serves as a consistency check for the way that the data was fit. If we don't assume any particular pairing state, it demands that any theory for the mechanism of superconductivity in $\text{YBa}_2\text{Cu}_3\text{O}_{6.95}$ must predict that κ remains approximately constant with temperature.

The value of 70 ± 6 is consistent with the average value of 72 found by Gohng and Finnemore[6] using reversible magnetization. They found that they obtained better results when κ varied from 76.9 at 82 K to 67.5 at 88 K, but they provided no explanation of why. Probably, their measured κ is in fact κ_2 which is defined by[102, p. 931]

$$\left. \frac{dH}{dM} \right|_{H_{c2}} = \frac{1}{4\pi 1.16(2\kappa_2^2 - 1)}. \quad (7.15)$$

Note that $\kappa_2(T)$ becomes identical to κ only at T_c . The temperature dependence that Gohng and Finnemore observe is roughly consistent with $\kappa_2(T)$ for an isotropic s -wave weak coupling BCS superconductor. In weak coupling BCS theory, $\kappa_2(T)$ has a much stronger temperature dependence than $\kappa(T) = \lambda(T)/\xi(T)$ [102, p. 879, p. 871, p. 936]. Various combinations of s -, d -, and p -wave pairing, impurity scattering, paramagnetic contributions, and the degree of strong coupling can produce a vast array of behavior in $\lambda(T)$, $H_{c2}(T)$, $\xi(T)$ and $\kappa(T)$, much of which is not yet calculated. Moreover, the degree of accuracy in the results presented here offer little possibility of distinguishing between a constant κ and a weakly varying $\kappa(T)$.

Since μ SR experiments measure the field distribution in *static* fields, pinning shows up in the lineshape only as a source of “smearing”. This means that properties such as the Ginzburg-Landau parameter κ can be observed in the μ SR lineshape even below T_{irr} , the temperature at which pinning sets in. The disorder in the FLL introduced by the pinning increases the error in the determination of κ . In contrast, measurements of reversible magnetization $M(H)$ (see Eqs. 4.51 and 4.57) can only be performed above T_{irr} . I believe that the μ SR results presented here represent the best measurements to date of κ , $\xi(T)$ and $H_{c2}(T)$ in $\text{YBa}_2\text{Cu}_3\text{O}_{6.95}$ over the majority of the temperature range.

An important point which has not been duly emphasized in this thesis is that the modified London model uses $\xi(T)$ rather than $H_{c2}(T)$ to determine the μ SR lineshape. In Eq. 7.7, ξ represents the radius of the vortex core and the reduced field b approximates the suppression of the superconducting order parameter due to the density of the cores. H_{c2} is inferred from ξ strictly for the convenience of the fitting program. If Eq. 7.1 does not hold exactly, as may be the case for theories other than weak coupling BCS, then it is more appropriate to express b as

$b = \frac{4\pi}{\sqrt{3}} \xi_r^2$ (Eq. 7.10) rather than $b = B_o/H_{c2}(T)$. However, the results for $\kappa = \lambda/\xi$ should be model-independent whether or not $H_{c2}(T)$ is strictly proportional to $\xi^{-2}(T)$.

Can the pairing state be determined by the temperature dependence of either λ or ξ ? Since μ SR data is more sensitive to λ than ξ and theoretical calculations of $\lambda(T)$ are more readily available than $\xi(T)$, our results for ξ are not worth examining further at this time. With the data for the temperature dependence of $H_{c2} \propto \xi^{-2}$ (see Fig. 7.10), the weak coupling s -wave BCS results for a spherical Fermi surface cannot even be distinguished from those for a cylindrical Fermi surface.

The $\lambda(T)$ results are more detailed. For high fields (1.9 T to 6.5 T), a fit to a power law

$$\frac{\lambda_{ab}^{-2}(T)}{\lambda_{ab}^{-2}(0)} = 1 - \left\{ \frac{T}{T_c} \right\}^p \quad (7.16)$$

gives $p = 2.89 \pm 0.23$ assuming $T_c = 93.5$ K. (Introducing the uncertainty in T_c would increase the reported error for p .) The features of the lineshape (such as the minimum, cusp and maximum fields) have a lower order temperature dependence ($p < 2.89$) due to the influence of the field dependence of the order parameter [the term $(1 - b)$ in Eq. 7.7]. Because the degree of disorder (Fig. 7.16) appears to decrease near T_c while staying relatively constant at lower temperatures, the temperature dependence of the convolution should have a lower exponent than that for the minimum and cusp fields. For example, at 1.9 T the convolution has an exponent $p = 1.84 \pm 0.13$ while the minimum field has $p = 2.20 \pm 0.13$ and the cusp field has $p = 2.16 \pm 0.13$. The temperature dependence of $\sigma(T)$ in high fields suggests that in the intermediate field regime, where we could not measure $\sigma(T)$ easily due to low statistics, the temperature dependence of the disorder will cause the exponent p in Eq. 7.16 to be underestimated because the measured quantity, the cusp field, is determined by both λ and the size of the convolution. Furthermore, for data taken at 0.25 T, $p = 2.61 \pm 0.13$ when the flux expulsion was allowed to vary ($c_B = -3.68 \pm 0.64$ G) but $p = 3.14 \pm 0.14$ when the flux expulsion was fixed to the value -0.65 G predicted by magnetization measurements on a crystal from the mosaic. Obviously, the cusp field results suffer from errors in the size and temperature dependence of the flux expulsion. If the free fit is appropriate, the above arguments explain why the power found in the cusp frequency in a moderate field is smaller than that for the magnetic penetration depth as measured from the lineshape in high

fields. Clearly, caution on many fronts is in order when attempting to accurately measure the temperature dependence of the magnetic penetration depth.

The features of the observed μ SR lineshape are not as sharp as those calculated for theoretical lineshapes with perfect FLLs. From consideration of the smearing seen in the experimental data, we concluded that the root-mean-square deviation of the vortices from their ideal positions in the FLL ($\langle s^2 \rangle^{1/2}/L$) is $\leq 5.5\%$ (Sec. 7.6.5). The careful oxygen annealing of the high quality crystals used in these experiment makes it unlikely that any of the observed smearing is due to an inhomogeneous distribution of penetration depths. For the high field data, the superconducting solenoid forming the Helios magnet is spatially quite homogeneous. Drifts in Helios were corrected for using a trim coil regulated by an NMR magnetic field probe to keep the applied field constant (see the silver signal in Fig. 7.14). The distribution of demagnetizing factors for the crystals in the mosaic (see Sec. 4.9) may contribute to the smearing, although the crystals were pieced together tightly to minimize this problem. Measurements of smearing in a single crystal of $\text{YBa}_2\text{Cu}_3\text{O}_{6.95}$,[§] which show less smearing than those in a mosaic, demonstrate (from preliminary fits) only a 30% smaller value for $\langle s^2 \rangle^{1/2}/L$. In light of this, the majority of the smearing present ($> 70\%$) arises from microscopic disorder of the FLL due to pinning of individual vortices, and perhaps as much as 30% is due to the distribution of demagnetizing factors.

If single crystals are more pure than thin films, it may be that the T^2 temperature dependence found for thin films at low temperatures[95] is brought about by the impurities.[11,96] As discussed in Ch. 6, the number of points measured are too few and the scatter is too large in the low temperature region of the intermediate and high field μ SR data to be able to determine the pairing state of $\text{YBa}_2\text{Cu}_3\text{O}_{6.95}$. The overall temperature dependence (from zero to T_c) is also strongly affected by impurity levels, the degree of strong coupling, anisotropy, nodes in the gap, *etc.*, [109,11] which makes the assignment of the pairing state still more difficult. For example, Prohammer and Carbotte have calculated $H_{c2}(T)$ [110] and $\lambda(T)$ [109] for *s*-wave superconductivity and two likely models of *d*-wave superconductivity in both the weak and strong limits. The *d*-wave model with $\hat{k}_x^2 - \hat{k}_y^2$ symmetry, which is favored by many theorists (see Ref. [23] and references therein),

[§]Performed by Robert Kiefl *et al.* at TRIUMF in December of 1992.

predicts an $H_{c2}(T)$ which looks promising, but the temperature dependence of the penetration depth is linear over too large a range to fit the present μ SR data.

Bulut and Scalapino[23] used a weak coupling model on a metal with antiferromagnetic spin fluctuations to test s -wave and d -wave superconductivity against NMR results for the copper and oxygen Knight shifts and T_1 nuclear relaxation rates. They found that s -wave superconductivity fits the Knight shifts better while d -wave superconductivity fits the relaxation rates better.

Qualitatively, a gap anisotropy in an s -wave model won't affect $\lambda(T)$ in the low temperature limit, but it will change the overall temperature dependence, probably by reducing the range of temperatures over which $\lambda(T)$ has an exponential temperature dependence. It is possible that our results for $\lambda_{ab}(T)$ are consistent with s -wave superconductivity with a large gap anisotropy in the \hat{a} - \hat{b} plane and some strong coupling. This might produce the observed power law dependence—an exponent greater than that for weak coupling BCS and no clear plateau. However, the low temperature dependence is more important than the dependence over the whole temperature range, in which case the high field data does not contain enough different temperatures to determine the pairing state. The intermediate field data taken at 2.5 kG in Chapter 6 suggests a linear dependence, which would be reflective of d -wave superconductivity.

Chapter 8

Conclusions

In summary, the μ SR lineshape is determined by both the penetration depth λ and the coherence length ξ in fields high enough that $\lambda \gg L > \xi$. For a single experimental run at a given temperature and field, λ and ξ (or alternatively λ^{-2} and H_{c2}) cannot both be uniquely determined because nearly identical lineshapes are produced for a range of coupled values of λ and ξ . One would prefer to assume the value of ξ or H_{c2} from other experiments because λ affects the lineshape more strongly than do ξ or H_{c2} , but estimates of $\xi(T)$ from measurements of $H_{c2}(T)$ are very rough, except perhaps near T_c . Fortunately, values for both λ^{-2} and H_{c2} in $\text{YBa}_2\text{Cu}_3\text{O}_{6.95}$ were found by simultaneously fitting runs with different applied fields for each temperature. In moderate fields ($\lambda \gtrsim L \gg \xi$), the lineshape is mostly independent of ξ and H_{c2} .

Extensive measurements of the μ SR lineshape in a mosaic of $\text{YBa}_2\text{Cu}_3\text{O}_{6.95}$ single crystals were made in high fields (1.9 T, 4.1 T, 4.7 T and 6.5 T) parallel to the mosaic's \hat{c} axis. While the detailed temperature dependence of ξ and H_{c2} remains uncertain at low temperatures, their values are $H_{c2||\hat{c}}(10 \text{ K}) \approx 90 \text{ T}$ and $\xi_{ab}(10 \text{ K}) \approx 0.0019 \mu\text{m}$. The temperature dependence of λ in the $\hat{a}\text{-}\hat{b}$ plane, which is better determined by the μ SR measurements, was found to follow

$$\lambda_{ab}^{-2}(T)/\lambda_{ab}^{-2}(0) = 1 - \{T/T_c\}^p$$

with an exponent $p = 2.89 \pm 0.23$ over the temperature range 10 K to 75 K. The features in the lineshape (such as the cusp field) have a weaker temperature dependence for higher fields with correspondingly smaller exponents than that for the penetration depth when fit to a similar expression (Eq. 6.3). The weaker temperature dependence is due to the influence of the coherence length, the field dependence of superconducting order parameter [proportional to $1 - B/H_{c2}(t)$] and the temperature dependence of the disorder in the FLL. This means that fits to the London model,

which ignores the coherence length, must not be used to determine temperature dependence of the magnetic penetration depth in high fields. The Ginzburg-Landau parameter $\kappa = \lambda/\xi$ was found to be independent of temperature between 30 K and 75 K and to have a value of 70 ± 6 . This is the first measurement to date of κ in $\text{YBa}_2\text{Cu}_3\text{O}_{6.95}$ for this temperature range.

Any proposed pairing state for the superconductor $\text{YBa}_2\text{Cu}_3\text{O}_{6.95}$ must be consistent with the temperature-independent κ found here. The exact temperature dependence of λ_{ab} at low temperatures was not determined with enough accuracy (either at moderate or high fields) to support or rule out specific pairing states. The fact that the overall temperature dependence has an exponent $p = 2.9$ is important, because this contradicts the higher exponents ($p \approx 3.5$) found in sintered powders of $\text{YBa}_2\text{Cu}_3\text{O}_{6.95}$, which often seem to be nearly consistent with the Gorter-Casimir two-fluid model—a power law with the exponent fixed to 4. The temperature dependence of λ_{ab} over all temperature in our $\text{YBa}_2\text{Cu}_3\text{O}_{6.95}$ mosaic is not much stronger than weak coupling BCS (roughly equivalent to a power law with exponent $p = 2.22$), so the penetration depth could possibly be consistent with an *s*-wave superconductor with strong coupling (which would increase p) and some anisotropy in the gap [thereby reducing the region over which $\lambda_{ab}(T \gtrsim 0)$ has a plateau]. However, in fields of 2.5 kG where more temperatures were measured, there appears to be a linear temperature dependence below 25 K, which would support *d*-wave superconductivity. Very recent experiments using accurate microwave measurements[97,98] and high statistics μSR measurements in a single crystal of $\text{YBa}_2\text{Cu}_3\text{O}_{6.95}$ [99] confirm the linear temperature dependence.

The quality of the μSR lineshapes at high fields should provide sufficient evidence against the argument that “junk” effects such as impurities within the sample which cause pair-breaking or inclusions of magnetic impurity phases (which introduces extra relaxation at low temperatures with a Curie law temperature dependence) are artificially modifying the temperature dependence of λ_{ab} in these crystals compared to that inferred from unoriented sintered powders. It is much more difficult to extract unambiguous information from unoriented sintered powders than from single crystals since the lineshapes they produce are powder-averaged over $\lambda(\theta)$ and $\xi(\theta)$ [or alternatively $\lambda^{-2}(\theta)$ and $H_{c2}(\theta)$], although ignoring the angular dependence of H_{c2} and assuming a temperature-independent penetration depth anisotropy makes it possible to estimate the magnetic

penetration depth in the $\hat{a}\text{-}\hat{b}$ plane from unoriented samples.[111,81,53,77,76,27] It is possible that the anisotropy ($\Gamma = \lambda_c/\lambda_{ab}$) itself is temperature dependent; theoretical calculations for a Josephson-junction layered superconductor indicate this possibility.[101] Moreover, morphology effects such as weak links, porosity, crystallite size, and angular-dependent pinning effects may affect the temperature dependence of the measured lineshape. The values determined for $\lambda_{ab}(10\text{ K})$ from powders are certainly consistent with those found here in single crystals, reflecting the small error occurring in λ arising from a relatively large error occurring in linewidth ($\Delta B \propto \lambda^{-2}$). Overall, the additional complications of powder averaging makes sintered powder samples less reliable than single crystals for the measurement of $\lambda_{ab}(T)$.

As measured by the high field data, the magnetic penetration depth in the $\hat{a}\text{-}\hat{b}$ plane of $\text{YBa}_2\text{Cu}_3\text{O}_{6.95}$ is $0.1491 \pm 0.0017\ \mu\text{m}$ at 10 K. As measured in medium fields (0.25 T) at a temperature of 10 K, λ is between $0.1405\ \mu\text{m}$ and $0.1352\ \mu\text{m}$ depending on the amount of flux expulsion assumed. In low fields (an applied field of 100 G), fitting to a simple Gaussian gave an anisotropy $\Gamma = \lambda_c/\lambda_{ab}$ of about 5 and a penetration depth between $0.1380\ \mu\text{m}$ and $0.1510\ \mu\text{m}$; we could be more certain if we knew the degree of flux expulsion and if we had a complete theory of low field FLL geometries in the presence of pinning. Fits to data taken in 100 G when $\vec{B} \parallel \hat{c}$ (*i.e.*, $\theta = 0$), gave $\lambda_{ab} = 0.1270 \pm 0.0012\ \mu\text{m}$ at $T = 10\text{ K}$. Combining all of these measurements, it appears that $\lambda_{ab}(10\text{ K})$ is approximately $0.1390\ \mu\text{m}$ with the generous error of $0.0120\ \mu\text{m}$. On the other hand, the most thorough analysis was performed on the high field data, which suggests that the true value of the penetration depth at 10 K is closer to $0.1490 \pm 0.0120\ \mu\text{m}$.

Pinning-induced disorder in the FLL causes a Gaussian broadening of the theoretical lineshape. With the applied field parallel to the \hat{c} axis of $\text{YBa}_2\text{Cu}_3\text{O}_{6.95}$, we observe values for the width of the Gaussian broadening ranging between 12 G at an applied field of 100 G, 18 G at 0.25 T, 13.5 G at 1.9 T and 4.1 T and 15.5 G at 4.7 T. At the intermediate field ($\lambda > L \gg \xi$) of 0.25 T, both the lineshape and the Gaussian broadening are at their widest. The 12 G broadening observed at 100 G corresponds to rms disorder in the FLL given by $\langle s^2 \rangle^{1/2}/L \approx 4\%$, though this value may be underestimated since the penetration depth appears to be underestimated. In high fields ($B_o > 1\text{ T}$), the broadening corresponds to rms disorder between 5.5% and 6.5%, with the lower

value being more reliable since the convolution was overestimated slightly for the 4.7 T field due to interference from a large background signal. In any case, the values for disorder should be considered as upper bounds since a distribution of demagnetization factors for the crystals in the mosaic may contribute as much as 30% to the smearing. It is important to remember that μ SR is only sensitive to variation in the local field, such as that caused by nearest neighbor disorder in the FLL. Therefore, with μ SR, the measured mean deviation of vortices from their ideal positions in the FLL cannot distinguish between disorder which maintains some amount of long range hexagonal order and that which allows slow rotations and undulations of the FLL's unit cell vectors.[75] Unfortunately, the degree of disorder present in our experiments (along with the background signal) was large enough to mask any expected details in the lineshape at low fields, such as a splitting in the cusp field, which may have indicated the presence of chains of vortices in the FLL.

Bibliography

- [1] W. Meissner and R. Ochsenfeld. Ein neuer Effekt bei Eintritt der Supraleitung (A new effect at the onset of superconductivity). *Naturwissenschaften*, page 787, (1933).
- [2] F. London and H. London. The electromagnetic equations of the superconductor. *Proc. Roy. Soc. London (A)*, pages 71–88, (1935).
- [3] V.L. Ginzburg and L.D. Landau. *Zh. Eksp. Teor. Fiz.*, **20**, 1044, (1950). (in Russian).
- [4] E.M. Lifshitz and L.P. Pitaevskii. *Statistical Physics, Part 2*, volume 9 of *Landau and Lifshitz Course of Theoretical Physics*. Pergamon Press, 1980.
- [5] Zhidong Hao, John R. Clem, M.W. McElfresh, L. Civale, A.P. Malozemoff, and F. Holtzberg. Model for the reversible magnetization of high- κ type-II superconductors: Application to high- T_c superconductors. *Physical Review B*, **43**, 2844–2852, (1991).
- [6] Jungho Gohng and D.K. Finnemore. Critical fields and vortex structure of $\text{YBa}_2\text{Cu}_3\text{O}_{7-\delta}$ derived from reversible magnetization. *Physical Review B*, **46**, 398–403, (1992).
- [7] A.A. Abrikosov. On the magnetic properties of superconductors of the second group. *Sov. Phys. JETP*, **5**, 1174–1182, (1957).
- [8] R.P. Huebener. *Magnetic Flux Structures in Superconductors*. Solid State Sciences 6. Springer-Verlag, 1979.
- [9] J.G. Bednorz and K.A. Müller. Possible superconductivity. *Z. Phys.*, **B 64**, 189, (1986).
- [10] M.K. Wu, J.R. Ashburn, C.J. Torng, P.H. Hor, R.L. Meng, L. Gao, Z.J. Huang, Y.Q. Wang, and C.W. Chu. Superconductivity at 93K in a new mixed-phase Y-Ba-Cu-O compound system at ambient pressure. *Physical Review Letters*, **58**, 908, (1987).
- [11] James F. Annett, Nigel Goldenfeld, and S.R. Renn. The pairing state of $\text{YBa}_2\text{Cu}_3\text{O}_{7-\delta}$. In Donald M. Ginsberg, editor, *Physical Properties of High Temperature Superconductors II*, page 571. World Scientific, 1991.
- [12] Y.J. Uemura, G.M. Luke, B.J. Sternlieb, J.H. Brewer, J.F. Carolan, W.N. Hardy, R. Kadono, J.R. Kempton, R.F. Kiefl, S.R. Kreitzman, P. Mulhern, T.M. Riseman, D.Ll. Williams, B.X. Yang, S. Uchida, H. Takagi, J. Gopalakrishnan, A.W. Sleight, A.R. Strzlecki, M.A. Subramanian, C.L. Chien, M.Z. Chieplak, G. Xiao, V.Y. Lee, B.W. Statt, C.E. Stronach, W.J. Kossler, and X.H. Yu. Universal correlations between T_c and n_s/m^* (carrier density / effective mass) in high- T_c cuprate superconductors. *Physical Review Letters*, **62**, 2317–2320, (1989).

- [13] Y.J. Uemura, G.M. Luke, B.J. Sternlieb, L.P. Le, J.H. Brewer, R. Kadono, R.F. Kiefl, S.R. Kreitzman, T.M. Riseman, C.L. Seaman, J.J. Neumeier, M.B. Maple, G. Saito, and H. Yamochi. Recent topics of μ SR studies on high- T_c systems. Paper in proceedings of the NATO Advanced Research Workshop, Crete, Oct. 1989, 1990.
- [14] Y.J. Uemura, L.P. Le, G.M. Luke, B.J. Sternlieb, W.D. Wu, J.H. Brewer, T.M. Riseman, C.L. Seaman, M.B. Maple, M. Ishikawa, D.G. Hinks, J.D. Jorgensen, G. Saito, and H. Yamochi. Basic similarities among cuprate, bismuthate, organic, chevrel-phase and heavy fermion superconductors shown by penetration-depth studies. *Physical Review Letters*, **66**, 2665–2669, (1991).
- [15] W.H. Li, J.W. Lynn, and Z. Fisk. Magnetic order of the Cu planes and chains in $R\text{Ba}_2\text{Cu}_3\text{O}_{6+x}$. *Physical Review B*, **41**, 4098–4111, (1990).
- [16] J. H. Brewer, E. J. Ansaldo, J. F. Carolan, A.C.D. Chaklader, W.N. Hardy, D. R. Harshman, M.E. Hayden, M. Ishikawa, N. Kaplan, R. Keitel, J. R. Kempton, R. F. Kiefl, W. J. Kossler, S. R. Kreitzman, A. Kulpa, Y. Kuno, G. M. Luke, H. Miyatake, K. Nagamine, Y. Nakazawa, N. Nishida, K. Nishiyama, S. Ohkuma, T. M. Riseman, G. Roehmer, P. Schleger, D. Shimada, C.E. Stronach, T. Takabatake, Y.J. Uemura, Y. Watanabe, D.Ll. Williams, T. Yamazaki, and B.X. Yang. Antiferromagnetism and superconductivity in oxygen deficient $\text{YBa}_2\text{Cu}_3\text{O}_x$. *Physical Review Letters*, **60**, 1073–1076, (1988).
- [17] J.H. Brewer, J.F. Carolan, W.N. Hardy, B.X. Yang, P. Schleger, R. Kadono, J.R. Kempton, R.F. Kiefl, S.R. Kreitzman, G.M. Luke, T.M. Riseman, D.Ll. Williams, K. Chow, P. Dosanjh, B. Gowe, R. Krahn, and M. Norman. Coexistence of superconductivity and static magnetic order in $\text{YBa}_2\text{Cu}_3\text{O}_x$. *Physica C*, **162–164**, 33–34, (1989).
- [18] J.H. Brewer, J.F. Carolan, W.N. Hardy, H. Hart, R. Kadono, J.R. Kempton, R.F. Kiefl, S.R. Kreitzman, G.M. Luke, T.M. Riseman, P. Schleger, B.J. Sternlieb, Y.J. Uemura, D.Ll. Williams, and B.X. Yang. Magnetic ordering in $\text{YBa}_2\text{Cu}_3\text{O}_x$ studied by μ^+ spin rotation. *Physica C*, **162–164**, 157–158, (1989).
- [19] G. Shirane, J. Als-Nielsen, M. Nielsen, J.M. Tranquada, H. Chou, S. Shamoto, and M. Sato. Magnetic correlations in $\text{YBa}_2\text{Cu}_3\text{O}_{6+x}$ at superconducting concentrations. *Physical Review B*, **41**, 6547–6552, (1990).
- [20] P.M. Gehring, J.M. Tranquada, G. Shirane, J.R.D. Copley, R.W. Erwin, M. Sato, and S. Shamoto. Magnetic correlations and energy gap in superconducting $\text{YBa}_2\text{Cu}_3\text{O}_{6.6}$ with $T_c = 53$ K. *Physical Review B*, **44**, 2811–2814, (1991).
- [21] Takashi Imai. Analysis of nuclear relaxation experiments in high T_c oxides based on Mill-Rice Hamiltonian. *Journal of the Physical Society of Japan*, **59**, 2508–2521, (1990).
- [22] H. Alloul, T. Ohno, and P. Mendels. ^{89}Y NMR evidence for a Fermi-liquid behavior in $\text{YBa}_2\text{Cu}_3\text{O}_{6+x}$. *Physical Review Letters*, **63**, 1700–1703, (1989).
- [23] N. Bulut and D.J. Scalapino. Weak-coupling model of spin fluctuations in the superconducting state of the layered cuprates. *Physical Review B*, **45**, 2371–2384, (1992).

- [24] Y.J. Uemura, V.J. Emery, A.R. Moodenbaugh, M. Suenaga, D.C. Johnston, A.J. Jacobson, J.T. Lewandowski, J.H. Brewer, R.F. Kiefl, S.R. Kreitzman, G.M. Luke, T. Riseman, C.E. Stronach, W.J. Kossler, J.R. Kempton, X.H. Yu, D. Opie, and H.E. Schone. Systematic variation of magnetic-field penetration depth in high- T_c superconductors studied by muon-spin relaxation. *Physical Review B (Rapid Commun.)*, **38**, 909–912, (1988).
- [25] D.R. Harshman, G. Aeppli, E.J. Ansaldo, B. Batlogg, J.H. Brewer, J.F. Carolan, R.J. Cava, M. Celio, A.C.D. Chaklader, W.N. Hardy, S.R. Kreitzman, G.M. Luke, D.R. Noakes, and M. Senba. Temperature dependence of the magnetic penetration depth in the high- T_c superconductor $\text{Ba}_2\text{YCu}_3\text{O}_{9-\delta}$: Evidence for conventional s-wave pairing. *Physical Review B*, **36**, 2386, (1987).
- [26] H. Keller, W. Kündig, I.M. Savić, H. Simmler, B. Stäubli-Pümpin, M. Warden, D. Zech, P. Zimmermann, E. Kaldis, J. Karpinski, S. Rusiecki, J.H. Brewer, T.M. Riseman, J.W. Schneider, Y. Maeno, and C. Rossel. Muon-spin rotation (μSR) study of the temperature dependence of the London penetration depth in copper oxide superconductors. *Physica C*, **185–189**, 1089–1090, (1991).
- [27] D.R. Harshman, L.F. Schneemeyer, J.V. Waszczak, G. Aeppli, R.J. Cava, B. Batlogg, L.W. Rupp, E.J. Ansaldo, and D.L. Williams. Magnetic penetration depth in single-crystal $\text{YBa}_2\text{Cu}_3\text{O}_{7-\delta}$. *Physical Review B*, **39**, 851–854, (1989).
- [28] B. Pümpin, H. Keller, W. Kündig, I.M. Savić, J.W. Schneider, H. Simmler, P. Zimmermann, E. Kaldis, S. Rusiecki, C. Rossel, and E.M. Forgan. Magnetic and electronic properties of $\text{YBa}_2\text{Cu}_3\text{O}_x$ ($6.5 < x < 7.0$) studied by muon spin rotation. *Journal of the Less-Common Metals*, **164 & 165**, 994–1008, (1990).
- [29] B. Pümpin, H. Keller, W. Kündig, W. Odermatt, I.M. Savić, J.W. Schneider, H. Simmler, P. Zimmermann, E. Kaldis, S. Rusiecki, Y. Maeno, and C. Rossel. Muon-spin-rotation measurements of the London penetration depths in $\text{YBa}_2\text{Cu}_3\text{O}_{6.97}$. *Physical Review B*, **42**, 8019–8029, (1990).
- [30] W.C. Lee, R.A. Klemm, and D.C. Johnston. Superconducting fluctuation diamagnetism above T_c in $\text{YBa}_2\text{Cu}_3\text{O}_7$, $\text{La}_{1.8}\text{Sr}_{0.2}\text{CuO}_4$, and $\text{Bi}_{2-x}\text{Pb}_x\text{Sr}_2\text{CaCu}_2\text{O}_{8+\delta}$. *Physical Review Letters*, **63**, 1012–1015, (1989).
- [31] J. Rammer. Temperature and field dependence of the vortex structure in high- T_c superconductors. *Physica C*, **177**, 421–430, (1991).
- [32] D.J. Bishop, P.L. Gammel, D.A. Huse, and C.A. Murray. Magnetic flux-line lattices and vortices in the copper-oxide superconductors. *Science*, **255**, 165–172, (1992). and references within.
- [33] E.H. Brandt. Magnetic field density of distorted vortex lattices. *Physica C*, **162–164**, 257–258, (1989).
- [34] J.H. Brewer, R.F. Kiefl, J.F. Carolan, P. Dosanjh, W.N. Hardy, S.R. Kreitzman, Q. Li, T.M. Riseman, P. Schleger, H. Zhou, E.J. Ansaldo, D.R. Noakes, L.P. Le, G.M. Luke, Y.J. Uemura, K. Hepburn-Wiley, and C.E. Stronach. Site of the positive muon in $\text{YBa}_2\text{Cu}_3\text{O}_x$. *Hyperfine Interactions*, **63**, 177–182, (1990).

- [35] R.L. Lichti, T.R. Adams, and T.L. Gibson. Stability of muon-oxygen bond sites in $\text{RBa}_2\text{Cu}_3\text{O}_7$. *Hyperfine Interactions*, **63**, 199–206, (1990).
- [36] M. Weber, P. Birrer, F.N. Gygax, B. Hitti, E. Lippelt, H. Maletta, and A. Schenck. Identification of μ^+ -sites in the 1-2-3 compound. *Hyperfine Interactions*, **63**, 207–212, (1990).
- [37] N. Nishida and H. Miyatake. Positive muon sites and possibility of anyons in the $\text{YBa}_2\text{Cu}_3\text{O}_x$ system. *Hyperfine Interactions*, **63**, 183–198, (1990).
- [38] W.K. Dawson, C.H. Halim, S.P. Weathersby, J.A. Flint, J.C. Lam, T.J. Hoffman, C. Boekema, K.C.B. Chan, R.L. Litchi, D.W. Cooke, M.S. Jahan, and J.E. Crow. Magnetism and candidate muon-probe sites in $\text{RBa}_2\text{Cu}_3\text{O}_y$. *Hyperfine Interactions*, **63**, 219–226, (1990).
- [39] R.F. Kiefl, J.H. Brewer, I. Affleck, J.F. Carolan, P. Donsanjh, W.N. Hardy, T. Hsu, R. Kadono, J.R. Kempton, S.R. Kreitzman, Q. Li, A.H. O’Rielly, T.M. Riseman, P.W. Schleger, P.C.E. Stamp, H. Zhou, L.P. Le, G.M. Luke, B. Sternlieb, Y.J. Uemura, H.R. Hart, and K.W. Lay. Search for anomalous internal magnetic fields in high- T_C superconductors as evidence for broken time reversal symmetry. *Physical Review Letters*, **64**, 2082–2085, (1990).
- [40] Ruixing Liang, P. Dosanjh, D.A. Bonn, D.J. Baar, J.F. Carolan, and W.N. Hardy. Growth and properties of superconducting YBCO single crystals. *Physica C*, **195**, 51–58, (1992).
- [41] S.F.J. Cox. Implanted muon studies in condensed matter science. *J. Phys. C.*, **20**, 1987.
- [42] A. Schenck. *Muon Spin Rotation Spectroscopy: Principles and Applications in Solid State Physics*. Adam Hilger Ltd., 1985.
- [43] J. Chappert and R.I. Grynspan, editors. *Muons and Pions in Materials Research*. North-Holland, 1987.
- [44] Particle Data Group. Review of particle properties. *Reviews of Modern Physics*, **56**, s10, 1984.
- [45] T. Bowen. The surface muon beam. *Physics Today*, July, 1985.
- [46] J.H. Brewer. μ^+ SR with surface muon beams. In *Proceedings of the Second International Topical Meeting on Muon Spin Rotation*. North-Holland, (1980).
- [47] J.L. Beveridge, J. Doornbos, D.M. Garner, D.J. Arseneau, I.D. Reid, and M. Senba. A spin rotator for surface μ^+ beams on the new M20 channel at TRIUMF. *Nucl. Instr. and Methods in Physics Research*, **A240**, 1985.
- [48] R.S. Hayano, Y.J. Uemura, J. Imazato, N. Nishida, T. Yamazaki, and R. Kubo. Zero- and low-field spin relaxation studied by positive muons. *Physical Review B*, **20**, (1979).
- [49] A. Abragam. *Principles of Nuclear Magnetism*. Oxford, 1971.
- [50] D.R. Noakes, J.H. Brewer, D.R. Harshman, E.J. Ansaldo, and C.Y. Huang. Electron, muon, and nuclear spin dynamics in SmRh_4B_4 and ErRh_4B_4 . *Physical Review B*, **35**, 6597–6607, (1987).

- [51] R. Kubo and T. Toyabe. Magnetic resonance and relaxation. North Holland, 1967.
- [52] Ralph Eric Turner. Skewed-field technique in muon-spin rotation: Kubo-Toyabe longitudinal and transverse relaxation functions. *Physical Review B*, **31**, 112–120, (1985).
- [53] T.M. Riseman, J.H. Brewer, B.R. Cyca, J.F. Carolan, W.N. Hardy, R.F. Kiefl, M. Celio, W.J. Kossler, Y.J. Uemura, G.M. Luke, B.J. Sternlieb, H. Hart, K.W. Lay, H. Kojima, I. Tanaka, and K. Kakurai. μ^+ SR lineshape of oriented and unoriented high- T_c superconductors. *Physica C*, **162–164**, 1555–1556, (1989).
- [54] William H. Press, Brian P. Flannery, Saul A. Teukolsky, and William T. Vetterling. *Numerical Recipes: the Art of Scientific Computing (FORTRAN Version)*. Cambridge University Press, 1989.
- [55] Tanya M. Riseman and Jess H. Brewer. The rotating reference frame transformation in μ SR. *Hyperfine Interactions*, **65**, 1107–1111, (1990).
- [56] Robert H. Norton and Reinhard Beer. New apodizing functions for Fourier spectrometry. *J. Opt. Soc. Am.*, **66**, 259–264, (1976).
- [57] Charles P. Poole, Jr., Timir Datta, and Horacia A. Farach. *Copper Oxide Superconductors*. John Wiley and Sons, 1988.
- [58] W.E. Lawrence and S. Doniach. Theory of layer structure superconductors. In E. Kanda, editor, *Proceedings of the 12th International Conference on Low Temperature Physics, Kyoto*, pages 361–362. 1970.
- [59] R.A. Klemm, A. Luther, and M.R. Beasley. Theory of the upper critical field in layered superconductors. *Physical Review B*, **12**, 877–891, (1975).
- [60] D.E. Prober, R.E. Schwall, and M.R. Beasley. Upper critical fields and reduced dimensionality of the superconducting layered compounds. *Physical Review B*, **21**, 2717, (1980).
- [61] W.J. Gallagher, T.K. Worthington, T.R. Dinger, F. Holtzberg, D.L. Kaiser, and R.L. Sandstrom. Anisotropy in the magnetic properties of single-crystal $Y_1Ba_2Cu_3O_{7-x}$. *Physica B*, **148**, 228, (1988).
- [62] D.E. Farrell, J.P. Rice, D.M. Ginsberg, and J.Z. Liu. Experimental evidence of a dimensional crossover in $Y_1Ba_2Cu_3O_{7-\delta}$. *Physical Review Letters*, **64**, 1573–1576, (1990).
- [63] V.G. Kogan. London approach to anisotropic type-II superconductors. *Physical Review B*, **24**, 1572–1575, (1981).
- [64] W.H. Kleiner, L.M. Roth, and S.H. Autler. Bulk solutions of Ginzburg-Landau equations for type II superconductors: Upper critical field region. *Physical Review A*, **133**, 1226, (1964).
- [65] Sara L. Thiemann, Z. Radovic, and V.G. Kogan. Field structure of vortex lattices in uniaxial superconductors. *Physical Review B*, **39**, 11406–11412, (1989).
- [66] V.G. Kogan, N. Nakagawa, and S.L. Thiemann. Interaction of vortices in uniaxial superconductors. *Physical Review B*, **42**, 2631–2634, (1990).

- [67] L.L. Daemen, L.J. Campbell, and V.G. Kogan. Flux-line lattice in uniaxial superconductors at low magnetic inductions. *Physical Review B*, **46**, 3631–3637, (1992).
- [68] A.I. Buzdin and A.Yu. Simonov. Penetration of inclined vortices into layered superconductors. *Soviet Physics JEPT Letters*, **51**, 191–195, (1990).
- [69] A.I. Buzdin and A.Yu. Simonov. Magnetic flux penetration into layered superconductors. *Soviet Physics JEPT*, **71**, 1165–1171, (1990).
- [70] V.G. Kogan and J.R. Clem. Uniaxial type-II superconductors near the upper critical field. *Physical Review B*, **24**, 2497, (1981).
- [71] L.J. Campbell, M.M. Doria, and V.G. Kogan. Vortex lattice structures in uniaxial superconductors. *Physical Review B*, **38**, 2439, (1988).
- [72] Neil W. Ashcroft and N. David Mermin. *Solid State Physics*, page 86. Holt, Rinehart, and Winston, 1976.
- [73] A. Sudbø and E.H. Brandt. Reconstruction of vortex lattices at low inductions. *Physical Review Letters*, **68**, 1758–1761, (1992).
- [74] E.H. Brandt. Flux distribution and penetration depth measured by muon spin rotation in high- T_c superconductors. *Physical Review B*, **37**, 2349–2352, (1988).
- [75] E.H. Brandt. Magnetic field density of perfect and imperfect flux line lattices in type II superconductors. I. Application of periodic solutions. *Journal of Low Temperature Physics*, **73**, 355–390, (1988).
- [76] T.M. Riseman, J.H. Brewer, J.F. Carolan, W.N. Hardy, R.F. Kiefl, D.Ll. Williams, H. Zhou, L.P. Le, G.M. Luke, B.J. Sternlieb, Y.J. Uemura, B. Hunter, K.N.R. Taylor, H. Hart, and K.W. Lay. Characterization of high temperature superconductors with muon spin rotation. In Calvin G. Burnham, editor, *2nd World Congress on Superconductivity*, pages 160–169. World Scientific, 1992. Progress in High Temperature Superconductivity—vol. **28**.
- [77] Tanya M. Riseman. Methods of determining the magnetic penetration depth of high- κ superconductors from μ SR measurements. *Hyperfine Interactions*, **63**, 65–70, (1990).
- [78] S.K. Yip and J.A. Sauls. Nonlinear Meissner effect in CuO superconductors. *Physical Review Letters*, **69**, 2264–2267, (1992).
- [79] D. Herlach, G. Majer, J. Major, J. Rosenkranz, M. Schmolz, W. Schwarz, A. Seeger, W. Templ, E.H. Brandt, U. Essmann, K. Fürderer, and M. Gladisch. Magnetic flux distribution in the bulk of the pure type-II superconductor niobium measured with positive muons. *Hyperfine Interactions*, **63**, 41–48, (1990).
- [80] D.R. Harshman, A.T. Fiory, and R.J. Cava. Local magnetic fields in the pinned vortex state: Effect on the μ^+ -spin rotation line shape. *Physical Review Letters*, **66**, 3313–3316, (1991). See correction, **67**, p. 2748 (1991).
- [81] Tanya Maria Riseman. μ SR measurement of the magnetic penetration depth in high- T_c superconductors. Master's thesis, University of British Columbia, Vancouver, British Columbia, Canada, April 1989.

- [82] E.M. Forgan, D.McK. Paul, H.A. Mook, P.A. Timmins, H. Keller, S. Sutton, and J.S. Abell. Observation by neutron diffraction of the magnetic flux lattice in single-crystal $\text{YBa}_2\text{Cu}_3\text{O}_{7-\delta}$. *Letters to Nature*, **343**, 735–737, (1990).
- [83] J.A. Osborn. Demagnetizing factors of the general ellipsoid. *Physical Review*, **67**, 351–357, (1945).
- [84] E.M. Forgan, S.L. Lee, S. Sutton, F. Wellhofer, J.S. Abell, C.E. Gough, S.F.J. Cox, and C.A. Scott. μSR investigation of anisotropy and temperature dependence of magnetic penetration lengths in crystals of $\text{YBa}_2\text{Cu}_3\text{O}_{7-d}$. *Superconductivity Science and Technology*, **3**, 217–221, (1990).
- [85] P.L. Gammel, D.J. Bishop, J.P. Rice, and D.M. Ginsberg. Images of the vortex chain state in untwinned $\text{YBa}_2\text{Cu}_3\text{O}_{7-\delta}$ crystals. *Physical Review Letters*, **68**, 3343–3346, (1992).
- [86] W.D. Wu, L.P. Le, B.J. Sternlieb, G.M. Luke, Y.J. Uemura, P. Dosanjh, and T.M. Riseman. μSR studies of flux pinning in $\text{Bi}_2\text{Sr}_2\text{CaCu}_2\text{O}_8$ and $\text{Pb}_{0.7}\text{Bi}_{1.3}\text{Sr}_2\text{CaCu}_2\text{O}_8$. *Physical Review B*, **47**, 8172–8186, (1993).
- [87] B.J. Sternlieb, G.M. Luke, Y.J. Uemura, J.H. Brewer, R. Kadono, J.R. Kempton, R.F. Kiefl, S.R. Kreitzman, T.M. Riseman, D.Ll. Williams, J. Gopalakrishnan, A.W. Sleight, A.R. Strzelecki, and M.A. Subramanian. The magnetic and superconducting phase diagram of $\text{Bi}_2\text{Sr}_{3-x}\text{Y}_x\text{Cu}_2\text{O}_8$ as determined by muon spin rotation. *Physical Review B (Brief Report)*, **40**, 11320–11323, (1989).
- [88] B.J. Sternlieb, L.P. Le, G.M. Luke, Y.J. Uemura, J.H. Brewer, J.F. Carolan, P. Dosanjh, W.N. Hardy, R. Kadono, R.F. Kiefl, S.R. Kreitzman, T.M. Riseman, P.W. Schleger, M.R. Davis, C.E. Stronach, Y. Hidaka, T. Murakami, J. Gopalakrishnan, A.W. Sleight, M.A. Subramanian, and A.R. Strzelecki. $\mu^+\text{SR}$ studies of flux mobility in the mixed state of $\text{Bi}_2\text{Sr}_2\text{CaCu}_2\text{O}_8$. *Physica C*, **162–164**, 679–680, (1989).
- [89] David R. Nelson and H. Sebastian Seung. Theory of melted flux liquids. *Physical Review B*, **39**, 9153–9174, (1989).
- [90] V.N. Gorbunov and V.P. Smilga. μSR studies of type-II superconductors: two-dimensional strong pinning. *Hyperfine Interactions*, **63**, 109–116, (1990).
- [91] G.J. Dolan, F. Holtzberg, C. Field, and T.R. Dinger. Anisotropic vortex structure in $\text{YBa}_2\text{Cu}_3\text{O}_7$. *Physical Review Letters*, **62**, 2184–2187, (1989).
- [92] A.D. Sidorenko, V.P. Smilga, and V.I. Fesenko. Muonic studies of type II superconductors. *Hyperfine Interactions*, **63**, 49–63, (1990).
- [93] D.A. Bonn, Ruixing Liang, T.M. Riseman, D.J. Baar, D.C. Morgan, Kuan Zhang, P. Dosanjh, T.L. Duty, A. MacFarlane, G.D. Morris, J.H. Brewer, W.N. Hardy, C.Kallin, and A.J. Berlinsky. Microwave determination of the quasiparticle scattering time in $\text{YBa}_2\text{Cu}_3\text{O}_{6.95}$. Submitted to *Physical Review B*, , (1993).
- [94] B. Mühlshlegel. The thermodynamic functions of the superconductor. *Z. für Physik*, **155**, 313–327, (1959).

- [95] S.M. Anlage, B.W. Langley, G. Deutcher, J. Halbritter, and M.R. Beasley. Measurements of the temperature dependence of the magnetic penetration depth in $\text{YBa}_2\text{Cu}_3\text{O}_{7-\delta}$ superconducting thin films. *Physical Review B*, **44**, 9764–9767, (1991).
- [96] James Annett, Nigel Goldenfeld, and S.R. Renn. Interpretation of the temperature dependence of the electromagnetic penetration depth in $\text{YBa}_2\text{Cu}_3\text{O}_{7-\delta}$. *Physical Review B*, **43**, 2778–2781, (1991).
- [97] W.N. Hardy, D.A. Bonn, D.C. Morgan, R. Liang, and Kuan Zhang. Precision measurements of the temperature dependence of λ in $\text{YBa}_2\text{Cu}_3\text{O}_{6.95}$: Strong evidence for nodes in the gap function. accepted by *Physical Review Letters*, , (1993).
- [98] D.A. Bonn, D.C. Morgan, Kuan Zhang, R. Liang D.J. Baar, , and W.N. Hardy. Microwave surface impedance as a probe of unconventional superconductivity in $\text{YBa}_2\text{Cu}_3\text{O}_{6.95}$. Santa Fe, (1993). Proceedings of the International Conference on Spectroscopy in Novel Superconductors.
- [99] J. Sonier and R.F. Kiefl, (1993). Private Communication.
- [100] R.F. Kiefl, T.M. Riseman, G. Aeppli, E.J. Ansaldo, J.F. Carolan, R.J. Cava, W.N. Hardy, D.R. Harshman, N. Kaplan, J.R. Kempton, S.R. Kretzman, G.M. Luke, B.X. Yang, and D.Ll. Williams. Temperature dependence of the magnetic penetration depth in $\text{YBa}_2\text{Cu}_3\text{O}_7$ measured by muon spin rotation. *Physica C*, **153–155**, 757–758, (1988).
- [101] L.L. Daemen, L.N. Bulaevskii, M.P. Maley, and J.Y. Coulter. Critical current of Josephson-coupled systems in perpendicular fields. *Physical Review Letters*, **70**, 1167–1170, (1993).
- [102] R.D. Parks. *Superconductivity*. Marcel Dekker, Inc., 1969.
- [103] K. Nakao, N. Miura, K. Tatsuhaara, H. Takeya, and H. Takei. Magnetic hysteresis of $\text{YBa}_2\text{Cu}_3\text{O}_{7-x}$ single crystals in very high magnetic fields above 100 T. *Physical Review Letters*, **63**, 97–100, (1989).
- [104] F.M. Mueller, C.M. Fowler, B.L. Freeman, W.L. Hults, J.C. King, and J.L. Smith. Measurement of the de Haas-van Alphen effect in $\text{YBa}_2\text{Cu}_3\text{O}_{6.97}$ using megagauss fields. *Physica B*, **172**, 253–260, (1991).
- [105] J.D. Goettee, J.S. Brooks, D.G. Rickel, B.L. Freeman, C.M. Fowler, J.C. King, P.M. Mankiewich, W.J. Skocpol, E.I. De Obaldia, M.L. O’Mally, and J.L. Smith. Megagauss exploration of the field-temperature phase diagram of $\text{YBa}_2\text{Cu}_3\text{O}_7$ epitaxial films. *Physical Review Letters*, preprint, (1992). Los Alamos LA-UR-92-3100.
- [106] Eugen Holzschuh. Direct measurement of muonium hyperfine frequencies in Si and Ge. *Physical Review B*, **27**, 102–111, (1983).
- [107] V. Aseev and J. Beveridge. Surface muons in the solenoid helios. Technical Report Design Note TRI-DN-92-1, TRIUMF, 4004 Wesbrook Mall, Vancouver, B.C., Canada, V6T 2A3, 1992.
- [108] E.H. Brandt. Elastic energy of the vortex state in type II superconductors. I. High inductions. *Journal of Low Temperature Physics*, **26**, 709–733, (1977)].

- [109] M. Prohammer and J.P. Carbotte. London penetration depth of d -wave superconductors. *Physical Review B*, **43**, 5370–5374, (1991).
- [110] M. Prohammer and J.P. Carbotte. Upper critical field of s - and d -wave superconductors with anisotropic effective mass. *Physical Review B*, **42**, 2032–2040, (1990).
- [111] W. Barford and J.M.F. Gunn. A theoretical interpretation of μ SR experiments to measure the London penetration depth in anisotropic type-II superconductors. In J. Müller and J.L. Olsen, editors, *Proceedings of the International Conference on High Temperature Superconductors and Materials and Mechanisms of Superconductivity*, page 691. North-Holland, 1988.

Appendix A

Preferred Rotating Reference Frame Frequencies

ν_o	ν_{RRF}	Δt	# per osc.
18	16	0.062500 = 1 / 16 = 200 × 0.0003125	8.00
22	20	0.050000 = 1 / 20 = 160 × 0.0003125	10.00
27	25	0.040000 = 1 / 25 = 128 × 0.0003125	12.50
34	32	0.031250 = 1 / 32 = 100 × 0.0003125	16.00
42	40	0.025000 = 1 / 40 = 80 × 0.0003125	20.00
50	48	0.062500 = 3 / 48 = 200 × 0.0003125	8.00
52	50	0.020000 = 1 / 50 = 64 × 0.0003125	25.00
62	60	0.050000 = 3 / 60 = 160 × 0.0003125	10.00
66	64	0.015625 = 1 / 64 = 50 × 0.0003125	32.00
77	75	0.040000 = 3 / 75 = 128 × 0.0003125	12.50
82	80	0.012500 = 1 / 80 = 40 × 0.0003125	40.00
98	96	0.031250 = 3 / 96 = 100 × 0.0003125	16.00
102	100	0.010000 = 1 / 100 = 32 × 0.0003125	50.00
114	112	0.062500 = 7 / 112 = 200 × 0.0003125	8.00
122	120	0.025000 = 3 / 120 = 80 × 0.0003125	20.00
127	125	0.040000 = 5 / 125 = 128 × 0.0003125	12.50
130	128	0.007813 = 1 / 128 = 25 × 0.0003125	64.00
142	140	0.050000 = 7 / 140 = 160 × 0.0003125	10.00
146	144	0.062500 = 9 / 144 = 200 × 0.0003125	8.00
152	150	0.020000 = 3 / 150 = 64 × 0.0003125	25.00
162	160	0.006250 = 1 / 160 = 20 × 0.0003125	80.00
177	175	0.040000 = 7 / 175 = 128 × 0.0003125	12.50
178	176	0.062500 = 11 / 176 = 200 × 0.0003125	8.00
182	180	0.050000 = 9 / 180 = 160 × 0.0003125	10.00
194	192	0.015625 = 3 / 192 = 50 × 0.0003125	32.00

Table A.1: Preferred RRF frequencies for the case of the data's frequency 2 MHz greater than the RRF frequency. Used criterion that the RRF time bin size δt be less than 0.07 μs .

ν_o	ν_{RRF}	δt	# per osc.
202	200	0.005000 = 1 / 200 = 16 × 0.0003125	100.00
210	208	0.062500 = 13 / 208 = 200 × 0.0003125	8.00
222	220	0.050000 = 11 / 220 = 160 × 0.0003125	10.00
226	224	0.031250 = 7 / 224 = 100 × 0.0003125	16.00
227	225	0.040000 = 9 / 225 = 128 × 0.0003125	12.50
242	240	0.012500 = 3 / 240 = 40 × 0.0003125	40.00
252	250	0.020000 = 5 / 250 = 64 × 0.0003125	25.00
258	256	0.007813 = 2 / 256 = 25 × 0.0003125	64.00
262	260	0.050000 = 13 / 260 = 160 × 0.0003125	10.00
274	272	0.062500 = 17 / 272 = 200 × 0.0003125	8.00
277	275	0.040000 = 11 / 275 = 128 × 0.0003125	12.50
282	280	0.025000 = 7 / 280 = 80 × 0.0003125	20.00
290	288	0.031250 = 9 / 288 = 100 × 0.0003125	16.00
302	300	0.010000 = 3 / 300 = 32 × 0.0003125	50.00
306	304	0.062500 = 19 / 304 = 200 × 0.0003125	8.00
322	320	0.003125 = 1 / 320 = 10 × 0.0003125	160.00
327	325	0.040000 = 13 / 325 = 128 × 0.0003125	12.50
338	336	0.062500 = 21 / 336 = 200 × 0.0003125	8.00
342	340	0.050000 = 17 / 340 = 160 × 0.0003125	10.00
352	350	0.020000 = 7 / 350 = 64 × 0.0003125	25.00
354	352	0.031250 = 11 / 352 = 100 × 0.0003125	16.00
362	360	0.025000 = 9 / 360 = 80 × 0.0003125	20.00
370	368	0.062500 = 23 / 368 = 200 × 0.0003125	8.00
377	375	0.040000 = 15 / 375 = 128 × 0.0003125	12.50
382	380	0.050000 = 19 / 380 = 160 × 0.0003125	10.00
386	384	0.007813 = 3 / 384 = 25 × 0.0003125	64.00
402	400	0.002500 = 1 / 400 = 8 × 0.0003125	200.00
418	416	0.031250 = 13 / 416 = 100 × 0.0003125	16.00
422	420	0.050000 = 21 / 420 = 160 × 0.0003125	10.00
427	425	0.040000 = 17 / 425 = 128 × 0.0003125	12.50
434	432	0.062500 = 27 / 432 = 200 × 0.0003125	8.00
442	440	0.025000 = 11 / 440 = 80 × 0.0003125	20.00
450	448	0.015625 = 7 / 448 = 50 × 0.0003125	32.00
452	450	0.020000 = 9 / 450 = 64 × 0.0003125	25.00
462	460	0.050000 = 23 / 460 = 160 × 0.0003125	10.00
466	464	0.062500 = 29 / 464 = 200 × 0.0003125	8.00
477	475	0.040000 = 19 / 475 = 128 × 0.0003125	12.50
482	480	0.006250 = 3 / 480 = 20 × 0.0003125	80.00
498	496	0.062500 = 31 / 496 = 200 × 0.0003125	8.00

ν_o	ν_{RRF}	δt	# per osc.
502	500	0.010000 = 5 / 500 = 32 × 0.0003125	50.00
514	512	0.007813 = 4 / 512 = 25 × 0.0003125	64.00
522	520	0.025000 = 13 / 520 = 80 × 0.0003125	20.00
527	525	0.040000 = 21 / 525 = 128 × 0.0003125	12.50
530	528	0.062500 = 33 / 528 = 200 × 0.0003125	8.00
542	540	0.050000 = 27 / 540 = 160 × 0.0003125	10.00
546	544	0.031250 = 17 / 544 = 100 × 0.0003125	16.00
552	550	0.020000 = 11 / 550 = 64 × 0.0003125	25.00
562	560	0.012500 = 7 / 560 = 40 × 0.0003125	40.00
577	575	0.040000 = 23 / 575 = 128 × 0.0003125	12.50
578	576	0.015625 = 9 / 576 = 50 × 0.0003125	32.00
582	580	0.050000 = 29 / 580 = 160 × 0.0003125	10.00
594	592	0.062500 = 37 / 592 = 200 × 0.0003125	8.00
602	600	0.005000 = 3 / 600 = 16 × 0.0003125	100.00
610	608	0.031250 = 19 / 608 = 100 × 0.0003125	16.00
622	620	0.050000 = 31 / 620 = 160 × 0.0003125	10.00
626	624	0.062500 = 39 / 624 = 200 × 0.0003125	8.00
627	625	0.040000 = 25 / 625 = 128 × 0.0003125	12.50
642	640	0.001563 = 1 / 640 = 5 × 0.0003125	320.00
652	650	0.020000 = 13 / 650 = 64 × 0.0003125	25.00
658	656	0.062500 = 41 / 656 = 200 × 0.0003125	8.00
662	660	0.050000 = 33 / 660 = 160 × 0.0003125	10.00
674	672	0.031250 = 21 / 672 = 100 × 0.0003125	16.00
677	675	0.040000 = 27 / 675 = 128 × 0.0003125	12.50
682	680	0.025000 = 17 / 680 = 80 × 0.0003125	20.00
690	688	0.062500 = 43 / 688 = 200 × 0.0003125	8.00
702	700	0.010000 = 7 / 700 = 32 × 0.0003125	50.00
706	704	0.015625 = 11 / 704 = 50 × 0.0003125	32.00
722	720	0.012500 = 9 / 720 = 40 × 0.0003125	40.00
727	725	0.040000 = 29 / 725 = 128 × 0.0003125	12.50
738	736	0.031250 = 23 / 736 = 100 × 0.0003125	16.00
742	740	0.050000 = 37 / 740 = 160 × 0.0003125	10.00
752	750	0.020000 = 15 / 750 = 64 × 0.0003125	25.00
754	752	0.062500 = 47 / 752 = 200 × 0.0003125	8.00
762	760	0.025000 = 19 / 760 = 80 × 0.0003125	20.00
770	768	0.007813 = 6 / 768 = 25 × 0.0003125	64.00
777	775	0.040000 = 31 / 775 = 128 × 0.0003125	12.50
782	780	0.050000 = 39 / 780 = 160 × 0.0003125	10.00
786	784	0.062500 = 49 / 784 = 200 × 0.0003125	8.00

ν_o	ν_{RRF}	δt	# per osc.
802	800	$0.001250 = 1 / 800 = 4 \times 0.0003125$	400.00
818	816	$0.062500 = 51 / 816 = 200 \times 0.0003125$	8.00
822	820	$0.050000 = 41 / 820 = 160 \times 0.0003125$	10.00
827	825	$0.040000 = 33 / 825 = 128 \times 0.0003125$	12.50
834	832	$0.015625 = 13 / 832 = 50 \times 0.0003125$	32.00
842	840	$0.025000 = 21 / 840 = 80 \times 0.0003125$	20.00
850	848	$0.062500 = 53 / 848 = 200 \times 0.0003125$	8.00
852	850	$0.020000 = 17 / 850 = 64 \times 0.0003125$	25.00
862	860	$0.050000 = 43 / 860 = 160 \times 0.0003125$	10.00
866	864	$0.031250 = 27 / 864 = 100 \times 0.0003125$	16.00
877	875	$0.040000 = 35 / 875 = 128 \times 0.0003125$	12.50
882	880	$0.012500 = 11 / 880 = 40 \times 0.0003125$	40.00
898	896	$0.007813 = 7 / 896 = 25 \times 0.0003125$	64.00
902	900	$0.010000 = 9 / 900 = 32 \times 0.0003125$	50.00
914	912	$0.062500 = 57 / 912 = 200 \times 0.0003125$	8.00
922	920	$0.025000 = 23 / 920 = 80 \times 0.0003125$	20.00
927	925	$0.040000 = 37 / 925 = 128 \times 0.0003125$	12.50
930	928	$0.031250 = 29 / 928 = 100 \times 0.0003125$	16.00
942	940	$0.050000 = 47 / 940 = 160 \times 0.0003125$	10.00
946	944	$0.062500 = 59 / 944 = 200 \times 0.0003125$	8.00
952	950	$0.020000 = 19 / 950 = 64 \times 0.0003125$	25.00
962	960	$0.003125 = 3 / 960 = 10 \times 0.0003125$	160.00
977	975	$0.040000 = 39 / 975 = 128 \times 0.0003125$	12.50
978	976	$0.062500 = 61 / 976 = 200 \times 0.0003125$	8.00
982	980	$0.050000 = 49 / 980 = 160 \times 0.0003125$	10.00
994	992	$0.031250 = 31 / 992 = 100 \times 0.0003125$	16.00
1002	1000	$0.005000 = 5 / 1000 = 16 \times 0.0003125$	100.00

Appendix B

High Field χ^2 Scans and Lineshapes

	Run #	# of Events ($\times 10^6$)	Temp. (K)	B_o (T)	B_{BK} (T)
"10 K"	45	5.43	10.10(7)	1.903046	1.90334
	31	14.36	10.25(5)	4.07874	4.07879
	70	13.31	9.9(1)	4.73702	4.737
"20 K"	76	2.26	20.17(5)	1.903396	1.903762
	30	2.237	19.84(5)	4.07852	4.07881
	69	3.47	19.90(5)	4.73718	4.73702
"30 K"	75	7.68	30.00(5)	1.903528	1.903743
	29	14.67	30.17(5)	4.07866	4.07885
	68	1.40	30.1(3)	4.73704	4.73703
"40 K"	74	2.09	40.20(6)	1.903306	1.903747
	33	3.77	40.27(5)	4.07837	4.07881
	67	3.22	40.13(10)	4.73663	4.73702
	55	4.18	41.25(10)	6.50706	6.50775
"50 K"	44	2.76	50.10(5)	1.903164	1.903352
	28	16.14	50.04(5)	4.07875	4.07885
	66	11.55	50.0(5)	4.73688	4.73704
	54	21.13	48.9(3)	6.50727	6.50774
"60 K"	73	3.48	60.50(5)	1.903401	1.90377
	27	5.79	60.02(5)	4.07827	4.07886
	65	4.52	58.9(5)	4.73652	4.73709
"70 K"	43	6.662	70.52(10)	1.903143	1.9034
	57	8.24	70.5(9)	4.07876	4.07927
	64	13.50	70.2(1.1)	4.73661	4.73708
	53	19.96	70.3(4)	6.50699	6.50804
"75 K"	72	2.31	74.88(6)	1.90332	1.90379
	34	3.71	75.0(5)	4.07831	4.07904
	62	3.13	74.7(5)	4.73641	4.73713
" $T > T_c$ "	20	2.98	100(2)	4.07877	
	58	3.45	102.0(4)	4.73677	
	50	4.79	101.5(5)	6.50721	
	38	2.28	119.15(3)	1.903254	
	37	4.04	119(1)	4.07855	

Table B.1: This table shows the temperature, number of events and the applied field for each high field run. The groups of runs below T_c were fitted together with shared λ^{-2} and H_{c2} .

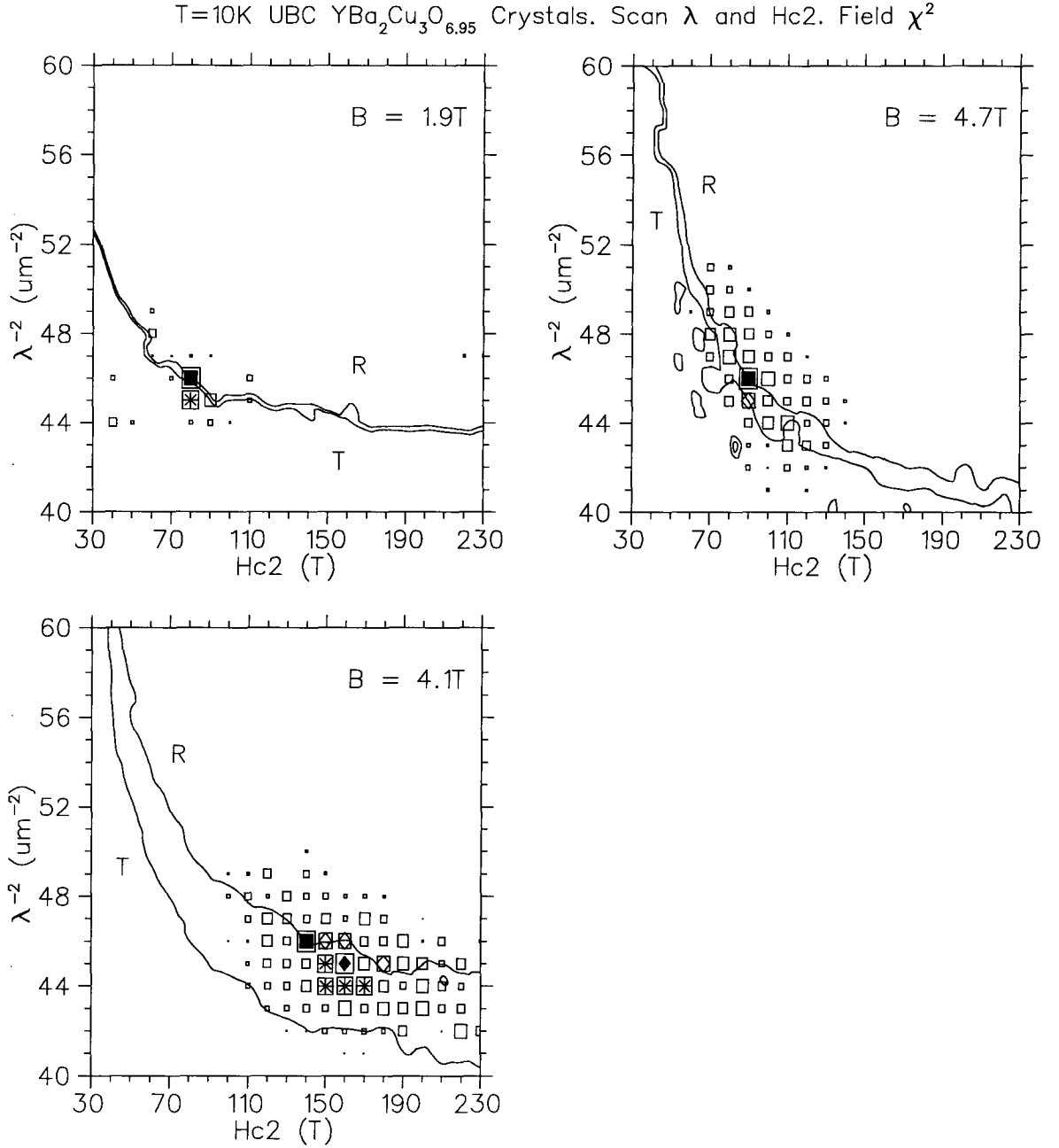


Figure B.1: This figure displays the goodness of fit (χ^2) as a function of λ^{-2} and H_{c2} for individual runs at $T = 10\text{ K}$ with fields of 1.9 T , 4.1 T and 4.7 T . The solid square marks the minimum (χ_m^2), the solid diamonds mark $\chi^2 \leq \chi_m^2 + 1$, the stars mark $\chi^2 \leq \chi_m^2 + 2$ and the open diamonds mark $\chi^2 \leq \chi_m^2 + 3$. The smaller boxes represent higher values of χ^2 up to $\chi_m^2 + 10$. The curve marked "R" is a contour of those fits which have the same average field (B_o) as the best fit for the run. (Relative to the background field, B_o is -2.75 G for 1.9 T , 2.03 G for 4.1 T and 0.94 G for 4.7 T .) The curve marked "T" is the contour of those fits which have the same average field (B_o) as the best global fit (see figure B.9) for the 10 K runs. (B_o is -2.94 G for 1.9 T , -0.59 G for 4.1 T and 0.23 G for 4.7 T .)

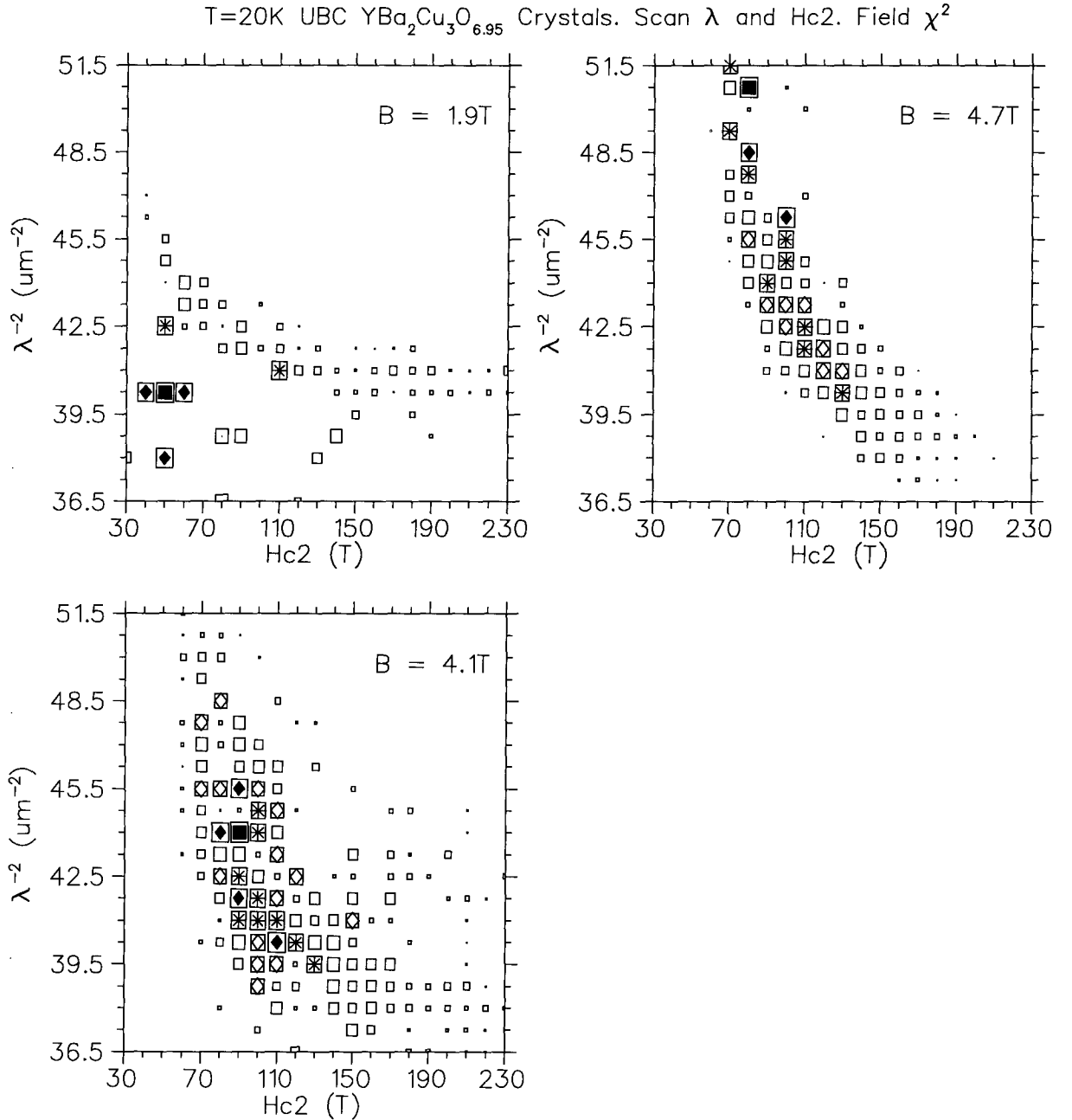


Figure B.2: This figure displays the goodness of fit (χ^2) as a function of λ^{-2} and H_{c2} for individual runs at $T = 20\text{ K}$ with fields of 1.9 T , 4.1 T and 4.7 T . The solid square marks the minimum (χ_m^2), the solid diamonds mark $\chi^2 \leq \chi_m^2 + 1$, the stars mark $\chi^2 \leq \chi_m^2 + 2$ and the open diamonds mark $\chi^2 \leq \chi_m^2 + 3$. The smaller boxes represent higher values of χ^2 up to $\chi_m^2 + 10$. Due to the low statistics of these runs, the average field contours are not informative. (Relative to the background field, the average field of the best fit is -2.75 G for 1.9 T , 2.03 G for 4.1 T and 0.94 G for 4.7 T . The average field of the best global fit (see figure B.9) for the 20 K runs is -2.94 G for 1.9 T , -0.59 G for 4.1 T and 0.23 G for 4.7 T .)

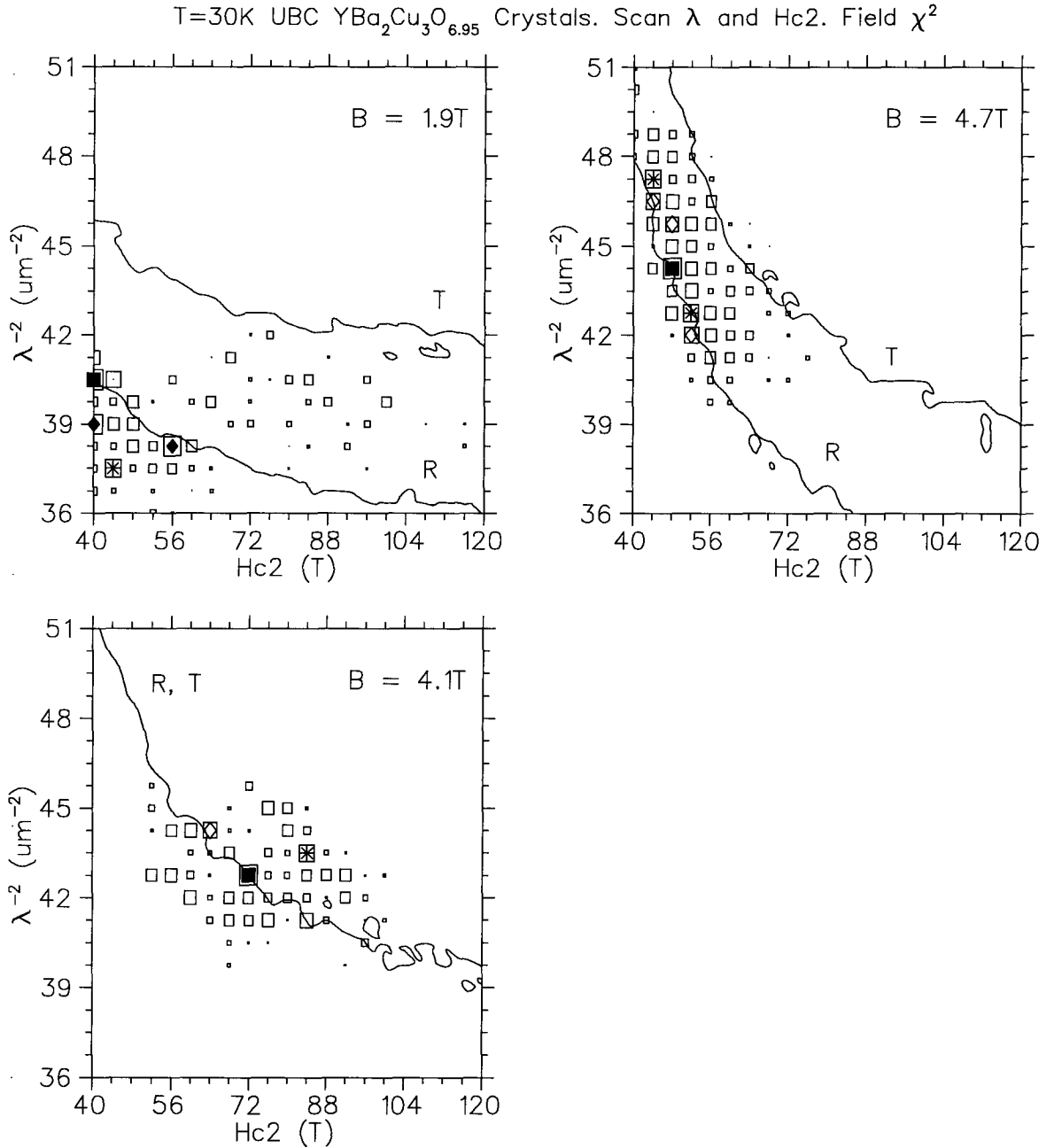


Figure B.3: This figure displays the goodness of fit (χ^2) as a function of λ^{-2} and H_{c2} for individual runs at $T = 30\text{ K}$ with fields of 1.9 T , 4.1 T and 4.7 T . The solid square marks the minimum (χ_m^2), the solid diamonds mark $\chi^2 \leq \chi_m^2 + 1$, the stars mark $\chi^2 \leq \chi_m^2 + 2$ and the open diamonds mark $\chi^2 \leq \chi_m^2 + 3$. The smaller boxes represent higher values of χ^2 up to $\chi_m^2 + 10$. The curve marked “R” is a contour of those fits which have the same average field (B_o) as the best fit for the run. (Relative to the background field, B_o is -5.87 G for 1.9 T , -1.93 G for 4.1 T and -3.04 G for 4.7 T .) The curve marked “T” is the contour of those fits which have the same average field (B_o) as the best global fit (see figure B.9) for the 30 K runs. (B_o is -2.16 G for 1.9 T , -1.93 G for 4.1 T and 0.18 G for 4.7 T .)

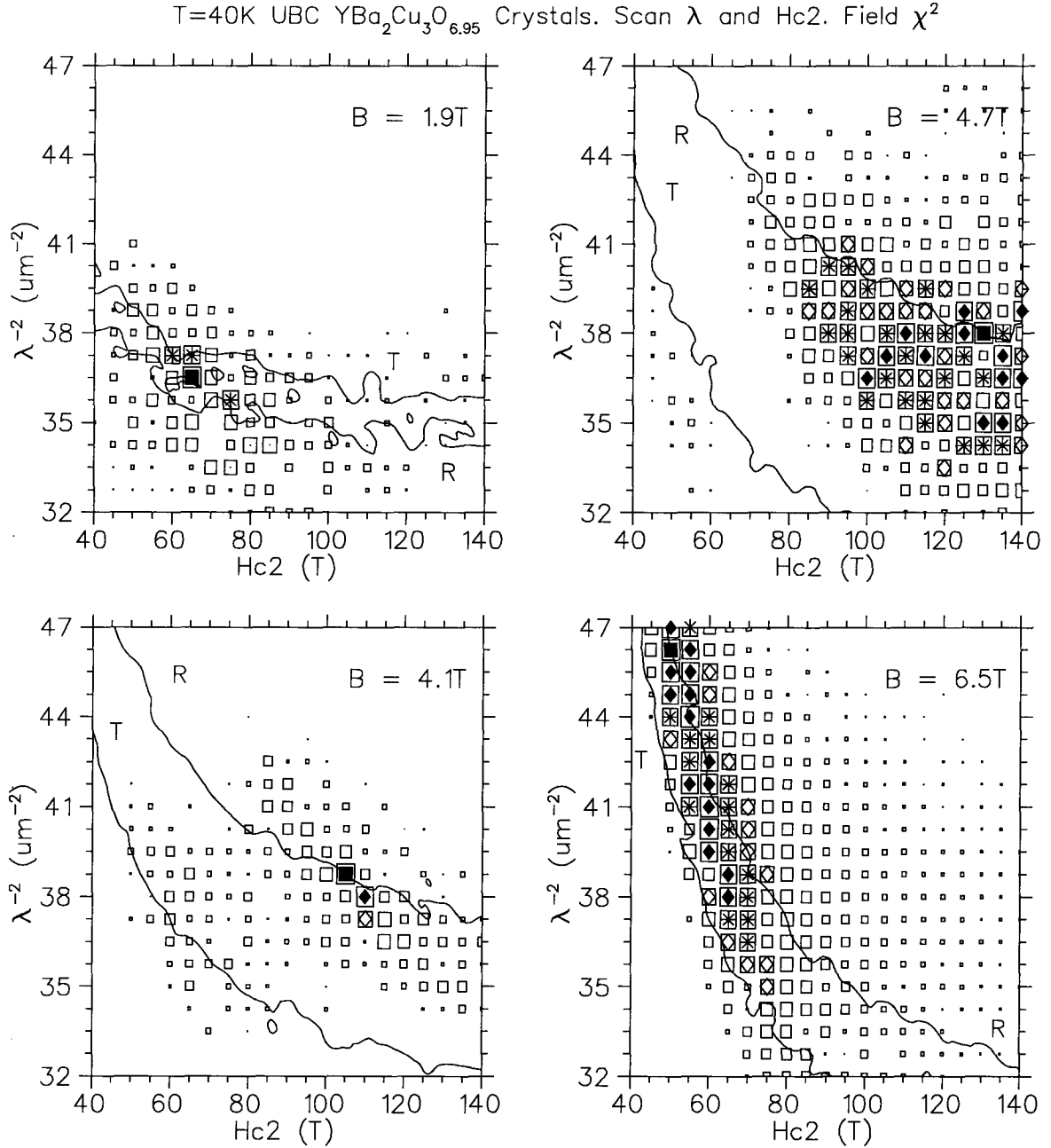


Figure B.4: This figure displays the goodness of fit (χ^2) as a function of λ^{-2} and H_{c2} for individual runs at $T = 40$ K with fields of 1.9 T, 4.1 T, 4.7 T and 6.5 T. The solid square marks the minimum (χ_m^2), the solid diamonds mark $\chi^2 \leq \chi_m^2 + 1$, the stars mark $\chi^2 \leq \chi_m^2 + 2$ and the open diamonds mark $\chi^2 \leq \chi_m^2 + 3$. The smaller boxes represent higher values of χ^2 up to $\chi_m^2 + 10$. The curve marked “R” is a contour of those fits which have the same average field (B_o) as the best fit for the run. (Relative to the background field, B_o is -5.27 G for 1.9 T, -0.77 G for 4.1 T, 1.37 G for 4.7 T and -4.49 G for 6.5 T.) The curve marked “T” is the contour of those fits which have the same average field (B_o) as the best global fit (see figure B.9) for the 40 K runs. (B_o is -4.42 G for 1.9 T, -4.40 G for 4.1 T, -3.91 G for 4.7 T and -6.86 G for 6.5 T.)

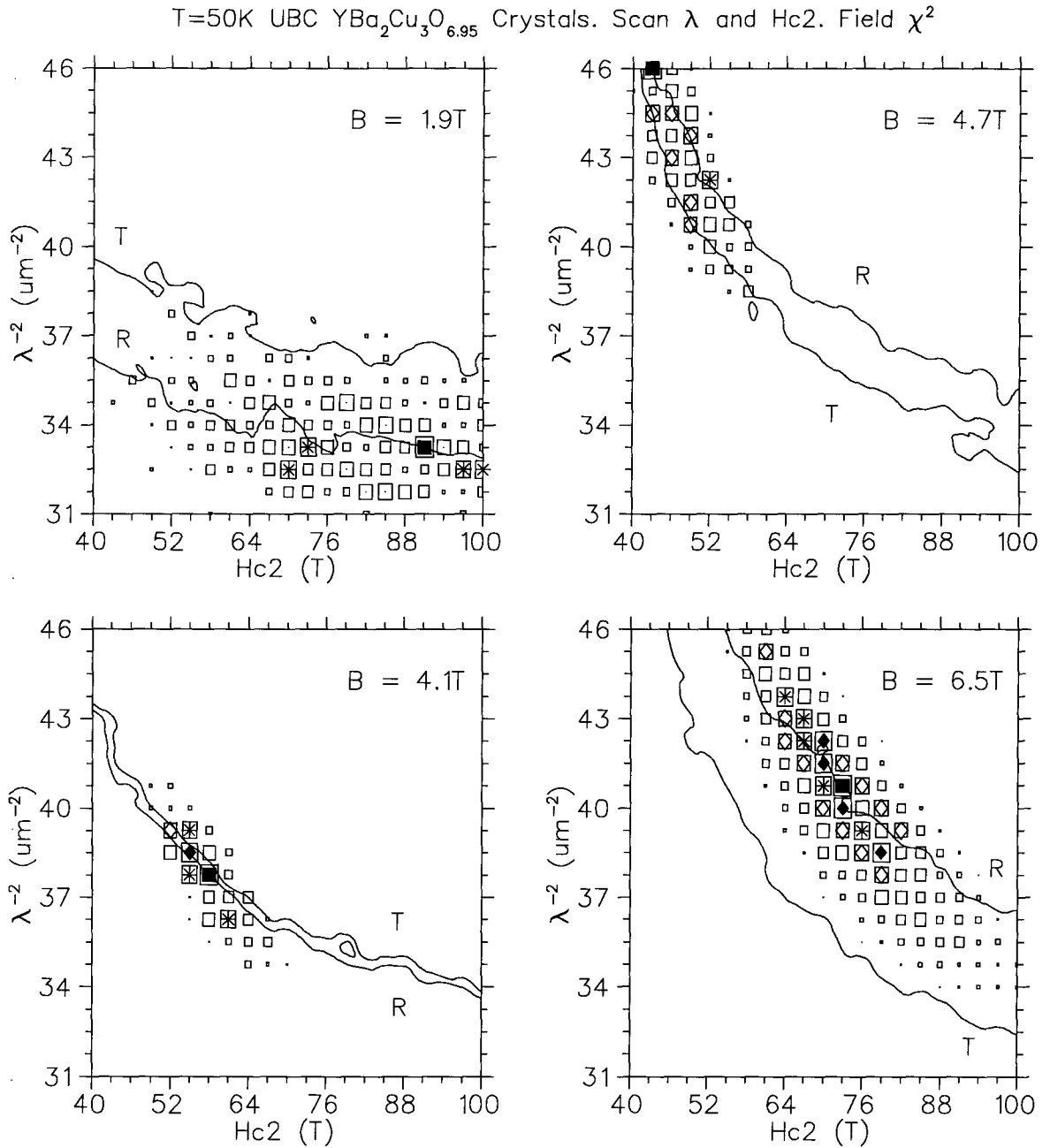


Figure B.5: This figure displays the goodness of fit (χ^2) as a function of λ^{-2} and H_{c2} for individual runs at $T = 50\text{ K}$ with fields of 1.9 T , 4.1 T , 4.7 T and 6.5 T . The solid square marks the minimum (χ_m^2), the solid diamonds mark $\chi^2 \leq \chi_m^2 + 1$, the stars mark $\chi^2 \leq \chi_m^2 + 2$ and the open diamonds mark $\chi^2 \leq \chi_m^2 + 3$. The smaller boxes represent higher values of χ^2 up to $\chi_m^2 + 10$. The curve marked "R" is a contour of those fits which have the same average field (B_o) as the best fit for the run. (Relative to the background field, B_o is -4.15 G for 1.9 T , -1.23 G for 4.1 T , -0.46 G for 4.7 T and -1.87 G for 6.5 T .) The curve marked "T" is the contour of those fits which have the same average field (B_o) as the best global fit (see figure B.10) for the 50 K runs. (B_o is -1.88 G for 1.9 T , -0.95 G for 4.1 T , -1.62 G for 4.7 T and -4.72 G for 6.5 T .)

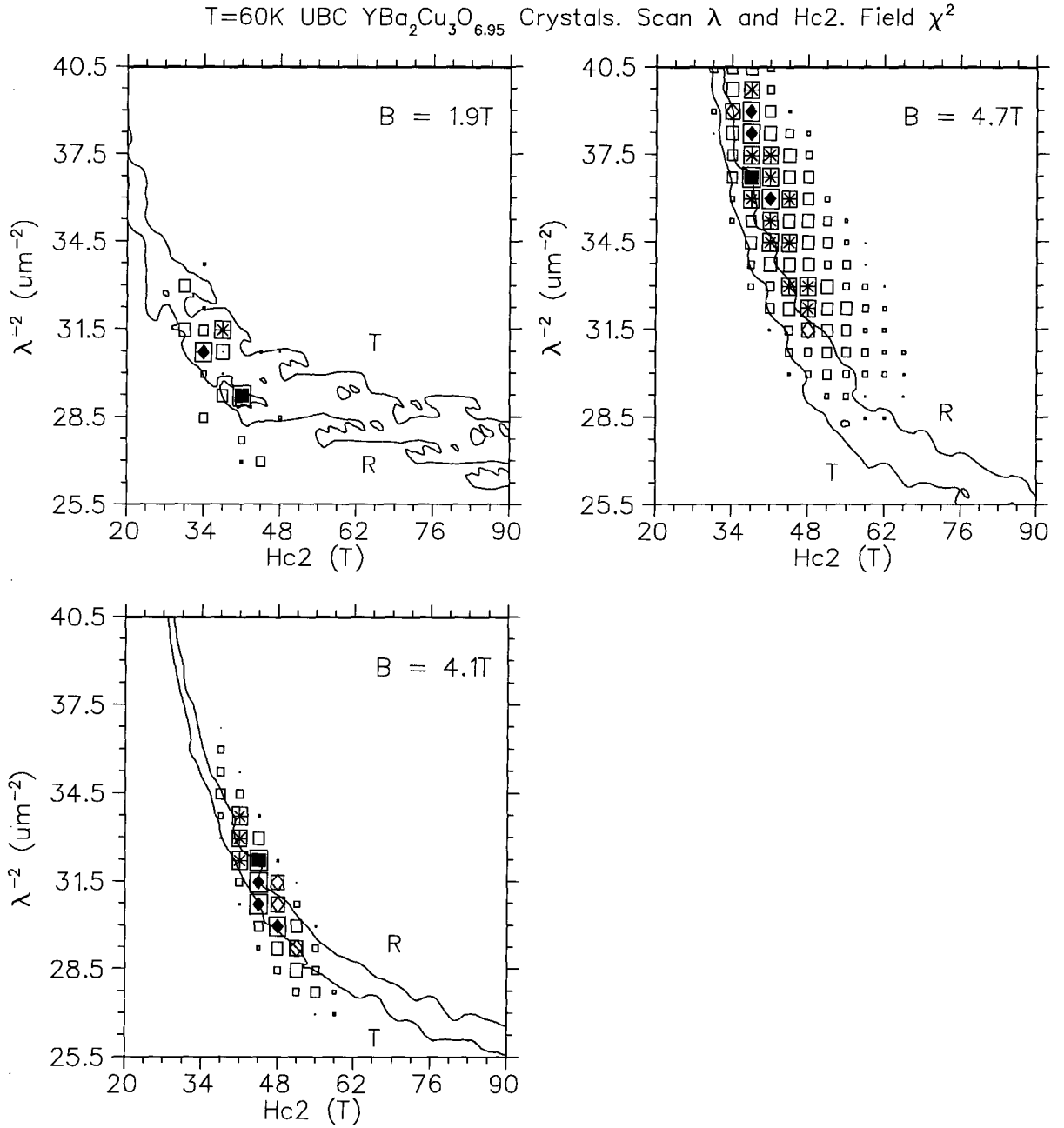


Figure B.6: This figure displays the goodness of fit (χ^2) as a function of λ^{-2} and H_{c2} for individual runs at $T = 60\text{ K}$ with fields of 1.9 T , 4.1 T and 4.7 T . The solid square marks the minimum (χ_m^2), the solid diamonds mark $\chi^2 \leq \chi_m^2 + 1$, the stars mark $\chi^2 \leq \chi_m^2 + 2$ and the open diamonds mark $\chi^2 \leq \chi_m^2 + 3$. The smaller boxes represent higher values of χ^2 up to $\chi_m^2 + 10$. The curve marked “R” is a contour of those fits which have the same average field (B_o) as the best fit for the run. (Relative to the background field, B_o is -5.03 G for 1.9 T , -5.23 G for 4.1 T and -4.59 G for 4.7 T .) The curve marked “T” is the contour of those fits which have the same average field (B_o) as the best global fit (see figure B.10) for the 60 K runs. (B_o is -3.688 G for 1.9 T , -5.85 G for 4.1 T and -5.64 G for 4.7 T .)

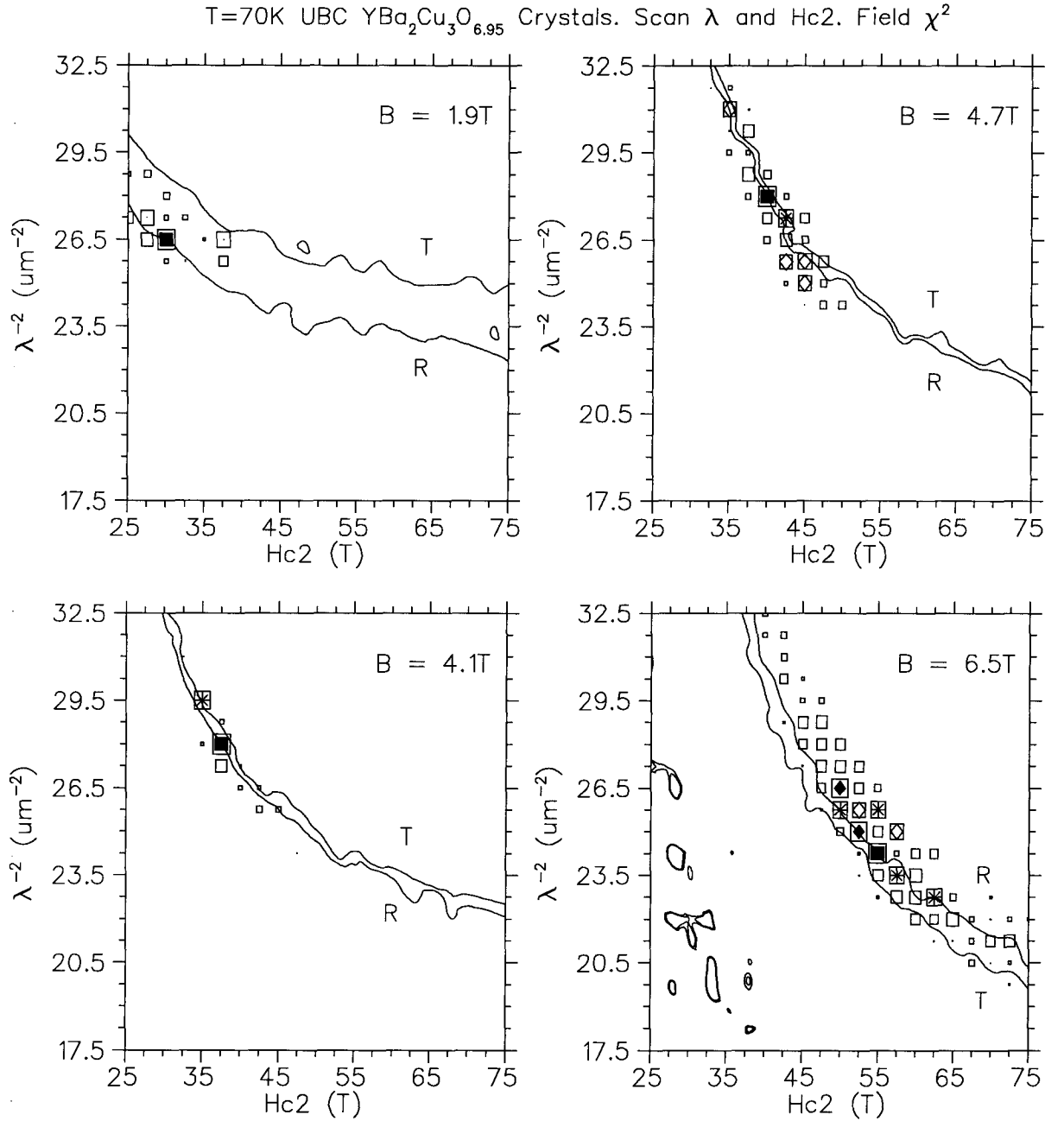


Figure B.7: This figure displays the goodness of fit (χ^2) as a function of λ^{-2} and H_{c2} for individual runs at $T = 70$ K with fields of 1.9 T, 4.1 T, 4.7 T and 6.5 T. The solid square marks the minimum (χ^2_m), the solid diamonds mark $\chi^2 \leq \chi^2_m + 1$, the stars mark $\chi^2 \leq \chi^2_m + 2$ and the open diamonds mark $\chi^2 \leq \chi^2_m + 3$. The smaller boxes represent higher values of χ^2 up to $\chi^2_m + 10$. The curve marked "R" is a contour of those fits which have the same average field (B_o) as the best fit for the run. (Relative to the background field, B_o is -4.07 G for 1.9 T, -5.34 G for 4.1 T, -4.91 G for 4.7 T and -9.97 G for 6.5 T.) The curve marked "T" is the contour of those fits which have the same average field (B_o) as the best global fit (see figure B.10) for the 70 K runs. (B_o is -2.57 G for 1.9 T, -5.09 G for 4.1 T, -4.72 G for 4.7 T and -10.47 G for 6.5 T.)

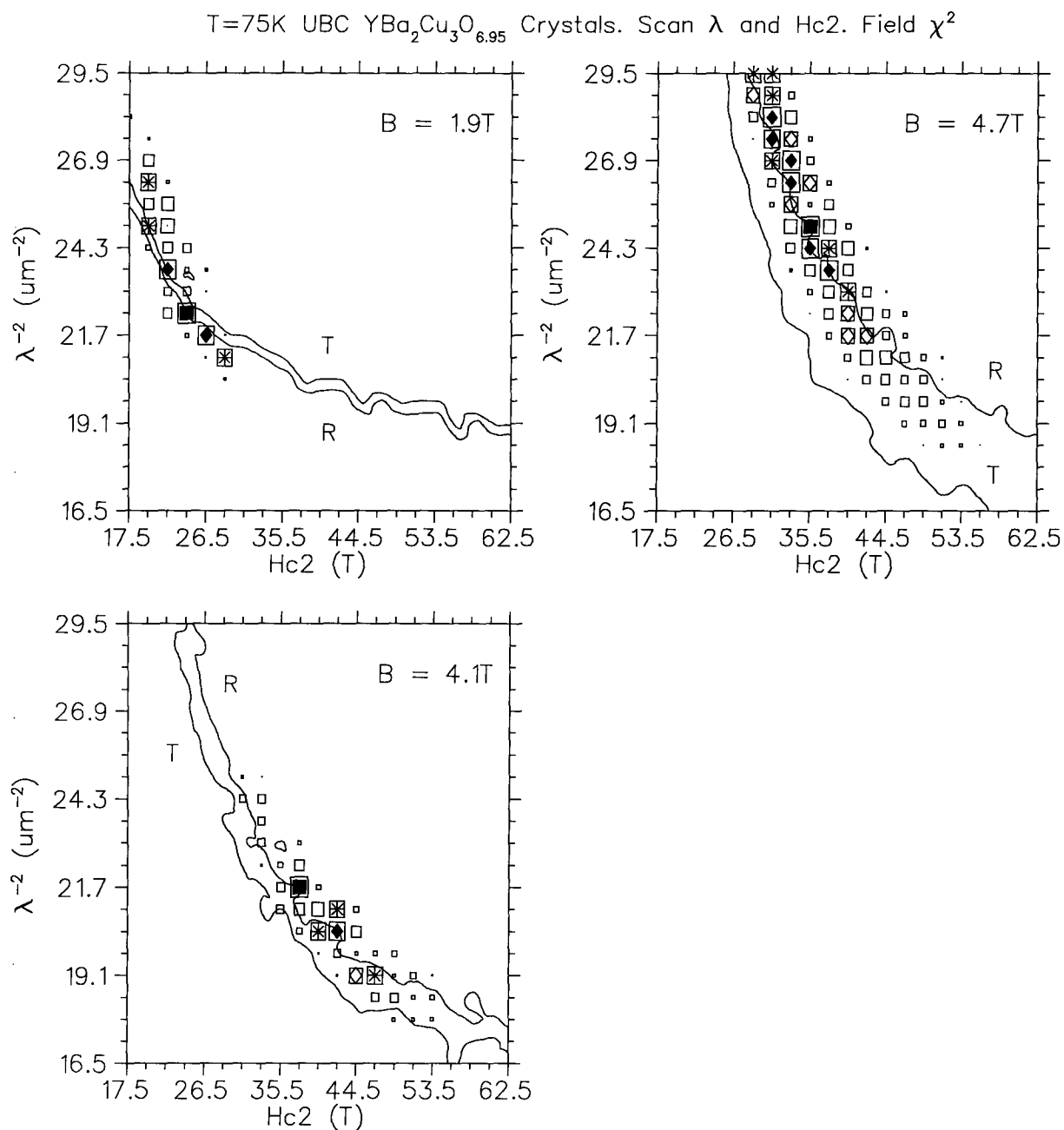


Figure B.8: This figure displays the goodness of fit (χ^2) as a function of λ^{-2} and H_{c2} for individual runs at $T = 75\text{ K}$ with fields of 1.9 T, 4.1 T and 4.7 T. The solid square marks the minimum (χ_m^2), the solid diamonds mark $\chi^2 \leq \chi_m^2 + 1$, the stars mark $\chi^2 \leq \chi_m^2 + 2$ and the open diamonds mark $\chi^2 \leq \chi_m^2 + 3$. The smaller boxes represent higher values of χ^2 up to $\chi_m^2 + 10$. The curve marked “R” is a contour of those fits which have the same average field (B_o) as the best fit for the run. (Relative to the background field, B_o is -4.94 G for 1.9 T, -6.67 G for 4.1 T and -5.73 G for 4.7 T.) The curve marked “T” is the contour of those fits which have the same average field which have the same average field (B_o) as the best global fit (see figure B.10) for the 75 K runs. (B_o is -4.69 G for 1.9 T, -7.33 G for 4.1 T and -7.21 G for 4.7 T.)

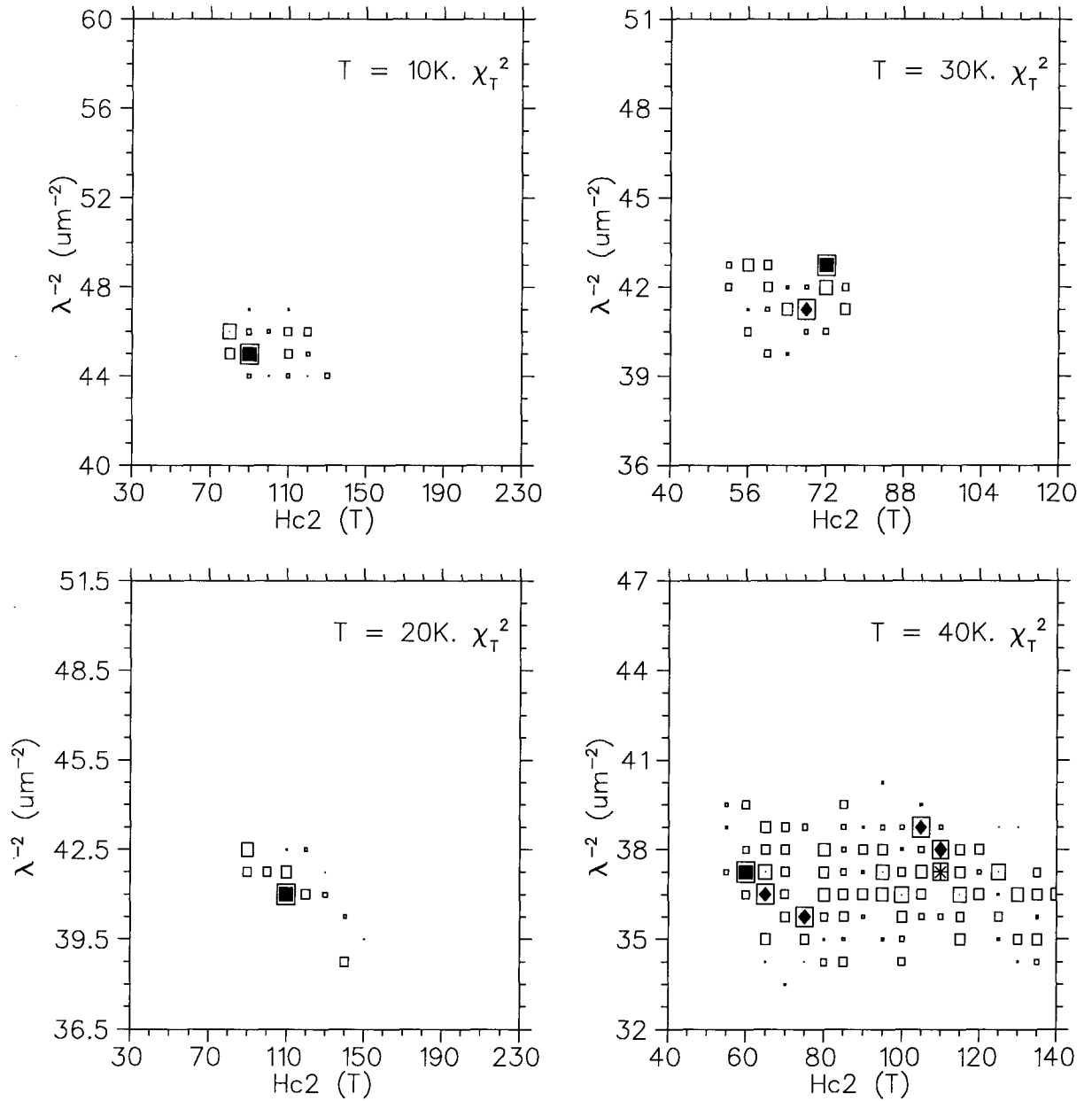


Figure B.9: This figure displays the total goodness of fit (χ^2_T) as a function of the fixed parameters λ^{-2} and H_{c2} resulting from simultaneous MINUIT fits (a.k.a. global fits) of the runs at fields of 1.9 T, 4.1 T, 4.7 T and 6.5 T. The solid square marks the minimum ($\chi^2_{T,m}$), the solid diamonds mark $\chi^2 \leq \chi^2_{T,m} + 1$, the stars mark $\chi^2 \leq \chi^2_{T,m} + 2$ and the open diamonds mark $\chi^2 \leq \chi^2_{T,m} + 3$. The smaller boxes represent higher values of χ^2 up to $\chi^2_{T,m} + 10$.

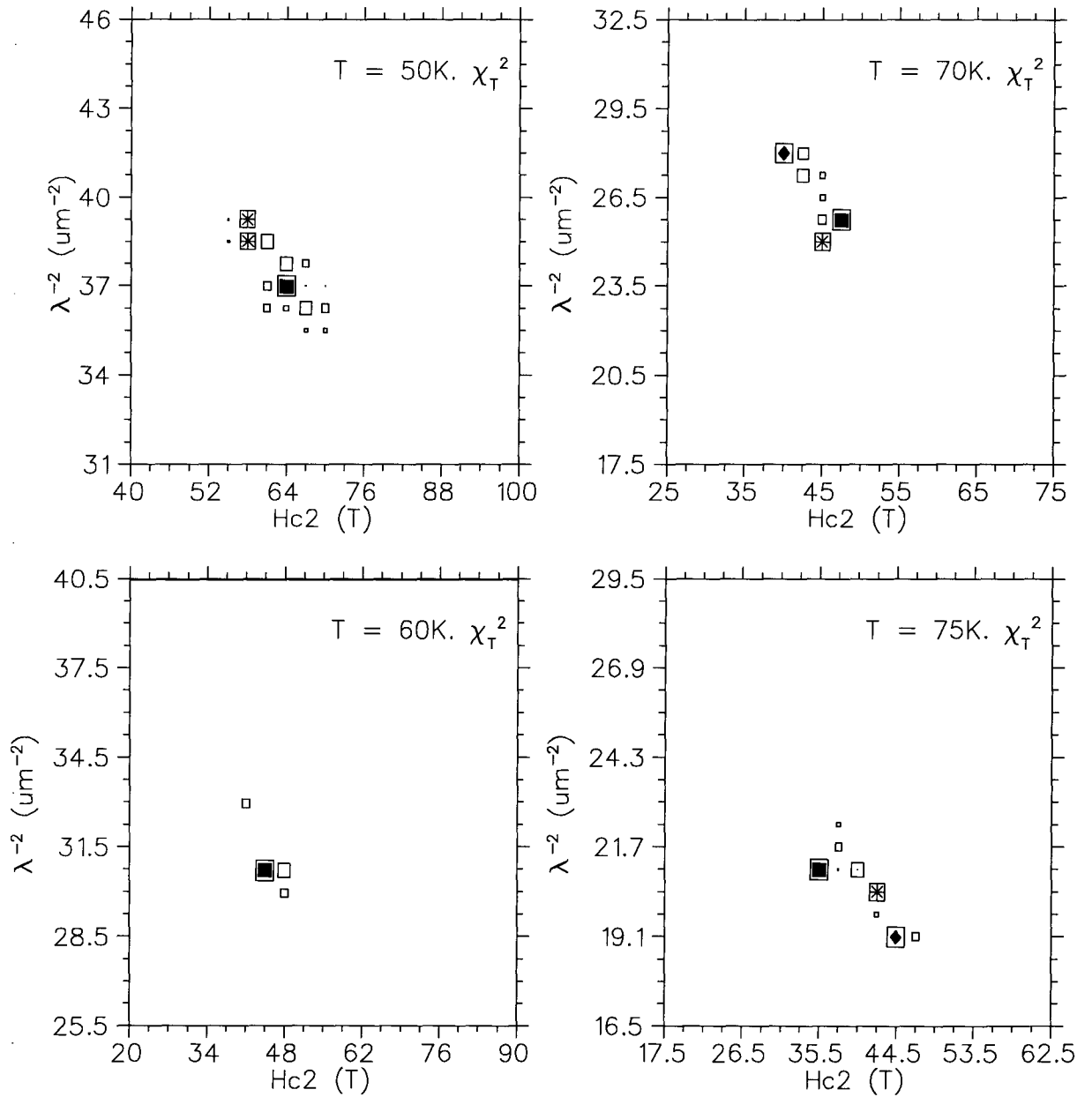


Figure B.10: This figure displays the total goodness of fit (χ^2_T) as a function of the fixed parameters λ^{-2} and H_{c2} resulting from simultaneous MINUIT fits (a.k.a. global fits) of the runs at fields of 1.9 T, 4.1 T, 4.7 T and 6.5 T. The solid square marks the minimum ($\chi^2_{T,m}$), the solid diamonds mark $\chi^2 \leq \chi^2_{T,m} + 1$, the stars mark $\chi^2 \leq \chi^2_{T,m} + 2$ and the open diamonds mark $\chi^2 \leq \chi^2_{T,m} + 3$. The smaller boxes represent higher values of χ^2 up to $\chi^2_{T,m} + 10$.

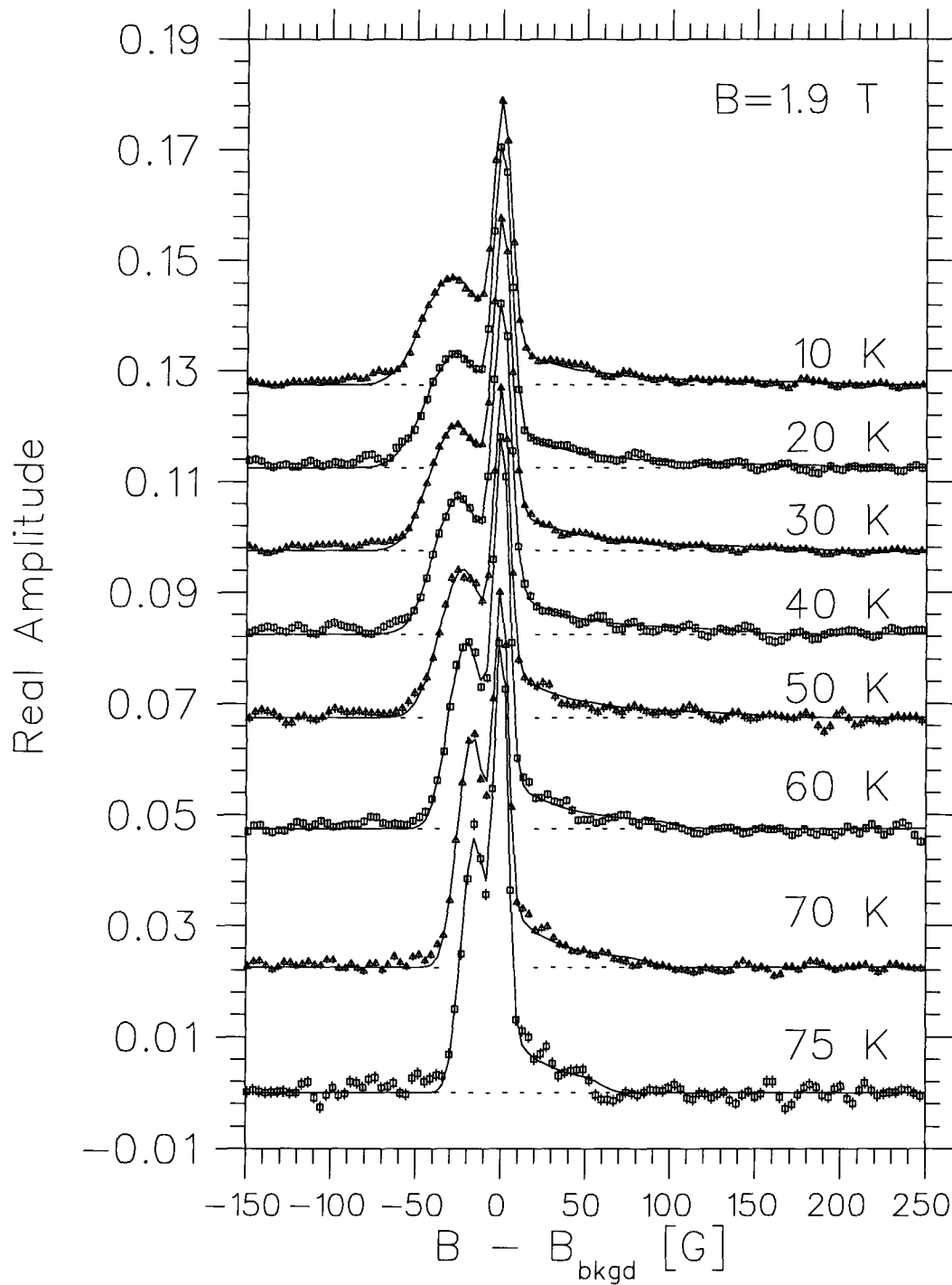


Figure B.11: High Field μ SR lineshapes and fits to the Modified London Model, for data at a field of $B = 1.9 \text{ T}$. The lineshapes have been plotted relative to the background field in Gauss ($1 \text{ G} = 10^{-4} \text{ T}$), with an arbitrary vertical offset.

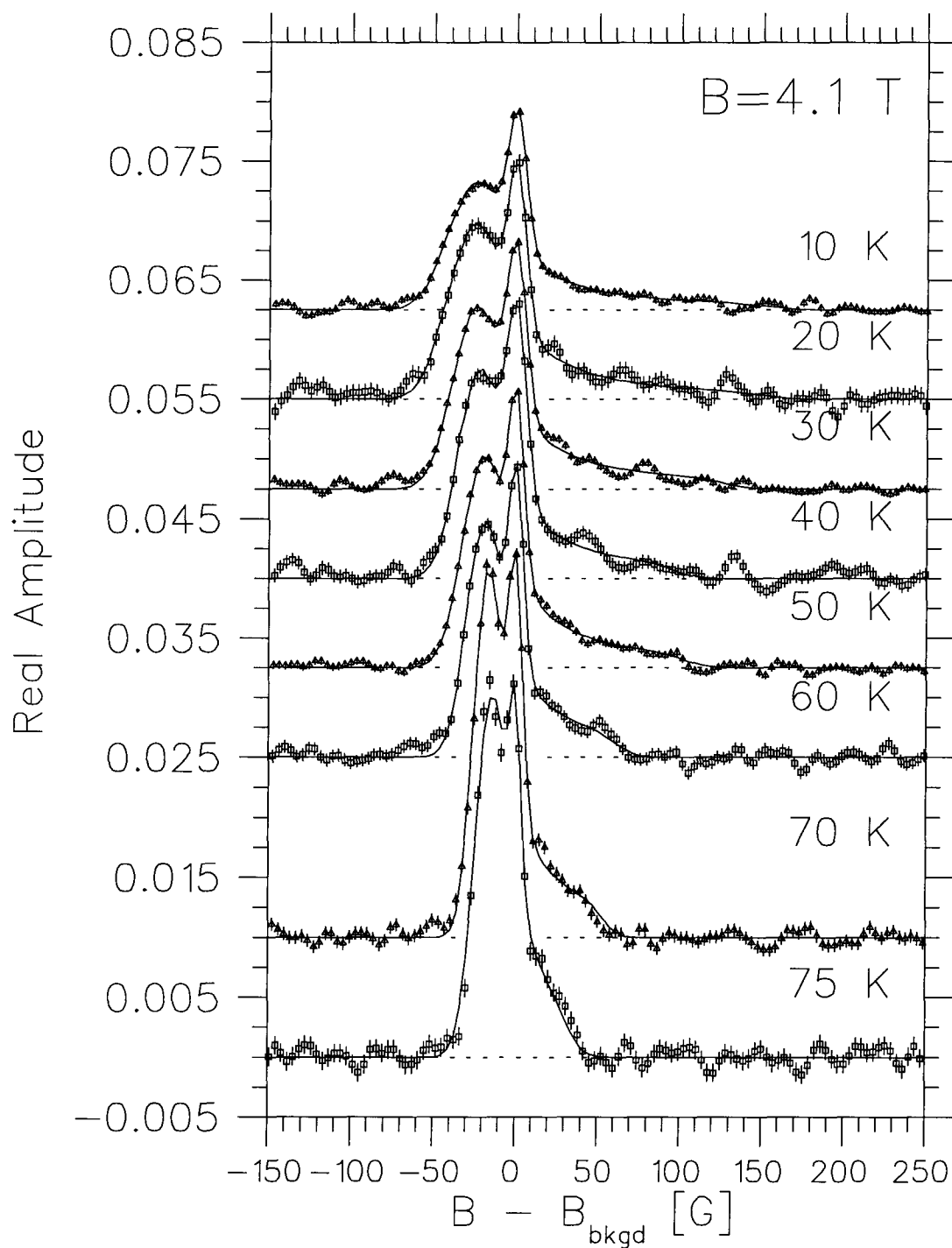


Figure B.12: High Field μ SR lineshapes and fits to the Modified London Model, for data at a field of $B = 4.1$ T. The lineshapes have been plotted relative to the background field in Gauss ($1 \text{ G} = 10^{-4} \text{ T}$), with an arbitrary vertical offset.

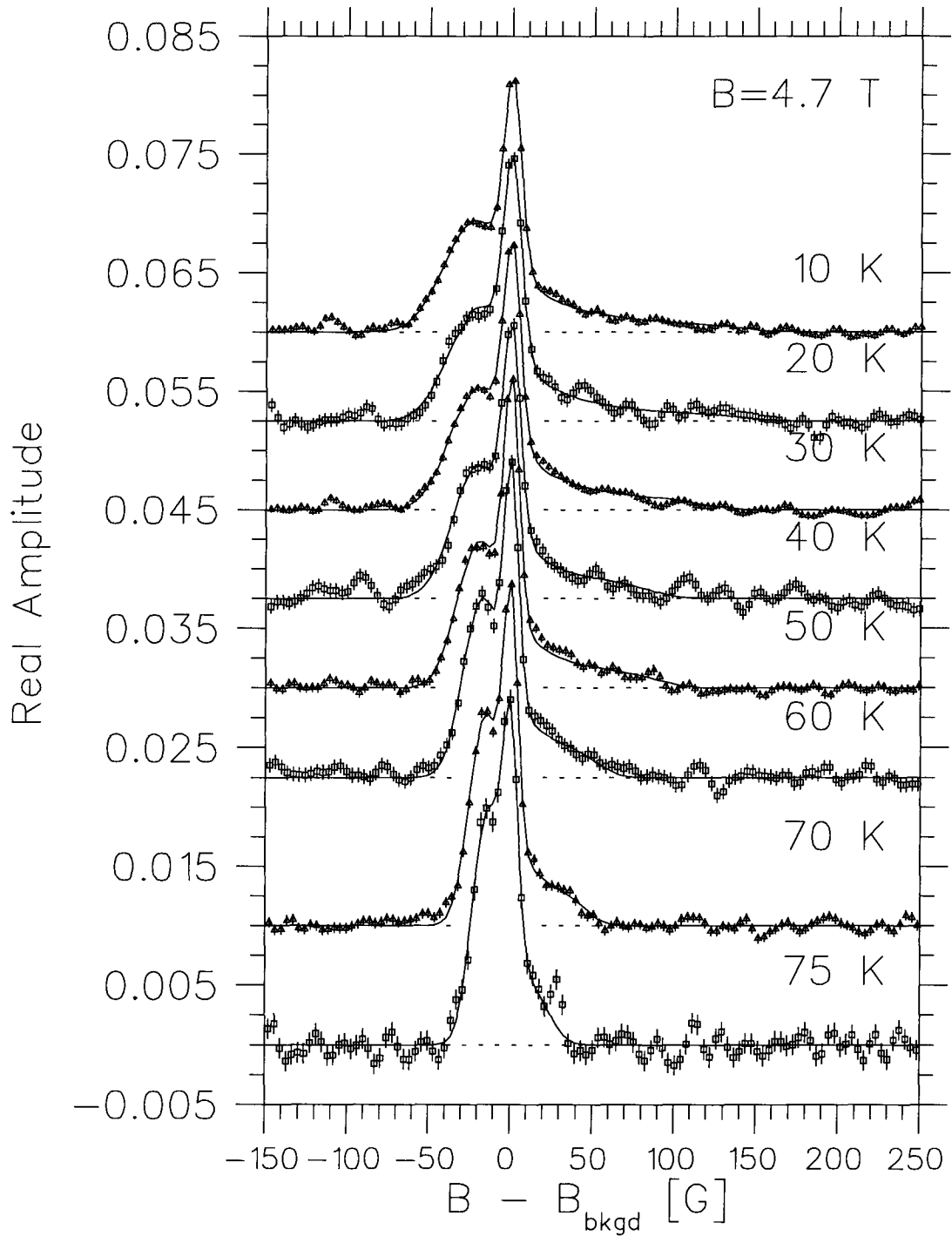


Figure B.13: High Field μ SR lineshapes and fits to the Modified London Model, for data at a field of $B = 4.7$ T. The lineshapes have been plotted relative to the background field in Gauss ($1 \text{ G} = 10^{-4} \text{ T}$), with an arbitrary vertical offset.

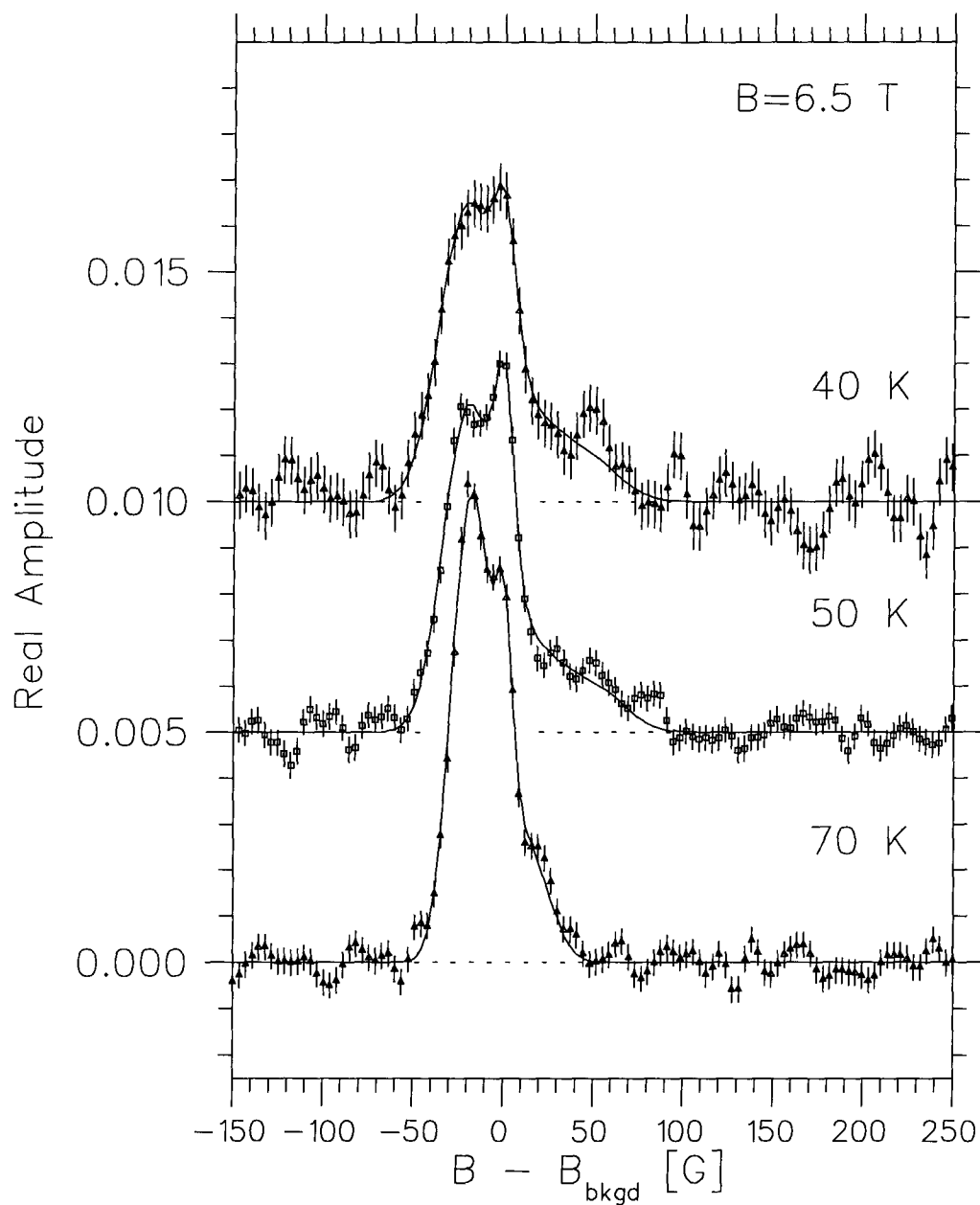


Figure B.14: High Field μ SR lineshapes and fits to the Modified London Model, for data at a field of $B = 6.5$ T. The lineshapes have been plotted relative to the background field in Gauss ($1 \text{ G} = 10^{-4} \text{ T}$), with an arbitrary vertical offset.

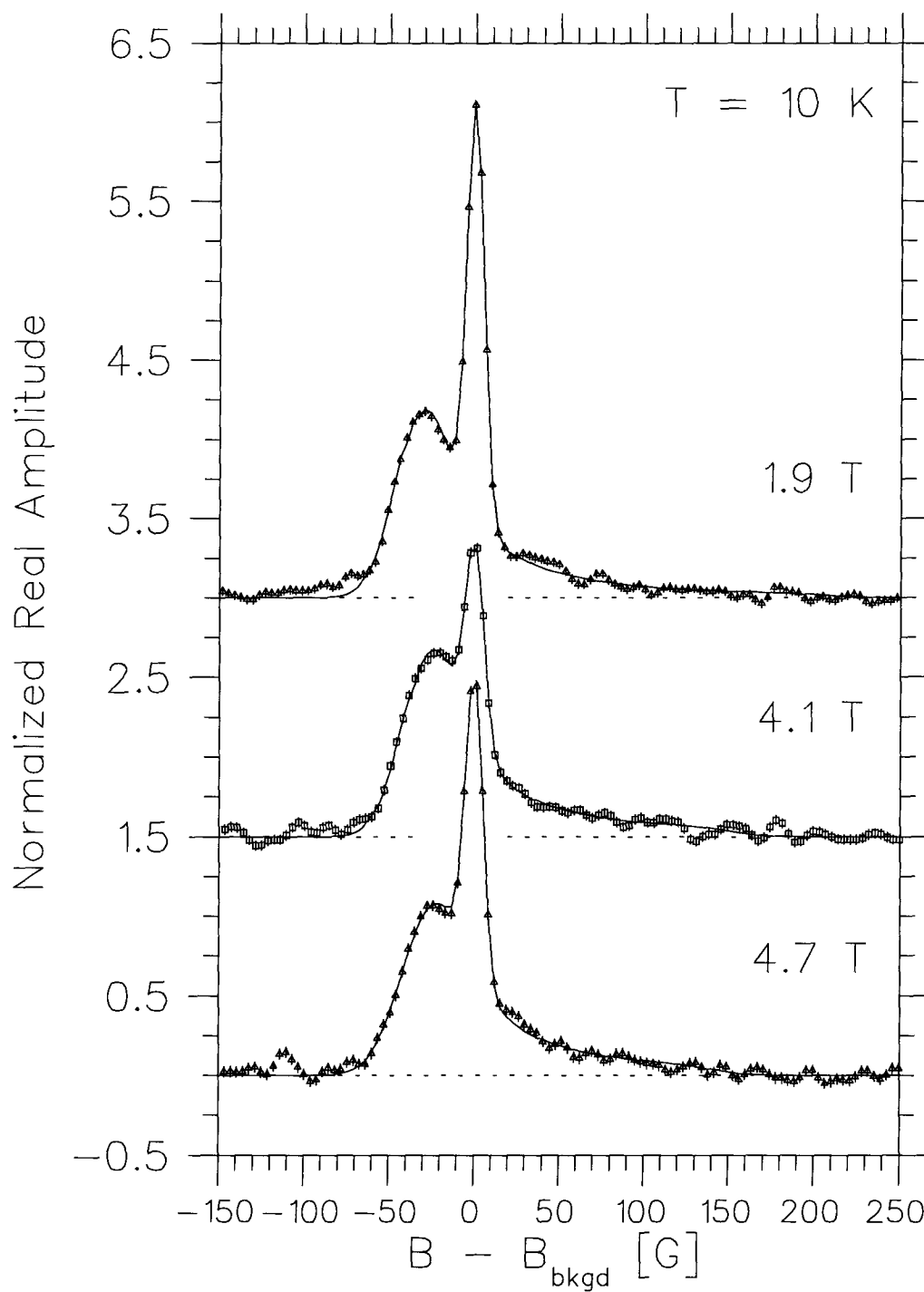


Figure B.15: High Field μ SR lineshapes and fits to the Modified London Model, for data at a temperature of 10 K. The lineshapes have been plotted relative to the background field in Gauss ($1 \text{ G} = 10^{-4} \text{ T}$), with an arbitrary vertical offset.

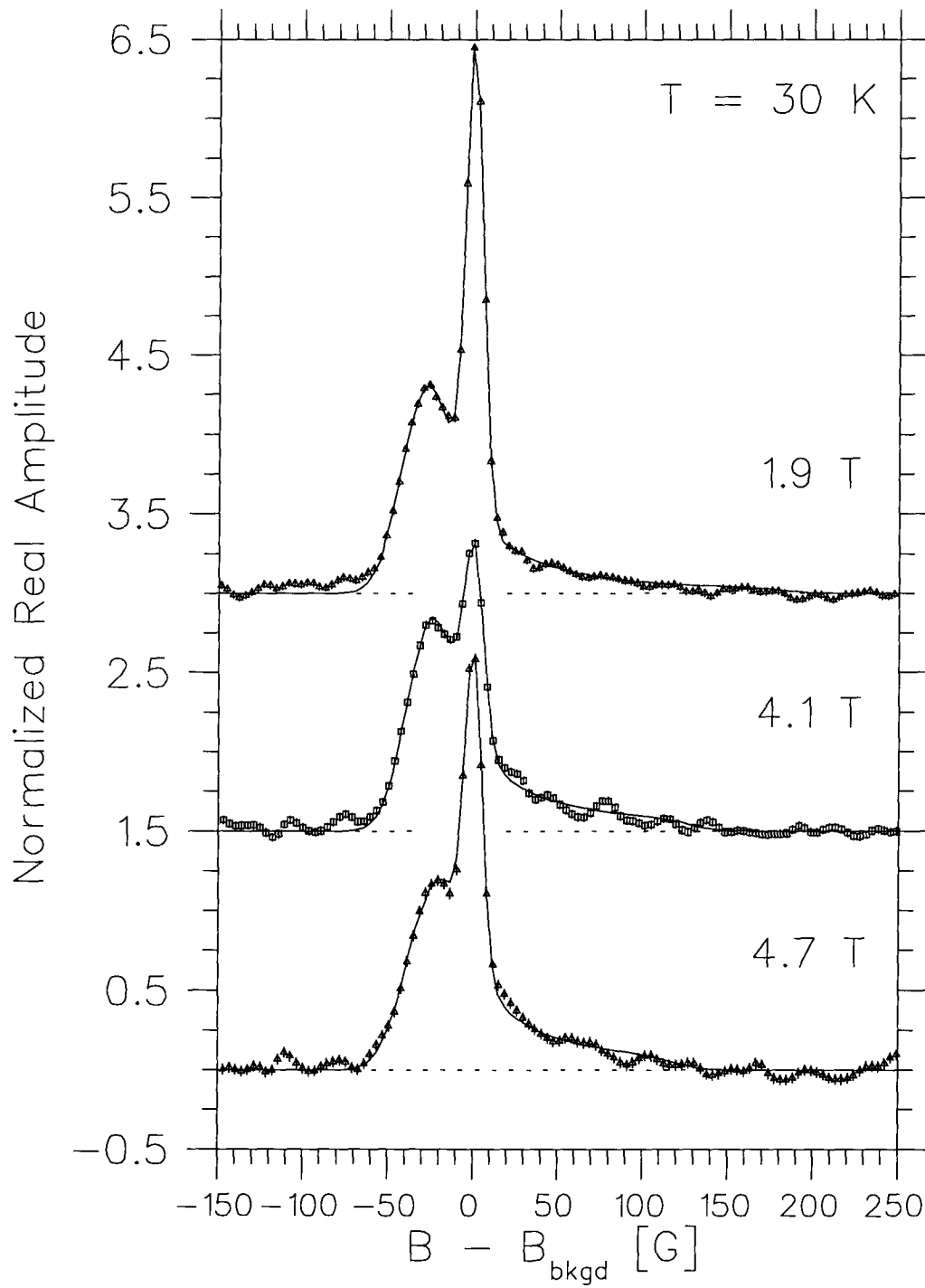


Figure B.16: High Field μ SR lineshapes and fits to the Modified London Model, for data at a temperature of 30 K. The lineshapes have been plotted relative to the background field in Gauss ($1 \text{ G} = 10^{-4} \text{ T}$), with an arbitrary vertical offset.

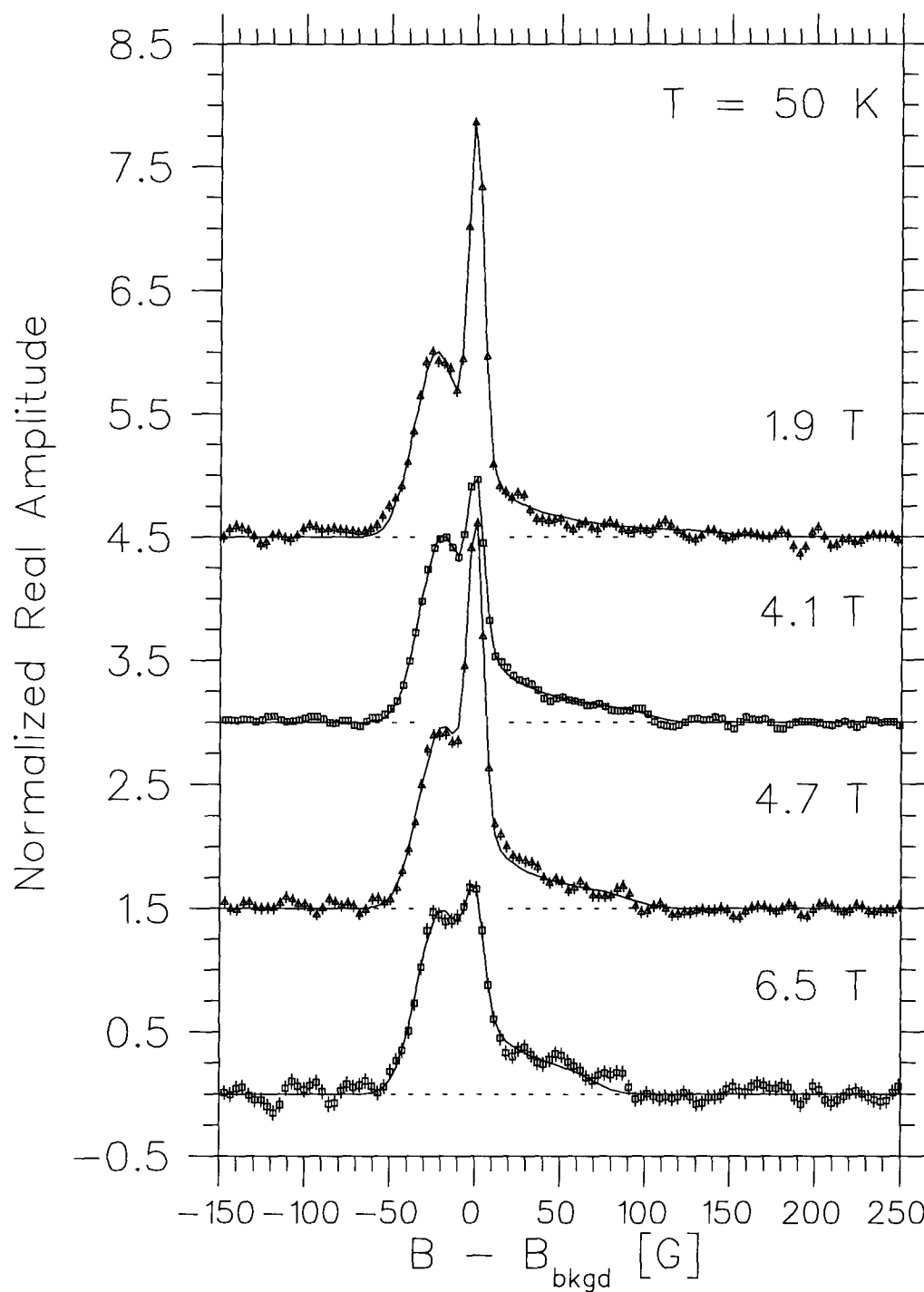


Figure B.17: High Field μ SR lineshapes and fits to the Modified London Model, for data at a temperature of 50 K. The lineshapes have been plotted relative to the background field in Gauss ($1 \text{ G} = 10^{-4} \text{ T}$), with an arbitrary vertical offset.

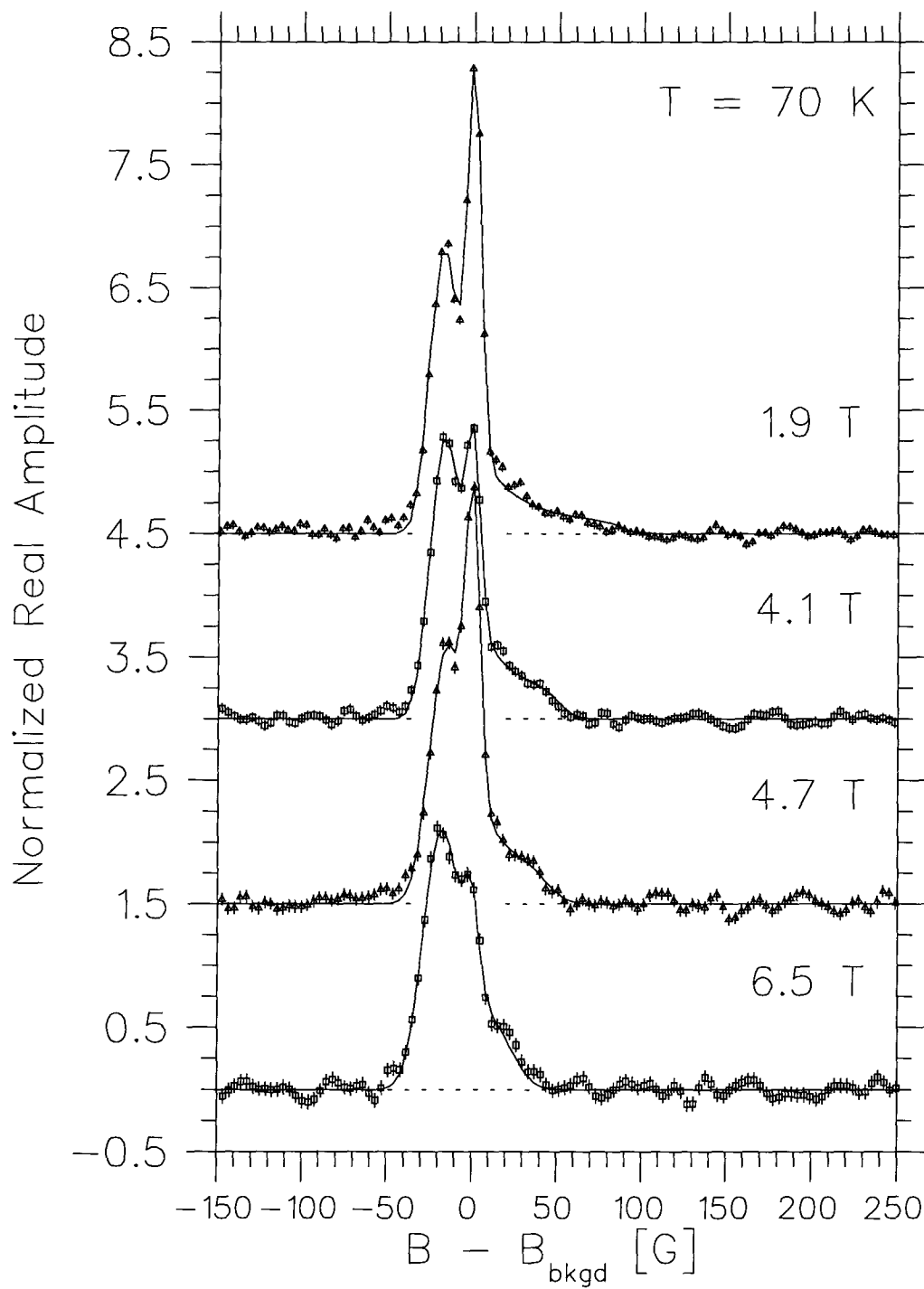


Figure B.18: High Field μ SR lineshapes and fits to the Modified London Model, for data at a temperature of 70 K. The lineshapes have been plotted relative to the background field in Gauss ($1 \text{ G} = 10^{-4} \text{ T}$), with an arbitrary vertical offset.